Development of High-performance Vanadium Oxide Cathodes for Rechargeable Metal-ion Batteries

Yinan Lu

A thesis presented for the degree of Doctor of Philosophy

Supervised by

Dr. Buddha Deka Boruah

Professor Ivan P. Parkin

Department of Chemistry

Mathematical and Physical Sciences Faculty

University College London

November 2024

Declaration

I, Yinan Lu, confirm that the work presented in this thesis is my own. Where information has been derived from other sources (publications, websites, and databases), I confirm that this has been indicated in the thesis. All the figures from publications (including my own work) have obtained their copyright permission from the journal publisher.

Abstract

Vanadium pentoxide (V₂O₅) deems as promising cathode candidate for rechargeable metal-ion batteries owing to a layered structure, high chemical and thermal stability, electrochemical safety, low cost, and ease of preparation. As a cost-effective option for cathode materials in both lithium-ion batteries (LIBs) and zinc-ion batteries (ZIBs), V₂O₅ has attracted great attention due to its high theoretical specific capacity values. However, several challenges impede its practical use, including insufficient practical capacity, sluggish ion diffusion, low intrinsic conductivity, and limited cycling stability. To address these limitations, this thesis has developed strategies including hydrogenation, doping, and defect engineering to improve the electrochemical and optical performance of V₂O₅-based cathode materials. Through an indepth examination of the physicochemical characteristics and a detailed study of the charge storage mechanisms, the thesis emphasizes the importance of V₂O₅ modifications in enhancing battery performance. The findings offer valuable insights for the future development of highperformance, rechargeable metal-ion batteries. This research consists of three projects: enhancing the optical and electrochemical properties of hydrogenated V₂O₅ for photoaccelerated lithium-ion batteries, designing pre-doped V2O5-based materials for highperformance zinc-ion batteries, and developing cation-doped V₂O₅ electrodes with engineered oxygen vacancies for lithium-ion batteries. The specific aims and outcomes are summarized below. A detailed summary of the objectives and key results of these three research areas is provided below.

(1) Photovoltaic cells integrated with batteries face challenges such as additional ohmic resistance and inefficiencies caused by mismatches in energy transfer among their components. To address these limitations, researchers are exploring the development of photo-accelerated batteries that combine energy harvesting and storage into a single device. This approach could reduce expenses, boost energy conversion efficiency and develop lightweight devices. This work introduces a novel strategy for designing photocathodes using hydrogenated vanadium pentoxide (H:V₂O₅) nanofibers, which enhances optical activity, electronic conductivity, and ion diffusion rates within photo-accelerated Li-ion batteries. Compared to pristine V₂O₅, the H:V₂O₅ showed better electrochemical performance, with a 43% and 41% increase in specific capacity under dark and illuminated

conditions, respectively, at a current density of 2000 mA g⁻¹. Characterization techniques, like energy-dispersive X-ray spectroscopy (EDS), X-ray photoelectron spectroscopy (XPS), UV-Visible (UV-Vis) spectroscopy, and photoluminescence (PL), revealed that the enhanced photocurrent generation was linked to defect mid-gap states, associated with oxygen-related defects and hydroxyl groups, which increased optical absorption and photoactivity. Moreover, density functional theory (DFT) simulations further confirmed that the presence of oxygen vacancies significantly reduces the energy barrier for Li-ion diffusion. This research holds great promise for the development of high-performance photocathodes in future energy storage applications.

- (2) Rechargeable ZIBs are gaining significant attention because of their affordability, abundant raw materials, and eco-friendly nature. The use of aqueous electrolytes in ZIBs also offers a substantial safety advantage over the flammable organic electrolytes commonly used in LIBs. Despite these benefits, the development of high-performance cathode materials for ZIBs remains a critical challenge. This work applies cation doping approach to synthesize and evaluate four distinct materials: pristine vanadium oxide (V₂O₅), sodium-doped vanadium oxide (Na-V₂O₅), potassium-doped vanadium oxide (K-V₂O₅), and ammonium-doped vanadium oxide (NH₄-V₂O₅). Transmission electron microscopy (TEM) and X-ray diffraction (XRD) identify the interplanar distance of pristine V₂O₅ expanded upon cation insertion. Among all samples, the NH₄-V₂O₅ electrode achieved the highest specific capacity, reaching 310.8 mAh g⁻¹ at a current density of 100 mA g⁻¹, along with superior cycling stability. This enhanced performance is attributed to the highest V⁴⁺/V⁵⁺ redox couple ratio, the pillar effect introduced by ammonium cations, and the increased interlayer spacing. These findings provide important insights for the design and development of advanced cathode materials in the future.
- (3) Different cations have been explored individually for LIBs, the mechanisms behind cation doping remain complex and not fully elucidated, posing challenges in selecting the most effective cations. In this research, hydrothermal synthesis was employed to create three distinct types of cation-doped V₂O₅ nanofibers, which were characterized using scanning electron microscopy (SEM) and TEM. The introduction of cations resulted in several beneficial modifications: expanded interlayer spacing, increased concentration of oxygen vacancies, and an elevated V⁴⁺/V⁵⁺ ratio. These structural and chemical enhancements

collectively facilitated enhanced Li⁺ ion diffusion, improved capacity, stable cycling performance, and reduced charge transfer resistance. Among the synthesized materials, NAVO demonstrated outstanding electrochemical performance, achieving discharge capacities of 249.1 and 122.0 mAh g⁻¹ at current densities of 100 and 2000 mA g⁻¹, respectively. Furthermore, it demonstrated impressive cycling stability, with an initial specific capacity of 222.1 mAh g⁻¹ at 1000 mA g⁻¹, retaining 150.5 mAh g⁻¹ after 30 cycles, corresponding to over 67% capacity retention. This study sheds light on the impact of cation doping on the electrochemical performance in LIBs and paves the way toward the development of lithium-ion batteries with improved energy density, power performance, and cycle life.

Impact Statement

This PhD project emphasizes different advanced approaches including hydrogenation, doping, and defect engineering to improve the electrochemical and optical performance of V₂O₅-based cathode materials in LIBs and ZIBs. The impact and highlights of this thesis were summarized below:

In the first study, the development of photocathodes in LIBs has witnessed significant progress in recent times. The dual-functional photocathode has shown improved capacity and rate performance under illumination conditions. Herein, the first hydrogenated V₂O₅ photocathode for photo-accelerated LIBs was proposed. The design integrates hydrogenated V₂O₅ nanofibers with reduced graphene oxide, poly(3-hexylthiophene) (P3HT), and poly(vinylidene fluoride) (PVDF), forming a heterojunction that facilitates photo-charge separation and conductivity. The hydrogenation process substantially increased the specific capacity of the material under both illuminated and dark conditions, demonstrating enhancements in optical activity, electronic conductivity, and ion diffusion rates. The study also proposed a mechanism involving oxygen-deficiency defects, offering a foundation for future advancements in photoaccelerated battery technology.

In the second study, considerable advancements have been made in developing cathode materials for rechargeable Zn-ion batteries. Vanadium-based cathode materials, such as V₂O₅, have shown great promise due to their ability to reversibly store Zn²⁺ ions and maintain long-term cycling stability while offering higher capacities. However, several challenges need to be addressed to achieve high-performance batteries. These challenges include the sluggish diffusion of zinc ions caused by high energy barriers within the V₂O₅ layers, the requirement for a pre-activation process, electrode structure degradation over time, and resulting capacities lower than theoretical values. This work synthesized four types of materials, including pristine V₂O₅, NH₄-V₂O₅, Na-V₂O₅, and K-V₂O₅, and evaluated their electrochemical behavior. NH₄-V₂O₅ outperformed the others, benefiting from an increased V⁴⁺/V⁵⁺ redox couple, especially the higher presence of V⁴⁺, which boosted its electrochemical capabilities. Moreover, *ex-situ* HRTEM images and d-spacing measurements for NH₄-V₂O₅ were performed both before and after cycling, providing additional confirmation of the material's structural resilience following

prolonged cycling tests. These findings offer critical insights into the future design and development of high-performance cathode materials for ZIBs.

In the third study, the methods to boost capacity for LIBs have been extensively studied. It has been observed that cation doping not only contributes to stabilizing the crystal structure during cycling but also plays a crucial role in expanding the interlayer distance, thereby improving overall capacity. However, the specific roles of different cations in this context have not been extensively studied. Herein, cation-doped V₂O₅-based cathodes were fabricated via hydrothermal technique. The incorporated cations generated oxygen vacancies and elevated the concentration of V⁴⁺, suggesting a potential mechanism that enhances charge storage capacity and improves ion diffusion. Among the tested materials, NAVO displayed superior electrochemical performance, even at high current densities. These results contribute valuable knowledge for designing cathode materials suitable for high-energy and high-power LIBs, addressing needs in electric vehicles and portable electronics that demand rapid charging and long-term durability.

Overall, these accomplishments, encompassing both material innovations and insights into underlying mechanisms, are believed to drive the advancement of lithium-ion and zinc-ion batteries, benefiting both academic research and commercial applications. The application of various engineering techniques to modify V_2O_5 offers an essential strategy for improving battery performance. By bridging fundamental physiochemical principles with electrochemical performance enhancements, the development of V_2O_5 -based cathode materials will advance the rechargeable metal-ion batteries technology to the next level.

Acknowledgements

I would like to express my heartfelt gratitude to my primary supervisor, Dr. Buddha Deka Boruah, for his invaluable guidance, support, and mentorship throughout my doctoral journey. His dedication to his students and his expertise in scientific research has profoundly shaped my academic growth. I am especially grateful for his patience and encouragement during this challenging yet rewarding experience. I would also like to extend my sincere thanks to my subsidiary supervisor, Prof. Ivan P. Parkin, whose affirmation and understanding have been a constant source of encouragement for me. His support has provided me with the confidence to achieve my goals.

I am deeply appreciative of all my collaborators who contributed to my doctoral research. My heartfelt thanks go to Prof Michael De Volder, Dr. Bo Wen, Dr. Arvind Pujari, and Dr Holly Andersen, for their invaluable insights and contributions. I want to thank Prof. Alex M. Ganose and Dr. Ruiqi Wu (Imperial College London) for their assistance and collaboration on the computational work in Chapter 3. A special thanks to Dr. Tianlei Wang, who generously assisted with the TEM and SEM imaging, and to Dr. Joanna Borowiec, who provided invaluable support with XPS testing.

I want to express my deepest gratitude to Dr. Tianlei Wang for the tremendous support he provided during one of the most challenging periods of my life. His guidance and compassion helped me navigate through my struggles with depression, and I will always cherish the time we spent working together. To my emotional support circle: Dr. Rica, Dr. Burcu, Dr. Iman, and Dr. Galyam thank you for the laughter, tears, and TGIF we shared. To all the members in EMS2 group, thank you all and it is really an honour to work with you all. To all the other wonderful members of the Institute for Materials Discovery, I feel incredibly fortunate to have met all of you; the friendships we have built are a lifelong treasure that I will always cherish.

Finally, I would like to express my deepest gratitude to my family for their infinite love and continuous support during my PhD study.

Abbreviation

AC Active carbon

AFI Antiferromagnetic insulating

AIBs Aluminum-ion batteries

ALD Atomic layer deposition

AZIBs Aqueous zinc-ion batteries

BSE Backscattered electrons

CE Coulombic efficiency

CIBs Calcium-ion batteries

CPS Counts per second

CV Cyclic voltammetry

DFT Density functional theory

DI Deionized

EC Ethylene carbonate

EDS Energy-dispersive X-ray spectroscopy

EIS Electrochemical impedance spectroscopy

EPR Electron paramagnetic resonance

EVs Electric vehicles

GDC Galvanostatic discharge-charge

GITT Galvanostatic intermittent titration technique

H₂O₂ Hydrogen peroxide

HER Hydrogen evolution reaction

HRTEM High-resolution TEM

IDEs Interdigitated electrodes

IR Infrared

I-V Current-voltage

KCl Potassium chloride

KI Potassium iodide

KIBs Potassium-ion batteries

LCO LiCoO₂

LFP LiFePO₄

LIBs Lithium-ion batteries

LiTFSI Lithium bis(trifluoromethanesulfonyl)imide

LMO LiMn₂O₄

LWIR Long-wave infrared emissivity

M Metal

MgIBs Magnesium-ion batteries

MIBs Metal-ion batteries

MIT Metal-insulator transition

NaOH Sodium hydroxide

NH₄VO₃ Ammonium metavanadate

NIBs Sodium-ion batteries

NMC Nickel-manganese-cobalt

NMP N-Methyl-2-pyrrolidone

OCP Open-circuit potential

OER Oxygen evolution reaction

P3HT Poly(3-hexylthiophene)

PAW Projector-augmented wave

PBAs Prussian blue analogues

PC Propylene carbonate

Photo-ZIBs Photo-rechargeable zinc-ion batteries

PL Photoluminescence

PM Paramagnetic metal

ppm Parts per million

PTFE Polytetrafluoroethylene

PVDF Poly(vinylidene fluoride)

R_{ct} Charge transfer resistance

rGO Reduced graphene oxide

R_s Solution resistance

SAED Selected area electron diffraction

SE Secondary electrons

SEI Solid electrolyte interface

SEM Scanning electron microscopy

SHE Standard hydrogen electrode

TARC Temperature-adaptive radiative coating

TEM Transmission electron microscopy

TGA Thermogravimetric analysis

UV Ultraviolet

UV-Visible UV-Visible

V Vanadium

V₂O₃ Divanadium trioxide

V₂O₅ Vanadium pentoxide

V₃O₅ Trivanadium pentoxide

V₃O₇ Trivanadium heptaoxide

VASP Vienna ab initio simulation Package

V_O Oxygen vacancies

VO₂ Vanadium dioxide

XPS X-ray photoelectron spectroscopy

XRD X-ray diffraction

ZIBs Zinc-ion batteries

Zn(CF₃SO₃)₂ Zinc triflate

2D Two dimensional

3D Three dimensional

Table of Content

Declaration	1
Abstract	2
Impact Statement	5
Acknowledgements	7
Abbreviation	8
Table of Content	12
List of Figures	16
List of Tables	23
Chapter 1	24
1.1 Introduction	25
1.2 Vanadium Oxide	27
1.2.1 V ₂ O ₃	28
1.2.2 V ₃ O ₅	30
1.2.3 VO ₂	31
1.2.4 V ₂ O ₅	33
1.3 Rechargeable Metal-ion Batteries	38
1.3.1 Lithium-ion Batteries	39
1.3.2 Zinc-ion Batteries	44
1.3.3 Sodium-ion Batteries	48
1.3.4 Potassium-ion Batteries	49
1.3.5 Aluminum-ion Batteries	50
1.3.6 Magnesium-ion Batteries	51
1.3.7 Calcium-ion Batteries	51
1.4 Synthesis of Nanostructured V ₂ O ₅	55

1.4.1 Hydrothermal Method	55
1.4.2 Solvothermal Method	56
1.4.3 Sol-gel Approach	56
1.4.4 Atomic Layer Deposition	56
1.4.5 Other Methods	57
1.5 Engineering of V ₂ O ₅ Cathode	58
1.5.1 Doping	58
1.5.2 Defect Engineering	62
1.5.3 Structural Water Optimization	65
1.5.4 Micro/macroscopic Structure Engineering	67
1.6 Research Objectives and Outline	68
Chapter 2	71
2.1 Overview	72
2.2 Hydrothermal Synthesis	72
2.3 Materials Characterizations	73
2.3.1 Scanning Electron Microscopy	73
2.3.2 Transmission Electron Microscopy	75
2.3.3 X-ray Diffraction	76
2.3.4 Raman Spectroscopy	77
2.3.5 X-ray Photoelectron Spectroscopy	78
2.3.6 Ultraviolet-Visible Spectroscopy	79
2.3.7 Thermogravimetric Analysis	80
2.4 Electrochemical Characterizations	81
2.4.1 Coin-cell Assembly	81
2.4.2 Cyclic Voltammetry	83
2.4.3 Galvanostatic Discharge-charge Test	83

2.4.4 Long Cycling Test	84
2.4.5 Electrochemical Impedance Spectroscopy	84
Chapter 3	85
3.1 Introduction	86
3.2 Experimental Section	87
3.2.1 Chemicals	87
3.2.2 Synthesis of V ₂ O ₅ and H:V ₂ O ₅ .	87
3.2.3 Preparation of Photocathodes	88
3.2.4 Electrode and Device Assembly	88
3.2.5 Material Characterisations	88
3.2.6 Electrochemical Characterisations	88
3.2.7 Theoretical Methods	89
3.3 Results and Discussion	90
3.3.1 Cathode Characterizations	90
3.3.2 Electrochemical Performances	93
3.3.3 DFT Simulations	102
3.4 Summary	104
Chapter 4	106
4.1 Introduction	107
4.2 Experimental Section	108
4.2.1 Chemicals	108
4.2.2 Synthesis of V ₂ O ₅ , NH ₄ -V ₂ O ₅ , Na-V ₂ O ₅ and K-V ₂ O ₅	108
4.2.3 Preparation of Cathodes and Coin-cells	109
4.2.4 Electrochemical Characterisations	109
4.2.5 Material Characterisations	110
4.3 Results and Discussion	110

4.3.1 Cathode Characterizations	110
4.3.2 Electrochemical Performance	119
4.4 Summary	126
Chapter 5	128
5.1 Introduction	129
5.2 Experimental Section	130
5.2.1 Chemicals	130
5.2.2 Synthesis of V ₂ O ₅ , NH ₄ -V ₂ O ₅ , Na-V ₂ O ₅ and K-V ₂ O ₅	130
5.2.3 Preparation of cathodes and coin-cells	131
5.2.4 Material Characterisations	131
5.2.5 Electrochemical Characterisations	132
5.3 Results and Discussion	133
5.3.1 Cathode Characterizations	133
5.3.2 Electrochemical Performances	142
5.4 Summary	150
Chapter 6	151
6.1 Conclusions	152
6.2 Outlook	153
Reference	157
Publication List	102

List of Figures

Figure 1.1: The demonstration of worldwide primary energy consumption from 2018 to 2023,
by fuel type in exajoules from Statista. ³
Figure 1.2: Demonstration of different thermodynamically stable vanadium oxides and their applications
Figure 1.3: (a) Along the (001) direction; (b) along the (110) direction in the perspective view of V ₂ O ₃ . Reproduced with permission. Copyright 2023, American Chemical Society. (c) Generic temperature-pressure phase diagram of bulk V ₂ O ₃ . Reproduced with permission. Copyright 2021, American Association for the Advancement of Science. (d) Schematic illustration of the oxidation at full charge state of V ₂ O ₃ . Reproduced with permission. Copyright 2020, American Chemical Society. (e) Crystal structure of V ₃ O ₅ . Reproduced with permission. Copyright 2023, American Chemical Society. Copyright 2023, American Chemical Society. Copyright 2023, American Chemical Society. Copyright 2026, Phases with different crystallographic orientations. Reproduced with permission. Copyright 2016, Springer Nature. Society. Springer Nature. Springer Nature. Society. Springer Nature. Springer Nature. Society. Springer Nature. Springer Nature Nat
Figure 1.5: The crystal structure of orthorhombic V ₂ O ₅ with (a) along b-axis, (b) along c-axis and (c) coordination environment around a single V atom. Reproduced with permission. ⁷⁹ Copyright 2018, Elsevier.
Figure 1.6: Schematic diagram of charging and discharging process of LIBs40
Figure 1.7: Illustration of the development history of Zn-based batteries
Figure 1.8: Schematic illustration of the working principle of ZIBs47
Figure 1.9: (a) Metal/ion redox potential <i>vs.</i> SHE; (b) mean size of the ionic species (Shannon ionic radium for 6-fold coordinated cations); ²¹⁷ (c) theoretical volumetric and gravimetric capacities; ²⁰² (d) Earth abundance and production cost; ^{202,218} (e) comparison of various aspects of metal ion batteries. ²¹⁹
Figure 1.10: SEM images of various V_2O_5 nanomaterials. (a) Yolk–shell V_2O_5 . Reproduced with permission. Copyright 2018, Royal Society of Chemistry. (b) Centimetre-long V_2O_5 nanowires. Reproduced with permission. Copyright 2010, Wiley-VCH. (c) V_2O_5 nanofibers.

Reproduced with permission. ²²² Copyright 2022, Elsevier. (d) Hollow V ₂ O ₅ microspheres with
multiple double-walled shells. Reproduced with permission. ²²⁷ Copyright 2018, Royal Society
of Chemistry. (e) V ₂ O ₅ hollow microspheres. Reproduced with permission. ²²⁸ Copyright 2017
Elsevier. (f) 3D-V ₂ O ₅ . Reproduced with permission. ²³² Copyright 2020, Elsevier. (g) ALD
V ₂ O ₅ on c-Al ₂ O ₃ . Reproduced with permission. ²³⁸ Copyright 2017, American Chemical
Society. (h) V ₂ O ₅ nanofibers. Reproduced with permission. ²⁴⁴ Copyright 2019, Elsevier
Insets: (a, c, f) low magnification SEM images; (b, d, e) TEM images of corresponding V ₂ O ₅
nanomaterials58
Figure 1.11: Mechanism of formation of interface-defective V ₂ O ₅ nanochips through the effect
of the combusted graphene in the system by using the electrospun PAN fiber templates to
enhance the ZIBs performance (inset of the DSC curves shows the thermal behavior of all
samples in the temperature range of 25-400 °C). Reproduced with permission. ²⁶⁹ Copyright
2021, Elsevier
Figure 1.12: Schematic diagram of O _v -V ₂ O ₅ prepared by mechanical ball milling. Reproduced
with permission. ²⁷¹ Copyright 2022, Wiley-VCH64
Figure 2.1: Apparatus of hydrothermal autoclave
Figure 2.2: Physical instrument (a) Zeiss EVO LS15 and (b) JEOL JSM-7600F used to capture
SEM images74
Figure 2.3: Physical instrument JEOL JEM-2100 TEM used to obtain TEM and SAED images.
Figure 2.4: The Panalytical Empyrean XRD instrument used to obtain the crystal information
of samples
Figure 2.5: The Renishaw inViaTM confocal Raman microscope used to get Raman
spectroscopy measurements
Figure 2.6: The ThermoFisher Scientific XPS machine used for XPS tests in this research79
Figure 2.7: The Perkin Elmer Lambda 750S instrument used for UV-Vis measurements80
Figure 2.8: Physical instrument PerkinElmer TGA 4000 used for TGA measurements81
Figure 2.9: Demonstration of coin-cell assembly. (a) dark cell assembly and (b) light cell
assembly82

Figure 2.10: Pictures of our electrochemical testers. (a) galvanic static tester, (b) Neware 4000 tester and (c) Autolab.
Figure 3.1: (a) Schematic representation of a photodetector based on Au-V ₂ O ₅ or H:V ₂ O ₅ -Au interdigitated electrodes shown on the left, alongside a digital image on the right. (b) Digital photograph of an optical cell. Reproduced with permission. ¹⁹ Copyright 2023, Wiley-VCH.
Figure 3.2: SEM, TEM, and HRTEM images of (a–d) V ₂ O ₅ and (e–h) H:V ₂ O ₅ . Reproduced with permission. ¹⁹ Copyright 2023, Wiley-VCH
Figure 3.3: SAED patterns of (a) V ₂ O ₅ and (c) H:V ₂ O ₅ . EDS mappings of (b) V ₂ O ₅ and (d) H:V ₂ O ₅ . Reproduced with permission. ¹⁹ Copyright 2023, Wiley-VCH92
Figure 3.4: (a) XRD patterns and (b) Raman spectra of V ₂ O ₅ and H:V ₂ O ₅ , confirming the orthorhombic crystal structure of V ₂ O ₅ . (c) High-resolution XPS spectra of the V 2 <i>p</i> region and (d) O 1 <i>s</i> region for both V ₂ O ₅ and H:V ₂ O ₅ . (e) UV-Vis absorption spectra of V ₂ O ₅ and H:V ₂ O ₅ , with the inset in (e) displaying the PL spectra of the samples. Reproduced with permission. ¹⁹ Copyright 2023, Wiley-VCH.
Figure 3.5: (a) Current–voltage characteristics of the V ₂ O ₅ and (b) H:V ₂ O ₅ photodetectors under dark and illuminated conditions. (c) Response current over time for the photodetectors during alternating dark and light cycles at a bias voltage of 1 V. Reproduced with permission. ¹⁹ Copyright 2023, Wiley-VCH.
Figure 3.6: (a) CV curves of V_2O_5 and (b) $H:V_2O_5$ at various scan rates $(0.1 - 1.0 \text{ mV s}^{-1})$ in dark conditions. Comparative CVs of V_2O_5 and $H:V_2O_5$ at scan rates of (c) 0.5 mV s ⁻¹ and (d) 1.0 mV s ⁻¹ under dark conditions. (e, f) i_p/K versus $v^{1/2}$ plots for C1 (\approx 3.33 V)/A1 (\approx 3.36 V) and C2 (\approx 3.12 V)/A2 (\approx 3.51 V) peaks. Reproduced with permission. ¹⁹ Copyright 2023, Wiley-VCH.
Figure 3.7: Comparative CV curves of V_2O_5 and $H:V_2O_5$ at scan rates of (a) 0.2 mV s ⁻¹ , (b) 0.6 mV s ⁻¹ , and (c) 0.8 mV s ⁻¹ under dark and illuminated conditions, respectively. (d) CV curves of $H:V_2O_5$ at varying scan rates under illumination. Reproduced with permission. Copyright 2023, Wiley-VCH.
Figure 3.8: CV curves of H:V ₂ O ₅ at scan rates of (a) 0.5, (b) 0.8, and (c) 1 mV s ⁻¹ under dark and illuminated conditions. (d) Comparative CVs of V ₂ O ₅ and H:V ₂ O ₅ at a scan rate of 0.5 mV

s ⁻¹ under illumination. (e) Analysis of diffusion constants for H:V ₂ O ₅ in dark and illuminated conditions. (f) Diffusion constant comparison of V ₂ O ₅ and H:V ₂ O ₅ under illuminated conditions. Reproduced with permission. ¹⁹ Copyright 2023, Wiley-VCH97
Figure 3.9: (a, b) GDC curves comparing V ₂ O ₅ and H:V ₂ O ₅ at specific currents of 500 and 2000 mA g ⁻¹ under dark conditions. (c-f) GDC curves for H:V ₂ O ₅ at specific currents of 500, 2000, 200, and 1000 mA g ⁻¹ , measured under both dark and illuminated conditions. (g) Differential capacity (dQ/dV) curves for V ₂ O ₅ and H:V ₂ O ₅ at 500 mA g ⁻¹ in dark conditions. (h) dQ/dV curves of H:V ₂ O ₅ at 500 mA g ⁻¹ , comparing results under dark and illuminated conditions. Reproduced with permission. ¹⁹ Copyright 2023, Wiley-VCH
Figure 3.10: (a) Nyquist plots comparing V ₂ O ₅ and H:V ₂ O ₅ under light exposure. (b) Nyquist plots of H:V ₂ O ₅ measured in both dark and illuminated conditions. (c) Equivalent circuit model associated with the Nyquist plots. Reproduced with permission. Copyright 2023, Wiley-VCH.
Figure 3.11: (a) Rate performance comparison of V ₂ O ₅ and H:V ₂ O ₅ under dark conditions, highlighting specific capacity enhancements achieved through hydrogenation. (b) Rate performance of H:V ₂ O ₅ tested under both dark and illuminated conditions, illustrating increased specific capacities under illumination due to the contribution of photo-generated charges in the storage process. (c) Cycling stability of H:V ₂ O ₅ at 500 mA g ⁻¹ under dark and illuminated conditions, demonstrating the effect of illumination on sustained capacity improvement over time. Reproduced with permission. ¹⁹ Copyright 2023, Wiley-VCH101
Figure 3.12: (a) Open-circuit potentials as a function of illumination duration for V ₂ O ₅ and H:V ₂ O ₅ optical cells, followed by discharge at 0.05 mA cm ⁻² in dark conditions. (b) Analysis of absolute CV areas for an H:V ₂ O ₅ cell across different temperatures. (c) Plot of capacity enhancement, with capacity values normalized to those measured at 25°C. Reproduced with permission. ¹⁹ Copyright 2023, Wiley-VCH
Figure 3.13: (a) Diagram of the V ₂ O ₅ crystal structure, indicating potential pathways for Li ⁺ diffusion. (b) Lithium diffusion barrier along path A in V ₂ O ₅ with oxygen vacancies. (c) Lithium diffusion barrier along path A in V ₂ O ₅ with hydrogenated oxygen sites. Reproduced with permission. Copyright 2023, Wiley-VCH
Figure 4.1: SEM images showing (a) V ₂ O ₅ , (b) NH ₄ -V ₂ O ₅ , (c) Na-V ₂ O ₅ and (d) K-V ₂ O ₅ . Reproduced with permission. ³³⁹ Copyright 2024. Tsinghua University Press

Figure 4.2: TEM and HRTEM images of (a, b) V ₂ O ₅ , (d, e) NH ₄ -V ₂ O ₅ , (g, h) Na-V ₂ O ₅ , (j, k)
K-V ₂ O ₅ , along with SAED patterns for (c) V ₂ O ₅ , (f) NH ₄ -V ₂ O ₅ , (i) Na-V ₂ O ₅ , and (l) K-V ₂ O ₅ .
Inset: iFFT patterns from selected areas in HRTEM images. Reproduced with permission. ³³⁹
Copyright 2024, Tsinghua University Press
Figure 4.3: EDS elemental maps for (a) V ₂ O ₅ , (b) NH ₄ -V ₂ O ₅ , (c) Na-V ₂ O ₅ and (d) K-V ₂ O ₅ .
Reproduced with permission. ³³⁹ Copyright 2024, Tsinghua University Press
Figure 4.4: XRD patterns for (a) V_2O_5 , (b) $NH_4-V_2O_5$, (c) $Na-V_2O_5$ and (d) $K-V_2O_5$.
Reproduced with permission. ³³⁹ Copyright 2024, Tsinghua University Press
Figure 4.5: UV-Vis absorption spectra for (a) V ₂ O ₅ , (b) NH ₄ -V ₂ O ₅ , (c) Na-V ₂ O ₅ , and (d) K-
V_2O_5 . Inset: Tauc plots of the respective samples. Reproduced with permission. ³³⁹ Copyright
2024, Tsinghua University Press
Figure 4.6: Raman spectra for (a) V_2O_5 , (b) $NH_4-V_2O_5$, (c) $Na-V_2O_5$ and (d) $K-V_2O_5$.
Reproduced with permission. ³³⁹ Copyright 2024, Tsinghua University Press
Figure 4.7: XPS spectra showing (a) O 1s and (b) V $2p_{1/2}$ and V $2p_{3/2}$ for the samples.
Reproduced with permission. ³³⁹ Copyright 2024, Tsinghua University Press
Figure 4.8: TGA curves for (a) V ₂ O ₅ , (b) NH ₄ -V ₂ O ₅ , (c) Na-V ₂ O ₅ and (d) K-V ₂ O ₅ . Reproduced
with permission. 339 Copyright 2024, Tsinghua University Press
Figure 4.9: CV curves for (a) V ₂ O ₅ , (b) NH ₄ -V ₂ O ₅ , (c) Na-V ₂ O ₅ , and (d) K-V ₂ O ₅ electrodes
recorded at scan rates from 0.2 to 1.0 mV s ⁻¹ within a potential range of 0.2 to 1.6 V.
Comparison of CV profiles for all samples at scan rates of (e) 0.5 and (f) 1.0 mV s ⁻¹ .
Reproduced with permission. ³³⁹ Copyright 2024, Tsinghua University Press
Figure 4.10: Estimated capacity contributions for (a) V ₂ O ₅ , (b) NH ₄ -V ₂ O ₅ , (c) Na-V ₂ O ₅ and (d)
K-V ₂ O ₅ electrodes. Reproduced with permission. ³³⁹ Copyright 2024, Tsinghua University
Press
Figure 4.11: GDC curves for (a) V ₂ O ₅ , (b) NH ₄ -V ₂ O ₅ , (c) Na-V ₂ O ₅ , and (d) K-V ₂ O ₅ at various
specific currents from 100 to 5000 mA g ⁻¹ within a voltage range of 0.2 to 1.6 V. Comparative
GDC curves of the electrodes at specific currents of (e) 500 and (f) 5000 mA g ⁻¹ , respectively.
(g) Rate tests showing the electrodes' performance. Reproduced with permission. ³³⁹ Copyright
2024, Tsinghua University Press.

Figure 4.12: Nyquist plots and equivalent circuit model for cells with V ₂ O ₅ , NH ₄ -V ₂ O ₅ , Na-
V_2O_5 , and K- V_2O_5 . Reproduced with permission. ³³⁹ Copyright 2024, Tsinghua University
Press
Figure 4.13: Long-term cycling performance of NH ₄ -V ₂ O ₅ , with CE indicating Coulombic
efficiency in the plot. Reproduced with permission. ³³⁹ Copyright 2024, Tsinghua University
Press
Figure 4.14: TEM and HRTEM images with interlayer d-spacing for (a-c) pristine NH ₄ -V ₂ O ₅ ,
(d-f) NH ₄ -V ₂ O ₅ after 500 cycles, and (g-i) NH ₄ -V ₂ O ₅ after 1000 cycles. Reproduced with
permission. 339 Copyright 2024, Tsinghua University Press. 125
Figure 5.1: SEM images of the (a-b) V ₂ O ₅ , (c-d) NAVO, (e-f) NHVO and (g-h) KVO133
Figure 5.2: TEM and HRTEM images of the (a-b) V ₂ O ₅ , (d-e) NAVO, (g-h) NHVO, (j-k) KVO,
and SAED patterns of (c) V_2O_5 , (f) NAVO, (i) NHVO, (l) KVO. Inset: iFFT patterns of selected
area in HRTEM images
Figure 5.3: EDS elemental mapping of the (a) V ₂ O ₅ , (b) NAVO, (c) NHVO and (d) KVO. All
the scale bars represent the 250 nm
Figure 5.4: XRD patterns of the (a) V_2O_5 , (b) NAVO, (c) NHVO and (d) KVO136
Figure 5.5: UV-Vis absorption spectroscopy of the (a) V ₂ O ₅ , (b) NAVO, (c) NHVO and (d)
KVO. Inset: tauc plots of corresponding samples
Figure 5.6: Raman spectra of the (a) V_2O_5 , (b) NAVO, (c) NHVO and (d) KVO139
Figure 5.7: XPS spectra of four samples: (a) O 1s and (b) V $2p_{1/2}$ and V $2p_{3/2}$ 141
Figure 5.8: CV curves of the (a) V_2O_5 , (b) NAVO, (c) NHVO and (d) KVO electrodes recorded
at various scan rates ranging from 0.2 to $1.0~\text{mV}~\text{s}^{-1}$, within a potential window of 2 to 4 V. A
comparison of the CV profiles at scan rates of (e) $0.5~\text{mV}~\text{s}^{\text{-1}}$ and (f) $1.0~\text{mV}~\text{s}^{\text{-1}}$ for all samples.
142
Figure 5.9: The estimated capacity contributions for the (a) V ₂ O ₅ , (b) NAVO, (c) NHVO and
(d) KVO electrodes. 143
Figure 5.10: Diffusion constant analysis of the V ₂ O ₅ , NAVO, NHVO and KVO electrodes for
(a) A2 and (b) C1 peaks

Figure 5.11: GDC curves of the (a) V ₂ O ₅ , (b) NAVO, (c) NHVO and (d) KVO at different
specific currents, ranging from 100 to 2000 mA g ⁻¹ , across the voltage range of 2 to 4 V.
Comparative GDC curves of the electrodes at specific currents of (e) 100 and (f) 1000 mA g ⁻¹ ,
respectively
Figure 5.12: Rate tests exhibiting the performance of the electrodes at various current densities.
147
Figure 5.13: Long-term cycling test of V ₂ O ₅ , NAVO, NHVO and KVO electrodes at (a) 200,
(b) 1000 mA g ⁻¹ . (c) Long-term cycling test of NAVO, where CE represents Coulombic
efficiency in the plot
Figure 5.14: Nyquist plots and equivalent circuit model for cells containing V ₂ O ₅ , NAVO,
NHVO and KVO

List of Tables

Table 1.1: Comparison of several kinds of cathode materials for LIBs
Table 1.2: Summary of the electrochemical properties of the cation doped V ₂ O ₅ samples in
MIBs
Table 3.1: Slopes for cathodic (C1 and C2) and anodic (A1 and A2) peaks of V ₂ O ₅ and H:V ₂ O
in illuminated conditions96
Table 4.1: Calculated b-values for the cathodic and anodic peaks of V ₂ O ₅ , NH ₄ -V ₂ O ₅ , Na-V ₂ O ₅
and K-V ₂ O ₅
Table 4.2: Comparison of the electrochemical performance of NH ₄ -V ₂ O ₅ in this study with
other reported V ₂ O ₅ -based materials in ZIBs from the literature
Table 5.1: Calculated b-values for anodic and cathodic peaks of V ₂ O ₅ , NAVO, NHVO and
KVO143
Table 5.2: Slopes for anodic (A1 and A2) and cathodic (C1 and C2) and peaks of V2O5, NAVO
NHVO and KVO from the corresponding CV curves

Chapter 1

Background and Literature Review

This chapter of the thesis describes the development of vanadium oxides-based cathode materials for metal-ions batteries and summarizes the synthetic methods and engineering methods for V_2O_5 . The primary aim of this thesis is to explore and enhance the energy storage capacities of V_2O_5 cathodes for both Li-ion and Zn-ion batteries.

1.1 Introduction

According to a United Nations report, the world's population is rapidly expanding. ¹ At the beginning of the industrial revolution, the global population was around 700 million. Today, it exceeds 8.1 billion. Projections indicate an increase of almost 2 billion individuals over the next three decades, potentially peaking at nearly 10.4 billion by the mid-2080s. In conjunction with this growing population, the accelerated processes of industrialization and modernization have caused a significant escalation in energy demand. Global energy consumption is anticipated to attain approximately 660 quadrillion British Thermal Units by the year 2050, representing a 15% increase relative to the levels observed in 2021. ² To meet the global energy demand, fossil fuels remain the dominant energy sources due to their cost-efficiency and reliability. As depicted in Figure 1.1, fossil fuel consumption reached 488.9, 490.07, 463.68, 491.7, 494.05 and 504.83 exajoules between 2018 and 2023, respectively. Concurrently, renewable energy sources have shown a consistent upward trend, ascending from 25.83 to 50.58 exajoules within the same timeframe. The emission of CO₂ from fossil fuels combustion is a major factor causing global warming. The current energy system accounts for approximately 75% of global greenhouse gas emissions. ⁴ The amount of CO₂ in the atmosphere has sharply risen from 365 parts per million (ppm) in 2002 to over 420 ppm in 2024. ⁵ Given the urgency of climate change and global warming, it is imperative to transition to a greener and more sustainable energy system.

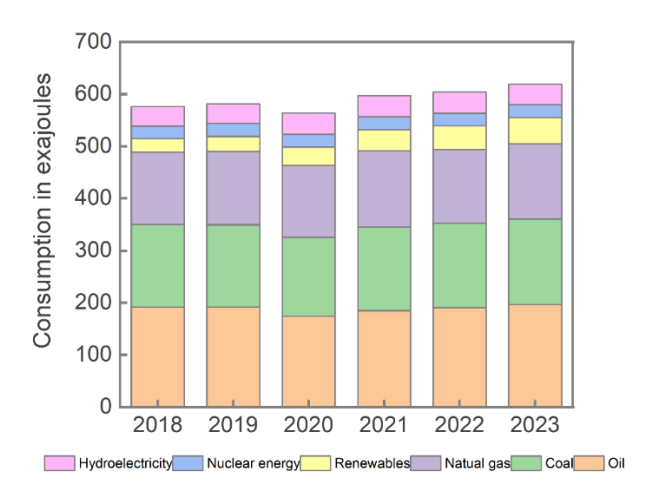


Figure 1.1: The demonstration of worldwide primary energy consumption from 2018 to 2023, by fuel type in exajoules from Statista.³

To achieve this goal, the Paris Agreement was established. It targets to limit the global temperature rise to 1.5 °C above pre-industrial levels by advocating for a 45% reduction in greenhouse gas emissions by 2030 and achieving net-zero emissions by 2050. ⁶ At the 28th United Nations Climate Change Conference, an essential agreement was made to accelerate the transition away from fossil fuels and to enhance renewable energy capacity threefold by 2030. ⁷

Renewable energy sources such as wind, solar, and tidal power are subject to weather and climate conditions. Their intermittent and fluctuation nature bring instability into powder systems. The integration of energy storage systems can efficiently capture and store renewable energy for later use. Energy storage systems, categorized based on their operational principles, include pumped hydropower, electrochemical, electromechanical, and thermal storage. Pumped hydropower stands out for its affordability and storage capabilities, comprising 92.3% of the market share in 2020. 8 Despite this, the construction of hydropower stations faces cost and geological limitations, restricting its application. Electrochemical energy storage systems, on the other hand, are gaining popularity due to their geographical flexibility, rapid response capabilities, and reliable power delivery, making them an excellent match for renewable energy storage and distribution. The electrochemical storage market is projected to grow significantly, with the rechargeable batteries market expanding from an estimated 5.4 billion U.S. dollars in 2022 to over 17.5 billion U.S. dollars by 2028. 9 The most popular rechargeable batteries now include lead-acid, nickel-cadmium, nickel-metal hydride, and lithium-ion batteries (LIBs). In 2022, LIBs accounted for 95% of the global market share owing to their exceptional energy density (150–200 Wh kg⁻¹), long cycle life, and low maintenance requirement. LIBs outperform other batteries across a wide range of applications, such as personal electronic devices, electric vehicles, hybrid electric vehicles and smart grid. ¹⁰

As energy demands continue to rise, existing battery systems are struggling to meet the growing needs. Advancing battery technology depends on progress in materials science, particularly in the development of high-performance electrode materials, which play an important role in pushing the boundaries of current battery performance. Discovering and developing next-generation electrode materials is crucial to bridging the gap between rising energy demands and battery capabilities, paving the way for a more sustainable and energy-efficient future.

1.2 Vanadium Oxide

Vanadium (V) ranks as the 6th most abundant transition metal and the 20th most abundant element in the Earth's crust. 11, 12 In nature, it rarely occurs in its elemental form due to its reactivity. Vanadium is sensitive to oxygen and capable of reacting with nitrogen and carbon at elevated temperature. ¹³ With its electronic configuration of [Ar] $3d^34s^2$, V is a versatile element that exhibits multiple oxidation states. These various oxidation states enable the formation of oxides either in single oxidation states or mixed oxidation states, such as the Magnéli phase (V_nO_{2n-1}) and the Wadsley phase (V_nO_{2n+1}) . ¹⁴ There are five thermally stable stoichiometric phases: divanadium trioxide (V₂O₃), trivanadium pentoxide (V₃O₅), vanadium dioxide (VO₂), trivanadium heptaoxide (V₃O₇), and vanadium pentoxide (V₂O₅). The remaining metastable phases tend to decompose to stable phases. The crystalline structure of vanadium oxides vary based on the coordination number of oxygen atoms, forming octahedral, square pyramidal, trigonal bipyramidal, and tetrahedral geometries with shared corners, edges and faces. ¹⁵ The strong electron-electron interactions in various phases of vanadium oxides, caused by the localized nature of the partially filled "d" orbitals, endow these materials with exceptional optical, ^{16, 17} electrical, ¹⁸ electrochemical, ¹⁹ and magnetic properties. ²⁰ As shown in Figure 1.2, Vanadium oxides are used in a range of applications, including microelectronics^{21, 22}, energy storage devices^{23, 24}, and smart windows^{25, 26}. Additionally, they play a significant role in catalysis²⁷, further highlighting their versatility in advanced technological fields.

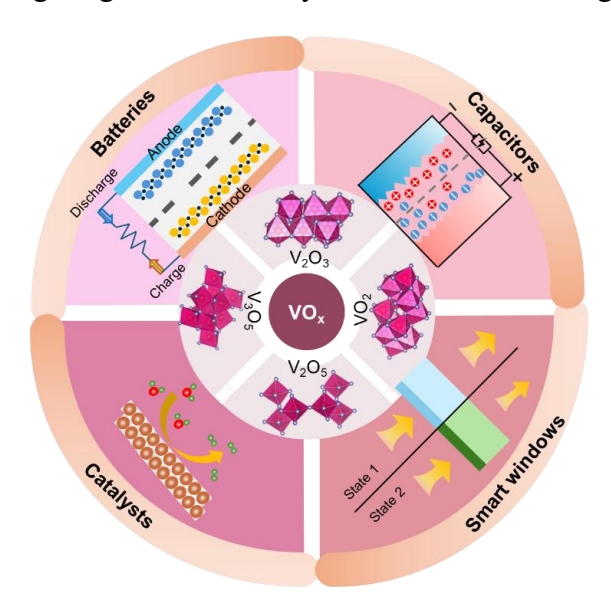


Figure 1.2: Demonstration of different thermodynamically stable vanadium oxides and their applications.

$1.2.1 \ V_2O_3$

As illustrated in Figure 1.3 a-b, V_2O_3 features a typical rhombohedral corundum-type crystal structure (space group: R3c) with lattice parameters of a = b = 4.9492(2) Å and c = 13.988(1) Å at room temperature. ²⁸ It is characterized by three dimensional (3D) V-V chains formed by V atoms, each surrounded by a distorted octahedron of O atoms. ²⁹ Notably, calcining the material at 600 °C for several hours results in the formation of vanadium vacancies (indicated by the red circle in Figure 1.3 (a), making it suitable for use in aqueous zinc metal batteries. ³⁰ However, due to the low valence state of vanadium (+3), the surface of V_2O_3 tend to oxidize to high valence state (V_3) when exposed to air.

The metal-insulator transition (MIT) in V₂O₃ was first observed by Morin, it experiences a complex phase diagram depending on temperature, pressure, or doping, undergoing a firstorder transition between 150 and 160 K from a rhombohedral paramagnetic metal (PM) phase to a monoclinic antiferromagnetic insulating (AFI) phase (space group: i2/a), with unit cell parameters of $\alpha = 7.2727 \text{ Å}$, b = 5.0027 Å, c = 5.5432 Å, and $\beta = 96.762^{\circ}$, as shown in Figure 1.3 c. 31. In this low-temperature phase, V₂O₃ is classified as a "Mott insulator," characterized by a bandgap of 0.6 eV, which is within the typical range for semiconductors. At ambient temperature and pressure, it crystallizes in the corundum structure with four V atoms in the primitive unit cell where V cations are coordinated by a distorted octahedron of O²⁻ ions. ³² Therefore, at room temperature, V₂O₃ demonstrates moderate electronic conductivity, significantly surpassing that of other transition metal oxides, such as MnO₂ and Fe₂O₃, etc. ³³ Trastoy et al. reported a strong interaction between magnetism and electronic transport in V₂O₃ during the MIT. ³⁴ Also, Hu et al. demonstrated that the MIT in V₂O₃ thin films was influenced by changes in the trigonal distortion, or equivalently, variations in the c/a ratio. ³⁵ Moreover, Liu et al. reported a significant modulation of the MIT transition temperature in flexible V₂O₃/mica heterostructures induced by mechanical bending strain. ³⁶ In recent years, advanced techniques such as angle-resolved photoemission spectroscopy, ³⁷ scanning microwave impedance microscopy, ³⁸ and emission Mössbauer spectroscopy³⁹ have been introduced to observe the MIT process in V₂O₃.

V₂O₃ has applications in the cathode material for metal-ion batteries (MIBs), catalysis, and supercapacitors, *etc*. It exhibits a low capacity at potentials above 2 V (*vs.* Li⁺/Li) and lacks a distinct plateau in its charge/discharge curves, leading Tranchant *et al.* to deem it unsuitable as a cathode for LIBs in 1980. ⁴⁰ However, Li *et al.* reported in 2004 that V₂O₃ has a high

theoretical lithium storage capacity of 1070 mAh g⁻¹ when utilized as an anode material for LIBs. 41 The 3D V-V framework of V₂O₃ creates abundant open tunnel structures that significantly facilitate the intercalation and deintercalation of Li⁺ ions. ⁴² For example, Liang et al. prepared V₂O₃@carbon nanofibers as flexible anode materials in LIBs via electrospinning. The electrode demonstrated a specific discharge capacity of 495 mAh g⁻¹ at 1 A g⁻¹ after 1000 cycles. Remarkably, the material achieved a specific capacity of 336 mAh g⁻¹ at 5 A g⁻¹ and maintained a capacity of 290 mAh g⁻¹ even after 10,000 cycles, suggesting excellent capacity retention and long-cycle lifespan. Sun et al. developed an aqueous LIBs electrode using metallic rhombohedral V₂O₃ ⁴³ which maintained a Coulombic efficiency (CE) close to 100%, and presented excellent reversibility throughout extended charge/discharge tests, with no significant gas evolution observed within the cycling voltage range. For zinc-ion batteries (ZIBs), conventional low-valent V₂O₃ struggles to accommodate Zn²⁺ intercalation during the discharge process due to its inherently unsuitable structure and suboptimal physicochemical properties. To address this, Luo et al. employed an in-situ anodic oxidation strategy to utilize V₂O₃ in aqueous ZIBs⁴⁴ forming a hierarchical microcuboid structure capable of accommodating nearly two electrons during intercalation. They also discovered that H₂O acted as a reactant in the initial charge oxidation of V₂O₃. Additionally, the porous structure of V₂O₃, with its high specific surface area, provided more reaction sites and facilitated a faster phase transition from V₂O₃ to V₂O_{5-x}·nH₂O. As shown in Figure 1.3 d, the small size and high surface area of the V₂O₃ nanoparticles further enhanced the first charge oxidation process. As a result, V₂O₃ achieved a Zn²⁺ discharge capacity of 625 mAh g⁻¹ at 0.1 A g⁻¹, corresponding to 1.75 electron intercalation. Remarkably, the material retained 87% and 78% of its capacity when the current increased to 10 and 20 A g⁻¹, respectively, and maintained 100% capacity retention after 10,000 cycles at 10 A g⁻¹. Moreover, V₂O₃ can also be used in other MIBs, such as potassiumion batteries (KIBs), ^{42, 45} sodium-ion batteries (NIBs), ^{46, 47} magnesium-ion batteries (MgIBs), ⁴⁸ etc. In addition, V₂O₃ and its complexes have been extensively utilized as catalysts in various applications, including chemical looping dry reforming of methane, ⁴⁹ ammonium perchlorate decomposition, ⁵⁰ the hydrogen evolution reaction (HER), ^{51, 52} and the oxygen evolution reaction (OER) 53, 54.

Furthermore, V_2O_3 exhibits a conductivity of $\sim 10^3~\Omega^{-1}$ cm⁻¹, which is significantly higher than that of monoclinic VO_2 ($\sim 4~\Omega^{-1}$ cm⁻¹) and comparable to Ru ($\sim 10^4~\Omega^{-1}$ cm⁻¹). ⁵⁵ Also, V_2O_3 is stable in both acidic and basic environments, ⁵⁶ making it a promising candidate for energy

storage applications, particularly for supercapacitors. However, the specific capacitances reported for V_2O_3 -based materials are still insufficient, indicating the need for the development and synthesis of novel V_2O_3 -based structures with enhanced performance. ⁵⁷

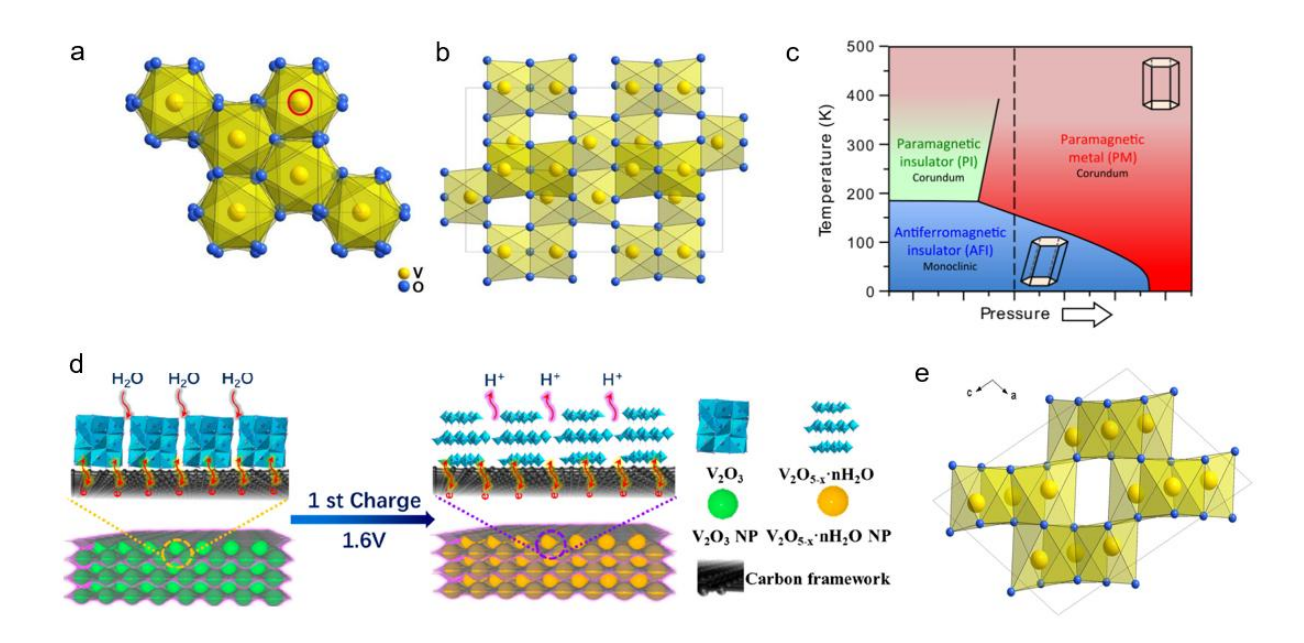


Figure 1.3: (a) Along the (001) direction; (b) along the (110) direction in the perspective view of V₂O₃. Reproduced with permission. ¹¹ Copyright 2023, American Chemical Society. (c) Generic temperature-pressure phase diagram of bulk V₂O₃. Reproduced with permission. ³⁷ Copyright 2021, American Association for the Advancement of Science. (d) Schematic illustration of the oxidation at full charge state of V₂O₃. Reproduced with permission. ⁴⁴ Copyright 2020, American Chemical Society. (e) Crystal structure of V₃O₅. Reproduced with permission. ¹¹ Copyright 2023, American Chemical Society.

1.2.2 V₃O₅

The crystal structure of V_3O_5 was first reported in 1954, ⁵⁸ and exhibits monoclinic symmetry (space group P2/c). ⁵⁹ The lattice parameter of the unit cell are a= 11.93 Å, b= 3.6 Å and c= 11.5 Å. The O atoms occupy octahedral sites, with V atoms positioned at the centre of each octahedron (Figure 1.3 e). Along the c axis, there are two types of octahedral chains: face-sharing and corner-sharing octahedra. These chains create a framework with large open spaces, making V_3O_5 suitable for accommodating lithium ions. ⁶⁰ The structure reflects the mixed

oxidation states of vanadium (+3 and +4), which results in distinct ordering within the lattice influencing the material's electronic and magnetic properties.

Despite its potential, V₃O₅ has been relatively less explored due to the strict synthesis conditions. Stabilizing the V₃O₅ phase by using solid-state chemistry while maintaining precise stoichiometry between O and V through solution-based methods is difficult, making V₃O₅ a rare material for electrochemical and other applications. However, Chen et al. successfully synthesized V₃O₅ microcrystals via vacuum calcination and employed them as an anode material for LIBs, achieving a high capacity of 628 mAh g⁻¹ at 100 mA g⁻¹, good rate capability (125 mAh g⁻¹ at 50 A g⁻¹), and stable cycling performance (117 mAh g⁻¹ after 2,000 cycles). ⁶⁰ Besides, Wan et al. prepared FeCoNi/V₃O₅ heterojunctions as highly efficient electrocatalysts for the OER. ⁶¹ The FeCoNi demonstrated excellent electrical conductivity and outstanding OER catalytic performance, while the V₃O₅ component in the heterostructured nanoparticles contributed to an increased oxygen vacancies content. Moreover, Abdullah et al. proposed a Ni-doped V₃O₅ pseudocapacitive cathode with an excellent charge storage. ⁶² The half-cell V₃O₅ can achieve a maximum capacitance of 5529 F g⁻¹ at 1 A g⁻¹ in a KOH solution, with corresponding energy and power densities of 116.8 Wh kg⁻¹ and 204.8 W kg⁻¹, respectively. An asymmetrical cell configured as Ni-doped V₃O₅ // active carbon (AC) demonstrated specific capacity, energy density and power density values of 428 F g⁻¹, 200 Wh kg⁻¹, and 1121 W kg⁻¹, respectively, in a 3 M KOH solution.

1.2.3 VO₂

VO₂ exists in several polymorphic phases, as shown in Figure 1.4, including VO₂ (B), VO₂ (A), VO₂ (M), VO₂ (R), *etc*. ⁶³ VO₂ is a well-researched inorganic phase-change material known for its reversible phase transition, which involves changes in crystallographic, magnetic, optical, and electrical properties. Specifically, it transitions from an insulating monoclinic phase VO₂ (M), to a conducting metallic rutile phase VO₂ (R) at a critical temperature of approximately 68 °C. ⁶⁴ This transition, characterized by a sharp decrease in infrared (IR) transmittance in the metallic phase, makes VO₂ a promising candidate for thermochromic energy-efficient windows, which can reduce energy consumption in buildings. VO₂ is particularly suitable for smart window materials due to its ability to quickly and efficiently regulate IR transmission across its MIT with minimal impact on visible light transmission. Additionally, VO₂ exhibits a unique capacity to alter its long-wave infrared emissivity (εLWIR) during the MIT. For instance, Wang

et al. prepared a VO2-based multilayer structure which could regulate its near-infrared transmittance and ELWIR spontaneously. ⁶⁵ Tang et al. designed a flexible temperature-adaptive radiative coating (TARC) by embedding lithographically patterned W-doped VO₂ within a dielectric BaF₂ layer, positioned atop a reflective gold layer. ⁶⁶ The TARC film exhibited a low εLWIR of approximately 0.2 in its insulating state and a high εLWIR of around 0.9 in its metallic state. Besides, VO₂ (B), which has notable applications as a cathode material in electrochemical devices due to its unique open atomic framework and good room-temperature conductivity. For example, Cen et al. reported ultrathin VO2 (B) nanosheets as cathode material for high-performance hybrid MgIBs. ⁶⁷ Jang et al. synthesized 1D/2D VO₂ (B) nanowire/g-C₃N₄ hybrid architectures as cathode materials for high-performance LIBs. ⁶⁸ Kang et al. utilized mesoporous VO2 (B) nanorods deposited onto graphene architectures for enhanced rate capability and cycle life of LIB cathodes. ⁶⁹ Gu et al. proposed W-doped VO₂ (B) nanosheets built 3D networks for fast lithium storage at high temperatures. ⁷⁰ In addition, Zhang et al. adjusted the valence state of vanadium in VO₂ (B) by extracting oxygen anions to achieve high-performance aqueous ZIBs. ⁷¹ And Guan et al. reported ultra-long cycle H-doped VO₂ (B) cathode for high capacity aqueous ZIBs. 72 However, like other metastable VO2 phases, the structural instability of VO₂ (B) limits its suitability for long-term cyclic stability in supercapacitor applications.

Moreover, VO₂, known as a semiconductor with a band gap of 0.7 eV, is rarely considered as a catalyst or photocatalyst. However, through phase engineering, VO₂ can be effectively utilized as a photocatalyst for hydrogen evolution. Vanadium oxide composites hold significant potential to enhance water dissociation kinetics and reduce charge-transfer resistance. ^{73, 74} For example, Wang *et al.* fabricated body-centred cubic nanostructured VO₂, which demonstrated excellent photocatalytic activity, achieving a hydrogen production rate of 800 mmol m⁻²h⁻¹ from a water and ethanol mixture under ultraviolet (UV) light at a power density of about 27 mW cm⁻². ⁷⁵ Chen *et al.* synthesized MoS₂/VO₂ hybrids using a two-step hydrothermal method, showing that the phase transition of VO₂ has a substantial impact on the HER properties of the heterostructures, with an onset potential of 99 mV and a Tafel slope of 85 mV dec⁻¹. ⁷⁶

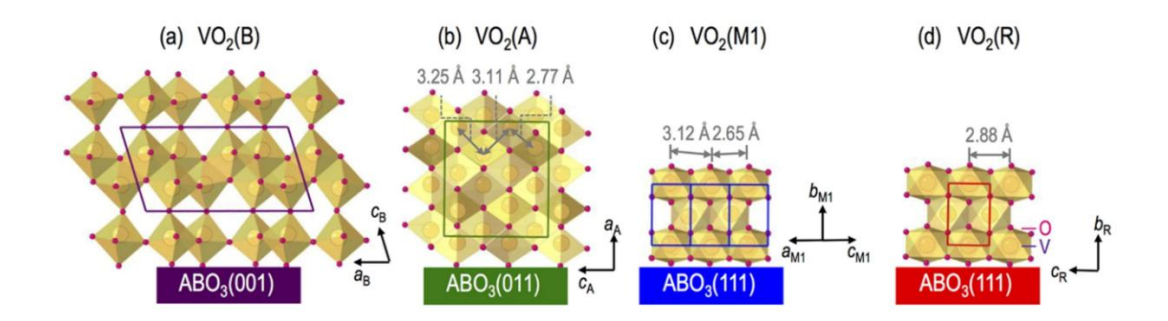


Figure 1.4: Schematics of (a) VO₂(B), (b) VO₂(A), (c) VO₂(M1) and (d) VO₂(R) phases with different crystallographic orientations. Reproduced with permission. ⁶³ Copyright 2016, Springer Nature.

1.2.4 V₂O₅

Among other types of vanadium oxides, V₂O₅ is the most stable one owing to the highest oxidation state. 77 It has different polymorphs including the most stable α -V₂O₅ (orthorhombic), and metastable β-V₂O₅ (tetragonal or monoclinic), γ-V₂O₅ (orthorhombic) and δ-V₂O₅ (monoclinic). ⁷⁸ The unit cell structure of α -V₂O₅ belongs to the Pmnm space group, with lattice parameters of a = 11.150 Å, b = 3.563 Å, and c = 4.370 Å. Additionally, other phases such as β -V₂O₅ and γ -V₂O₅ can be derived from the α -V₂O₅ phase through transformation under hightemperature and high pressure conditions. ^{11,79} Figure 1.5 illustrates the crystal structure of the α-V₂O₅ characterized by a layered structure consisting of corner- and edge- sharing square pyramids. These layers are bonded by weak van der Waals bonds along c-axis between adjacent vanadium and oxygen atoms of neighbouring pyramids. In each layer, there are three types of oxygen atoms, distinguished by different coordination, labelled as O1, O2, and O3. The apical vanadyl oxygen (O1) is singly coordinated, with a relatively short V-O bond length of approximately 1.54 Å. The O2 atoms serve as bridging oxygens, connecting two adjacent vanadium atoms at the corners of the VO5 pyramids, with a V–O bond length of about 1.77 Å. The triply coordinated O3 oxygen links three vanadium atoms through edge-sharing VO5 pyramids, with V-O bond lengths measuring approximately 1.88 Å, 1.88 Å, and 2.02 Å, respectively. Besides, the orthorhombic V₂O₅ can also be depicted as distorted VO6 octahedral. The octahedra form a layered and anisotropic structure with addition of oxygen atoms at the bottom of these square pyramids. The additional oxygen establishing a weak V...O van der Waals bond with a bond length of about 2.81Å. 15, 80, 81

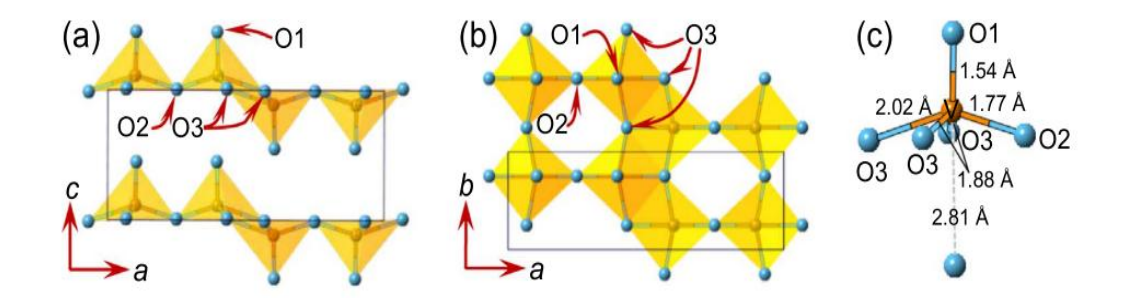


Figure 1.5: The crystal structure of orthorhombic V₂O₅ with (a) along b-axis, (b) along c-axis and (c) coordination environment around a single V atom. Reproduced with permission. ⁸⁰ Copyright 2018, Elsevier.

In addition, V. Eyert et al. ⁸¹ studied the electronic structure of V₂O₅. The electronic properties are modified significantly by strong hybridization between O 2p and crystal field split V 3d states. Strong deviations of the VO6 octahedra from cubic coordination give rise to the narrow split-off conduction band as a characteristic feature of V₂O₅. Evgenii M et al. ⁸² used quantum-chemical calculations to study the electronic structure of α -V₂O₅, γ' -V₂O₅, and γ -MeV₂O₅ (Me = Li, Na) bronzes. They found that Computed E_g values are equal to 3.17, 1.21 and 1.18 eV for γ' -V₂O₅, γ -LiV₂O₅, and γ -NaV₂O₅, respectively. The nature of the alkali metal atom is determined to have little influence on the structure and electronic states of the bronzes. In addition, techniques such as resonant photoemission spectroscopy, ⁸³ Raman spectroscopy, ⁸⁴ X-ray absorption near edge spectra, ⁸⁵ and resonant soft X-ray emission spectroscopy ⁸⁶ are used to study the electronic structure of V₂O₅.

V₂O₅ possesses several remarkable properties, including a layered structure, high chemical and thermal stability, electrochemical safety, low cost, and ease of preparation. These characteristics make V₂O₅ an ideal material for applications in electrochemical energy storage, catalysis, solar cells, gas sensors, electrochromic devices, and optoelectronic devices. As a cost-effective cathode material for LIBs, V₂O₅ has attracted great attention due to its high theoretical specific capacity values (294 and 441 mAh g⁻¹ for a 2 and 3 Li-ion intercalation, respectively). ⁸⁷ V₂O₅ was initially proposed as a Li-ion intercalation host by Whittingham *et al.* in 1976, ⁸⁸ and it can theoretically host lithium ions within its layered structure or undergo a conversion reaction. The lithium-ion insertion/(de)insertion reaction of V₂O₅ as the cathode during discharge can be expressed as:

$$V_2O_5 + xLi^+ + xe^- \iff Li_xV_2O_5$$

The phases of $\text{Li}_x \text{V}_2 \text{O}_5$ depend on the number of Li^+ insertion (x): α -phase (x < 0.01), β -phase $(0.3 \le x \le 0.4)$, ϵ -phase (0.35 < x < 0.7), δ -phase (0.7 < x < 1) and γ -phase (1 < x < 2). Further lithiation, the γ -phase irreversibly converts to a rock salt-structured ω -phase (2 < x < 3). ⁸⁹⁻⁹³ α -, ε - and δ - phases consists of VO₅ square pyramids and are accompanied by an orthorhombic phase with the increased puckering in the layers. The deep charge/discharge (x > 1 in Li_xV₂O₅) of the V₂O₅ results in an irreversible crystal structural change. When 2 Li⁺ ions are inserted, the V_2O_5 remains in the γ -phase permanently. Though the formed γ -phase also consists of VO_5 square pyramids, but it is highly puckered and irreversible. Finally, when the third lithium ion is inserted into the V_2O_5 layers, the irreversible formation of the ω -phase (2 < x < 3) Li_xV₂O₅ emerges. The ω -phase owns a tetragonal structure, which is different with the initial V_2O_5 phase. ⁹⁴ However, the average voltage for Li insertion and extraction in vanadium oxides ranges from approximately 2.2 to 2.6 V vs. Li/Li⁺. This voltage is too low for use as a cathode and remains too high for it to function effectively as an anode in LIBs. 95 Besides, its poor intrinsic electronic/ionic conductivity and structural stability, poor kinetics of the lithium ion insertion/(de)insertion reaction, and an unclear lithiation mechanism are the main factors restricting its practical application. Xue et al. synthesized hollow porous V₂O₅ microspheres (HPVOMs) as the electrode material in LIBs, which exhibited good capacity, rate capability, and stability, delivering 407.9 mAh g⁻¹ at 1.0 A g⁻¹ after 700 cycles. ⁹⁶ In addition, the LiFePO₄/HPVOM full cell had a discharge capacity of 109.9 mAh g⁻¹ after 150 cycles at 0.1 A g⁻¹. Dong et al. reported that V₂O₅ porous microspheres cathode can achieve a reversible capacity of 989.8 mA h g⁻¹ at 0.5 A g⁻¹ after 350 cycles in LIBs. ⁹⁷ In addition, Tan et al. prepared large-scale carambola-like V₂O₅ nanoflowers arrays on microporous reed carbon as enhanced electrochemical performances LIBs cathode. It achieved a stable capacity of 273 mAh g⁻¹ after 100 cycles at 0.2 C, and maintained a capacity of 180 mAh g⁻¹ even after 500 cycles at 1.0 C. Moreover, Su et al. synthesized V₂O₅ yolk-shell microspheres as the electrode in aqueous LIBs, with ultrafast rate capabilities (149.7 mAh g⁻¹ at 15 A g⁻¹). ⁹⁸ In full-cell tests, the VO//LiMn₂O₄ coin-cells demonstrated excellent cycle life, retaining 71.5% of their capacity after 500 cycles at 1 A g⁻¹, and exhibited ultrafast rate capabilities, delivering 87.4 mAh g⁻¹ at 15 A g⁻¹.

As for ZIBs, V₂O₅ also holds significant potential for applications due to its high theoretical specific capacity of 589 mAh g⁻¹ based on two electron transfers, its relatively low production cost, and its appropriate layered structure that facilitates the insertion and extraction of zinc

ions. ⁹⁹ During discharge, zinc ions intercalate into the V_2O_5 layers, resulting in a change in layer spacing, while V^{5+} is gradually reduced to V^{3+} and V^{4+} . Conversely, during charging, zinc ions are extracted from the V_2O_5 cathode, diffusing via the electrolyte, and reduced to metallic zinc deposited at the zinc electrode. Meanwhile, the layer spacing nearly returns to its original state, and V^{3+} is oxidized back to V^{4+} and V^{5+} . The overall reaction can be represented as:

$$V_2O_5 + xZn \rightleftharpoons Zn_xV_2O_5$$

Liu *et al.* synthesized two kinds of V₂O₅ hollow spheres by optimizing the annealing temperature as the cathode materials in ZIBs. ¹⁰⁰ The obtained V₂O₅ annealed at 350 °C electrode exhibited both high specific capacity (437.5 mAh g⁻¹ at 0.2 A g⁻¹) and high energy density (306.25 Wh kg⁻¹ at a power density of 140 W kg⁻¹). The superior performance can be contributed to its hollow interior, which helps buffer the lattice expansion of the V₂O₅ electrode and accommodates structural changes, while also facilitating rapid electronic and ionic transport. Reported by Wang *et al.*, the 2D amorphous V₂O₅/graphene (A-V₂O₅/G) heterostructures in ZIBs delivered an impressive capacity of 489 mAh g⁻¹ at 0.1 A g⁻¹ and maintained an excellent rate capability of 123 mAh g⁻¹ even at 70 A g⁻¹. ¹⁰¹ Additionally, the novel prototype planar miniaturized zinc-ion microbatteries (A-V₂O₅/G-ZIMBs) exhibited a high volumetric capacity of 20 mAh cm⁻³ at 1 mA cm⁻² and exceptional cycle life, retaining 80% of their capacity after 3,500 cycles. Their ability for in-series integration highlighted their strong potential as safe, high-performance microscale power sources. Furthermore, V₂O₅ is also being explored for use in Na-ion, ¹⁰² K-ion, ¹⁰³ Mg-ion, ¹⁰⁴ Ca-ion, ¹⁰⁵ and Al-ion batteries.

Among various vanadium oxides, V_2O_5 has received more attention for supercapacitor applications due to its wide range of oxidation states, high specific capacitance, and low acquisition cost. Velmurugan *et al.* fabricated a symmetric device, $V_2O_5||PVA-KOH||V_2O_5$, on a thin flexible substrate, using both annealed (A-500) and as-prepared (RT) V_2O_5 films as electrode materials separately. ¹⁰⁷ The A-500 devices achieved a maximum energy density of 0.68 μ Wh cm⁻², significantly surpassing that of the RT electrodes (0.05 μ Wh cm⁻²). Additionally, the symmetric A-500 exhibited outstanding cycle stability, maintaining a CE of 99% over 30,000 cycles. In addition, Sahu *et al.* synthesized graphene nanoribbon@V₂O₅ nanostrip composites to enhance the conductivity of V_2O_5 , achieving a high energy density of 42.09 Wh kg⁻¹ and a power density of 475 W kg⁻¹. ¹⁰⁸ Similarly, Sun *et al.* developed a 3D monolithic aerogel consisting of uniform carbon nanofiber/V₂O₅ core-shell nanostructures. ¹⁰⁹ This

composite aerogel demonstrated a high specific capacitance of 595.1 F g⁻¹, an impressive energy density of 82.65 Wh kg⁻¹, and excellent cycling stability (>12,000 cycles).

In addition, there are many studies about V₂O₅ as the electrocatalysts applied in water splitting. V₂O₅ demonstrated good OER performance due to the multivalent states of the V element, which can enrich active intermediates (*OH, *O, and *OOH) by modulating the valence electron structure of vanadium. 110, 111 Mounasamy et al. prepared 2D V₂O₅ flat nanorods, which exhibited excellent OER properties, achieving a low Tafel slope of 88 mV dec-1 and an overpotential (n_{OER}) of 310 mV at a current density of 10 mA cm⁻², and cycling stability over 12 h. 112 The V₂O₅-based composites, such as IrO₂/V₂O₅, 113 V₂O₅-Fe₃O₄/rGO, 114 CoV₂O₆-V₂O₅ coupled with porous N-doped reduced graphene oxide¹¹¹ have been reported for OER in recent years. In terms of the HER, V₂O₅ is typically regarded as inactive due to its weak H* adsorption on V sites, which hinders H* formation at the active sites. 115 To enhance the HER performance of V₂O₅, three primary strategies can be employed: defects creation, interfacial engineering, and composite formation. 11 Li et al. synthesized V₂O₅ nanosheet arrays containing oxygen vacancies (V_O) on Co foam using a hydrothermal method. ¹¹⁶ By adjusting the pH of the NH₄VO₃ precursor solution to 1, they achieved a V_O concentration of 34.2% in the V₂O₅ nanosheet arrays (named as Co-V₂O₅-H). The Co-V₂O₅-H sample demonstrated a low overpotential of 51 mV at a current density of 10 mA cm⁻², outperforming V₂O₅ powder and samples with lower V_O concentrations. Meena et al. directly synthesized V₂O₅ particles on Ni foam using a one-step hydrothermal method. 117 The resulting V₂O₅/Ni(OH)₂@NF catalyst exhibited a low overpotential of 39 mV at 10 mA cm⁻², comparable to that of Pt (35 mV @ 10 mA cm⁻²). Additionally, the hierarchical V₂O₅@Ni₃S₂ hybrid nanoarray synthesized by Zhong et al. demonstrated a favourable overpotential of 95 mV at 10 mA cm⁻², attributed to the enhanced interfaces between V₂O₅ and Ni₃S₂. ¹¹⁸

Furthermore, the chemical and thermal stability, layered structure, narrow bandgap, and photocatalytic properties also make V_2O_5 a practical material for fabricating electrochemical and optoelectronic devices, such as photocatalytic degradation of dye, photoelectrochemical water splitting, and photo-supercapacitors, *etc.* ¹¹⁹⁻¹²⁴ Photo-batteries, in which one of the battery electrodes is made of a photoactive material that can be charged directly by light without the use of a solar cell, thereby increasing the efficiency of the solar energy conversion and storage process. V_2O_5 is a photo-responsive material with a small bandgap ($\sim 2.3 \text{ eV}$) that

allows for light absorption in the visible range, making it suitable as a dual-function electrode material in the photo-rechargeable batteries.

Boruah et al. were the first to demonstrate the photo-rechargeable properties of hydrothermally synthesized V₂O₅ for ZIBs¹²⁵ and LIBs¹²⁶. Specifically, a cathode formulation combining V₂O₅ nanofibers with poly(3-hexylthiophene-2,5-diyl) and reduced graphene oxide was proposed for use in photo-rechargeable zinc-ion batteries (photo-ZIBs) in 2020. 125 This configuration delivered gravimetric capacities of approximately 190 mAh g-1 under dark conditions and around 370 mAh g⁻¹ when illuminated, with a photo-conversion efficiency of roughly 1.2%. In 2021, the same photo-active cathodes were adapted in photo-LIBs, which exhibited a capacity increase of over 57% under illumination and can be charged up to approximately 2.82 V using light, with the photo-conversion efficiencies of about 2.6% under 455 nm light and around 0.22% under 1 sun illumination. 126 The improved electrochemical performance is due to the fact that these cathodes exhibit a good absorption in the visible spectrum and enable the separation and storage of charges required for direct light charging without the need for solar cells. Moreover, V₂O₅ nanofibers allow charge conduction along the nanofiber length, reducing the probability of recombination for photo-excited carriers before extraction. Later, Wilhelm et al. reported utilizing carbon-coated electrospun V₂O₅ nanofibers as photo-responsive cathodes for lithiumion batteries. 127 The materials delivered a high discharge capacity of 160 mAh g⁻¹, which could be increased up to 184 mAh g^{-1} (C rate of 0.75) under light illumination. The photo-conversion efficiencies could reach 5.07%.

1.3 Rechargeable Metal-ion Batteries

Rechargeable metal-ion batteries are a type of battery that stores and releases electrical energy by facilitating the reversible movement of metal ions between the positive and negative electrodes. Known for their high energy density, long lifespan, and efficient recharging capabilities, these batteries, including lithium-ion, zinc-ion, sodium-ion, potassium-ion, calcium-ion, magnesium-ion, Aluminum-ion batteries, are widely used in various applications.

1.3.1 Lithium-ion Batteries

The pursuit of sustainable energy storage solutions has intensified in recent years, driven by the motivation of mitigating environmental degradation and the quest for higher energy density systems. Lithium becomes a promising candidate owing to its highly reducing potential (–3.04 V vs. standard hydrogen electrode (SHE)), and its low atomic mass. Additionally, the small atomic radius of Li-ions enables a high diffusion coefficient when used as the charge carrier, making lithium-based systems theoretically ideal for meeting the high energy density and power demands of portable energy storage devices.

LIBs have emerged as the leading battery technology due to their long lifespan, high energy density, and superior power density. ^{128, 129} The introduction of LIBs by Sony® in 1991, featuring graphite anode and lithium cobalt oxide cathode, marked a significant milestone in rechargeable battery technology. Despite their success, there is a growing trend to cut down on cobalt due to its geopolitical and supply-related risks, ¹³⁰ prompting a shift towards alternatives to improve battery energy density. The expanding market for electric vehicles, consumer electronics, and other portable electronics devices has significantly increased the demands for batteries that offer higher capacity and power density. The current LIBs may not fully meet all the requirements. Safety concerns associated with LIBs, including risks of thermal runaway and explosions, have been reported. Developing a battery system that is both safe and environmentally friendly, while still offering high electrochemical performance is the major task.

1.3.1.1 Mechanism

A LIB is composed of four major parts: anode, cathode, separator, and electrolyte. The working mechanism of typical LIBs is illustrated in Figure 1.6, using a LiCoO₂ (LCO)/graphite cell as an example. During charging, lithium ions de-intercalate from the cathode (LCO), diffuse through the electrolyte, and move across the separator's nanopores to intercalate into the anode material. Simultaneously, electrons flow in the opposite direction through the external circuit to maintain electro-neutrality. During discharge, lithium ions migrate from the anode back to the cathode.

The reactions at the LCO cathode during cycling can be expressed as:

$$LiCoO_2 \rightleftharpoons Li_{(1-x)}CoO_2 + xLi^+ + xe^-$$

The reactions at the graphite anode during cycling can be expressed as:

$$6C + xLi^+ + xe^- \rightleftharpoons Li_xC_6$$

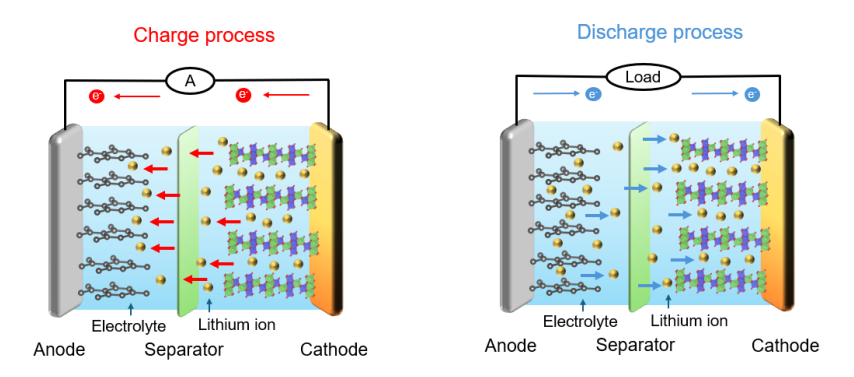


Figure 1.6: Schematic diagram of charging and discharging process of LIBs.

1.3.1.2 Cathode Materials

Whittingham designed the earliest iterations of a cathode similar to the current cathode materials. ¹³¹ He utilized layered crystal structures of nearly metallic metal dichalcogenides like TiS₂ and TaS₂ to store Li-ions. Whittingham termed this process the "intercalation mechanism," which exhibited high reversibility due to minimal changes in the crystal structure. He attributed this phenomenon to ordered layered structure of TiS₂, consisting of alternating Ti and S sheets. The absence of disordered Ti cations within the crystal lattice benefits Li-ion transfer, making the material highly suitable for this application.

In 1980, Godshall *et al.* proposed a high voltage metal oxide namely LCO used as cathode material, operating at elevated temperatures of 400–450 °C. ¹³² Later, Mizushima *et al.* reported a room temperature LCO cathode using organic electrolytes. ¹³³ LCO possessed a layered crystal structure similar to that of TiS₂ but provided several key advantages, including stability under ambient conditions (moisture) and a much higher Li-ion insertion voltage (3.5–4 V *vs.* Li/Li⁺ in propylene carbonate). However, fully delithiating LCO required a very high voltage (5 V *vs.* Li/Li⁺), which led to the oxidation of the organic electrolyte and instability of the cathode material. Consequently, complete delithiation resulted in a significant 5% irreversible capacity loss per cycle, as reported by Amatucci *et al.*, ¹³⁴ making it unsuitable for practical applications.

MnO₂ was explored as a cathode material for Li-based rechargeable batteries as early as 1974, prior to the development of LCO, and demonstrated a capacity of approximately 308 mAh g⁻¹ at 5 V versus Li/Li⁺, significantly higher than commercial LCO. Additionally, Mn had a substantial cost advantage over LCO due to its lower price. However, MnO₂ underwent severe structural changes when lithiated to form the rock salt structure of LiMnO₂, rendering it impractical as a rechargeable cathode material. It was not until 1983 that Thackeray introduced LiMn₂O₄ (LMO) with a 3D spinel structure, featuring a dual discharge plateau at 3 V and 4 V versus Li/Li⁺ as a promising alternative to LCO. Like LiMnO₂, LMO was significantly cheaper, less toxic, and offered better thermal stability in the charged state as well as higher power density due to its 3D framework. However, these advantages were offset by several challenges at lower discharge voltages, including Jahn–Teller distortion, volume expansion from phase transformations, and manganese dissolution from the cathode through a disproportionation reaction (2Mn³⁺ \rightarrow Mn²⁺ + Mn⁴⁺) triggered by HF acid, which forms as a byproduct of the reaction between LiPF₆ (electrolyte salt) and trace water impurities in the electrolyte.

Another class of cathode materials is the olivine-structured LiFePO₄. Initial studies focused on the low-cost LiFeO₂, which was explored by Sakurai *et al.* in 1996. However, it exhibited a low capacity (~100 mAh g⁻¹) and a severely sloped lithiation profile. Later, in 1989, Manthiram and Goodenough investigated polyanions like Fe₂SiO₄ with a NASICON framework, which showed a more favourable flat voltage plateau. In 1997, Padhi *et al.* further explored metal polyanions (PO₄) with 1D-ordered olivine structures, including LiFePO₄ (LFP), LiMnPO₄, LiCoPO₄, and LiNiPO₄, which demonstrated promising characteristics for battery applications. LiFeP₂O₇, Li₃Fe₂(PO₄)₃, Fe₄(P₂O₇)₃, and LiFePO₄ all exhibited the ability to reversibly insert and extract lithium ions. It was discovered that the Fe³⁺/Fe²⁺ redox couple in LiFePO₄ has the largest potential difference from the Fermi level of lithium, resulting in a lithiation voltage of 3.5 V versus Li/Li⁺. However, in contrast to spinel manganese and the layered dichalcogenides TiS₂ and CoO₂ cathode materials, LFP is not electrically conductive and does not exhibit increased conductivity at any state of lithiation. This limitation hindered the use of bulk LFP particles in cathodes, significantly obstructing its initial commercialization.

The LIB technologies discussed so far (LMO and LFP) have not, and still do not, play a significant role in modern electric vehicles (EVs). Instead, the most impactful and promising cathode materials for EV applications have been the layered nickel-manganese-cobalt (NMC) oxides. Its main advantages include increased capacity, a high decomposition temperature, the

use of lower-toxicity materials, and reduced costs from substituting both cobalt and nickel with inexpensive manganese. Initially, the cycle stability and electronic conductivity of NMC were lower than that of LCO, raising concerns about the commercial viability of ternary metal oxides. However, significant improvements in performance were observed when adjusting the ratios of the three metals, leading to extensive research aimed at finding the optimal combination. Each metal in the NMC system serves a distinct role: nickel contributes capacity by being oxidized from Ni²⁺ to Ni³⁺ to Ni⁴⁺, while manganese (Mn⁴⁺), although not electrochemically active, enhances structural stability and reduces costs. Cobalt (Co) is oxidized from Co²⁺ to Co³⁺ following the oxidation of Ni²⁺, which helps prevent nickel from migrating into lithium sites. While cobalt is expensive (approximately \$9,000 per ton) and has limited availability on Earth. As a result, the battery industry is increasingly shifting toward nickel-rich cathodes to enhance performance and reduce reliance on Co.

Research on NMC cathodes initially focused on low nickel ratios. In 2001, Ohzuku and Makimura synthesized and tested LiNi_{0.33}Mn_{0.33}Co_{0.33}O₂, ¹³⁵ while in the same year, Dahn et al. investigated LiNixCo_{1-2x}Mn_xO₂ (where x = 0.25 and 0.375). ¹³⁶ The work from both groups introduced the NMC class of materials to the battery field. In 2011, Z. Li and Whittingham et al. aimed to identify an optimal NMC ratio by testing NMC compositions 333, 442, and 992. 137 They found that NMC 442 exhibited a higher capacity at low currents and comparable capacities at higher currents, while also reducing costs by lowering the Co content from 33% to 20%. The commonly commercial NMC formulations include NMC 622, NMC 811, etc. However, the performance fading of Ni-rich NMC cathodes is mainly due to the effect of Li⁺/Ni²⁺ cation mixing, the influence of Li residues on the stability, the influence of overcharging on the capacity degradation, effects of high temperature on the structure stability. ¹³⁸ Several strategies, including element doping ^{139, 140} and surface coating, ^{141, 142} to address these issues have been reported in recent years. The high price of Co, poor structural and interfacial stability of Ni-rich NMC still hinder their large-scale applications. Therefore, the research on cheap, high-performance positive electrode materials is still the focus of the development of the lithium-ion battery industry.

Vanadium is a widely abundant transition metal that exhibits four oxidation states: V^{2+} , V^{3+} , V^{4+} , and V^{5+} . Vanadium-based nanomaterials have garnered significant interest for emerging energy storage systems. In 1975, Whittingham prepared vanadium oxides as the cathode material in LIBs, and found that the possibility of vanadium oxide as the host to accommodate

Li ions, 88 which triggered the boost of studies on vanadium oxides as cathode materials for LIBs. Among the various vanadium oxides, V₂O₅ is the most prevalent and stable form. ¹⁴³ Notably, V_2O_5 has a remarkably high reversible capacity compared to other cathode materials. Its intricate structure and diverse morphology make it an exceptional candidate for LIBs. The theoretical specific capacity of V₂O₅ is approximately 294 mAh g⁻¹ with two lithium-ion intercalations and about 441 mAh g⁻¹ with three lithium-ion intercalations, significantly exceeding the capacities of commonly used cathode materials. In 1992, West et al. utilized V₂O₅ xerogels as the electrode and pointed out that the xerogel host exhibited greater stability during lithium insertion, maintaining its structural integrity even after repeated cycling to a depth of 2 Li/V₂O₅. ¹⁴⁴ In 1997, Kumagal et al. synthesized vanadium oxides films, which could be charge and discharge cycled over 300 times at a current of 10 μA at 25 °C. ¹⁴⁵ In 2006, Zhou et al. prepared metastable VO₂ nanorods as cathode materials via hydrothermal method. ¹⁴⁶ The as-synthesized VO₂(B) nanorods demonstrated an initial discharge capacity of 310 mAh g⁻¹, and achieved at 250 mAh g⁻¹ by the 30th cycle within the potential range of 1–3.5 V. In the last decade, researchers have developed approaches to prohibit the growth of lithium dendrite by applying lithium as the anode. ¹⁴⁷ The revitalization of V₂O₅ as a promising cathode material for LIBs is due to the development of nanotechnology and the use of lithium metal as the anode where it eliminates the problem of no lithium ion in the cathode.

As mentioned above, vanadium oxides are promising electrode materials for high-performance LIBs as for its high specific capacity, low cost and abundant source. The issues for the further development of LIBs lies on its intrinsic low ionic diffusion coefficient, the challenge of controllable preparation, and moderate electronic conductivity, and inferior cycling stability. The electrochemical properties comparison is summarised in the Table 1.1 below from the same reference.

Table 1.1: Comparison of several kinds of cathode materials for LIBs.

Cathode materials	Lithium manganate oxide		Lithium cobaltite oxide	Ferrous lithium phosphate	Lithium nickel cobalt manganese oxide	Vanadium pentoxide
Main components	LiMn ₂ O ₄ ¹⁴⁹	LiMnO ₂ ¹⁵⁰	LiCoO ₂ ¹⁵¹	LiFeO ₄ ¹⁵²	Li(NiCoMn)O ₂ ¹⁵³	$V_2O_5^{154}$

Theoretical capacity (mAh g ⁻¹)	148	286	274	170	280	294
Actual capacity (mAh g ⁻¹)	100-120	200	135-145	130-140	>150	222.4
Operating voltage (V)	3.1-3.9	3.4-4.3	2.5-4.1	3.2-3.7	2.5-2.4	2-4
Cycle performance	>500th	poor	>300th	>2000th	>800th	>500

1.3.2 Zinc-ion Batteries

Despite LIBs being the primary sector in the rechargeable battery market, the development of LIBs has faced challenges such as the scarcity and high cost of lithium metal, the safety concerns regarding the toxicity and flammability of their electrolyte. ^{155, 156} Finding a compelling alternative is of necessity. Among emerging technologies, rechargeable ZIBs have attracted great attention for its potential to offer an advanced electrochemical performance. ZIBs present several notable advantages over LIBs. Firstly, zinc, being one of the most abundant elements on Earth, offers a cost-effective alternative to lithium. The price for zinc is around 2638 USD per ton ¹⁵⁷ while the price for lithium is approximately 10612.5 USD per ton. ¹⁵⁸ Secondly, the nonflammability, nontoxicity and nonvolatility of the aqueous electrolyte, avoiding the safety hazards presented in LIBs. Moreover, the ionic conductivity of aqueous electrolyte is two orders of magnitude higher than that of organic electrolytes, which facilitate power density and fast charging capability. ¹⁵⁹ On top of that, from an environmental aspect, ZIBs are inherently more sustainable due to the nontoxicity of zinc and its recyclability. ¹⁶⁰ Another benefit of aqueous batteries is the lower fabrication cost, as they do not require strict oxygen- and water-controlled assembly lines. ¹⁶¹

The history of zinc-based batteries dates back nearly 200 years prior to the current bloom situation, beginning with the invention of the Zn-CuSO₄ battery by Daniel in 1836, as presented in Figure 1.7. Zinc-manganese batteries have dominated the primary battery market since their invention by French engineer Georges Leclanché in 1860. ¹⁶² In 1878, the first alkaline Zn-air battery assembly was designed by Maiche. ¹⁶³ In 1941, zinc-silver (Zn-Ag) batteries were first

appeared. 164 In 1986, alkaline Zn/MnO2 batteries were developed based on these earlier Zn/MnO₂ batteries. ¹⁶⁵ However, the initial Zn/MnO₂ batteries were technologically outdated, costly, and resource-intensive. To improve resource efficiency, rechargeable alkaline Zn/MnO₂ batteries were introduced. Despite this, they still had drawbacks, such as low CE and rapid capacity decay due to the reversible reactions at the Zn/MnO₂ electrodes. ¹⁶⁶ In 2009, Xu et al. discovered that Zn2+ could be reversibly intercalated and extracted from the MnO2 electrode $(Zn^{2+} + 2e^{-} + 2MnO_2 \rightleftharpoons ZnMn_2O_4)$. ¹⁶⁷ Building on this finding, they introduced the concept of "ZIBs" for the first time in 2011. 168 The rechargeable aqueous zinc-ion batteries (AZIBs) using mild or ZnSO₄ or Zn(NO₃)₂ as the electrolyte, α -MnO₂ as the cathode material, and zinc as the anode. Polycrystalline MnO₂ (including α , β , R, δ , T, λ , ε , and γ phases), Prussian blue, and its analogs (e.g., copper hexacyanoferrate and zinc hexacyanoferrate) have garnered considerable attention as potential cathode materials. ¹⁶⁹⁻¹⁷¹ However, MnO₂ suffers from an unstable crystal structure, leading to poor cycling performance during charging and discharging. 172, 173 While Prussian blue and its analogs possess stable crystal structures, their Zn storage capacity remains low, typically below 100 mAh g⁻¹. ^{174, 175} In 2012, dual-ion hybrid zinc batteries (DHZBs) were designed and developed. ¹⁷⁶ In these systems, ions such as Li⁺, Na⁺, Mg²⁺, and Al³⁺ are used instead of Zn²⁺ to intercalate into the cathode material, enhancing ion mobility. These advancements have paved the way for new energy storage systems, offering a promising alternative to traditional LIBs. In 2016, aqueous zinc-organic polymer batteries were proposed, showing the beneficial impact of the conjugated backbone on material performance by enhancing electron transfer throughout the polymer chain. ¹⁷⁷ In 2017, Hu et al. developed a Zn/V₂O₅ dual-ion battery using a "water-in-salt" electrolyte composed of 21 m lithium bis(trifluoromethanesulfonyl)imide (LiTFSI), and 1 m zinc triflate (Zn(CF₃SO₃)₂). ¹⁷⁸

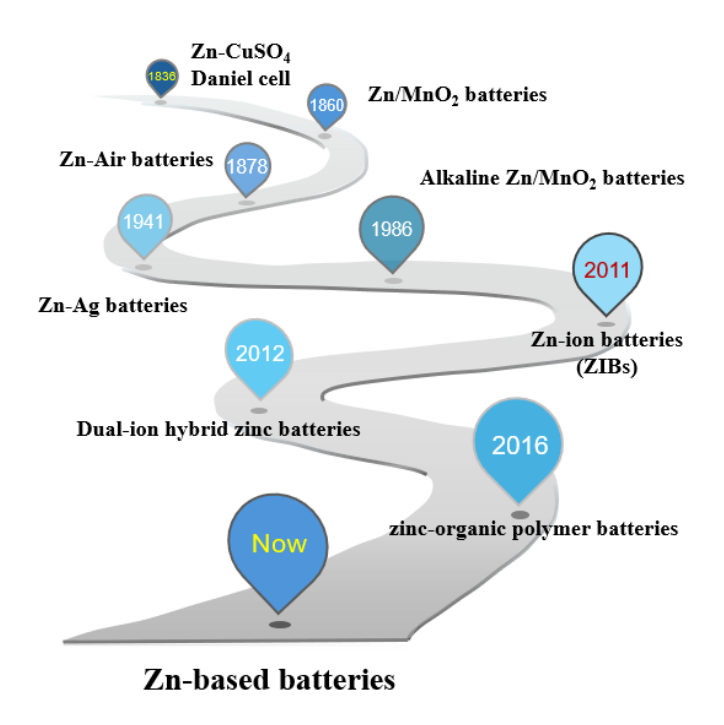


Figure 1.7: Illustration of the development history of Zn-based batteries.

ZIBs operate on the fundamental principle of electrochemical energy conversion. As shown in Figure 1.8, ZIBs have the similar structure analogous to that of LIBs including four components: the anode, separator, electrolyte, and the cathode. The electrochemical processes within ZIBs involve the intercalation and deintercalation of zinc ions between the anode and cathode during charge and discharge cycles. Separator is functioned to prevent short circuits caused the contact of the cathode and anode, while also providing pathways for the transit of zinc ions. anode, typically composed of metallic zinc due to the numerous merits, such as relatively low redox potential (-0.76V vs. SHE) and high theoretical specific capacity and volumetric density (820 mAh g⁻¹ and 5855 mAh cm⁻³), undergoes oxidation, releasing zinc ions into the electrolyte. These zinc ions migrate through the electrolyte to the cathode, where they intercalate into the host material, facilitating the flow of electrons through the external circuit, thereby generating electrical energy. During the charging process, the electrochemical reactions are reversed, restoring zinc metal in the anode. In addition, the aqueous electrolytes play a crucial role by facilitating the movement of Zn²⁺ ions between electrodes during charging and discharging. This process, which governs Zn²⁺ conductivity and the electrochemical window, relies on the composition of the electrolyte. 179 Commonly used aqueous electrolytes for ZIBs consist of solutions with various zinc salts such as ZnSO₄, ZnCl₂, and Zn(CF₃SO₃)₂.

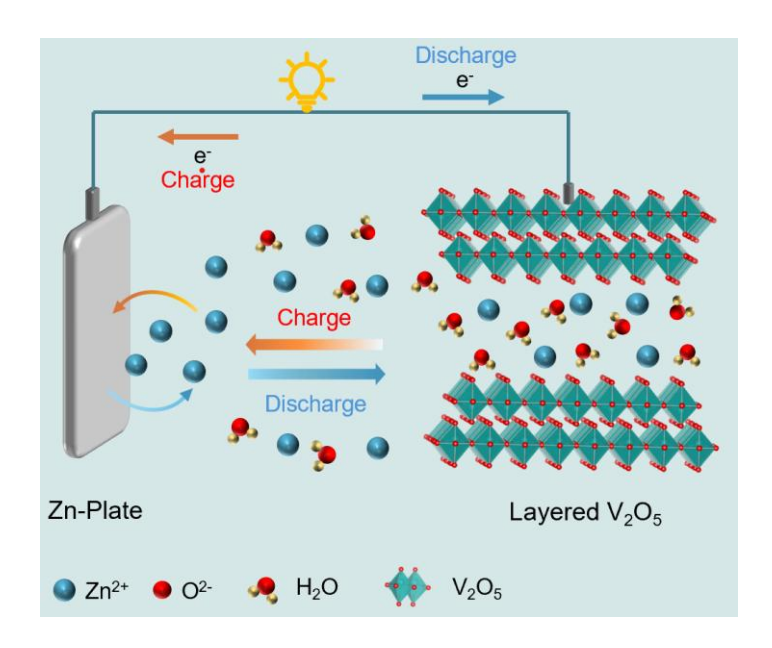


Figure 1.8: Schematic illustration of the working principle of ZIBs.

Although ZIB technology is very promising, it is still in the research phase, facing several limitations and challenges that need to be overcome before it can achieve commercial viability. For the zinc anode, it encounters challenges such as side reactions, by-products, and dendrite formation during Zn plating/stripping process. 129 Specifically, these side reactions, which include Zn anode corrosion and the cathodic HER, irreversibly deplete electrolytes and prompt the formation of insoluble by-products on the Zn anode surface. Dendrites, stemming from uneven Zn deposition, often breach separators, causing battery short circuits. Additionally, some dendrites easily detach from the Zn anode, becoming inactive "dead Zn." Consequently, these side reactions and dendrites result in reduced CE and significant capacity loss in AZIBs. For the aqueous electrolyte, Zn(CF₃SO₃)₂ stands out due to its notable merits such as a high diffusion coefficient and effective suppression of the HER. In Zn(CF₃SO₃)₂ electrolyte, CF₃SO₃ ions possess low electron density and high ionic polarization, making them bulky and prone to weak interactions with water molecules. Consequently, CF₃SO₃⁻ ions tend to form solvation structures with Zn²⁺ ions, thereby reducing the interaction between Zn²⁺ and water molecules significantly. This reduction occurs because the bulky CF₃SO₃⁻ anions limit the coordination number of water molecules, weakening the solvation effect of Zn²⁺. ¹⁶⁰ Although Zn(CF₃SO₃)₂ electrolyte enhances the electrochemical performance of AZIBs, it faces several challenges, such as high cost and environmental unfriendliness. For example, CF₃SO₃ anions are susceptible to hydrolysis, resulting in the formation of monohydrates (CF₃SO₃H) and trifluoromethane (CHF₃), which can lead to environmental pollution and health risks. Additionally, Zn(CF₃SO₃)₂ electrolyte tends to be expensive, necessitating the recycling of Zn(CF₃SO₃)₂ to mitigate costs and environmental impact. For the cathode, the primary challenge preventing the practical application is the lack of electrode materials that meet all critical criteria. These criteria include: (1) morphology and crystal structure to accommodate the highly polarized Zn²⁺ ions and support their sluggish diffusion, (2) relatively high discharge capacity, (3) high operating voltage, (4) structural stability for long-term cyclability, and (5) cost-effectiveness and environmental sustainability. ¹⁸⁰

Mn- and V-based cathode materials have been the primary focus in the development of ZIBs. ^{172, 181} Mn-based materials often suffer from rapid capacity decay due to structural instability, which results from manganese dissolution and structural transformations during cycling. ^{182, 183} In contrast, most V-based compounds exhibit better stability and capacity than Mn-based cathodes due to a higher degree of capacitive contributions and more stable crystal structures. ^{184, 185} However, the average operating voltage of most V-based compounds is approximately 0.75 V versus Zn/Zn²⁺, limiting their potential to achieve high energy density. ^{181, 186, 187} In addition, some new classes of cathode materials, such as PBAs (Prussian blue analogues), ¹⁸⁸ polyanionic compounds, ¹⁸⁹ metal sulfides, ¹⁹⁰ and organic compounds ¹⁹¹ have been also studied in recent years.

By addressing the above-mentioned challenges and leveraging the inherent advantages of zincion chemistry, researchers are aimed to explore the strategies to protect the zinc anode, develop cost-effective and innovative electrolytes, exploit suitable cathode materials for the insertion of zinc ions. These efforts can help pave the way for the widespread use of ZIBs, contributing to the realization of a cleaner and more sustainable energy future.

1.3.3 Sodium-ion Batteries

Sodium-ion batteries (NIBs) are considered a viable alternative to LIBs due to their similar chemical properties. Li and Na are both alkali metals from Group 1 of the periodic table and share the characteristic of having a single loosely bound electron in their valence shell, leading to the formation of Li⁺ and Na⁺ ions. ¹⁹² As electrochemical carriers, Li⁺ and Na⁺ have similar standard electrode potentials: Na (-2.71 V vs. SHE) is only 300 mV higher than Li (-3.04 V vs. SHE). ¹⁹³ NIBs also have the potential to offer high-power performance because Na⁺ diffuse

faster than Li⁺. ¹⁹⁴ Additionally, unlike the formation of Al-Li intermetallic compounds in LIBs, sodium does not thermodynamically form Al-Na compounds. As a result, Al foil can be used as the current collector for NIB negative electrodes, replacing the Cu foil typically used in LIBs. According to a cost analysis by Vaalma et al., switching from Cu to Al current collectors lowers battery costs, with a greater reduction than that achieved by simply replacing lithium with sodium. 195 Therefore, the ability to use Al current collectors for both the positive and negative electrodes in NIBs is a significant advantage in reducing overall costs. Moreover, the intercalation chemistry of lithium and sodium ions is quite similar, and thus, the materials tested for NIBs could be like those used in Li-ion systems. For example, layered AMO₂ (A = alkali metal, M = 3d transition metals) compounds have been widely researched as positive electrode materials for LIBs and NIBs since the initial reports on the electrochemical (de)intercalation of Li and Na in layered LiCoO2 and NaCoO2 in 1980. 133, 196 NIBs could present a viable alternative to complement LIBs applications, particularly in stationary storage applications. Though NIBs are generally cheaper in terms of material costs, reducing processing costs to competitive levels remains a challenge. Additionally, the long cycle life of NIBs can help offset high initial investments, making them an economically attractive option for large-scale, stationary applications.

1.3.4 Potassium-ion Batteries

Potassium-ion batteries (KIBs) have also gained considerable attention as a cost-effective alternative in recent years. Like sodium, potassium is abundant and does not form Al-K intermetallic compounds, allowing the use of Al foil as a current collector for negative electrodes in these batteries. ¹⁹⁷ KIBs are also expected to operate at higher voltages compared to NIBs and even LIBs. It has been previously demonstrated that the standard electrode potential of K/K⁺ electrodes in carbonate electrolyte solutions is lower than that of Li/Li⁺ electrodes, ¹⁹⁸ which is consistent with the calculated standard electrode potentials reported in earlier literature. ¹⁹⁹ This lower potential allows for lower cutoff voltages in negative electrodes without metallic potassium deposition, enabling KIBs to operate at higher voltages over a wider range than both NIBs and LIBs. In addition, KIBs offer high-power density due to the fast diffusion rate of K⁺ ions, which experience weaker Coulombic interactions. These unique properties make KIBs a promising alternative to LIBs, sparking growing interest in the field. Since the experimental validation of the low K/K⁺ potential and successful electrochemical K-

intercalation into graphite in 2015, ^{200, 201} extensive research has been conducted on KIBs and related materials, including positive and negative electrode materials, nonaqueous and solid electrolytes, and functional binders. ²⁰²⁻²⁰⁶ Layered K_xMO₂²⁰⁷ and PBAs ²⁰⁸ are widely studied as positive electrode materials for KIBs, while for negative electrodes, graphite, which is widely utilized and technically established in LIBs, is a promising candidate for KIBs. ²⁰⁰ To enable the practical application of KIBs, further advancements are needed in energy density, cyclability, and high-power capabilities. However, at this early stage, comprehensive safety assessments of KIBs, particularly for large-format batteries, remain limited. Developing safety strategies, such as using nonflammable materials and solid-state battery designs, will be a critical focus for future research.

1.3.5 Aluminum-ion Batteries

Aluminum-ion batteries (AIBs) are viewed as attractive electrochemical energy storage systems due to the widespread availability of Al, its high charge storage capacity of 2980 mAh g⁻¹/8046 mAh cm⁻³, and the relatively low redox potential of Al³⁺/Al. ²⁰⁹ Specifically, Al is a metal that is the most abundant element in the Earth's crust, with a concentration of 82,000 ppm, which is significantly higher than other metals, such as magnesium at 29,000 ppm, potassium at 18,400 ppm, sodium at 23,000 ppm, zinc at 75 ppm, and lithium at just 17 ppm. ^{210,211} Plus, AIBs displayed higher safety with wide operating temperature for applications. ²¹²

However, several key factors have constrained the development of AIBs in recent years. ²¹³ Firstly, finding suitable electrolytes that enable efficient plating and stripping of aluminum at room temperature has been challenging. Moreover, the scarcity of stable positive electrode materials has limited progress in AIB technology. Additionally, assembling batteries with ionic liquid electrolytes is particularly difficult due to their highly corrosive nature. Currently, AIBs technology seems better suited for stationary energy storage applications, given its long cycle life and relatively lower energy density. AIBs can complement redox flow batteries by offering high power and rapid response, which can enhance the stability of the electrical grid. As energy density improves, AIBs could also become viable for use in heavy-duty vehicles, due to their high specific power and intrinsic safety. ²¹¹

1.3.6 Magnesium-ion Batteries

Magnesium-ion batteries (MgIBs) are considered a promising alternative to LIBs due to the abundant availability and easy accessibility of magnesium in the Earth's crust. Magnesium, an alkaline earth metal, offers nearly double the volumetric capacity (3832 mAh mL⁻¹) of lithium and has a very negative reduction potential of -2.4 V vs. SHE. ²¹⁴ Additionally, magnesium metal anodes exhibit less dendrite formation compared to lithium. ²¹⁵ Magnesium is also less reactive with air, simplifying processing and handling, thus reducing safety risks. Moreover, magnesium is far more abundant in the Earth's crust, making it more readily available and significantly cheaper than lithium.

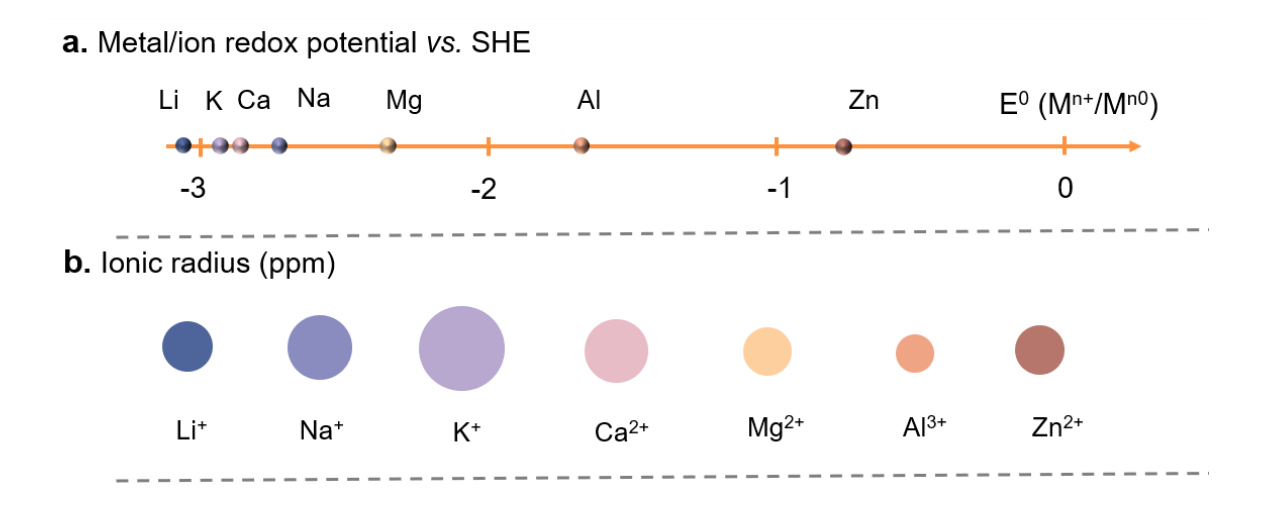
While alkali metals like lithium benefit from a passive solid electrolyte interface (SEI) that allows the transport of ions between the anode and electrolyte without major degradation, alkaline earth metals like magnesium tend to form analogous passivation films that impede cation diffusion. This might theoretically limit magnesium electrode performance, especially during charging. ²¹⁶ However, as early as 1927, effective magnesium electrodeposition was demonstrated using ethereal solutions of Grignard reagents, ²¹⁷ underscoring the viability of magnesium metal anodes in battery applications. Similarly, there are currently some factors that hinder the development of MgIBs. On one hand, electrolyte solutions that enable fully reversible Mg metal anodes are incompatible with high-voltage, high-capacity transition metal oxide cathodes due to complex surface interactions. On the other hand, Mg metal anodes cannot function reversibly in conventional electrolyte solutions that support high-voltage, high-capacity Mg insertion cathodes because of passivation effects that completely block their activity. ²¹⁸ Moreover, sluggish ion diffusion, limited cathode materials, electrolyte corrosiveness and lower energy density are other challenges that need to be addressed for MgIBs technology to advance towards practical application.

1.3.7 Calcium-ion Batteries

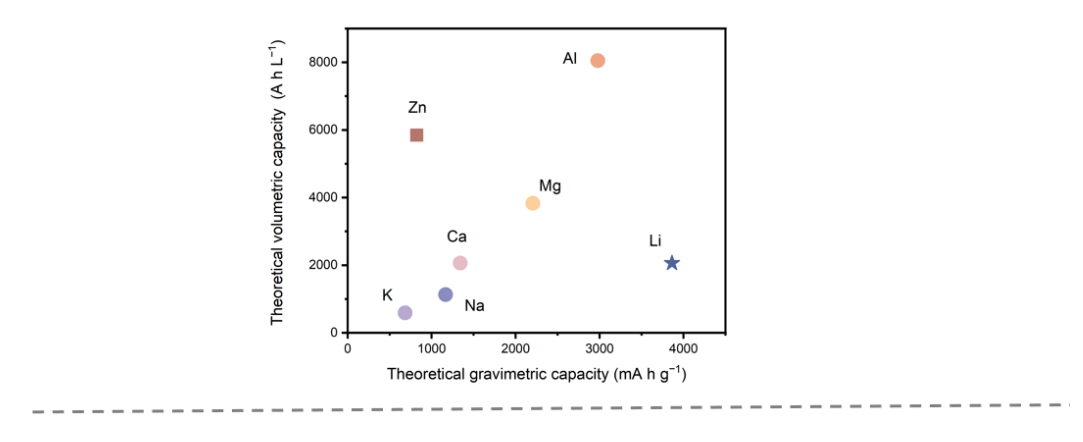
Calcium-ion batteries (CIBs) are appealing due to the abundance of calcium resources, the excellent volumetric and gravimetric capacities of calcium metal as an anode, and the potential for high energy density enabled by the multivalent nature of calcium ions. To be specific, Ca is the fifth most abundant element in the Earth's crust, featuring a widespread global resource distribution, nontoxicity, and outstanding thermal stability. ²¹⁹ Moreover, Ca is a divalent

alkaline earth metal with a highly strong oxidative ability, as reflected by its Ca²⁺/Ca redox potential of –2.87 V vs. SHE, close to the –3.04 V vs. SHE of lithium metal. ^{220, 221} Among multivalent metals being explored for battery applications, calcium has the most negative redox potential (Figure 1.9 a). In addition, calcium metal offers high volumetric and gravimetric capacities, reaching 2073 mAh cm⁻³ and 1337 mAh g⁻¹, respectively. ²⁹ Besides, its ionic radius is very similar to that of Na⁺ (Figure 1.9 b), a cation known for easy intercalation and deintercalation in a wide range of materials. ²²²

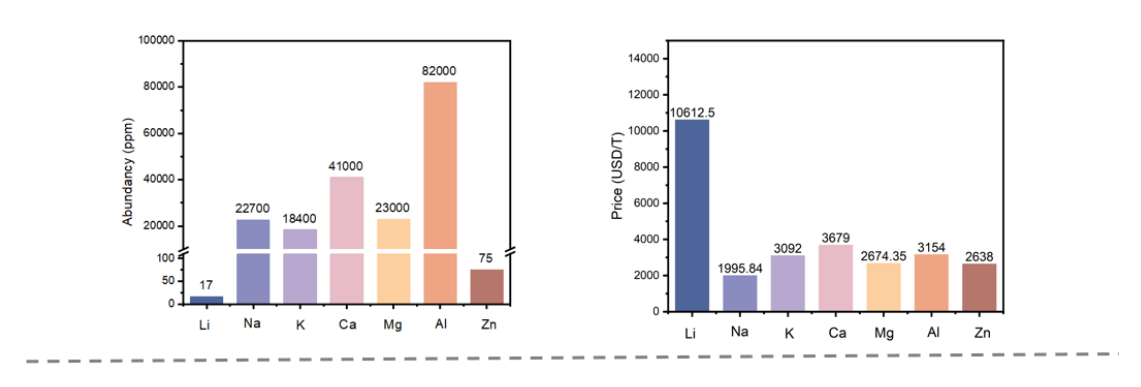
However, irreversible Ca stripping and plating and issues from intrinsic characters of Ca²⁺ are the two main obstacles that hinder the development of CIBs. ²²³ Like other multivalent metal ions, Ca²⁺ has a relatively high charge density and forms strong bonds with surrounding ions. ²²⁴ As a result, more energy is required for it to overcome the higher diffusion barrier and break interatomic bonds to move through the electrode. In some cases, these interactions are so strong that Ca²⁺ forms clusters, similar to [AlCl₄]⁻ or [MgCl]⁻, which act as migrating ions. This leads to sluggish diffusion kinetics in electrodes, resulting in high overpotential and poor power performance in CIBs.



c. Volumetric and gravimetric capacities



d. Abundancy and price



e. Evaluation of various aspects of MIBs

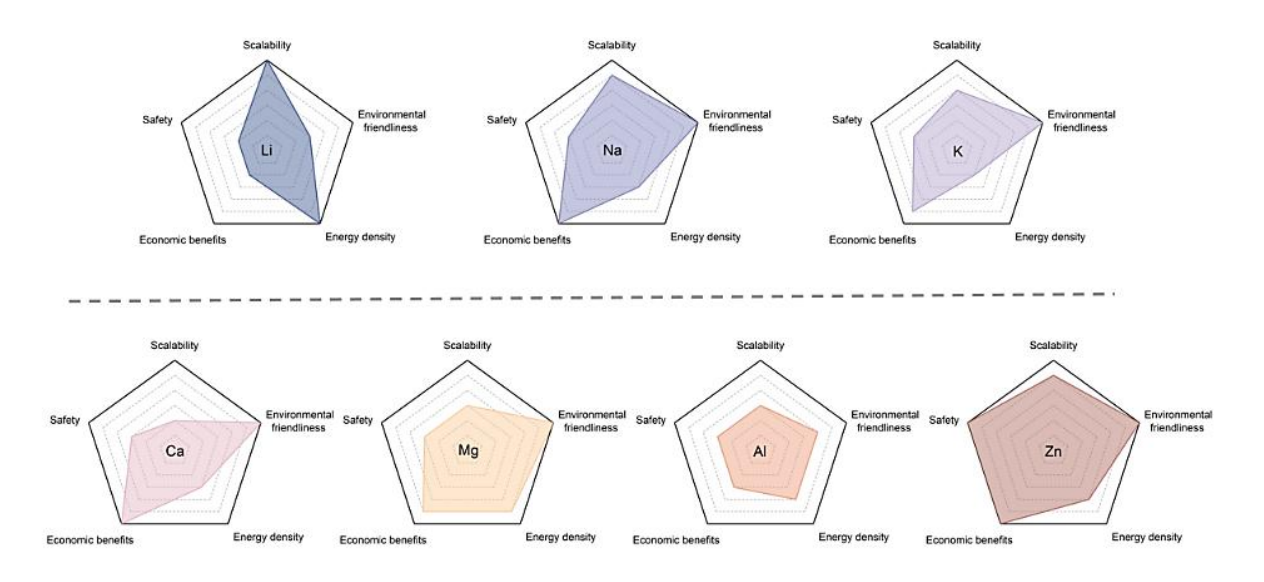


Figure 1.9: (a) Metal/ion redox potential vs. SHE; (b) mean size of the ionic species (Shannon ionic radium for 6-fold coordinated cations); ²²⁵ (c) theoretical volumetric and gravimetric capacities; ²¹⁰ (d) Earth abundance and production cost; ^{210,226} (e) comparison of various aspects of metal ion batteries. ²²⁷

In Figure 1.9, inherent characteristics and evaluation of mono- (Li⁺, Na⁺, and K⁺) and multivalent (Ca²⁺, Mg²⁺, Al³⁺, and Zn²⁺) metal ion batteries are presented. It is noting that a typical assessment focuses primarily on the anode, emphasizing the potential of pure metals due to their high specific capacity (Figure 1.9 c), relatively high density, and consequently elevated energy density. However, this approach often overlooks the less negative redox potentials of multivalent metals compared to lithium-based anodes (Figure 1.9 a), which can create unrealistic expectations about the volumetric energy densities of multivalent metal-ion batteries. While these batteries might achieve lower gravimetric energy densities due to the higher atomic weights of multivalent metals, their volumetric energy densities may not surpass those of lithium-based systems. ²²⁸

In conclusion, as the demand for diverse energy sources continues to rise, developing a range of complementary battery technologies is a crucial strategy for addressing the energy crisis. As shown in Figure 1.9 d-e, compared to LIBs, multivalent ion batteries, such as ZIBs, CIBs, MgIBs and AIBs, will undoubtedly play a significant role in this effort. The primary advantage of multivalent systems is their higher volumetric capacity, more abundant reserves, cheaper prices and the absence of dendrite formation during charging, addressing key safety and performance issues associated with lithium metal anodes. Especially in the ZIB system, its overall advantages are more obvious. However, it is important to note that unless lithium becomes prohibitively expensive, neither ZIBs nor other multivalent metal-ion batteries are likely to surpass LIBs in terms of energy density, which remains the key factor for portable electronics and electric vehicles. Besides, the nonaqueous and solid-state chemistry and electrochemistry of multivalent metals are significantly more complex than those of monovalent alkali metals, making it more challenging to develop and implement practical battery chemistries based on multivalent metals. Therefore, the main advantages of multivalent batteries lie in their lower cost and long-term sustainability, making them well-suited for stationary energy storage applications. The key advancements in high-energy multivalent metal batteries rely on the discovery of new materials for both high-voltage cathodes and electrolytes. The main challenges in developing these batteries include ensuring electrolyte compatibility with both the anode and cathode, as well as identifying high-voltage cathodes capable of facilitating multiple electron transfers at the same metal center while allowing for the fast diffusion of multivalent ions in the solid state.

1.4 Synthesis of Nanostructured V₂O₅

Various nanostructures of V₂O₅, such as nanotubes, nanowires, nanofibers, nanobelts, nanorods, nanoflowers, and mesoporous structures, have been synthesized by different methods, including hydrothermal method, solvothermal method, sol-gel, atomic layer deposition (ALD), electrospinning, electrochemical deposition, and so on.

1.4.1 Hydrothermal Method

Hydrothermal approach is the most common method to obtain nano-sized V₂O₅ with different morphologies and structures and is usually environmentally friendly without dangerous reagents or harmful solvents and surfactants. Xing et al. prepared a yolk-shell V₂O₅ structure assembled from ultrathin nanosheets via a facile hydrothermal method and was evaluated as supercapacitor materials, as shown in Figure 1.10 a. 229 This material exhibited a specific capacitance of 704.2 F g⁻¹ at 1.0 A g⁻¹ and a stable capacity retention of 89% over 4000 cycles at 3.0 A g⁻¹. Besides, Zhai et al. reported that centimetre-long V₂O₅ nanowires were prepared by a hydrothermal method in Figure 1.10 b. 18 The nanowires were single crystals of an orthorhombic V₂O₅ with a growth orientation along the [010] direction, and displayed a high capacity of 351 mAh g⁻¹ and a high CE of 99 % when used in LIBs. As shown in Figure 1.10 c, the V₂O₅ nanofibers were obtained by hydrothermal synthesis, reported by Liu et al. ²³⁰ As an positive electrode material in ZIBs, this material can achieve a specific capacity of up to 264.5 mAh g⁻¹ at a current density of 200 mA g⁻¹ by matching with aqueous Zn(CF₃SO₃)₂ electrolyte. Even at 2 A g⁻¹, It can also achieve a notable rate capability of 132.6 mAh g⁻¹. Furthermore, Javed et al. obtained the 2D layered V₂O₅ nanosheets on a flexible Ti substrate through a hydrothermal process, followed by a post-annealing treatment. The authors developed an ultrafast and flexible quasi-solid-state zinc-ion battery that delivered a capacity of 377.5 mAh g⁻¹ and an energy density of 622 Wh kg⁻¹ when charged at 4 A g⁻¹ in under 6 minutes. Additionally, it demonstrated an impressive power density of 6.4 kW kg⁻¹ at an extremely high current density of 20 A g⁻¹. ²³¹ In addition, V₂O₅ nanotubes, ²³² nanobelts, ²³³ nanorods, ²³⁴ nanoflowers⁷⁷ can be synthesized via the modified hydrothermal method.

1.4.2 Solvothermal Method

The solvothermal method allows for the well-controlled synthesis of highly crystalline and well-defined nanostructures, making them a powerful technique for producing V_2O_5 nanomaterials. However, it also comes with many challenges, including high pressure and temperature requirements, long reaction times, and safety issues. Wang *et al.* fabricated hollow V_2O_5 microspheres with multiple double-walled shells (in Figure 1.10 d) from using ascorbic acid-assisted solvothermal method. ²³⁵ This material with unique structures exhibited good electrochemical performance in LIBs. Additionally, Kim *et al.* proposed a novel V_2O_5 electrode architecture for synthesizing size-controlled V_2O_5 hollow microspheres with tuneable nanoscale building blocks, as shown in Figure 1.10 e, using a simple solvothermal reaction followed by annealing at 500 °C. ²³⁶ Moreover, nanostructured V_2O_5 hollow microspheres, ²³⁷ V_2O_5 /graphene nanocomposites, ²³⁸ and V_2O_5 /MWCNT composites ²³⁹ could be obtained via solvothermal synthesis.

1.4.3 Sol-gel Approach

Sol-gel methods are generally facile, environmental-friendly, and could prepare products in large-scale (up to the order of 10 grams). However, this method often requires post-synthesis thermal treatments to achieve the desired crystallinity and mechanical properties, and some sol-gel precursors can be expensive. Li *et al.* reported that nanorods-constructed 3D porous V₂O₅ architectures (3D-V₂O₅) for high-rate lithium storage were prepared through a simple sol-gel method followed by a heat treatment process, as shown in Figure 1.10 f. ²⁴⁰ Besides, Karami *et al.* synthesized V₂O₅ nanoflakes by poly vinyl alcohol-based sol-gel method, and used as positive electrodes for LIBs. ²⁴¹ At a current density of 100 mA g⁻¹, the discharge capacity of the material after 1 and 100 cycles was 430 mAh g⁻¹ and 280 mAh g⁻¹, respectively. Furthermore, there have also been reports on the preparation of V₂O₅ nanorods, ²⁴² thin films, ²⁴³ and nanosheets²⁴⁴ through the sol-gel method in recent years.

1.4.4 Atomic Layer Deposition

Atomic layer deposition is another effective method to synthesize V₂O₅ thin films, with the advantages of atomic-level thickness control, reproducibility, precise composition control and uniform coatings on complex geometries. However, its slow deposition rate, high cost, and

limited applicability for thicker films may limit its application. Chen *et al.* proposed a modified ALD process using ozone (O_3) as oxidant to prepare crystalline V_2O_5 thin films which are single-phase and orthorhombic on various substrates. ²⁴⁵ The as-deposited V_2O_5 films on planar electrodes exhibited high specific capacity, outstanding rate performance, and excellent cycling stability. Also, Sreedhara *et al.* reported that ultrathin epitaxial films of V_2O_5 have been grown on c-Al₂O₃ substrates via ALD (Figure 1.10 g), utilizing vanadyl acetylacetonate as the vanadium precursor along with oxygen plasma. ²⁴⁶ Besides, many studies on preparation of V_2O_5 thin films by ALD have been reported. ²⁴⁷⁻²⁵¹

1.4.5 Other Methods

In addition to the synthetic methods mentioned above, many other techniques can be employed for the synthesis of nano-sized V₂O₅ materials. For instance, Wilhelm *et al.* synthesized V₂O₅ nanofibers (VNFs) by simple electrospinning of VO(acac)₂ in a polymeric solution. The VNFs were further carbon-coated as dual-action cathode materials for photo-LIBs. ¹²⁷ Also, the porous V₂O₅ nanofibers (in Figure 1.10 h) prepared through an electrospinning technique followed by calcination were reported by Chen *et al.* ²⁵² The nanofibers are used as cathode materials for rechargeable AZIBs. Furthermore, Takahashi *et al.* synthesized single-crystal V₂O₅ nanorod arrays through template-based electrodeposition, ²⁵³ and electrochemical testing showed that these nanorod array electrodes exhibit significantly higher current density and energy storage capacity compared to sol-gel-derived V₂O₅ films. Similarly, the mesoporous V₂O₅ film with enhanced lithium-ion intercalation property was fabricated through the electrodeposition method. ²⁵⁴ Besides, Pan *et al.* proposed a strategy for preparing nano-sized V₂O₅ by thermal decomposition of vanadyl oxalate in air. ²⁵⁵ It demonstrated good discharge capacity and cycle stability during high-rate charge/discharge processes for high-rate lithium battery applications.

Moreover, single-crystal V_2O_5 nanoribbons (NRs) were synthesized using a vapor transport and deposition method, reported by Chan *et al.* ²⁵⁶

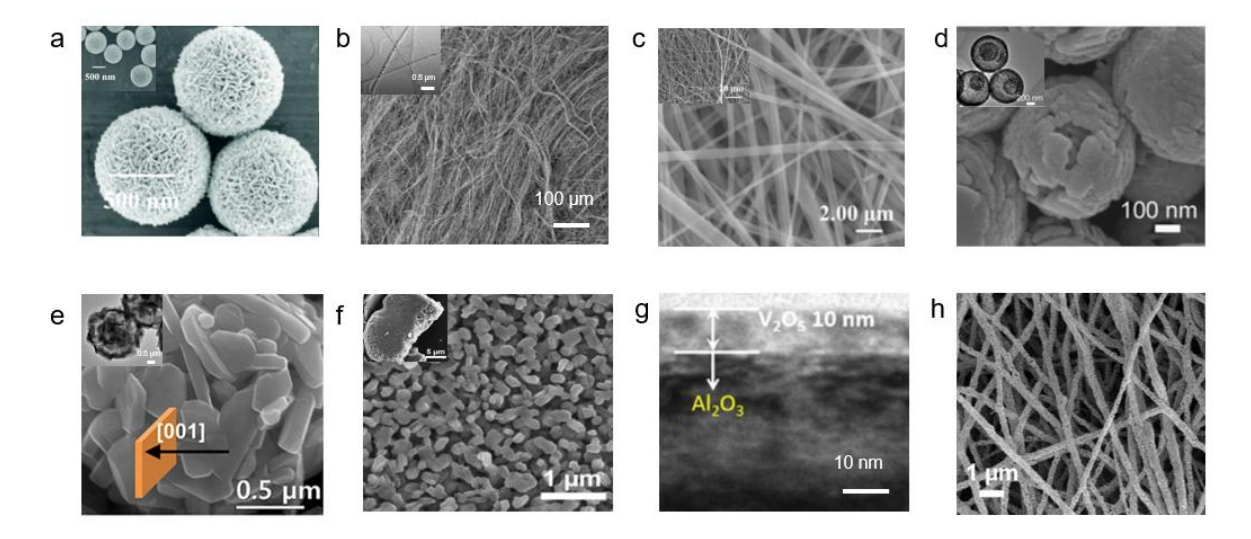


Figure 1.10: SEM images of various V₂O₅ nanomaterials. (a) Yolk–shell V₂O₅. Reproduced with permission. ²²⁹ Copyright 2018, Royal Society of Chemistry. (b) Centimetre-long V₂O₅ nanowires. Reproduced with permission. ¹⁸ Copyright 2010, Wiley-VCH. (c) V₂O₅ nanofibers. Reproduced with permission. ²³⁰ Copyright 2022, Elsevier. (d) Hollow V₂O₅ microspheres with multiple double-walled shells. Reproduced with permission. ²³⁵ Copyright 2018, Royal Society of Chemistry. (e) V₂O₅ hollow microspheres. Reproduced with permission. ²³⁶ Copyright 2017, Elsevier. (f) 3D-V₂O₅. Reproduced with permission. ²⁴⁰ Copyright 2020, Elsevier. (g) ALD V₂O₅ on c-Al₂O₃. Reproduced with permission. ²⁴⁶ Copyright 2017, American Chemical Society. (h) V₂O₅ nanofibers. Reproduced with permission. ²⁵² Copyright 2019, Elsevier. Insets: (a, c, f) low magnification SEM images; (b, d, e) TEM images of corresponding V₂O₅ nanomaterials.

1.5 Engineering of V₂O₅ Cathode

Researchers have proposed strategies such as doping, defect engineering, structural water optimization, and micro/macroscopic structure engineering. These methods can further improve electrochemical performance of V₂O₅ by increasing electroactive sites, improving charge transfer kinetics, accelerating charge diffusion and enhancing conductivity.

1.5.1 Doping

The electrical conductivity of V_2O_5 can be enhanced through cation doping with metal (M) species. The resulting M-doped V_2O_5 typically exhibits various distinct properties: 1) the substitution of V with M leads to the formation of lower valence state V, which increases

electronic conductivity. ¹⁴⁸ 2) The introduction of metal ions can result in the formation of MO6 octahedra within the V₂O₅ framework. These MO6 octahedral structures enhance the three-dimensional characteristics of V₂O₅, helping to maintain structural stability during the electrochemical insertion of ions and preventing deformation of the framework during cycling. ¹⁴⁸ 3) The local structural defects introduced by external metal cations can serve as nucleation centres for the phase transitions that occur during the Li⁺ insertion and extraction process, thereby enhancing the electrochemical cycling stability of the V₂O₅ electrode. Besides, these structural defects create additional pathways for Li⁺ diffusion. ¹⁵³ 4) Cation doping also reduces charge transfer resistance, which accelerates the kinetics of the Faradaic reaction. ¹⁵³ Therefore, there are some examples of metal-doping V₂O₅ as cathode materials applied in various metalions batteries.

Li *et al.* synthesized Sn-doped V₂O₅ films by the sol–gel method, ²⁵⁷ and the Sn-doped V₂O₅ film demonstrated significantly enhanced lithium-ion storage capacity, faster kinetics, and improved cyclic stability compared to the pure V₂O₅ film. After 50 cycles at a current density of 500 mA g⁻¹, the Sn-doped film maintains a specific capacity of 334 mAh g⁻¹, which is substantially higher than the 157 mAh g⁻¹ retained by the pure V₂O₅ film. Studied by means of CV, EIS, and CP tests, it was found that Sn doping effectively lowered electrochemical reaction resistance, increased reaction reversibility, and improved lithium-ion diffusivity. Besides, Li *et al.* prepared Mg-doped V₂O₅ nanomaterials via a surfactant-assisted hydrothermal technique, and used as the cathode in LIBs. ²⁵⁸ The initial discharge specific capacity could achieve 411.13 mAh g⁻¹ at 60 mA g⁻¹, with a capacity retention rate of 46.4% after 110 cycles.

Moreover, Wu *et al.* synthesized Fe-doping V₂O₅ nanobelts by hydrothermal method and used as cathode in ZIBs. ²⁵⁹ With the aid of Fe doping, the interlayer spacing increased up to 10.8 Å. This modification endowed the cathode with excellent structural stability, achieving an impressive cycle stability of 300 cycles at a low current density of 0.5 A g⁻¹ with a high retention rate of 94.6%. Even at 0.2 A g⁻¹, the Fe-doped V₂O₅ maintained a retention of 93.6% after 150 cycles. Ma *et al.* prepared Co-doping V₂O₅ nanobelts via hydrothermal applied in ZIBs. ²⁶⁰ The assembled battery demonstrated a high voltage of 1.7 V and delivered an impressive capacity of 432 mAh g⁻¹ at 0.1 A g⁻¹. At voltages above 1.0 V, it achieved a capacity of 227 mAh g⁻¹, accounting for 52.54% of the total capacity. Further analysis indicated that Co ion intercalation increased the Zn²⁺ absorption energy from 1.85 to 2.24 eV compared to pristine vanadium oxide bronze. Additionally, the battery exhibited excellent rate capability (163 mAh g⁻¹ at 10

A g⁻¹) and an exceptional lifespan of over 7,500 cycles, retaining 90.26% of its capacity. Also, Ren et al. developed a Zn²⁺ and H₂O intercalated V₂O₅ cathode using a one-step stirring method, which offered a safe and straightforward approach for producing vanadium-based cathode materials in large quantities, making it suitable for the commercialization of ZIBs. ²⁶¹ As a result, the materials demonstrated superior specific capacity and cycling performance, retaining nearly 100% of the initial capacity even after 3000 cycles at a high current density of 4 A g⁻¹. Additionally, due to this large-scale preparation method, the study applied the cathode materials to 21 700 cylindrical ZIBs, achieving a maximum discharge capacity of 75.03 mAh g⁻¹ at a current of 0.4 A. As illustrated in Table 1.2, other examples of metal-doping, including Cu, 106, ²⁶² Ga, ²⁶³ Sn, ²⁶⁴ Ce, ²⁶⁵ Al, ²⁶⁶ Co, ²⁶⁷ Mn, ²⁶⁸ Ag, ²⁶⁹ Na, ^{270, 271} Ni, ²⁷² K, ²⁷³ Zn, ²⁷⁴ and Zr²⁷⁵ are summarized. The enhanced electrochemical performance of doping is due to the following reasons: 1) In theory, alkaline-earth metal ions (such as Ca²⁺, Mg²⁺), divalent transition metal ions (like Cu²⁺, Mn²⁺, and Fe²⁺), and trivalent ions (e.g., Al³⁺) form stronger bonds with the O²⁻ ions in the V-O layer compared to monovalent ions (such as alkali metal ions) due to their higher positive charges. As a result, these ions are better at connecting the V-O layers, helping to maintain structural stability during the reversible insertion and extraction of metal ions (such as Li⁺ and Zn²⁺), preventing deformation. 2) The doped ions could enlarge the interlayer spacing of V₂O₅, which can accommodate more ion storage, thus enhancing the practical capacities of MIBs. 3) The doped cations could be served as ion carrier to increase the electrochemical performance.

Table 1.2: Summary of the electrochemical properties of the cation doped V₂O₅ samples in MIBs.

Precursor material	Doped metal	Initial capacity (mAh g ⁻¹)	Current density (mA g ⁻¹⁾	Cycling performance	Types
V ₂ O ₅ hollow microspheres	Cu	328	80	160 mAh g ⁻¹ @ C/2.8 after 50 cycles	LIBs ²⁶²
flower-like V ₂ O ₅	Ga	357.18	50	150.35 mAh g^{-1} @ 200 mA g^{-1} after 100 cycles	LIBs ²⁶³

V_2O_5	Sn	258.5	200	212 mAh g ⁻¹ @ 200 mA g ⁻¹ after 50 cycles	LIBs ²⁶⁴
V ₂ O ₅ microspheres	Ce	280.7	0.5C	193.7 mAh g ⁻¹ @ 5C after 200 cycles	LIBs ²⁶⁵
V ₂ O ₅ nanowires	Al	236.4	100	$190.9 \text{ mAh g}^{-1} @ 200 \text{ mA g}^{-1}$ after 150 cycles	LIBs ²⁶⁶
V ₂ O ₅ microflowers	Co	280	15	$166 \text{ mAh g}^{-1} @ 15 \text{ mA g}^{-1} \text{ after}$ 200 cycles	LIBs ²⁶⁷
V ₂ O ₅ plates	Mn	251	1C	201 mAh g ⁻¹ @ 1C after 50 cycles	LIBs ²⁶⁸
V_2O_5	Mg	411.13	60	$190.23 \text{ mAh g}^{-1} @ 300 \text{ mA g}^{-1}$ after 60 cycles	LIBs ²⁵⁸
V ₂ O ₅ film	Sn	350	500	334 mAh g $^{-1}$ @ 500 mA g $^{-1}$ after 50 cycles	LIBs ²⁵⁷
V ₂ O ₅ nanobelts	Zn	214.4	500	221.6 mAh g ⁻¹ @ 1 A g ⁻¹ after 650 cycles	ZIBs ²⁵⁹
V ₂ O ₅ nanobelts	Co	326	500	163 mAh g ⁻¹ @ 10 A g ⁻¹ after 7500 cycles	ZIBs ²⁶⁰
V ₂ O ₅ nanobelts	Ag	~ 340	500	144 mAh g^{-1} @ 20 A g^{-1} after 4000 cycles	ZIBs ²⁷⁶
V ₂ O ₅ nanobelts	Na	227	500	$120 \text{ mAh g}^{-1} @ 4 \text{ A g}^{-1} \text{ after}$ 1000 cycles	ZIBs ²⁷⁰
V ₂ O ₅	K, Ni	266	5000	275 mAh g $^{-1}$ @ 5 A g $^{-1}$ after 200 cycles	ZIBs ²⁷²
V ₂ O ₅ nanowires	Zn	287.3	500	208 mAh g $^{-1}$ @ 1 A g $^{-1}$ after 450 cycles	ZIBs ²⁶¹
V ₂ O ₅ nanoribbons	K	61.5	50	46.8 mAh g ⁻¹ @ 50 mA g ⁻¹ after 50 cycles	KIBs ²⁷³

V ₂ O ₅ nanofibers	Zn	71.2	1000	90.0 mAh g $^{-1}$ @ 100 mA g $^{-1}$ after 100 cycles	NIBs ²⁷⁴
NH ₄ V ₂ O ₅ nanorods	Zr	288	10	328 mAh g $^{-1}$ @ 200 mA g $^{-1}$ after 150 cycles	MgIBs ²
Layered V ₂ O ₅ sheets	Cu	155	25	25 mAh g ⁻¹ @ 100 mA g ⁻¹ after 300 cycles	AIBs ¹⁰⁶
V ₂ O ₅ nanowires	Na	196.3	50	$109.4 \text{ mAh g}^{-1} @ 2 \text{ A g}^{-1} \text{ after}$ 2000 cycles	CIBs ²⁷¹

1.5.2 Defect Engineering

Defect engineering has been widely recognized as an effective modification strategy for enhancing the electrochemical performance of materials. Specifically, defect engineering offers larger electroactive sites by triggering structural rearrangements and improves charge transfer kinetics by altering the electronic structure, leading to better performance in energy storage systems. Among the various defect engineering approaches explored in recent years, oxygen vacancy defect engineering stands out as one of the most extensively studied and acknowledged techniques. For instance, Yoo et al. developed interface-defective V₂O₅ nanochips through the unique effects of combusted graphene in the electrospun PAN fiber template method (in Figure 1.11), which enhanced the electrochemical kinetics and capacity of cathodes for optimized ZIBs performance. ²⁷⁷ The V₂O₅ nanochips featured interfacial oxygen vacancies resulting from partial oxygen removal during carbothermal reduction, improving high-rate capability and long-term cycling stability by accelerating charge diffusion and increasing electrical conductivity. Additionally, the combusted graphene induces a nappy, disordered surface morphology in the V₂O₅, with nanosizing effects caused by compressive strain from V₀ formation at the interfaces. This resulted in considerate high-rate cycling stability (74.6% retention after 300 cycles at 1.3 A g⁻¹) in ZIBs.

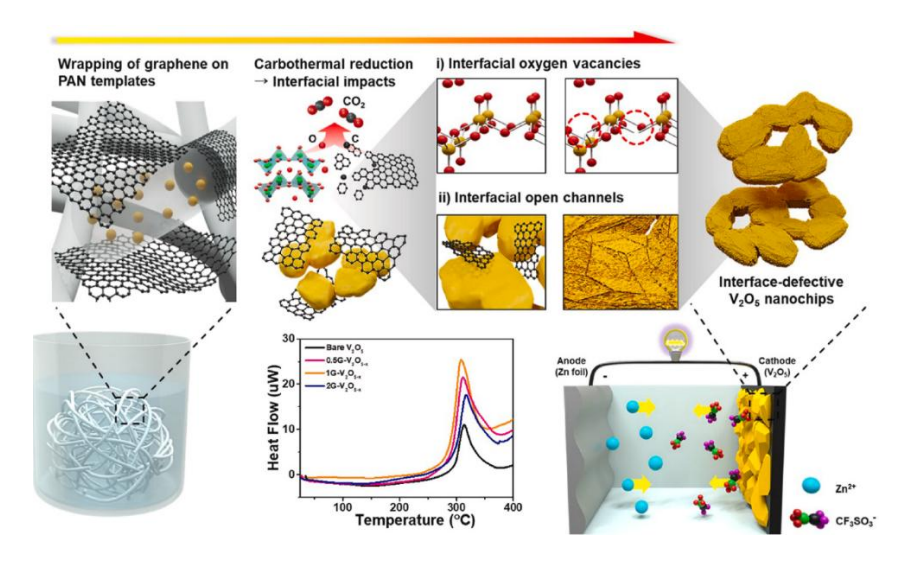


Figure 1.11: Mechanism of formation of interface-defective V_2O_5 nanochips through the effect of the combusted graphene in the system by using the electrospun PAN fiber templates to enhance the ZIBs performance (inset of the DSC curves shows the thermal behavior of all samples in the temperature range of 25–400 °C). Reproduced with permission. ²⁷⁷ Copyright 2021, Elsevier.

High-purity, well-crystallized V_2O_5 with oxygen vacancies can be achieved through heat treatment at an optimal temperature. Elevated temperatures effectively decompose V_2O_5 , leading to the formation of oxygen vacancy defects within the crystal structure. Xiao *et al.* synthesized pristine V_2O_5 (p- V_2O_5) by calcining vanadium (IV) acetylacetone at 650°C in air. Oxygen-deficient V_2O_5 (O_d - V_2O_5) was then produced by heating p- V_2O_5 at 400°C for 1 hour in V_2/V_2 atmosphere (V_2/V_2) was then produced by heating p- V_2/V_2 05 at 400°C for 1 hour in V_2/V_2 1 atmosphere (V_2/V_2 2 generated by heating V_2/V_2 3. This process increased the interlayer spacing of V_2/V_2 5 from 0.578 nm to 0.598 nm, indicating that the introduction of oxygen vacancies expanded the interlayer spacing of V_2/V_2 5. The larger interlayer spacing reduced residual V_2/V_2 6 ions within the structure during charge-discharge cycles, facilitating easier V_2/V_2 6 stronge and release, and improving reversibility. As a result, the V_2/V_2 6 cathode exhibited excellent capacity across a wide current density range from 0.1 A g-1 to 10 A g-1. Moreover, at 2 A g-1, the V_2/V_2 6 cathode retained 90% of its capacity after 1,000 cycles, whereas the p- V_2/V_2 6 electrode showed obviously lower stability, retaining only 59% of its capacity after 680 cycles.

Mechanical milling is a physical modification technique that effectively disrupts the lattice structure of V_2O_5 by applying compressive and shear forces, leading to the formation of oxygen vacancies. In this regard, Huang *et al.* directly induced oxygen vacancies in commercial V_2O_5

by using mechanical milling for 4 hours, as shown in Figure 1.12. 279 DFT calculations showed that the diffusion energy barrier for Zn^{2+} near these oxygen vacancies (between Zn_1 and Zn_2 positions) was significantly reduced, improving the storage and release of Zn^{2+} within the O_v - V_2O_5 lattice. This effect extended throughout the O_v - V_2O_5 lattice, even in areas distant from the oxygen vacancies (between Zn_2 and Zn_3), the Zn^{2+} diffusion energy barrier remains noticeably lower. Additionally, changes in the O1s peaks of the V_2O_5 cathode suggested that Zn^{2+} insertion resulted in the enhanced oxygen vacancy defects, and the peak recovered after Zn^{2+} deintercalation, confirming the high reversibility of mechanically milled oxygen-vacancy-rich V_2O_5 (O_v - V_2O_5). As a result, O_v - V_2O_5 achieved a specific capacity of 410.2 mAh g⁻¹ at 0.1 A g⁻¹, significantly outperforming pristine V_2O_5 , which delivered 286.9 mAh g⁻¹.



Figure 1.12: Schematic diagram of O_v-V₂O₅ prepared by mechanical ball milling. Reproduced with permission. ²⁷⁹ Copyright 2022, Wiley-VCH.

Other strategies have been reported based on defect engineering. For example, sonochemistry could be a promising technique for defect engineering in crystalline materials to enhance their performance in electrochemical energy storage. Hu *et al.* prepared a novel V₂O₅ cathode material with a unique amorphous and crystalline symbiotic structure through a salt-assisted sonication method, demonstrating good electrochemical performance. ²⁸⁰ As a cathode for LIBs, the optimized sample delivered an impressive capacity of approximately 400 mAh g⁻¹ at 0.02 A g⁻¹ and 193 mAh g⁻¹ at 3 A g⁻¹. This high capacity was attributed to the increased exposure of (001) planes, abundant ion storage sites at the interfaces, and percolation channels in the amorphous regions. Additionally, the material achieves a capacity of 175 mAh g⁻¹ with 81.8% retention after 500 cycles at 2 A g⁻¹.

Moreover, Ye *et al.* prepared oxygen vacancy-enriched V₂O₅ structures (O_v-ZVO) using a hydrothermal method, followed by annealing. ²⁸¹ In situ electron paramagnetic resonance (EPR) and XRD analysis revealed that a significant number of oxygen vacancies were created at relatively low reaction temperatures due to the partial removal of lattice water. The Zn||O_v-ZVO battery demonstrated an exceptional capacity of 402 mAh g⁻¹ at 0.1 A g⁻¹ and a notable energy output of 193 Wh kg⁻¹ at 2673 W kg⁻¹. As a proof of concept, the Zn||O_v-ZVO pouch cell achieved a high capacity of 350 mAh g⁻¹ at 0.5 A g⁻¹, highlighting its significant potential for practical applications.

Besides, Wang *et al.* developed a V₂O₅ cathode material with a high density of oxygen defects (O_d-V₂O₅@CC) through an in-situ chemical transition from ultrathin VS₄ nanosheet arrays on carbon cloth (VS₄@CC). ²⁸² This transition introduced a significant number of oxygen defects due to lattice reconfiguration. DFT calculations further confirmed that Zn²⁺ diffusion in oxygen-defective V₂O₅ could occur along the c-axis, rather than being confined to the ab-plane, enabling three-dimensional Zn²⁺ diffusion with rapid electrochemical kinetics and extensive capacitive storage. Additionally, the Zn²⁺ adsorption energies at the defective sites of V₂O₅ were close to a thermoneutral value (~0.18 eV), which supported reversible Zn²⁺ adsorption and desorption for highly stable Zn²⁺ storage performance. Leveraging these advantages, the engineered O_d-V₂O₅@CC electrode demonstrated impressive reversible capacities of 322.9 mAh g⁻¹ at 1 A g⁻¹ and 256.6 mAh g⁻¹ at 5 A g⁻¹, with stable cyclability of 220 mAh g⁻¹ after 500 cycles at 10 A g⁻¹. Notably, due to its binder-free design, the flexible O_d-V₂O₅@CC electrode also exhibited excellent electrochemical stability under mechanical deformation.

1.5.3 Structural Water Optimization

Structural H₂O molecules also play a crucial role in the structural changes and performance tuning of V₂O₅. The presence of water is typically unavoidable during hydrothermal synthesis and when using aqueous electrolytes. These structural water molecules influence the host structures by expanding interlayer spacing and altering overall morphology. Intercalated water molecules can significantly increase the interlayer spacing in layered V₂O₅, which reduces the interactions between Zn²⁺ ions and the host framework. This enhancement in spacing improves conductivity and facilitates rapid Zn²⁺ transport, leading to high-rate performance in ZIBs. For example, Yan *et al.* highlighted the crucial role of structural H₂O in the intercalation of Zn²⁺ into bilayer V₂O₅·nH₂O. ²⁸³ The results indicated that H₂O-solvated Zn²⁺ has a significantly

reduced effective charge, which lowered electrostatic interactions with the V_2O_5 framework and enhanced Zn^{2+} diffusion. This "lubricating" effect resulted in an aqueous Zn battery with a specific energy of approximately 144 Wh kg⁻¹ at 0.3 A g⁻¹. Additionally, the battery maintained an energy density of 90 Wh kg⁻¹ at a high power density of 6.4 kW kg⁻¹ (based on the cathode and 200% Zn anode).

Besides, previous studies have shown that thermal treatment significantly affected the structure and electrochemical properties of $V_2O_5 \cdot nH_2O$ in LIBs. ²⁸⁴⁻²⁸⁶ For instance, Wang *et al.* demonstrated the influences of treatment temperature and water content on capacity and rechargeability of V_2O_5 xerogel films. ²⁸⁴ Water contents of the $V_2O_5 \cdot nH_2O$ films depend on the deposition and post annealing temperatures. One film sprayed at 150 °C and annealed at 190 °C exhibited a large discharge capacity and the longest cycling life. By contrast, the films sprayed or annealed at high temperatures (~250 °C) showed poor electrochemical performance. XRD patterns of the films treated at different temperatures revealed that removal of too much water at high temperatures resulted in crystallization or a small interlayer spacing, which may restrict the diffusion of lithium ions inside $V_2O_5 \cdot nH_2O$ films.

Therefore, optimizing water content is crucial for enhancing the electrochemical performance of hydrated V_2O_5 , as excessive water does not necessarily improve performance. Excessive structural water can weaken interlayer forces, leading to structural collapse and poor ion storage. For instance, Sun *et al.* controlled heating temperatures to produce a series of hydrated VOH xerogels with varying water contents (n) for ZIBs. ²⁸⁷ The authors found that the interlayer spacing of $V_2O_5 \cdot nH_2O$ could be adjusted by varying the amount of structural water. Also, the amount of intercalated solvent water and the extent of V-dissolution were largely influenced by the initial value of "n" in $V_2O_5 \cdot nH_2O$. Their study demonstrated that at n = 0.26, the $V_2O_5 \cdot nH_2O$ electrode achieved the best electrochemical performance, with a specific capacity of 456.5 mAh g⁻¹ at 0.1 A g⁻¹ and over 94% capacity retention after 2000 cycles at 3 A g⁻¹. Moreover, according to Sun *et al.*'s study, structural water molecules facilitated the desolvation process of $[Zn(H_2O)_6]^{2+}$ at the electrolyte/electrode interface, lowering the energy barrier and enhancing the insertion and deinsertion kinetics of multihydrated Zn^{2+} ions. ²⁸⁸

1.5.4 Micro/macroscopic Structure Engineering

One of the main challenges with using V₂O₅ as cathodes in MIBs is its low conductivity, which impairs electron and charge transport and limits overall electrochemical performance. In addition to atomic-scale modifications such as guest-ion doping, defect introduction, and structural water optimization, enhancing conductivity at the micro/macroscopic scale is crucial. Compositing V₂O₅ with conductive materials is a key strategy in this regard. Previous studies have shown that carbon-based conductive materials, conductive polymers, and metal nanowires or films can significantly improve the ionic and electrical conductivities of V₂O₅. For example, a binder-free V₂O₅ nanofibers/CNTs hybrid film cathode was synthesized using a hydrothermal process, Reported by Liu et al. 289 This nanohybrid cathode in ZIBs achieved a significantly higher specific capacity of 390 mAh g⁻¹ compared to the capacity (263 mAh g⁻¹) of a pure V₂O₅ at 1 A g⁻¹. Additionally, it demonstrated a notable capacity of 250 mAh g⁻¹ at a higher current density of 5 A g⁻¹, indicating excellent rate performance. The incorporation of CNTs, which have high electrical conductivity, significantly enhanced the conductivity of the nanohybrid cathode and thereby improved its electrochemical performance. Besides, Juggernauth et al. developed a 3D V₂O₅/CNT hybrid architecture using chemical vapor deposition. ²⁹⁰ This technique allowed for the morphological tuning of vanadium oxide nanoarchitectures and their functional properties. Their study demonstrated that the surface areas and densities of these hybrid structures can be adjusted by controlling the operating pressure, which in turn modified the Gibbs free energy of crystal growth. This work highlighted the importance of morphology design in conjunction with conductive materials to enhance performance. Furthermore, Javed et al. demonstrated the creation of a flexible ZIB with a binder-free design, integrating V₂O₅ nanosheets and a titanium substrate. ²³¹ This configuration achieved impressive discharge capacity and cycle stability, due to enhanced electrical conductivity and increased exposure of active sites. In addition, Zhang et al. reported the use of edge-rich vertical graphene nanosheets to connect V₂O₅ with the substrate, effectively reducing interfacial resistance. ²⁹¹ The graphene nanosheets not only securely anchor the V₂O₅ but also accommodate volume changes during cycling, thereby enhancing the stability and extending the lifespan of the V₂O₅ electrode.

1.6 Research Objectives and Outline

The primary objective of this research is to explore and enhance the energy storage capacities of V_2O_5 cathodes for both Li-ion and Zn-ion battery chemistries. This involves modifying the properties of V_2O_5 to improve its charge storage capabilities, alongside optimizing its optical properties for the direct harvesting of light energy, thereby enabling light-accelerated charge storage. Additionally, this work investigates the role of cation pre-intercalation in V_2O_5 cathodes, aiming to provide a comprehensive understanding of how this process influences and potentially improves charge storage performance. Through this approach, the research aspires to contribute valuable insights into the mechanisms governing energy storage and light-assisted enhancement in advanced battery systems. The content of each chapter is outlined as follows:

Chapter 2: Provides the synthesis of materials essential to the research goals, employing various preparation methods aligned with the study's objectives. The synthesized materials underwent extensive characterization, which included assessments of morphology, structure, surface area, thermal stability, elemental composition, and optical properties. Analytical techniques used in these characterizations included scanning electron microscopy (SEM), transmission electron microscopy (TEM), X-ray diffraction (XRD), Raman spectroscopy, thermogravimetric analysis (TGA), X-ray photoelectron spectroscopy (XPS), and UV-Visible (UV-Vis) spectroscopy. Additionally, the materials were evaluated through the assembly of optical coin-cells and conventional coin-cells, followed by a series of electrochemical tests, including cyclic voltammetry (CV), galvanostatic discharge-charge (GDC), and electrochemical impedance spectroscopy (EIS).

Chapter 3: Introduces an innovative method for creating photocathodes utilizing hydrogenated vanadium pentoxide (H:V₂O₅) nanofibers, with results compared to unmodified V₂O₅. This approach provides a detailed insight into how hydrogenation modifies Li-ion storage capabilities. The hydrogenation process improves optical activity, electronic conductivity, and ion diffusion rates in photo-enhanced LIBs, resulting in substantial gains in charge storage performance under illumination. The results indicate that H:V₂O₅ shows significant increases in specific capacity under both dark and illuminated conditions. Additionally, it demonstrates improved diffusion kinetics and charge retention when exposed to light compared to the

unmodified material. This defect-engineering strategy shows strong potential for the design of high-performance photocathodes for next-generation energy storage technologies.

Chapter 4: Examines the strategy of pre-doping cations to modulate the energy barrier in layered vanadium pentoxide and adjust the oxidation states of vanadium, aiming to improve Zn^{2^+} ion storage capacity in AZIBs. AZIBs often face challenges, including slow zinc-ion diffusion due to the high energy barrier between V_2O_5 layers, structural degradation of the electrode over time, and, consequently, lower capacity than the theoretical potential. This study investigates the pre-doping of various cations (such as Na^+ , K^+ , and NH_4^+) into V_2O_5 to boost overall charge storage performance. The findings reveal that the presence of V^{4+} plays a crucial role in enhancing storage performance, while introducing NH_4^+ into V_2O_5 not only expands the interlayer spacing but also significantly raises the V^{4+}/V^{5+} redox couple ratio, resulting in superior electrochemical performance. This research advances our understanding and supports the development of high-capacity cathode materials, providing valuable insights for the design and optimization of cathodes to enhance the electrochemical performance of AZIBs.

Chapter 5: Expands on the strategy of pre-doping cations to lower the energy barrier in layered vanadium pentoxide and modulate vanadium oxidation states, with the goal of enhancing Li⁺ ion storage capacity in LIBs. This work explores the incorporation of different cations, including Na⁺, K⁺, and NH₄⁺, into V₂O₅ to improve overall charge storage properties. The results indicate that V⁵⁺ and V⁴⁺ plays a significant role in altering the charge storage performance. This study deepens our understanding and contributes to the development of high-capacity cathode materials for LIBs, offering key insights into the design and optimization of cathodes to boost electrochemical performance in LIBs.

Chapter 6: Provides a comprehensive summary and outlook for the thesis. It consolidates all key findings from the experimental work, offering a cohesive overview of the research outcomes and their implications. Building on the experimental insights, the chapter also presents an outlook on future research opportunities, highlighting potential directions to further advance the field. Suggestions for future work are grounded in the current findings, identifying areas where additional studies could optimize material performance, explore alternative

strategies, and enhance the understanding of electrochemical mechanisms. This outlook aims to inspire continued innovation in energy storage materials and guide further improvements in battery technology.

Chapter 2

Methodology and Characterization

This chapter of the thesis encompasses the synthesis of materials relevant to this research, encompassing various synthesis methods tailored to the objectives of the study. These materials underwent thorough characterization, spanning morphological, structural, surface areas, thermal stability, elemental composition and optical analyses utilizing techniques such as scanning electron microscopy (SEM), transmission electron microscopy (TEM), X-Ray diffraction (XRD), Raman spectroscopy, thermogravimetric analysis (TGA), X-ray photoelectron spectroscopy (XPS), and UV-Vis spectroscopy. Furthermore, the materials were subjected to comprehensive testing, involving the fabrication of optical coin-cells and conventional coin-cells, followed by electrochemical assessments including cyclic voltammetry (CV), galvanostatic discharge-charge (GDC), and electrochemical impedance spectroscopy (EIS).

2.1 Overview

This chapter provides a detailed description of the synthetic methods used to prepare the V_2O_5 -based cathode materials and outlines the characterization of their intrinsic properties prior to conducting electrochemical analyses. In addition to fundamental evaluations, energy storage mechanisms are explored through ex-situ structural characterizations of the materials. The characterization techniques are categorized into two main sections: structural and electrochemical characterizations, each summarized with respect to the testing standards and the equipment utilized.

2.2 Hydrothermal Synthesis

The method of synthesizing materials plays a pivotal role in shaping the morphological and structural attributes of electrode materials, consequently impacting their electrochemical performance. ^{148, 292-295} Vanadium oxide cathodes can be synthesised via sol-gel, ²⁹⁶ hydrothermal technique, ²⁹⁷ electrospinning, ²⁹⁸ spray drying, ²⁹⁹ electrochemical deposition³⁰⁰ and so on. Among these methods, the hydrothermal approach stands out for its versatility in material selection, ease of handling, and rapid approach. The term hydrothermal is of purely geological origin. It was first used by Sir Roderick a British geologist who employed water at elevated temperature and pressure to transform Earth's crust into various rocks and minerals. ³⁰¹ Hydrothermal research began in the 19th century, with the first published research paper made by K.F.E Schafthaul, who managed to synthesise a tiny quartz crystal from the transformation of precipitated silicic acid in a steam digestor. ³⁰² By the mid-20th century, hydrothermal research had entered a phase of refinement. With the advent of nanotechnology, the combination of hydrothermal approach and nanotechnology paved the way for processing advanced nanomaterials with highly controlled morphology.

Hydrothermal synthesis enables controlled nanostructure formation by modifying factors such as pH value, precursors, and surfactants. ¹¹ The ease of handling and preparation adds convenience to product fabrication, with a shorter processing time compared to other techniques. Hydrothermal reactions take place within a Polytetrafluoroethylene (PTFE)-lined stainless-steel autoclave reactor, as illustrated in the accompanying image (Figure 2.1). Reactants undergo heterogeneous reactions in the presence of an aqueous solution and

mineralizers under elevated temperature and pressure within the sealed autoclave, leading to dissolution and recrystallization. The solute dissolves in the hotter region due to temperature disparities across the chamber, precipitating as a supersaturated solution in the cooler region where seed crystals grow. Concurrently, the solute undergoes absorption, decomposition, and desorption at the growth surface, with adsorbed materials migrating across the surface as dissolved matter crystallizes. ³⁰³ During the process, aqueous system functions to build up the autogenous pressure coming from the vapour pressure, while the hydrolysis and gasification occur, along with the generation of H₂. ³⁰⁴ Mineralisers, which are either organic or inorganic additives, facilitate the solubility of the solute as well as alter its solubility temperature coefficient. ³⁰³ Studies have shown the size and morphology of the crystal are controlled not only by thermodynamic variables, such as composition of the reactants, pH value, temperature, and time, ³⁰⁴⁻³⁰⁶ but also by non-thermodynamic factors, such as the stirring rate. ³⁰⁷



Figure 2.1: Apparatus of hydrothermal autoclave.

2.3 Materials Characterizations

2.3.1 Scanning Electron Microscopy

Scanning electron microscopy (SEM) is an advanced imaging technique renowned for its ability to characterize material surface morphology and compositions at exceptionally high resolution. Through SEM, materials' surface morphology is depicted vividly in high-quality images. When a high-energy electron beam interacts with the sample surface, electrons undergo inelastic scattering, producing a spectrum of informative signals, such as backscattered

electrons (BSE), auger electrons, cathodoluminescence, secondary electrons (SE), and X-rays from various depths of the sample. Both BSE and SE present distinct advantages: BSE offer insights into composition, while SE predominantly provide higher-resolution morphological images due to their shallower penetration depth. In the SEM setup, electrons emitted by the electron gun, with an accelerating voltage ranging from 300 V to 30 kV, navigate through a complex arrangement of electron magnetic lenses to precisely focus the coherent beam onto the sample surface. Detectors play a pivotal role in capturing specific aspects of the electronprovided information. Depending on the equipped detector, SE detectors are tailored to capture high-resolution images of specimen topography, whereas BSE detectors facilitate comprehension of the material's composition. SEM was employed to scrutinize the morphology of the synthesized materials. This technique was selected due to its ability to provide rapid, large-area imaging at nanoscale resolution, which is particularly advantageous for evaluating particle agglomeration and surface uniformity in powder-based samples. Additionally, its compositional sensitivity via BSE imaging adds complementary insight into elemental distribution. SEM images were captured using either Zeiss EVO LS15 or JEOL JSM-7600F instrument (Figure 2.2) operating in secondary electron mode, with an electron beam voltage set at 15 kV. Before imaging, samples were affixed to a sample holder using conductive carbon tape and then sputter-coated with a 10 nm layer of gold using a Quorum Q150R Plus rotarypumped coater to enhance conductivity.





Figure 2.2: Physical instrument (a) Zeiss EVO LS15 and (b) JEOL JSM-7600F used to capture SEM images.

2.3.2 Transmission Electron Microscopy

Transmission electron microscopy (TEM) is extensively employed to explore the morphology, and crystalline structure of various samples at the nanoscale. In TEM, an electron beam emitted from the electron gun traverses through the specimen, leading to an interaction between the beam and the sample. Factors such as sample density and composition can impact the electron beam's transmission. Following transmission through the specimen, the electrons are refocused and magnified by a system of electromagnetic lenses, before being projected onto a screen for visualization of the electron image data. For a more comprehensive analysis of the materials' structure and morphology, TEM analyses were performed using a JEOL JEM-2100 TEM operating at a voltage of 200 kV (Figure 2.3). High-resolution TEM (HRTEM) was employed to scrutinize interplanar spacings, while selected area electron diffraction (SAED) facilitated the capture of two-dimensional electron diffraction patterns. The obtained images were analysed using DigitalMicrograph software. Energy-dispersive X-ray spectroscopy (EDS) was utilized for elemental and compositional analysis. TEM was specifically chosen for its high spatial resolution, which is essential for resolving the fine structural details and crystallinity of the nanomaterials that cannot be captured by SEM. The integration of HRTEM and SAED enabled direct observation of lattice fringes and crystal orientation, critical for confirming phase purity and structural integrity. Moreover, EDS mapping in the TEM provided localized elemental analysis at nanometre scale, which is vital for studying compositionally inhomogeneous regions. Sample preparation involved mixing with methanol, sonicating for 30 seconds, and depositing the dispersion onto a carbon-coated copper grid for examination.

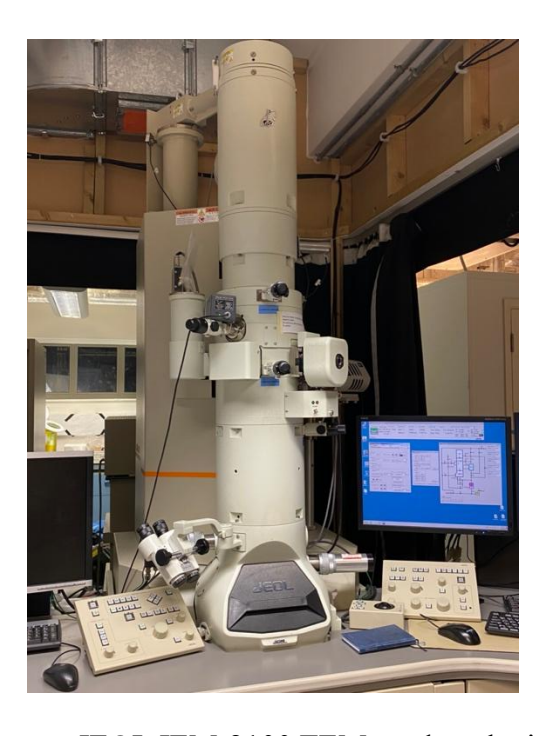


Figure 2.3: Physical instrument JEOL JEM-2100 TEM used to obtain TEM and SAED images.

2.3.3 X-ray Diffraction

X-ray diffraction (XRD) serves as a valuable technique for investigating the structure and phase of crystalline materials. A monochromatic X-ray beam is directed onto the surface of a crystalline material, interacting with its atomic planes. The phenomenon of XRD is fundamentally described by Bragg's law: $n\lambda = 2d \sin \theta$; where θ is the incident angle, d is the interlayer spacing, λ is the wavelength of the incident wave and n is the integer representing the order of the diffracted wave. During XRD, incident X-rays interact with the specimen and are scattered by periodically arranged crystals within it, resulting in continuous diffraction patterns. These patterns provide essential information about the crystal structure, phase, and crystalline size of the samples under examination. The path-length difference between two distinct X-rays can be calculated as $2dsin\theta$. Constructive interference occurs when the pathlength difference equals an integer multiple of the X-ray wavelength. The interplanar spacing, or d-spacing, which varies with crystal system and orientation, can be calculated from diffraction angles using equations based on lattice parameters. For example, in cubic systems, the spacing is determined by $d_{hkl} = \frac{a}{\sqrt{h^2 + k^2 + l^2}}$, where (h, k, l) are Miller indices and a is the lattice constant. By comparing the obtained diffraction patterns with standards from a database, it becomes possible to identify the phases present in the sample being analysed. The crystal

structure of materials was analysed using XRD, performed on a Panalytical Empyrean XRD instrument employing the Cu Kα radiation (Figure 2.4). Measurements were carried out at an operating voltage and current of 40 kV and 40 mA, respectively, with a step size of 0.05° and a scanning rate of 0.1° s⁻¹, spanning a 2θ range from 2° to 70°. XRD was critically applied for its non-destructive nature and its effectiveness in phase identification and crystallinity evaluation, especially for polycrystalline powder samples. Compared to spectroscopic techniques, XRD provides direct structural information at the atomic level, making it indispensable for confirming successful synthesis and assessing phase purity.

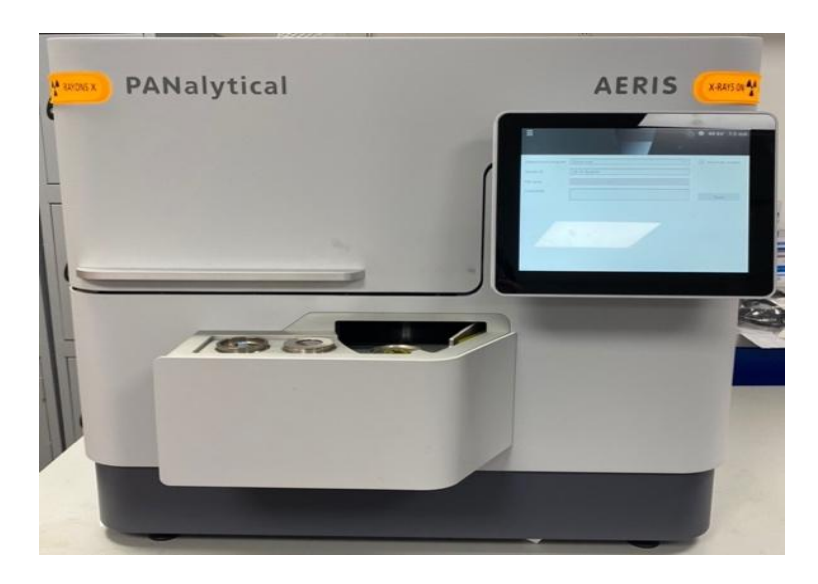


Figure 2.4: The Panalytical Empyrean XRD instrument used to obtain the crystal information of samples.

2.3.4 Raman Spectroscopy

Raman spectroscopy is a non-destructive technique employed for studying the vibrational and rotational characteristics of molecules within a sample. It operates based on the Raman effect, wherein Raman spectra emerge from the inelastic collision between laser beam radiation and the molecules in the sample. During Raman spectroscopy, when a monochromatic laser beam interacts with a sample, most of the photons undergo elastic scattering (Rayleigh scattering), resulting in the same frequency as the incident beam. However, a portion of the beam undergoes inelastic scattering, resulting in a frequency different from that of the incident beam. The frequency of the incident laser beams higher than the scattered frequency produces the Stokes line, while a lower frequency produces the Anti-Stokes line in the Raman spectrum. Raman spectroscopy measurements were conducted using the Renishaw inViaTM confocal Raman

microscope with a laser wavelength of 515 nm (Figure 2.5). Prior to testing, the machine was calibrated using a Si wafer to a wavenumber of 520.8 cm⁻¹. This analytical technique is utilized to identify molecular vibrational modes, rotational modes, and other low-frequency modes based on the detection of Raman scattering from the interaction between light and the material.



Figure 2.5: The Renishaw inViaTM confocal Raman microscope used to get Raman spectroscopy measurements.

2.3.5 X-ray Photoelectron Spectroscopy

X-ray photoelectron spectroscopy (XPS) serves as a quantitative surface analysis technique employed for elemental analysis of samples. It is a surface-sensitive analytical method involving the bombardment of a specimen's surface with X-rays and the measurement of the kinetic energy of the emitted electrons. During the XPS test, the specimen's surface is irradiated with X-rays, and the kinetic energy of the emitted electrons is examined. The emitted photoelectron results from the complete transfer of X-ray energy to a core level electron. An energy analyser scans a specific range of energies, detecting the photoemitted electrons from the specimen surface and generating a spectrum of intensities as a function of binding energy. XPS provides elemental information based on the photoelectric effect and is known for its surface sensitivity. This analysis was carried out utilizing the ThermoFisher Scientific XPS instrument (Figure 2.6). The XPS data were collected using monochromatic Al $K\alpha$ X-rays (1486.6 eV), with a pass energy of 50 and 200 eV for narrow and wide spectra, respectively. Notably, no significant sample charging was observed, and charge referencing was performed against adventitious carbon (C 1s, 284.8 eV). Spectra were presented with intensity in counts

per second (CPS), and experimental peaks were fitted using CasaXPS software. XPS was primarily utilized to qualitatively and quantitatively identify the variation in oxidation states of the cathode material. XPS offers high-resolution chemical state information limited to the surface region, where many electrochemical reactions and degradation processes occur. This makes it an indispensable tool for surface-sensitive characterization in battery material research.



Figure 2.6: The ThermoFisher Scientific XPS machine used for XPS tests in this research.

2.3.6 Ultraviolet-Visible Spectroscopy

UV-Vis spectroscopy is a method of analysis that quantifies the absorption or transmission of specific wavelengths of UV or visible light by a sample. Operating on the principle of absorption of light energy within the UV-Vis range, UV-Vis spectroscopy relies on electronic transitions between differing energy levels. As a beam of UV-Vis light traverses through a sample, certain wavelengths encounter absorption while others pass through. The absorbed wavelengths correspond to electronic transitions from ground state to excited state energy levels within the materials. UV-Vis spectrophotometers comprise essential components such as a light source, monochromator, sample holder, and detector. The light source emits a broad-spectrum encompassing UV and visible light, which subsequently undergoes wavelength selection via the monochromator. The resultant monochromatic light is then directed through the sample, where it interacts with the material. The detector measures the intensity of transmitted or absorbed light, generating an absorption spectrum. Typically represented as absorbance (A) versus wavelength (λ), this spectrum depicts characteristic peaks and troughs

corresponding to electronic transitions within the sample. UV-Vis was employed to acquire absorbance spectra of the sample and analyse the band gap of the materials. The analysis was conducted utilizing the Perkin Elmer Lambda 750S instrument (Figure 2.7). The wavelength range spanned from 800 nm to 250 nm, with a scan rate of 480nm/min. Each test involved the use of two quartz cuvettes: one acting as the reference cuvette filled with pure ethanol, and the other containing the sample dissolved in ethanol. In this investigation, UV-Vis spectroscopy was chosen for its simplicity and effectiveness in estimating the band gap of cathode materials. Its ability to reveal optical transitions complements structural and morphological analyses, offering a broader understanding of material properties.



Figure 2.7: The Perkin Elmer Lambda 750S instrument used for UV-Vis measurements.

2.3.7 Thermogravimetric Analysis

Thermogravimetric analysis (TGA) is a widely employed technique for tracking the mass variation of a material as a function of temperature. In TGA, the sample undergoes controlled heating at a uniform rate or is maintained at a constant temperature for a specified duration. A plot of weight loss against temperature, known as the TG curve, is generated. Two pivotal temperatures, the initial and final temperatures, are discerned on the TGA curve. Initial temperature marks the onset of mass change, while final temperature denotes the temperature at which the decomposition tends to cease, as detected by the thermo balance. The interval between these temperatures, termed the reaction interval, is pivotal for calculating the exact weight loss of the material. TGA apparatus comprises a sample pan suspended by a precise

balance within a furnace. The sample pan is heated during analysis, with the option to introduce either an inert or reactive gas into the furnace depending on interest, which exits through an exhaust. Mass loss of the sample inside the pan is continuously monitored and resulting graph of mass loss versus temperature illustrates the thermal transitions of the material. TGA measurements provide quantitative insights into various parameters, including residual solvent content, decomposition temperature of different materials, moisture content, and among others. In this thesis, TGA analysis was conducted on PerkinElmer TGA 4000 machine (Figure 2.8). The samples were loaded into a ceramic sample pan and heated from 30 °C to 100 °C at a ramping rate of 5 °C min⁻¹. The temperature was hold at 100 °C for 10 mins before continuing to heat to 350 °C at a rate of 10 °C min⁻¹. The nitrogen gas was supplied during the whole process at the rate of 20 mL min⁻¹. TGA was used for its ability to precisely quantify mass loss associated with water content and thermal stability. Its sensitivity to subtle weight changes makes it especially effective for evaluating hydration levels in electrode materials, which can affect electrochemical performance.



Figure 2.8: Physical instrument PerkinElmer TGA 4000 used for TGA measurements.

2.4 Electrochemical Characterizations

2.4.1 Coin-cell Assembly

Various electrochemical tests were conducted to evaluate the performance of cells assembled with different cathodes. The coin-cell format was used in this research project due to laboratory

equipment constraints. Additionally, coin-cells offer several advantages in research-based battery assembly, making them an ideal choice for initial testing. They require a smaller amount of active material, enabling efficient screening of different formulations while minimizing material waste. Their standardized design ensures reproducibility and facilitates comparative studies. By first optimizing the battery formulation using coin-cells, researchers can refine electrode compositions and electrochemical performance before scaling up to pouch cells, which involve larger active material loading and are more suited for large-scale fabrication.

The assembly of the coin-cell follows standard procedures and can be categorized into dark cell assembly and light cell assembly. For assembling a dark cell, a cathode disc is positioned in the centre of a CR2032 coin-cell case, followed by a separator made of Whatman glass microfiber filter paper. Subsequently, $100~\mu L$ of electrolyte is applied onto the separator. The anode is then placed on top of the separator, followed by a stainless-steel spacer (1 mm thick) and a conical spring. Finally, the cell is sealed with a negative mesh case, and the coin-cell battery is crimped using a hydraulic press. In contrast, for a light cell assembly, a light window is created by punching a 7 mm diameter hole in the centre of the positive case. A glass window is then affixed onto the positive case using parafilm. Three strips of current collector (Ti foil for ZIBs and Al foil for LIBs) are placed on top of the glass window to enhance conductivity. The remaining steps are identical to those of the dark cell assembly. However, in the light cell assembly, the spacer thickness is reduced to 0.2~mm. Figure 2.9~illustrates the cell configuration for both types of coin-cells.

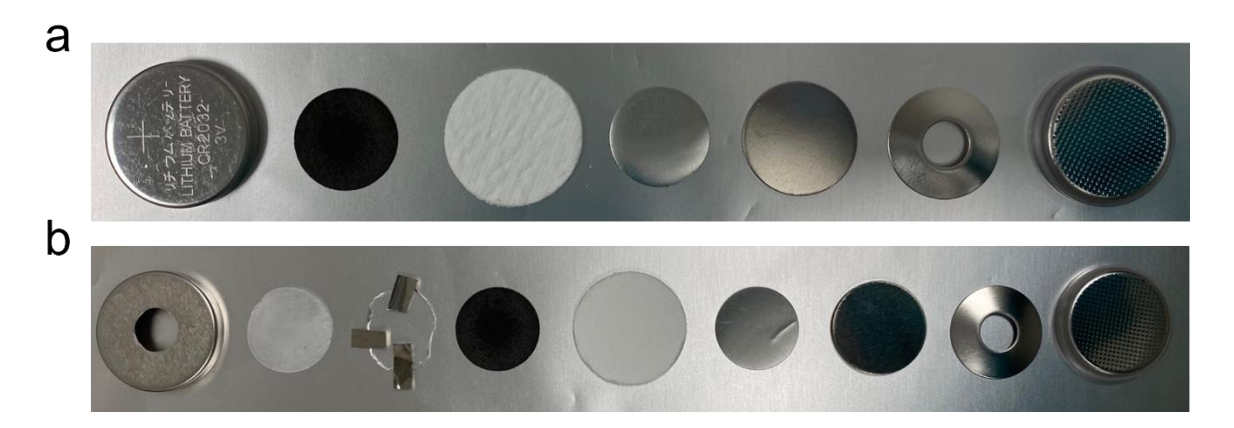


Figure 2.9: Demonstration of coin-cell assembly. (a) dark cell assembly and (b) light cell assembly.

2.4.2 Cyclic Voltammetry

Cyclic voltammetry (CV) was used to study the redox reactions and reversibility of battery under discharge and charge process at different scan rate. Before CV tests, all the cells were rested for 10 hours to activate the performance. All the CV tests were conducted on a Biologic VMP-3 galvanostat machine. For LIBs, the voltage was scanned between 2 to 4 V at 0.2, 0.4, 0.5, 0.8 and 1 mV s⁻¹, respectively. For ZIBs, the voltage was scanned between 0.2 to 1.6 V at 0.2, 0.4, 0.5, 0.8 and 1 mV s⁻¹, respectively. Nernst equation provides a way to calculate the electromotive force (E) of a cell under any condition. The Gibbs free energy change (ΔG) is a thermodynamic quantity that indicates spontaneous of the reaction also equal to the maximum useful work done in a process. ΔG for a cell reaction is related to the cell potential as shown in equation 2.2. Using the Nernst equation and the Gibbs free energy change can predict the distinctive peaks on the CV curves, where n is the number of transferred electrons, F is the Faraday constant.

$$E^{\circ}_{\text{cell}} = E^{\circ}_{\text{reduction}} - E^{\circ}_{\text{oxidation}}$$
 (2.1)

$$\Delta G^{\circ} = -nFE^{\circ}_{\text{cell}} \tag{2.2}$$

During the voltage sweep, ΔG can be deduced from thermodynamics, where Q is the concentration quotient of reduction and oxidation.

$$\Delta G = \Delta G^{\circ} + RT lnQ \tag{2.3}$$

Therefore,

$$-nFE = -nFE^{\circ} + RT lnQ \tag{2.4}$$

$$E = E^{\circ}_{\text{cell}} - \frac{RT}{nE} \ln \left(\frac{C_{\text{red}}}{C_{\text{cel}}} \right)$$
 (2.5)

2.4.3 Galvanostatic Discharge-charge Test

Galvanostatic discharge-charge test (GDC) is applied to know the capacity and efficiency of battery at being charged and discharged at various current density over the same potential window. It was measured using the Biologic VMP-3 galvanostat machine in Figure 2.10 (a). It gives the trend of battery capacity change. For the consistency, the charging condition for battery used in this study were current density. For LIBs, batteries were tested at various specific currents: 200, 500, 1000, 2000, 1000, 500, and 200 mA g⁻¹ over potential window of

2 to 4 V (versus Li/Li⁺). For ZIBs, batteries were test under 200, 500, 1000, 2000, 5000, 2000, 1000, 500, and 200 mA g⁻¹ over potential window of 0.2 to 1.6 V (versus Zn/Zn²⁺).

2.4.4 Long Cycling Test

The Neware (BTS4000) system in Figure 2.10 (b) was employed to conduct long cycling (LC) measurements. This test is designed to assess the stability of batteries and to monitor their capacity decay over time. Additionally, the cycling test provides data on the Coulombic efficiency of the battery.

2.4.5 Electrochemical Impedance Spectroscopy

Electrochemical impedance spectroscopy (EIS) was conducted using an Autolab PGSTAT302N instrument in Figure 2.10 (c). The pre-activated batteries underwent testing within a frequency range spanning from 10 mHz to 100 kHz, employing a voltage amplitude of 10 mV. The Nyquist plot, derived from the EIS data, furnishes crucial insights into the electrochemical characteristics of the batteries. Key parameters obtained from the Nyquist plot encompass solution resistance (R_s), reflecting the ohmic resistance of the electrolyte and other cell components; charge transfer resistance (R_{ct}), indicative of the resistance to electron transfer at the electrode-electrolyte interface; and Warburg impedance (W), correlating with ion diffusion within the electrode.

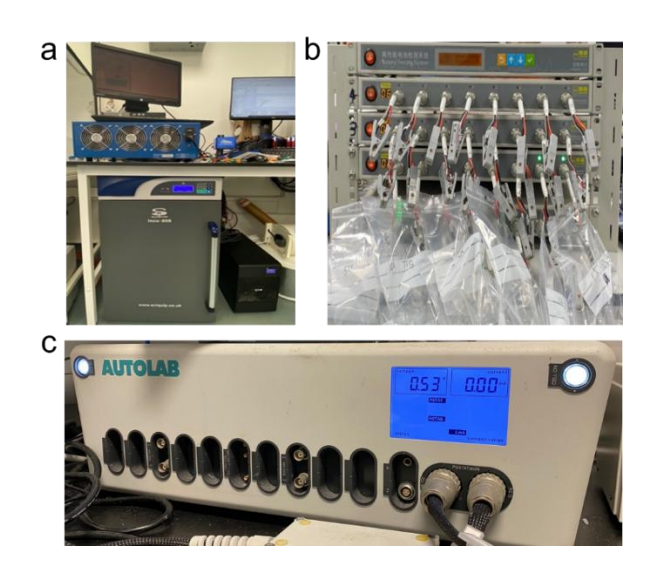


Figure 2.10: Pictures of our electrochemical testers. (a) galvanic static tester, (b) Neware 4000 tester and (c) Autolab.

Chapter 3

Hydrogenated V_2O_5 with Improved Optical and Electrochemical Activities for Photo-Accelerated Lithium-Ion Batteries

This chapter presents a unique approach for crafting photocathodes using hydrogenated vanadium pentoxide (H:V₂O₅) nanofibers. This method enhances optical activity, electronic conductivity, and ion diffusion rates within photo-accelerated Li-ion batteries. These findings reveal that H:V₂O₅ exhibits notable improvements in specific capacity under both dark and illuminated conditions. Furthermore, it demonstrates enhanced diffusion kinetics and charge storage performance when exposed to light, as compared to pristine counterparts. This strategy of defect engineering holds great promise for the development of high-performance photocathodes in future energy storage applications. This chapter is based on the published article. Yinan Lu et al., Small, 2024, 20, 2308869, DOI: 10.1002/smll.202308869.

3.1 Introduction

The 21st century faces an urgent demand for energy coupled with a pressing need to shift towards renewable sources, largely due to the environmental damage caused by fossil fuels. This energy scarcity presents a significant challenge worldwide. Although sustainable options like wind and solar power are available, their variability requires reliable energy storage systems to ensure a steady power supply. Conventionally, photovoltaic cells are linked to separate storage devices, 308 yet this setup can lead to drawbacks such as increased ohmic resistance and mismatches in energy transfer between components. These issues can reduce energy collection efficiency, raise costs, and add to the device's bulk and weight. 309, 310 To address these limitations, researchers are exploring the development of photo-accelerated batteries, which integrate energy harvesting and storage in a single unit. This approach promises to reduce expenses, boost energy conversion efficiency, and produce more compact, lightweight devices, which could be particularly useful in wearable tech and IoT applications. For such devices to perform optimally, the photoelectrode material should serve dual purposes, functioning both as a light-absorbing semiconductor and an energy storage medium. Moreover, it should minimize charge recombination, facilitate efficient movement of photo-generated charges, ^{125, 311} and support rapid ion transport to sustain effective diffusion channels. ³¹²

Research on photo-accelerated energy storage has primarily concentrated on lithium-ion battery systems because of their exceptional characteristics, including high energy density, light weight, and long cycle life. ³¹³⁻³¹⁵ In this field, vanadium pentoxide has emerged as a promising candidate for cathode materials in lithium-ion batteries, thanks to its affordability, wide availability, controllable morphology, and high theoretical capacity for lithium-ion intercalation. Various studies have explored V₂O₅ as a photocathode material. Wang et al., for instance, used LiV₂O₅ as a photocathode in photo-accelerated lithium-ion batteries, ³¹⁶ achieving a notable specific capacity of 185 mAh g⁻¹ under light exposure, a 270% improvement compared to capacity without light. Boruah *et al.* have also investigated V₂O₅ photocathodes in these systems, demonstrating enhanced charge storage performance under illumination. ¹²⁶

Recent advancements in the field of metal-ion batteries have seen significant progress in developing photocathodes, especially dual-functional ones that improve both capacity and rate performance under light exposure. However, research has predominantly concentrated on

unmodified materials such as VO₂(B), MoS₂, and V₂O₅. Key factors influencing the efficiency of photo-accelerated batteries include charge recombination, conduction of light-induced charges, and ion movement during insertion and extraction, all while maintaining optimal diffusion pathways. Therefore, fine-tuning these aspects in photocathodes is essential to enhance the performance of photo-accelerated batteries. This chapter introduces a novel approach using hydrogenated V₂O₅ as photocathodes for photo-accelerated lithium-ion batteries for the first time.

3.2 Experimental Section

3.2.1 Chemicals

All chemicals in the study were of analytical grade and used directly without any further purification. V₂O₅ powder, hydrogen peroxide (H₂O₂) solution 30% (w/w), ethanol, lithium bis(trifluoromethanesulfonyl)imide (LiTFSI), propylene carbonate (PC) and ethylene carbonate (EC) were purchased from Sigma-Aldrich, N-Methyl-2-pyrrolidone (NMP) was purchased from VWR international. Poly(vinylidene fluoride) (PVDF, Solef 6020) was from Solvay, CF (Sigracet GDL 39 AA carbon graphite paper) was purchased from sgl carbon, reduced graphene oxide (rGO) and poly(3-hexylthiophene) (P3HT) were Ossila, de-ionized (DI) water was from the lab. Coin-cell components were bought from kejing star company.

3.2.2 Synthesis of V₂O₅ and H:V₂O₅.

Initially, 0.728 g of V₂O₅ powder was combined with 60 ml of deionized water and stirred at room temperature for one hour. Next, a 30% hydrogen peroxide solution was added slowly while stirring continued for another hour. The resulting solution was then transferred to an autoclave and heated to 205 °C, where it was maintained for three days. Following this process, the product was purified through centrifugation with deionized water and ethanol, then annealed in air at 400 °C for two hours. To synthesize the H:V₂O₅ sample, the annealed V₂O₅ nanofibers were placed in a tube furnace and exposed to a controlled atmosphere of hydrogen gas (flow rate: 200 sccm) and helium gas (flow rate: 100 sccm) at 200 °C for two hours.

3.2.3 Preparation of Photocathodes

To prepare the photocathodes, 91 mg of active material (either V_2O_5 or hydrogenated V_2O_5 nanofibers), along with 2 mg of rGO and 2 mg of P3HT, were dispersed in 4 mL of NMP using sonication and mixing. Then, 5 mg of PVDF binder was added to the mixture. This electrode solution was then drop-cast onto carbon graphite paper and dried under vacuum at 120 °C to form the photocathodes.

3.2.4 Electrode and Device Assembly

The optical cells were designed by creating an opening of approximately 7 mm in diameter on a CR2032 coin-cell casing, which was then sealed with a glass window to allow light to pass through. The photocathode was placed inside, secured with Aluminum strips to improve electrical contact. As illustrated in Figure 3.1, the assembly of the optical coin-cell began with placing a Whatman[®] glass microfiber filter paper as a separator, followed by adding about 80 μ L of a 1.5M LiTFSI solution in an EC/PC (1:1) electrolyte, and finally positioning the lithium counter electrode.

3.2.5 Material Characterisations

The samples underwent characterization using a variety of analytical techniques. SEM was conducted with Zeiss EVO LS15, while XRD analysis utilized a Bruker D8 Advance with Cu Kα radiation. Raman spectroscopy was performed on Renishaw InViaTM, and UV/VIS/NIR spectroscopy were obtained using Lamda 750S. TEM, EDS, and SAED were using a JEOL JEM-2100 TEM operated at 200 kV. For XPS analysis, ThermoFisher Scientific XPS instrument was employed, and all data were collected using monochromatic Al Kα X-rays (1486.6 eV) with a pass energy of 50 and 200 eV for narrow and wide spectra, respectively.

3.2.6 Electrochemical Characterisations

CV and GDC tests were performed using the VMP3 Biologic electrochemical workstation. Cycling test was evaluated on a Neware system, and EIS measurements were conducted with an Autolab device. CV testing was done at scan rates from 0.1 to 1.0 mV s⁻¹, within a potential range of 2 to 4 V, under both dark and illuminated conditions (light source wavelength ~ 455

nm, intensity ~ 12 mW cm⁻²). GDC testing involved varying specific currents from 100 to 2000 mA g⁻¹, maintaining the same potential range and conditions. EIS measurements were conducted across a frequency range of 10 mHz to 100 kHz with a voltage amplitude of 10 mV, under both dark and illuminated conditions, using an electrolyte of 5M LiTFSI in EC/PC (1:1). The open-circuit potential (OCP) of V_2O_5 and $H:V_2O_5$ optical cells was recorded under light exposure, followed by discharging the cells with a specific current in darkness.

For electrical photo-response analysis, interdigitated electrodes (IDEs) of Au/Cr (40/10 nm) were fabricated on a Si_3N_4/Si substrate through UV lithography, as shown in Figure 3.1 (a). An equal amount of V_2O_5 and $H:V_2O_5$ was applied to the IDEs and dried in a vacuum at 120 °C. The photo-response was assessed by measuring current-voltage (I-V) characteristics, sweeping from -1.0 V to +1.0 V, under both dark and illuminated conditions. Additionally, current-time measurements were recorded under alternating dark and illuminated states at an applied voltage of 1.0 V.

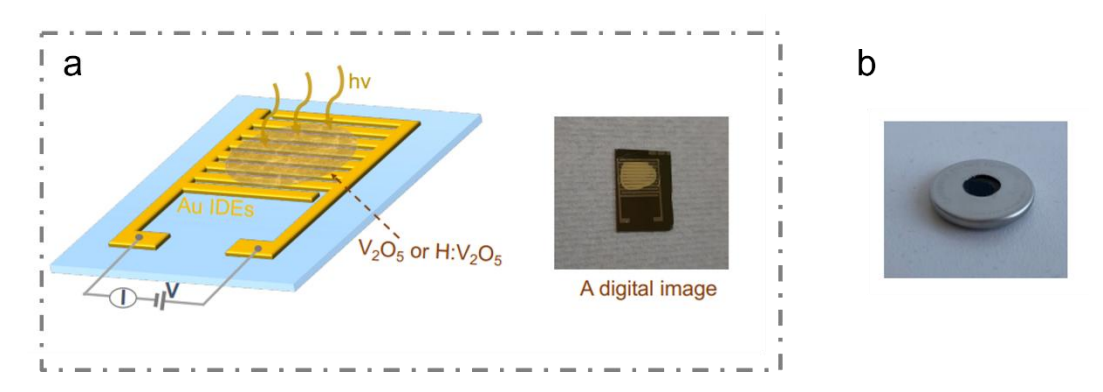


Figure 3.1: (a) Schematic representation of a photodetector based on Au-V₂O₅ or H:V₂O₅-Au interdigitated electrodes shown on the left, alongside a digital image on the right. (b) Digital photograph of an optical cell. Reproduced with permission. ¹⁹ Copyright 2023, Wiley-VCH.

3.2.7 Theoretical Methods

DFT calculations were used to highlight Li⁺ diffusion pathway for hydrogenated V₂O₅. This simulation was assisted by Prof. Alex M. Ganose and his student Ruiqi Wu from Imperial College. All calculations were conducted using plane-wave density functional theory (DFT) as implemented in the Vienna ab initio simulation Package (VASP). ³¹⁷⁻³²⁰ The interactions between core and valence electrons were described using the projector-augmented wave (PAW) method, and the PBEsol functional, an adaptation of PBE optimized for solids, was applied for

all computations. 321 A Hubbard U correction of 3.25 eV was used for the vanadium d-states. To achieve convergence within 0.01 meV/atom for the 14-atom primitive cell of V_2O_5 , a plane-wave energy cutoff of 700 eV and a $4\times3\times2$ Γ -centred k-point mesh were selected. Structural relaxation was performed with a force convergence criterion of 0.01 eV Å-1. The relaxed structures were found to agree well with experimentally determined lattice parameters, with discrepancies of less than 1.2%. The migration barriers for Li⁺ were computed using the climbing-image nudged elastic band method in the VTST code. 322 A $3\times3\times1$ supercell (10.78 Å \times 12.80 Å \times 11.57 Å) was employed for defect formation energy and nudged elastic band calculations, ensuring that periodic images of diffusing Li species or vacancy sites were separated by more than 10 Å in all directions. A k-point mesh of $2\times1\times2$ was used for these supercell calculations. Additionally, the ShakeNBreak package was utilized to identify ground-state configurations for oxygen vacancies and lithium interstitials. 323

3.3 Results and Discussion

3.3.1 Cathode Characterizations

The V₂O₅ nanofibers, produced via a hydrothermal synthesis method, exhibited diameters between 20 and 150 nm, as shown in Figure 3.2 (a). In-depth structural analysis through TEM and HRTEM, seen in Figure 3.2 (b-c), offered further insights into the nanofiber structure. The observed d-spacing of 0.218 nm matched the (002) planes, as illustrated in Figure 3.2 (d). The hydrogenated V₂O₅ (H:V₂O₅) samples maintained their nanofiber morphology, as evidenced by SEM and TEM images in Figure 3.2 (e-f). HRTEM analysis (Figure 3.2 (g-h)) displayed a d-spacing of 0.289 nm, corresponding to the (301) planes. SAED patterns for both V₂O₅ and H:V₂O₅, shown in Figure 3.3, confirmed that the orthorhombic crystal structure of V₂O₅ was preserved in both untreated and hydrogenated samples. X-ray diffraction patterns in Figure 3.4 (a) further verified the structural integrity, indicating a space group of Pmmn (59) and aligning with PDF card no. 03-065-0131. It is noteworthy that raising the hydrogenation temperature of V₂O₅ to 300 °C has been reported to result in the formation of a monoclinic VO₂ phase. ³²⁴ Therefore, a hydrogenation temperature of 200 °C was selected to maintain the original morphology and crystallinity of V₂O₅. Raman spectra (Figure 3.4 (b)) for both untreated and hydrogenated samples showed consistent shifts near 994, 484, and 405 cm⁻¹, associated with the vanadyl bond (V=O) stretching, symmetric stretching of V-O₍₃₎-V, and angle-bending

vibration of V-O₍₃₎-V, respectively. Additional peaks at approximately 701, 526, 304, and 284 cm⁻¹ were linked to the V-O-V bond stretching, V_3O phonon band, V-O_C bending vibration, and O_C -V-O_B bond-bending vibration, respectively. A Raman shift around 197 cm⁻¹ corresponds to the bending vibration of the O_C -V-O_B (A_g mode) bond. ³²⁵

The normalized V 2p spectra (Figure 3.4 (c)) displayed characteristic peaks corresponding to V $2p_{1/2}$ (~524.6 eV) and V $2p_{3/2}$ (~517.2 eV). XPS analysis of O 1s (Figure 3.4 (d)) highlighted a main peak at around 529.8 eV, attributed to lattice oxygen (V-O). In the hydrogenated sample, an additional broad peak at ~532 eV indicated the presence of both oxygen vacancies and oxygen-containing hydroxyl groups (-OH) introduced during hydrogenation, consistent with previous research. $^{281, 326-328}$ Elemental analysis via EDS mapping (Figure 3.3) confirmed a reduction in oxygen content following hydrogenation, with the atomic percentage ratio shifting from 67:33 (O:V) in untreated V₂O₅ to 64.9:35.1 (O:V) in hydrogenated V₂O₅.

Additionally, the UV–Vis absorption spectrum of the hydrogenated V₂O₅ (H:V₂O₅) sample (Figure 3.4 (e)) exhibited a broader absorption range than pristine V₂O₅, likely due to the formation of defect states. The inset in Figure 3.4 (e) displays the photoluminescence (PL) spectra, where an increase in the intensity of the broad peak is observed. This increase corresponds to mid-gap states between the valence and conduction bands of V₂O₅, which are attributed to the defect states introduced during the hydrogenation process. ^{329, 330}

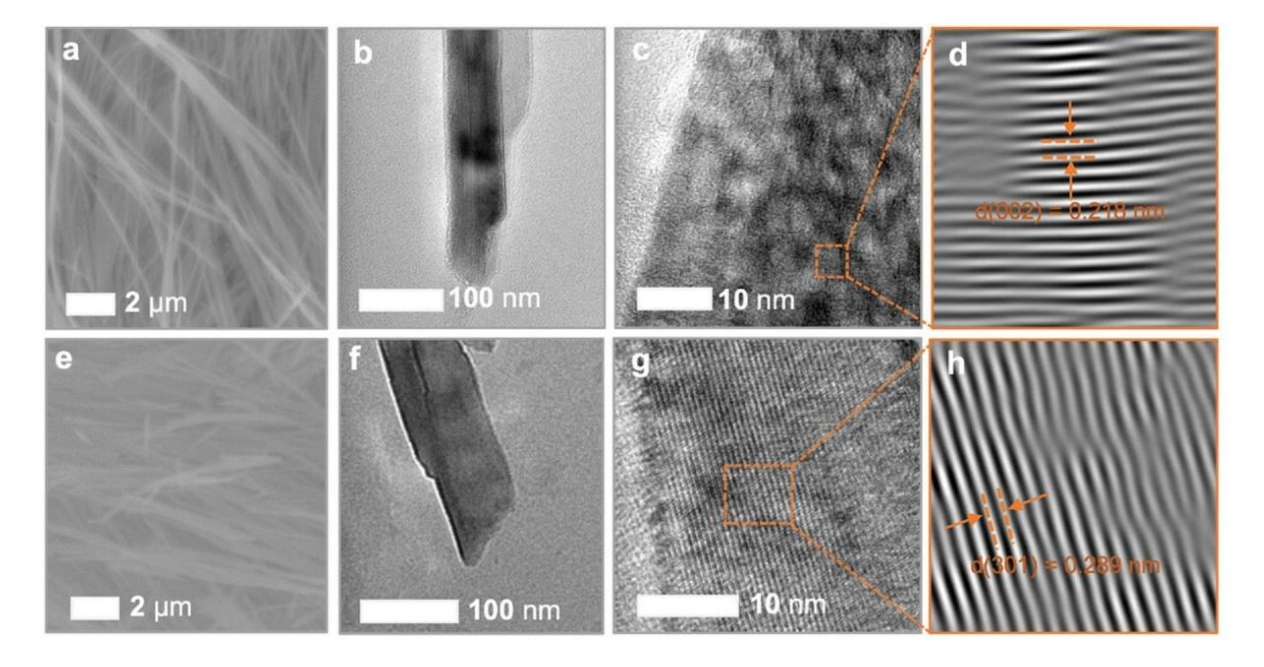


Figure 3.2: SEM, TEM, and HRTEM images of (a–d) V₂O₅ and (e–h) H:V₂O₅. Reproduced with permission. ¹⁹ Copyright 2023, Wiley-VCH.

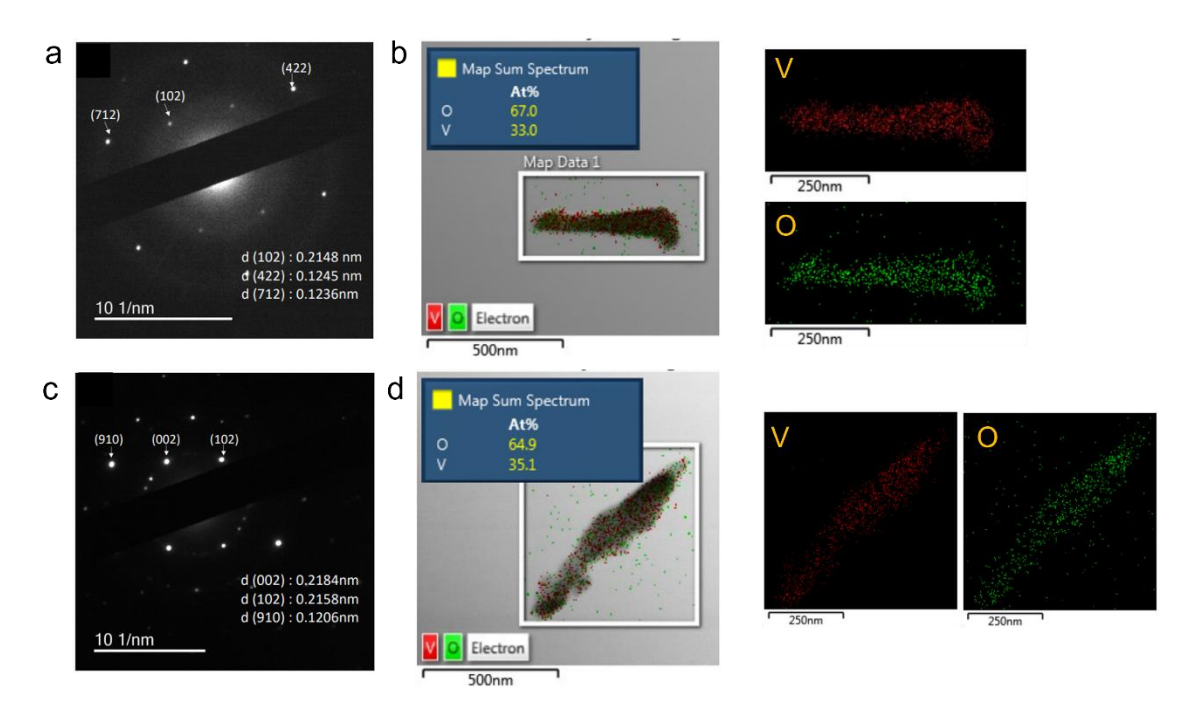


Figure 3.3: SAED patterns of (a) V₂O₅ and (c) H:V₂O₅. EDS mappings of (b) V₂O₅ and (d) H:V₂O₅. Reproduced with permission. ¹⁹ Copyright 2023, Wiley-VCH.

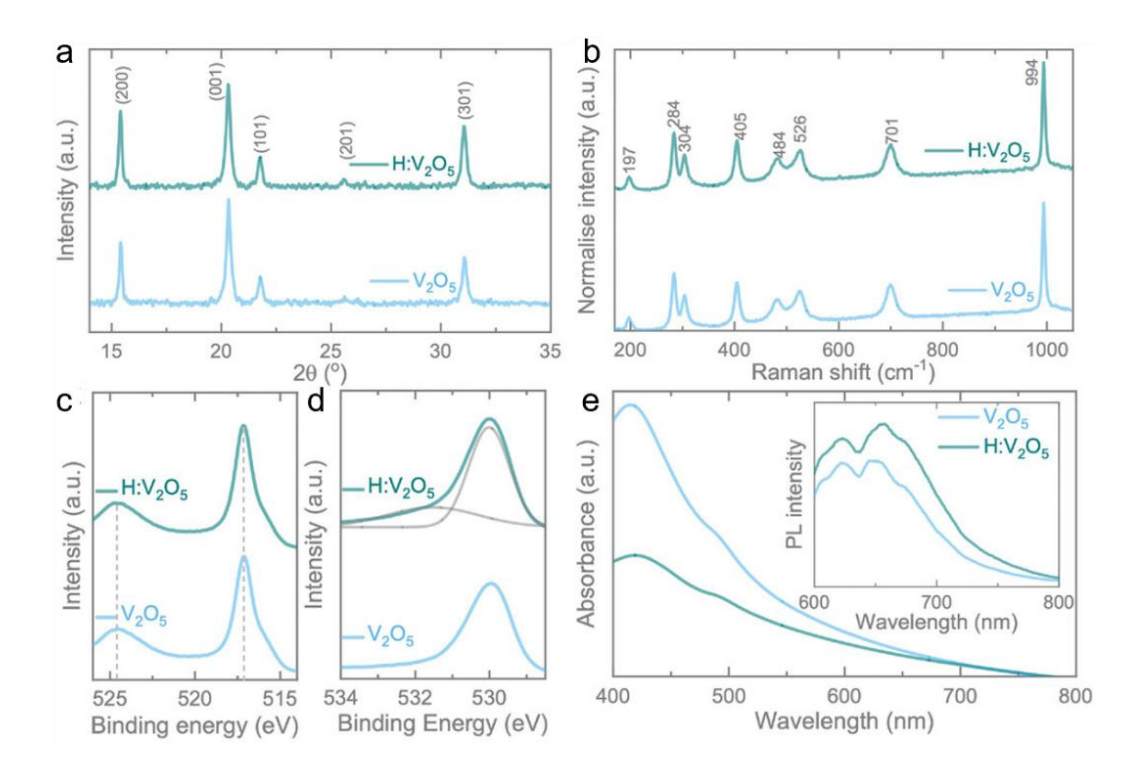


Figure 3.4: (a) XRD patterns and (b) Raman spectra of V_2O_5 and $H:V_2O_5$, confirming the orthorhombic crystal structure of V_2O_5 . (c) High-resolution XPS spectra of the V 2p region and (d) O 1s region for both V_2O_5 and $H:V_2O_5$. (e) UV-Vis absorption spectra of V_2O_5 and V_2O_5 with the inset in (e) displaying the PL spectra of the samples. Reproduced with permission. ¹⁹ Copyright 2023, Wiley-VCH.

3.3.2 Electrochemical Performances

The current–voltage characteristics of the photodetectors in both dark and illuminated conditions are presented in Figure 3.5 (a-b). The data reveal an increase in current under light exposure for both V_2O_5 and $H:V_2O_5$, verifying their photosensitive behaviour. The hydrogenated samples exhibited higher currents in both dark and illuminated states, indicating that the hydrogenation process enhanced both electrical conductivity and light responsiveness. The introduction of oxygen vacancies and hydroxyl groups during hydrogenation created defect states within the mid-gap region of the band gap, allowing some electrons to migrate to the conduction band, thereby increasing free charges and improving conductivity. $^{329,\,330}$ This observation is later confirmed through DFT calculations, with detailed information provided in section 3.3.3. Additionally, response current measurements (calculated as the difference between photo-current and dark current) were recorded over time under alternating dark and illuminated states at a bias voltage of 1 V. These results confirmed the enhanced photoresponses of the hydrogenated samples in comparison to pristine V_2O_5 , as shown in Figure 3.5 (c).

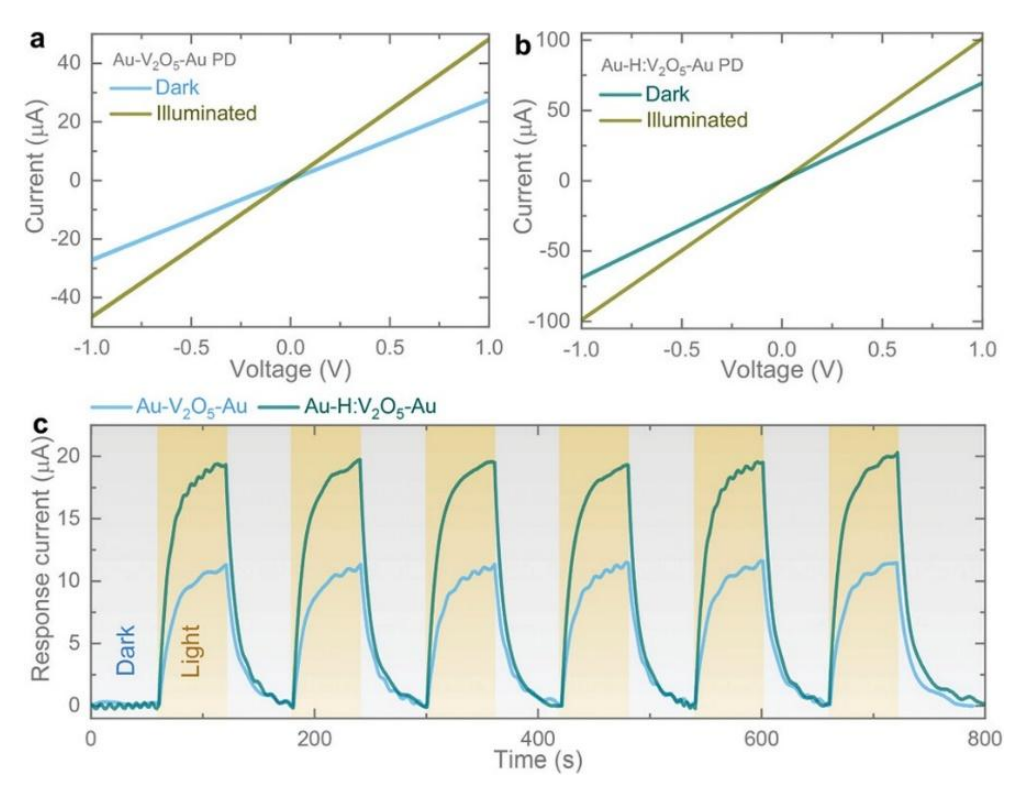


Figure 3.5: (a) Current–voltage characteristics of the V₂O₅ and (b) H:V₂O₅ photodetectors under dark and illuminated conditions. (c) Response current over time for the photodetectors during alternating dark and light cycles at a bias voltage of 1 V. Reproduced with permission.

19 Copyright 2023, Wiley-VCH.

The lithium-ion storage capabilities of the samples were evaluated using a CR2032 coin-cell optical configuration. CV for both pristine and hydrogenated samples were measured at different scan rates, ranging from 0.1 to 1.0 mV s⁻¹, within a potential range of 2.0 to 4.0 V (shown in Figure 3.6 (a-b)). The intercalation of Li⁺ ions into V₂O₅ involved multiple phase transitions, depending on the number of Li⁺ intercalation (x), resulting in distinct redox pairs. The redox processes are represented by cathodic peaks at approximately 3.33, 3.12, and 2.28 V, corresponding to transitions in V₂O₅ from the α -phase (x < 0.01) to the ϵ -phase (0.35 < x < 0.7), δ -phase (0.7 < x <1), and γ -phase (1 < x < 2), respectively. Similarly, anodic peaks were observed at around 2.58, 3.36, and 3.51 V. ³³¹ Notably, the hydrogenated samples exhibited higher peak currents for both cathodic and anodic reactions compared to pristine V₂O₅, suggesting enhanced lithium-ion storage capacity due to the hydrogenation treatment.

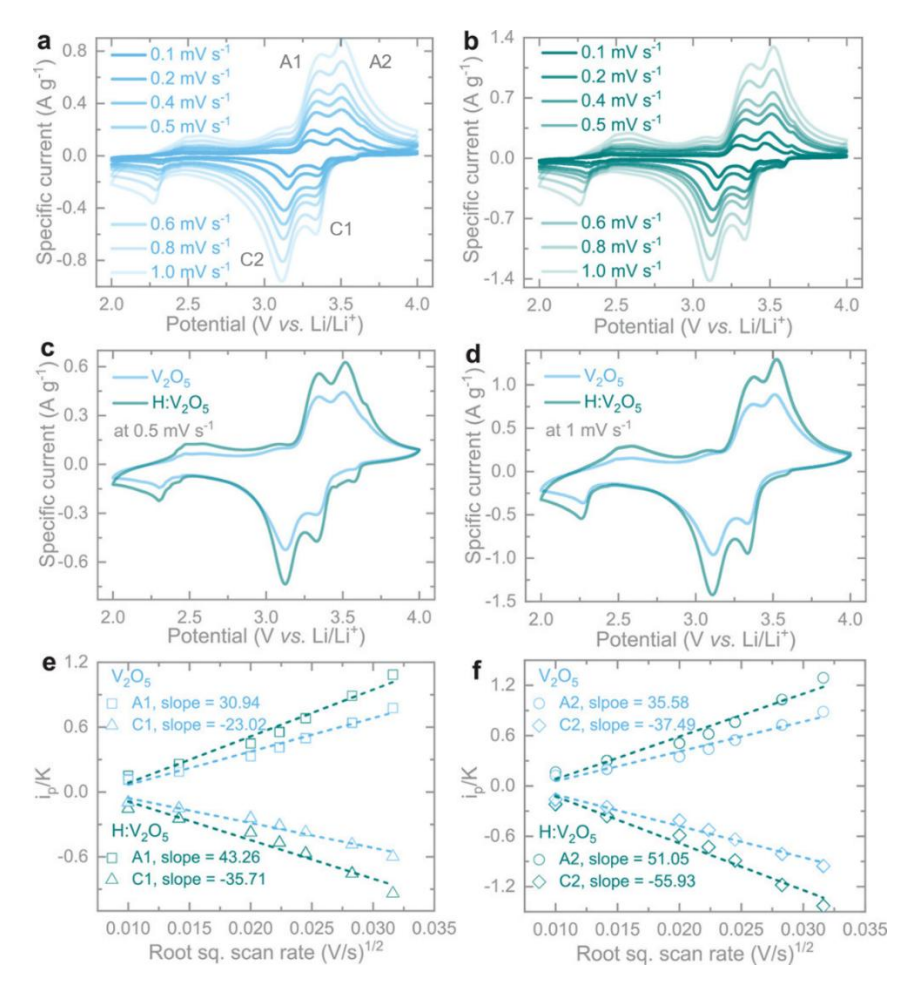


Figure 3.6: (a) CV curves of V₂O₅ and (b) H:V₂O₅ at various scan rates $(0.1 - 1.0 \text{ mV s}^{-1})$ in dark conditions. Comparative CVs of V₂O₅ and H:V₂O₅ at scan rates of (c) 0.5 mV s⁻¹ and (d) 1.0 mV s⁻¹ under dark conditions. (e, f) i_p/K versus $v^{1/2}$ plots for C1 (\approx 3.33 V)/A1 (\approx 3.36 V) and C2 (\approx 3.12 V)/A2 (\approx 3.51 V) peaks. Reproduced with permission. ¹⁹ Copyright 2023, Wiley-VCH.

Figure 3.6 (c-d) display the CV differences at scan rates of 0.5 and 1.0 mV s⁻¹, revealing a substantial increase in CV area of approximately 34% at 0.5 mV s⁻¹ and about 36.7% at 1.0 mV s⁻¹ as a result of hydrogenation. Additionally, Figure 3.7 (a-c) present comparative CVs at scan rates of 0.2, 0.6, and 0.8 mV s⁻¹, showing significant improvements in the redox peaks following hydrogenation.

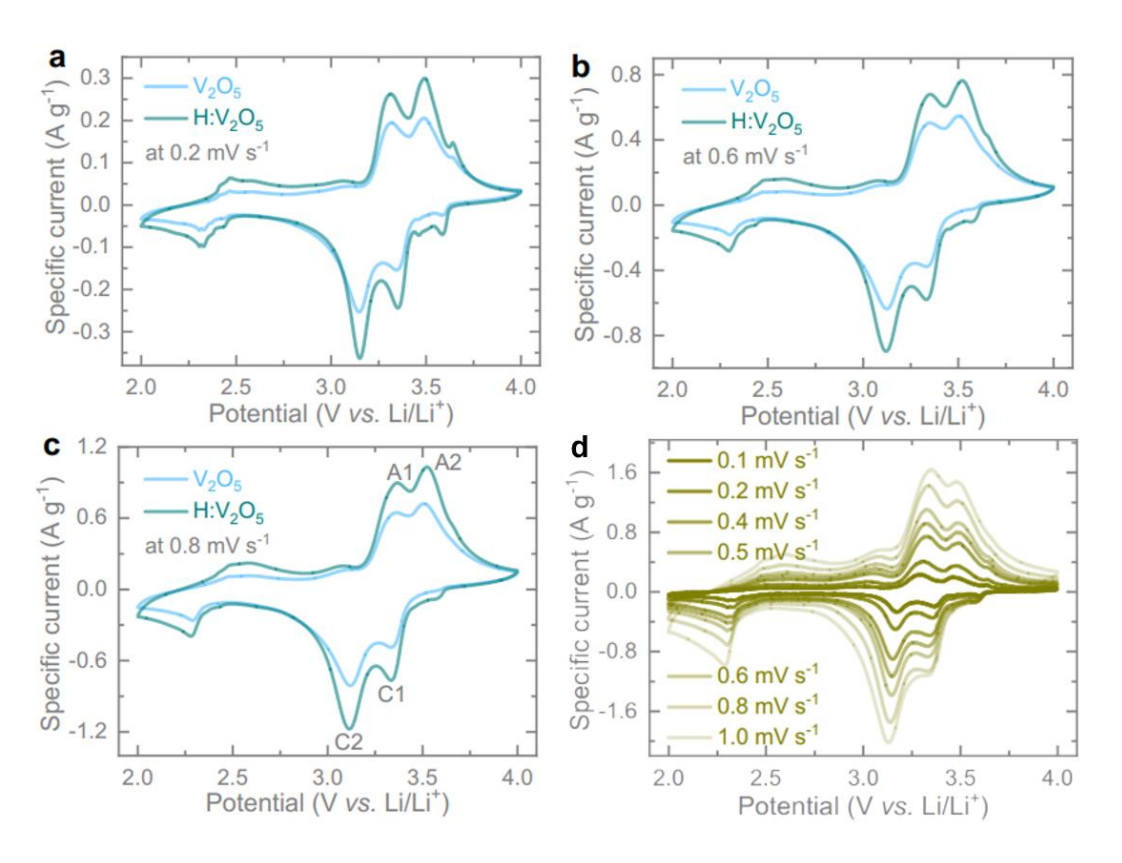


Figure 3.7: CV curves of V_2O_5 and $H:V_2O_5$ at scan rates of (a) 0.2 mV s⁻¹, (b) 0.6 mV s⁻¹, and (c) 0.8 mV s⁻¹ under dark and illuminated conditions, respectively. (d) CV curves of $H:V_2O_5$ at varying scan rates under illumination. Reproduced with permission. ¹⁹ Copyright 2023, Wiley-VCH.

The peak current (i_p) observed in the CV curves can be correlated to the diffusion constant (D) of Li^+ ions using the equation:

$$i_p = 0.4463F(F/RT)^{1/2}ACD^{1/2}v^{1/2} = KD^{1/2}v^{1/2}.$$

In this equation, T represents the cell testing temperature, F is the Faraday constant, C denotes the initial Li⁺ molar concentration in the electrolyte, R is the gas constant, and A signifies the electrode area. ³³² By keeping the electrode area constant for both pristine and hydrogenated samples, the slope of i_p/K versus $v^{1/2}$ can be utilized to estimate the diffusion constant. Figure 3.6 (e-f) displayed the plots of i_p/K versus $v^{1/2}$ for the cathodic peaks C1 (\approx -3.33 V)/A1 (\approx 3.36

V) and C2 (\approx -3.12 V)/A2 (\approx 3.51 V), respectively. The calculated increases in the diffusion constant after hydrogenation amount to 55.12% for C1 and 49.19% for C2 for the cathodic peaks, while the anodic peaks A1 and A2 show enhancements of 39.82% and 43.48%, respectively.

To further investigate the effect of light on the materials, CV measurements were performed on both pristine and hydrogenated samples under illumination with a wavelength of approximately 455 nm and an intensity around 12 mW cm⁻². Figure 3.7 (d) displays the CVs of H:V₂O₅ at scan rates ranging from 0.1 to 1.0 mV s⁻¹ under illuminated conditions. Comparative CVs of H:V₂O₅ at scan rates of 0.5, 0.8, and 1.0 mV s⁻¹, shown in Figure 3.8 (a-c), reveal a noticeable enhancement in charge storage capacity under light exposure, with enclosed CV areas increasing by about 47.4% at 0.5 mV s⁻¹ and 46.7% at 1.0 mV s⁻¹ compared to measurements in the dark. This significant boost in Li⁺ ion storage performance under illumination is attributed to increased optical activity due to hydrogenation. Additionally, when comparing the CVs of H:V₂O₅ and V₂O₅ at a scan rate of 0.5 mV s⁻¹ (Figure 3.8 (d)), H:V₂O₅ showed approximately 61.3% larger CV areas under light conditions. Figure 3.8 (e) also illustrates the increases in diffusion constants, with enhancements of around 43.7% (C1), 50.9% (A1), 59.5% (C2), and 35.8% (A2) in hydrogenated samples compared to pristine ones under illumination. The slopes for the respective cathodic and anodic peaks are presented in

Table 3.1. These results confirm improved Li⁺ ion diffusion kinetics following hydrogenation, regardless of light exposure. Moreover, under illumination, H:V₂O₅ displayed a significant improvement in Li⁺ ion diffusion rates compared to dark conditions, with estimated enhancements of approximately 27.33% and 48.2% for cathodic peaks C1 and C2, and 55.2% and 15.8% for anodic peaks A1 and A2 (Figure 3.8 (f)).

Table 3.1: Slopes for cathodic (C1 and C2) and anodic (A1 and A2) peaks of V_2O_5 and $H:V_2O_5$ in illuminated conditions.

	Slope			
Materials	C1	C2	A1	A2
V ₂ O ₅	-31.64	-51.96	44.48	43.52

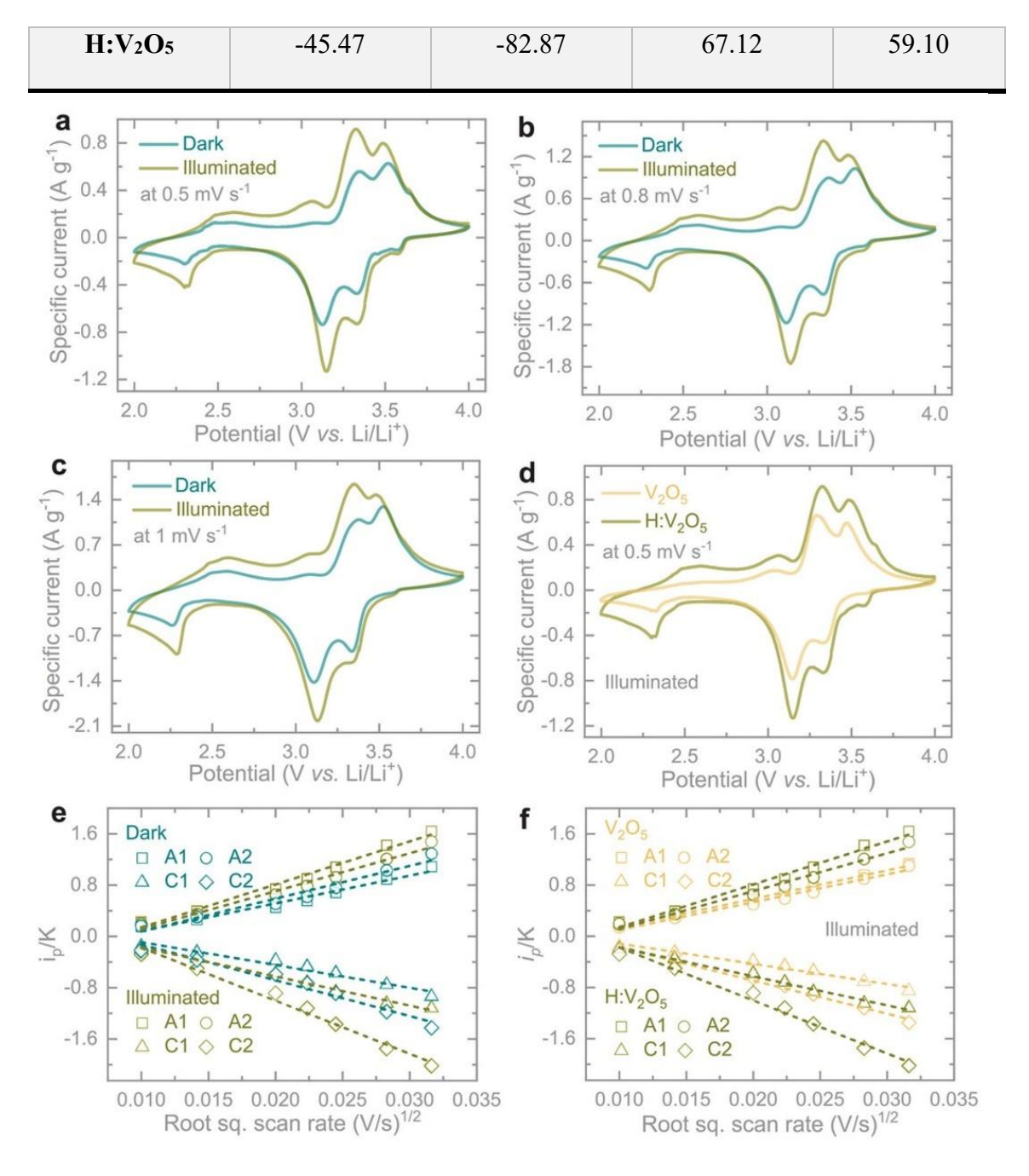


Figure 3.8: CV curves of H:V₂O₅ at scan rates of (a) 0.5, (b) 0.8, and (c) 1 mV s⁻¹ under dark and illuminated conditions. (d) Comparative CVs of V₂O₅ and H:V₂O₅ at a scan rate of 0.5 mV s⁻¹ under illumination. (e) Analysis of diffusion constants for H:V₂O₅ in dark and illuminated conditions. (f) Diffusion constant comparison of V₂O₅ and H:V₂O₅ under illuminated conditions. Reproduced with permission. ¹⁹ Copyright 2023, Wiley-VCH.

Additionally, GDC tests were conducted on both V₂O₅ and H:V₂O₅ samples at various specific currents, ranging from 200 to 2000 mA g⁻¹, within a potential range of 2–4 V (versus Li/Li⁺),

under both dark and illuminated conditions (light wavelength \sim 455 nm, intensity \sim 12 mW cm²). As expected and consistent with the CV results shown in Figure 3.6 and Figure 3.8, the hydrogenated samples demonstrated enhanced electrochemical performance over pristine V_2O_5 in both dark and illuminated environments. This improvement is evident in the comparative GDC curves (Figure 3.9 (a-b)), showing an increase in specific capacities. Specifically, the specific capacity increased from 114 to 151 mAh g⁻¹ (approximately a 32.45% improvement) at a specific current of 500 mA g⁻¹, and from 63 to 90 mAh g⁻¹ (around a 42.85% improvement) at a specific current of 2000 mA g⁻¹ in dark conditions. Furthermore, the comparative GDC curves of H:V₂O₅ under both dark and illuminated conditions (Figure 3.9 (c-f)) further verified the enhancement in charge storage capacity when exposed to light, which can be attributed to the contribution of photo-generated charges. The extracted dQ/dV curves (Figure 3.9 (g)), derived from the GDC tests, confirmed the improvements in Li⁺ ion storage for the H:V₂O₅ sample compared to V₂O₅ in dark conditions. Similarly, the dQ/dV plots for H:V₂O₅ (Figure 3.9 (h)) indicated the active participation of photo-generated charges in the charge storage process.

To further demonstrate the improved electrochemical performance, EIS testing was conducted. The Nyquist plots provided key insights into charge transfer resistance, showing that for $H:V_2O_5$, the resistance dropped from 16 to 14 Ω after hydrogenation under light exposure. Additionally, a decrease in equivalent series resistance is shown in Figure 3.10 (a). Figure 3.10 (b) illustrates a notable reduction in charge transfer resistance for $H:V_2O_5$, from 48 to 14 Ω , when comparing illuminated conditions to dark conditions. The equivalent circuit model for the Nyquist plots is presented in Figure 3.10 (c). These findings align with diffusion constant estimates from the CV curves, further confirming the enhanced electrochemical performance of $H:V_2O_5$ in both dark and illuminated settings.

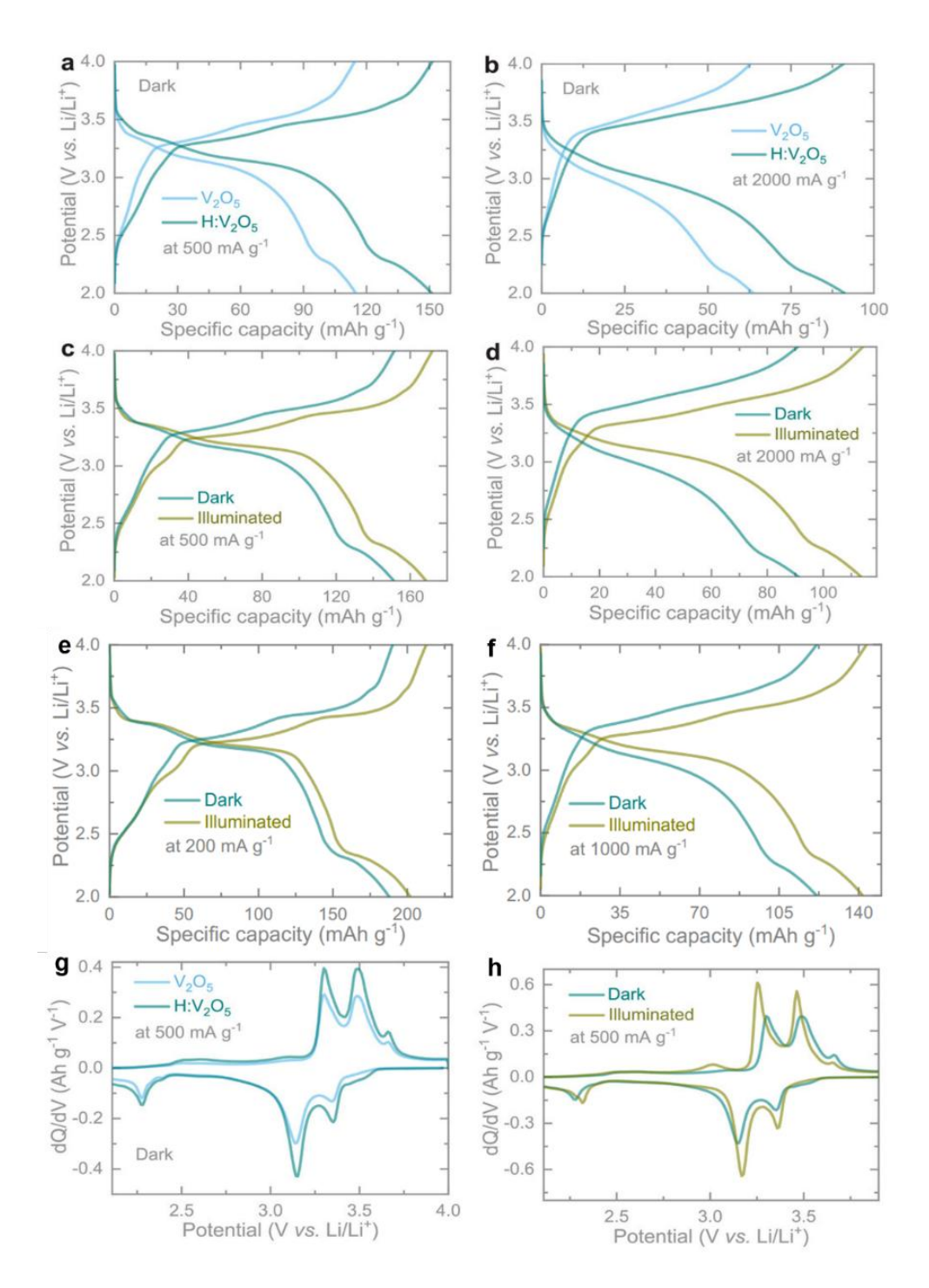


Figure 3.9: (a, b) GDC curves comparing V₂O₅ and H:V₂O₅ at specific currents of 500 and 2000 mA g⁻¹ under dark conditions. (c-f) GDC curves for H:V₂O₅ at specific currents of 500, 2000, 200, and 1000 mA g⁻¹, measured under both dark and illuminated conditions. (g) Differential capacity (dQ/dV) curves for V₂O₅ and H:V₂O₅ at 500 mA g⁻¹ in dark conditions. (h) dQ/dV curves of H:V₂O₅ at 500 mA g⁻¹, comparing results under dark and illuminated conditions. Reproduced with permission. ¹⁹ Copyright 2023, Wiley-VCH.

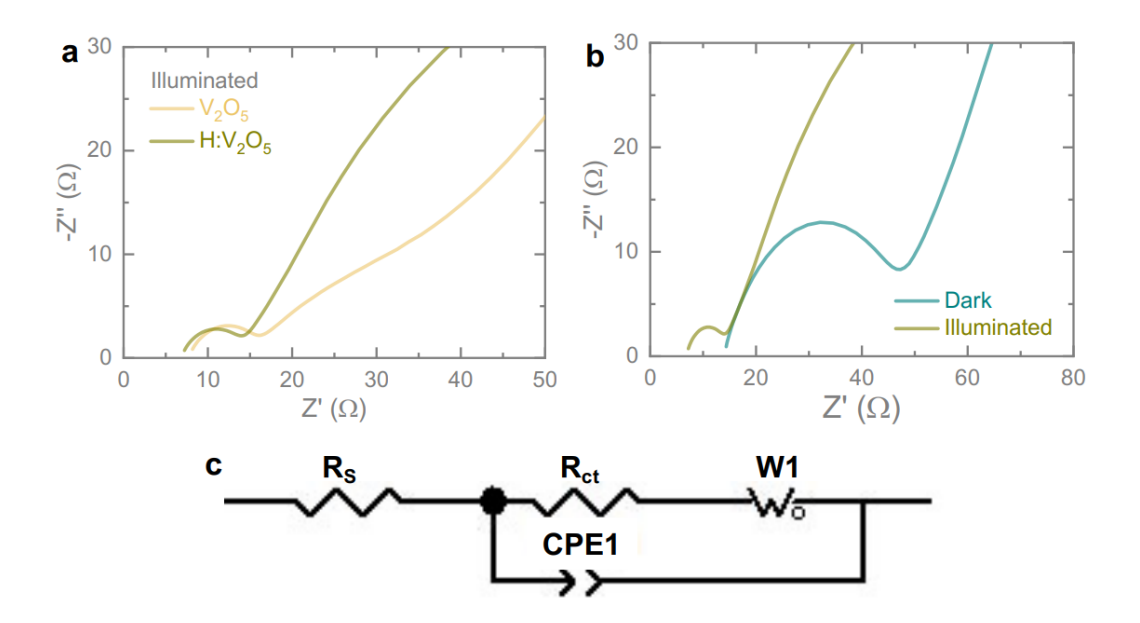


Figure 3.10: (a) Nyquist plots comparing V₂O₅ and H:V₂O₅ under light exposure. (b) Nyquist plots of H:V₂O₅ measured in both dark and illuminated conditions. (c) Equivalent circuit model associated with the Nyquist plots. Reproduced with permission. ¹⁹ Copyright 2023, Wiley-VCH.

In rate tests conducted in dark conditions (Figure 3.11 (a)), both V₂O₅ and H:V₂O₅ showed notable capacity gains after hydrogenation across all specific currents. Under illuminated conditions (Figure 3.11 (b)), H:V₂O₅ demonstrated even greater capacity enhancements compared to the dark at each specific current, attributed to the involvement of photo-generated charges in the charge storage process. Additionally, Figure 3.11 (c) presents extended cycling tests at a specific current of 500 mA g⁻¹ for H:V₂O₅ under both dark and illuminated conditions. After 50 cycles, H:V₂O₅ reached a capacity of 143 mAh g⁻¹ under illumination, compared to 122 mAh g⁻¹ in the dark, highlighting its excellent capacity retention and stability, with higher capacity maintained under light exposure.

The open-circuit potentials for both V₂O₅ and H:V₂O₅ optical cells were measured under illumination and during discharge in dark conditions (shown in Figure 3.12 (a)). This data supports the observed increase in discharge capacity after hydrogenation of V₂O₅. To assess the impact of the photothermal effect on charge storage performance, tests on H:V₂O₅ were conducted at temperatures ranging from 25 to 65 °C, with the corresponding CV areas at each temperature illustrated in Figure 3.12 (b). Notably, there was only an 11% capacity increase at 65 °C compared to 25 °C (as seen in Figure 3.12 (c)), which is minimal compared to the substantial 47% capacity enhancement observed under illumination versus dark conditions

(Figure 3.8 (c)). It is also worth mentioning that the LED light source used does not produce significant heat, even during extended illumination. Therefore, the observed capacity enhancement under illumination is largely due to the contribution of photo-generated charges rather than any photothermal effect.

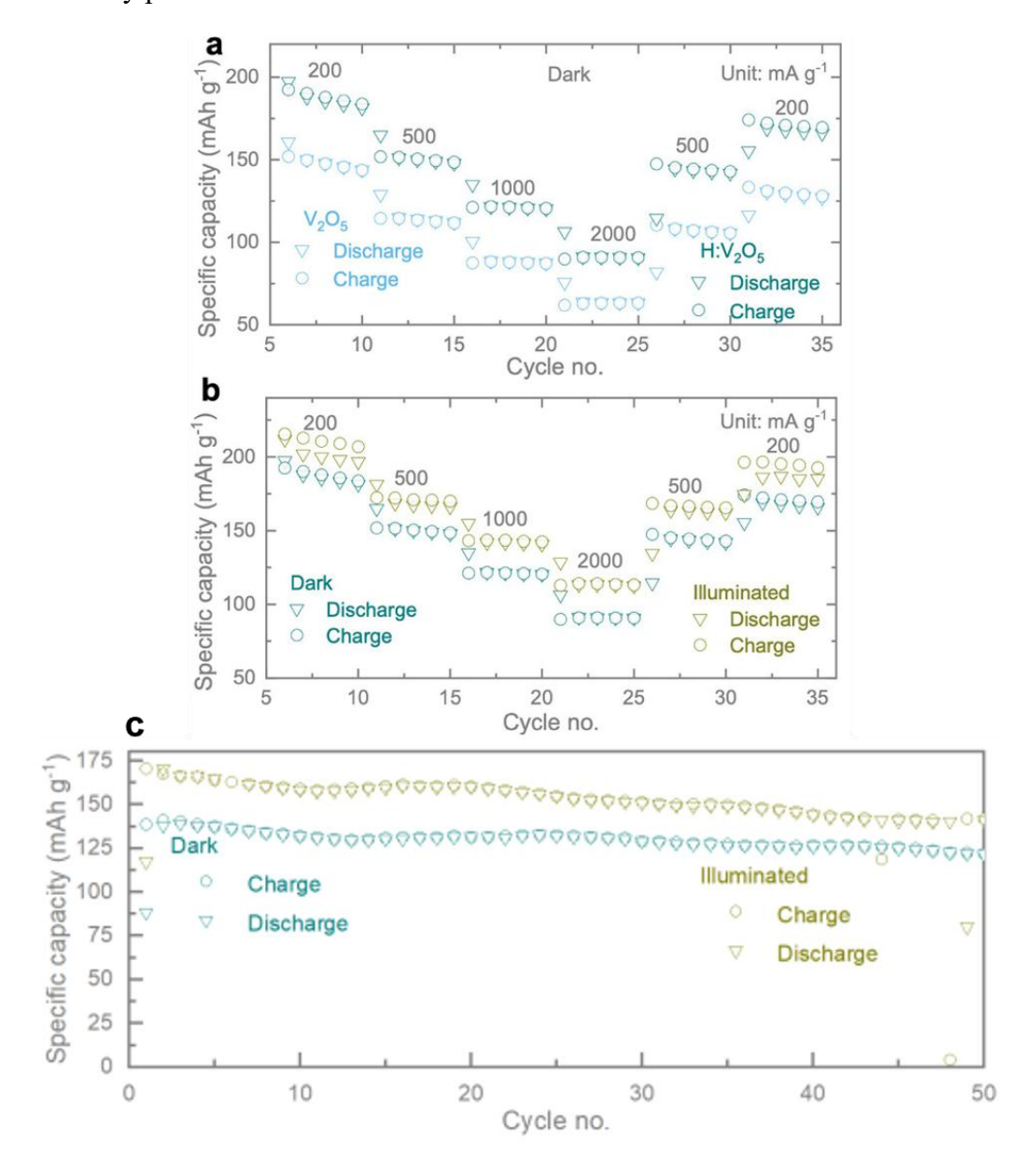


Figure 3.11: (a) Rate performance comparison of V₂O₅ and H:V₂O₅ under dark conditions, highlighting specific capacity enhancements achieved through hydrogenation. (b) Rate performance of H:V₂O₅ tested under both dark and illuminated conditions, illustrating increased specific capacities under illumination due to the contribution of photo-generated charges in the storage process. (c) Cycling stability of H:V₂O₅ at 500 mA g⁻¹ under dark and illuminated conditions, demonstrating the effect of illumination on sustained capacity improvement over time. Reproduced with permission. ¹⁹ Copyright 2023, Wiley-VCH.

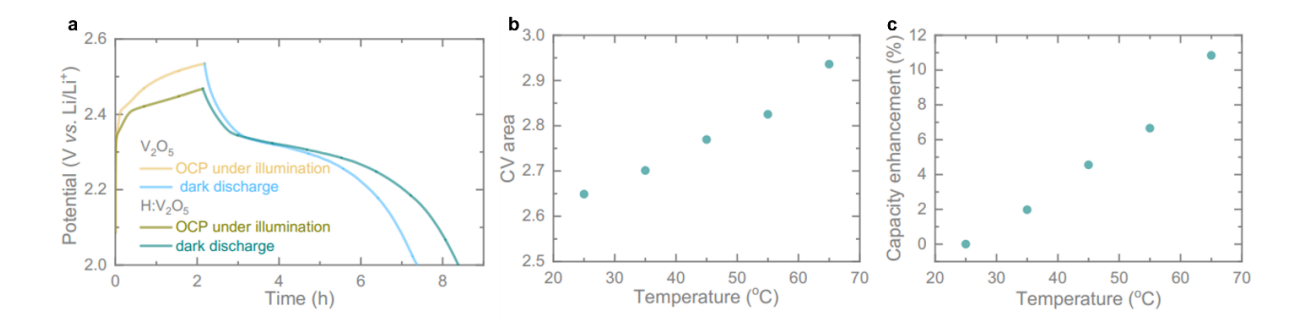


Figure 3.12: (a) Open-circuit potentials as a function of illumination duration for V_2O_5 and $H:V_2O_5$ optical cells, followed by discharge at 0.05 mA cm⁻² in dark conditions. (b) Analysis of absolute CV areas for an $H:V_2O_5$ cell across different temperatures. (c) Plot of capacity enhancement, with capacity values normalized to those measured at 25°C. Reproduced with permission. ¹⁹ Copyright 2023, Wiley-VCH.

3.3.3 DFT Simulations

To better understand the enhanced charge storage capabilities of hydrogenated V₂O₅ compared to its pristine form, DFT calculations were performed, focusing on Li⁺ migration. Figure 3.13 (a) provides a schematic of the V₂O₅ crystal structure, highlighting possible pathways for Li⁺ diffusion. Previous studies on pristine V₂O₅ have shown that lithium ions tend to diffuse along channels parallel to the layers (path A in Figure 3.13 (a)), which features a substantially lower energy barrier, nearly an order of magnitude smaller than other diffusion directions. ³³³ This establishes path A as the most favourable route for Li⁺ movement, contributing to the effective ion transport properties within the layered structure of V₂O₅. Consequently, the study concentrated on diffusion along this preferred direction.

The V₂O₅ structure includes three distinct oxygen sites—O(I), O(II), and O(III)—as shown in Figure 3.13 (a). During hydrogenation, it is expected that hydrogen atoms initially bond with oxygen sites, forming -OH groups, and that oxygen vacancies would also form, as removing -OH groups require less energy than removing oxygen atoms. DFT results suggest that neutral oxygen vacancies predominantly form at O(I) sites, which have the lowest defect formation energy of 0.85 eV under oxygen-poor conditions. In contrast, the formation energies for vacancies at O(II) and O(III) sites are 3.05 eV and 3.35 eV, respectively, indicating that their occurrence in significant quantities is unlikely (Figure 3.13 (b)).

For hydrogenated samples, the formation energies of -OH groups at O(I) and O(II) sites were similar, suggesting these groups would form in roughly equal amounts. The results show that

vacancies at O(I) sites slightly reduced the Li⁺ diffusion barrier by 2.5 meV, implying minimal impact on charge storage performance. However, hydrogenation at the OH(I) site significantly decreased the Li⁺ diffusion barrier by 250 meV, whereas OH(II) increased it by 63 meV (Figure 3.13 (c)). Given that both species would exist in equilibrium, the overall effect on Li⁺ migration is likely intermediate, leading to an overall reduction in the migration barrier. Thus, hydrogenated samples with oxygen vacancies and -OH sites are expected to exhibit efficient Li⁺ diffusion, contributing to increased capacity, enhanced rate capabilities, and improved optical and electrical conductivities. These findings indicate that the enhanced charge storage capacity is primarily influenced by the presence of -OH groups, which play a vital role in optimizing the charge storage process. This highlights the importance of defect engineering in enhancing the electrochemical performance of V₂O₅-based materials for energy storage applications.

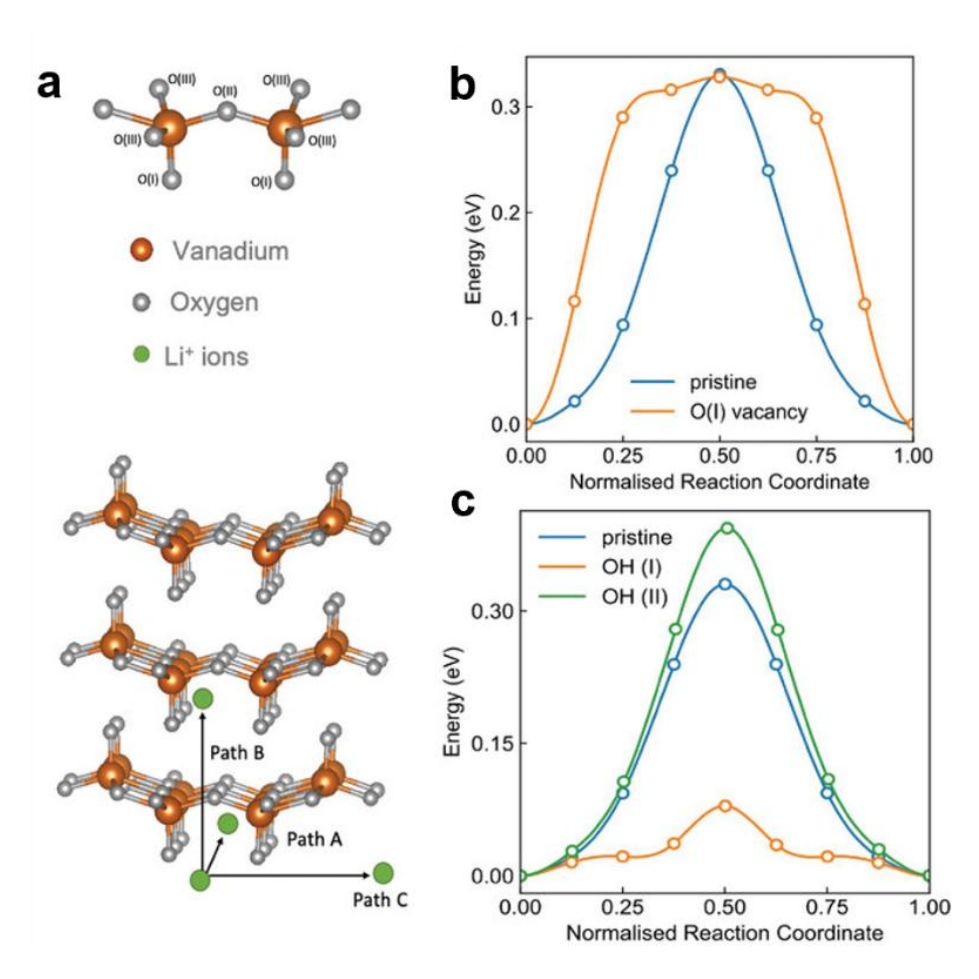


Figure 3.13: (a) Diagram of the V₂O₅ crystal structure, indicating potential pathways for Li⁺ diffusion. (b) Lithium diffusion barrier along path A in V₂O₅ with oxygen vacancies. (c) Lithium diffusion barrier along path A in V₂O₅ with hydrogenated oxygen sites. Reproduced with permission. ¹⁹ Copyright 2023, Wiley-VCH.

3.4 Summary

This chapter utilized a defect engineering strategy involving the hydrogenation of V_2O_5 (H:V₂O₅) nanofibers to improve the performance of photocathodes in photo-accelerated lithium-ion batteries. The electrodes are created by combining V_2O_5 nanofibers with rGO and P3HT, forming a heterojunction structure that promoted the separation and conduction of photo-generated charges. The hydrogenation process introduced oxygen defects and hydroxyl groups into the V_2O_5 structure, enhancing the material's conductivity, light-induced photo-response, and ion diffusion rates. These improvements collectively led to enhanced electrochemical energy storage capabilities. Notably, the H:V₂O₅ photocathodes demonstrated better performance than pristine V_2O_5 under both illuminated and dark conditions.

When exposed to light during the discharge process, photogenerated electrons migrate from V₂O₅ to the current collector via the charge transfer materials P3HT and rGO. This movement followed favourable energy pathways, allowing the electrons to combine with Li⁺ ions migrating from the oxidation reaction at the Li anode. Simultaneously, holes are blocked by P3HT, compensating with electrons from external circuits. Conversely, during the charging process under illumination, the photo-generated holes repel the Li⁺ ions within the V₂O₅ photocathodes, leading to their deintercalation. Concurrently, photogenerated electrons transited from the valence band to the conduction band of the photocathode. With the assistance of an external electrical bias, these photo-generated electrons flowed through the external circuit, promoting the reduction reaction at the Li anode. Together, these processes enhanced charge storage performance under illumination. The hydrogenated samples also exhibited an increased photocurrent generation, likely due to the creation of defect mid-gap states situated within the bandgap of V₂O₅. These states were associated with oxygen-related defects and hydroxyl groups, which led to enhanced optical absorption, thereby improving photoactivity. Consequently, these enhancements resulted in superior photo-enhanced capacities compared to pristine V₂O₅.

In summary, this research presented an innovative strategy that employed hydrogenated V_2O_5 as photocathodes in photo-accelerated LIBs. This study highlighted the effectiveness of defect engineering in optimizing photocathode properties for enhanced photo-accelerated performance, offering a promising direction for future photocathode design advancements. By introducing oxygen vacancies and hydroxyl groups via hydrogenation, the electrochemical and

optical properties of the material are significantly boosted. As a result, specific capacities were improved under both dark and illuminated conditions. Overall, it provided a straightforward and effective methodology for improving the performance of energy storage in photo-accelerated systems and laid the groundwork for future advancements in this field.

Chapter 4

Pre-doped Cations in V₂O₅ for High-performance Zn-ion Batteries

This chapter investigated four types of vanadium oxide materials: pristine vanadium oxide (V_2O_5) , sodium-doped vanadium oxide $(Na-V_2O_5)$, potassium-doped vanadium oxide $(K-V_2O_5)$, and ammonium-doped vanadium oxide $(NH_4-V_2O_5)$. Electrochemical tests revealed that $NH_4-V_2O_5$ exhibited superior performance compared to the other compositions. The introduction of V^{4+}/V^{5+} redox couples, particularly with an increase in V^{4+} presence, significantly boosted electrochemical performance. These findings offer valuable insights for the design and development of high-performance cathode materials for Zn-ion batteries in the future. This chapter is based on the published article. Yinan Lu et al., Nano Research Energy, 2024, DOI: 10.26599/NRE.2024.9120125.

4.1 Introduction

The rising demand for effective and eco-friendly energy storage is largely fuelled by the growing use of renewable sources and urgent concerns over climate change. While LIBs have been the primary technology in the market, their limitations, such as finite lithium resources, safety hazards, and restricted energy density have driven interest toward alternative battery solutions. 334-337 Among these, aqueous rechargeable ZIBs stand out due to their costeffectiveness, abundant resources, and environmental benefits. The use of aqueous electrolytes in ZIBs also provides a safety edge over the flammable organic electrolytes commonly used in LIBs. However, achieving high-performance cathode materials for ZIBs continues to pose a significant challenge. Extensive research has explored materials like manganese oxide, 338 Prussian blue analogs, ³³⁹ vanadium oxide compounds, ³⁴⁰ and organic substances ³⁴¹ for this purpose. Notably, vanadium oxide-based materials have garnered attention for their high theoretical capacity, multiple oxidation states, and layered structure favourable for zinc ion storage. Despite this promise, vanadium-based cathodes face issues such as slow ion diffusion and limited cycle stability. To address these challenges, techniques like cation doping and defect engineering have been applied to enhance performance. ^{30, 340} For example, Guo et al. created a K_{0.5}V₂O₅ layer with expanded interlayer spacing of 9.51 Å, achieving an increased capacity of around 90 mAh g⁻¹ at 10 mA g⁻¹. ³⁴² Xu et al. improved cycling stability by introducing Mg²⁺ doping into V₂O₅, expanding interlayer spacing to 10.76 Å and retaining 86.9% capacity after 500 cycles. ³⁴³ Similarly, Zheng et al. developed an Al³⁺ doped hydrated vanadate that delivered a high capacity of 380 mAh g⁻¹ at 50 mA g⁻¹, maintaining strong cycling performance over 3000 cycles. 344

The results indicate that cation doping not only contributes to the stabilization of the crystal structure during cycling but also plays a crucial role in increasing interlayer spacing, thereby boosting overall capacity. Nevertheless, the specific impacts of various cations in this area have not been thoroughly investigated. This research aimed to fill this gap by synthesizing and assessing four different materials: pristine vanadium oxide (V₂O₅), sodium-doped vanadium oxide (Na-V₂O₅), potassium-doped vanadium oxide (K-V₂O₅), and ammonium-doped vanadium oxide (NH₄-V₂O₅). The analysis of their electrochemical performance showed that NH₄-V₂O₅ exhibited superior performance compared to the other variants. Notably, the formation of V⁴⁺/V⁵⁺ redox couples, particularly the increase in V⁴⁺ levels, played a significant

role in enhancing electrochemical performance. These findings provide important insights for the design and development of advanced cathode materials in the future.

4.2 Experimental Section

4.2.1 Chemicals

All chemicals utilized in this study were of analytical grade and were used as received without any additional purification steps. Vanadium pentoxide, 30% hydrogen peroxide (H_2O_2) solution, ammonium metavanadate, potassium iodide (KI), polyethylene glycol (molecular weight 4000), sulfuric acid (95-97%), zinc triflate ($Zn(CF_3SO_3)_2$), ethanol, and poly(vinylidene fluoride) (PVDF) were sourced from Sigma-Aldrich. N-Methyl-2-pyrrolidone (NMP) was obtained from VWR International. Thermo Scientific supplied sodium hydroxide (NaOH) pellets with 98% purity. Potassium chloride (KCl) was acquired from EMSURE®, while reduced graphene oxide powder (rGO) and P3HT (Mw = 60,150, 97.6% regioregularity) were provided by Ossila.

4.2.2 Synthesis of V₂O₅, NH₄-V₂O₅, Na-V₂O₅ and K-V₂O₅.

Pristine V₂O₅ was prepared through a hydrothermal method. Initially, 1.0930 g of V₂O₅ powder was combined with 90 mL of deionized water and stirred at a speed of approximately 300 rpm for 30 minutes at ambient temperature. Subsequently, 15 mL of 30% H₂O₂ was added, and stirring was continued for another 30 minutes. The resulting clear orange solution was then transferred to a 150 mL autoclave, which was heated in an oven at 205 °C for three days. After cooling to room temperature, the products were thoroughly rinsed with deionized water and ethanol in an alternating manner, followed by drying in a vacuum oven at 70 °C overnight.

The NH₄-V₂O₅ material was synthesized using an established method. ³⁴⁵ In this process, 1.755 g of ammonium metavanadate was added to 90 mL of deionized water and stirred for 30 minutes. Then, 0.9 mL of sulfuric acid was introduced to the suspension, followed by another 30 minutes of stirring. The mixture was transferred into a 150 mL autoclave, which was heated in an oven at 100 °C for two days. Afterward, the products were cooled, thoroughly rinsed with deionized water and ethanol alternately, and dried in a vacuum oven at 70 °C overnight.

For the synthesis of Na-V₂O₅, a different method was followed. ³⁴⁶ Initially, 0.3636 g of pristine V₂O₅ was dissolved in a mixture of 60 mL of deionized water and 0.7 mL of NaOH solution (1 M). The solution underwent sonication at room temperature for one hour. Next, 0.2 g of polyethylene glycol (molecular weight 4000) was added, and the mixture was stirred for an additional 15 minutes. The solution was then moved to a 150 mL autoclave and heated in an oven at 180 °C for two days. After cooling, the products were alternately washed with deionized water and ethanol, followed by drying in a vacuum oven at 70 °C overnight.

The preparation of K-V₂O₅ was carried out using a previously established procedure. ³⁴² In this method, 0.5456 g of pristine V₂O₅, 0.747 g of KI, and 6.709 g of KCl were dissolved in 90 mL of deionized water, with magnetic stirring for 30 minutes. The resulting mixture was transferred to a 150 mL autoclave and heated in an oven at 200 °C for one day. Once cooled to room temperature, the products were washed alternately with deionized water and ethanol, followed by drying overnight in a vacuum oven at 70 °C.

4.2.3 Preparation of Cathodes and Coin-cells

For cathode preparation, 80 mg of active material (either V₂O₅, NH₄-V₂O₅, Na-V₂O₅, or K-V₂O₅), 10 mg of rGO, and 5 mg of P3HT were dispersed in 2 mL of NMP through sonication. Afterward, 5 mg of PVDF was incorporated into the mixture. This electrode solution was then drop-cast onto carbon graphite paper (Sigracet GDL 39 AA, SGL Carbon) serving as the current collector, followed by drying under vacuum at 70 °C to form the cathodes.

To assemble the CR 2032 coin-cells, a cathode disc was placed on the coin-cell case, followed by a layer of Whatman[®] glass microfiber filter paper used as the separator. Then, 150 μ L of 3M Zn(CF₃SO₃)₂ aqueous electrolyte was added, and a zinc counter electrode was positioned. The cell was sealed using a hydraulic crimping machine.

4.2.4 Electrochemical Characterisations

CV was performed using a Biologic VMP-3 galvanostat over a voltage range of 0.2~V to 1.6~V after allowing the cells to rest for 10 hours. The scans were conducted at different rates, from $0.2~to~1.0~mV~s^{-1}$. GDC measurements covered the same voltage range, using specific currents between $100~and~5000~mA~g^{-1}$. The electrode cycling stability was assessed with a Neware BTS4000 system at a constant current of $1000~mA~g^{-1}$ over 1000~cycles, within the same voltage

limits. EIS was conducted on an Autolab PGSTAT302N, with measurements spanning from 10 mHz to 100 kHz and using a 10 mV AC voltage.

4.2.5 Material Characterisations

The synthesized materials were analysed using multiple characterization techniques. SEM imaging was performed on a Zeiss EVO LS15, Oxford Instruments X-MaxN, and a Hitachi TMA4000Plus. TEM, along with EDS and SAED, was carried out on a JEOL JEM-2100 TEM operating at 200 kV. XRD patterns were acquired using a Panalytical Empyrean XRD system with Cu Kα radiation, set at 40 kV and 40 mA, with a 0.05° step size and a scan speed of 0.1° per second across a 2θ range of 5° to 70°. UV-Vis spectroscopy was conducted with a PerkinElmer Lambda 750S instrument. Raman analysis was done using a Renishaw inViaTM confocal Raman microscope with a 515 nm laser. XPS measurements were made using a ThermoFisher Scientific XPS instrument, utilizing monochromatic Al Kα radiation (1486.6 eV) with a pass energy of 50 eV for narrow scans and 200 eV for wide scans. No significant charging effects were noted, and spectra were referenced to adventitious carbon at 284.8 eV (C 1s). The XPS data were analysed with CasaXPS software and presented in counts per second. TGA was performed using a PerkinElmer TGA 4000 at a heating rate of 5 °C min⁻¹ under nitrogen flow at 20 mL min⁻¹, covering ambient temperature to 600 °C in alumina crucibles.

4.3 Results and Discussion

4.3.1 Cathode Characterizations

SEM analysis in Figure 4.1 (a) shows that the pristine V₂O₅ sample displays a nanofiber morphology, with diameters ranging from 20 to 100 nm. In contrast, the NH₄-V₂O₅ sample in Figure 4.1 (b) presents a nanoflake structure. Similarly, the Na-V₂O₅ and K-V₂O₅ samples, shown in Figure 4.1 (c-d), also exhibit nanofiber structures. The interplanar spacing for pristine V₂O₅ was measured at 2.0 Å, corresponding to the (202) plane, as confirmed by reference PDF 03-065-0131 (see Figure 4.2 (a) and (b)). This finding is further validated by SAED patterns in Figure 4.2 (c), where spots are associated with crystalline planes (201), (301), and (111) with d-spacings of 3.478, 2.925, and 2.673 Å, respectively. Additionally, a specific area in the high-resolution TEM image (Figure 4.2 (e)) shows a d-spacing of 7.2 Å, which corresponds to the

(020) plane according to XRD pattern PDF 01-078-2016. SAED analysis in Figure 4.2 (f) identified planes ($2\bar{1}1$), ($\bar{2}\bar{3}1$), ($\bar{2}\bar{2}3$), ($\bar{3}31$) and ($1\bar{5}2$), with respective d-spacings of 5.58, 3.70, 3.66, 3.20, and 2.66 Å. Figure 4.2 also shows the morphology of Na-V₂O₅ and K-V₂O₅. EDS mapping, as shown in Figure 4.3, confirmed that the cations were uniformly distributed throughout the materials. Additionally, XRD patterns in Figure 4.4 verified the crystal structures of V₂O₅ (orthorhombic, space group Pmmn (59)), NH₄-V₂O₅ (anorthic, space group P $\bar{1}$), Na-V₂O₅ (orthorhombic, space group Pnma (62)), and K-V₂O₅ (monoclinic, space group C12). The measurements align with data from SAED and HRTEM analyses. The lattice parameters were determined as follows: V₂O₅ (a = 11.5120 Å, b = 3.5640 Å, c = 4.3680 Å), NH₄-V₂O₅ (a = 13.1730 Å, b = 14.3310 Å, c = 16.0230 Å), K-V₂O₅ (a = 11.6570 Å, b = 3.6590 Å, c = 9.4600 Å), and Na-V₂O₅ (a = 9.3620 Å, b = 3.6080 Å, c = 22.0580 Å).

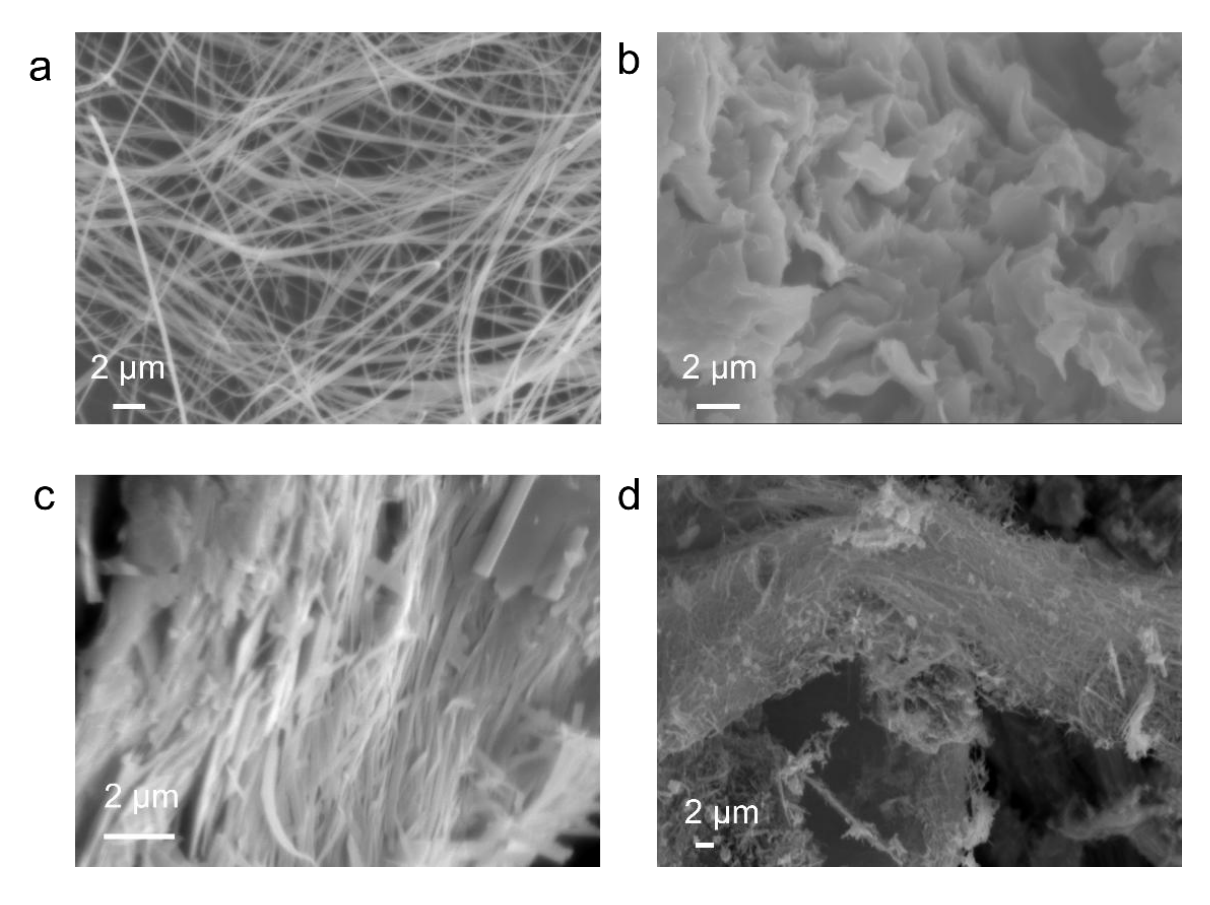


Figure 4.1: SEM images showing (a) V₂O₅, (b) NH₄-V₂O₅, (c) Na-V₂O₅ and (d) K-V₂O₅. Reproduced with permission. ³⁴⁷ Copyright 2024, Tsinghua University Press.

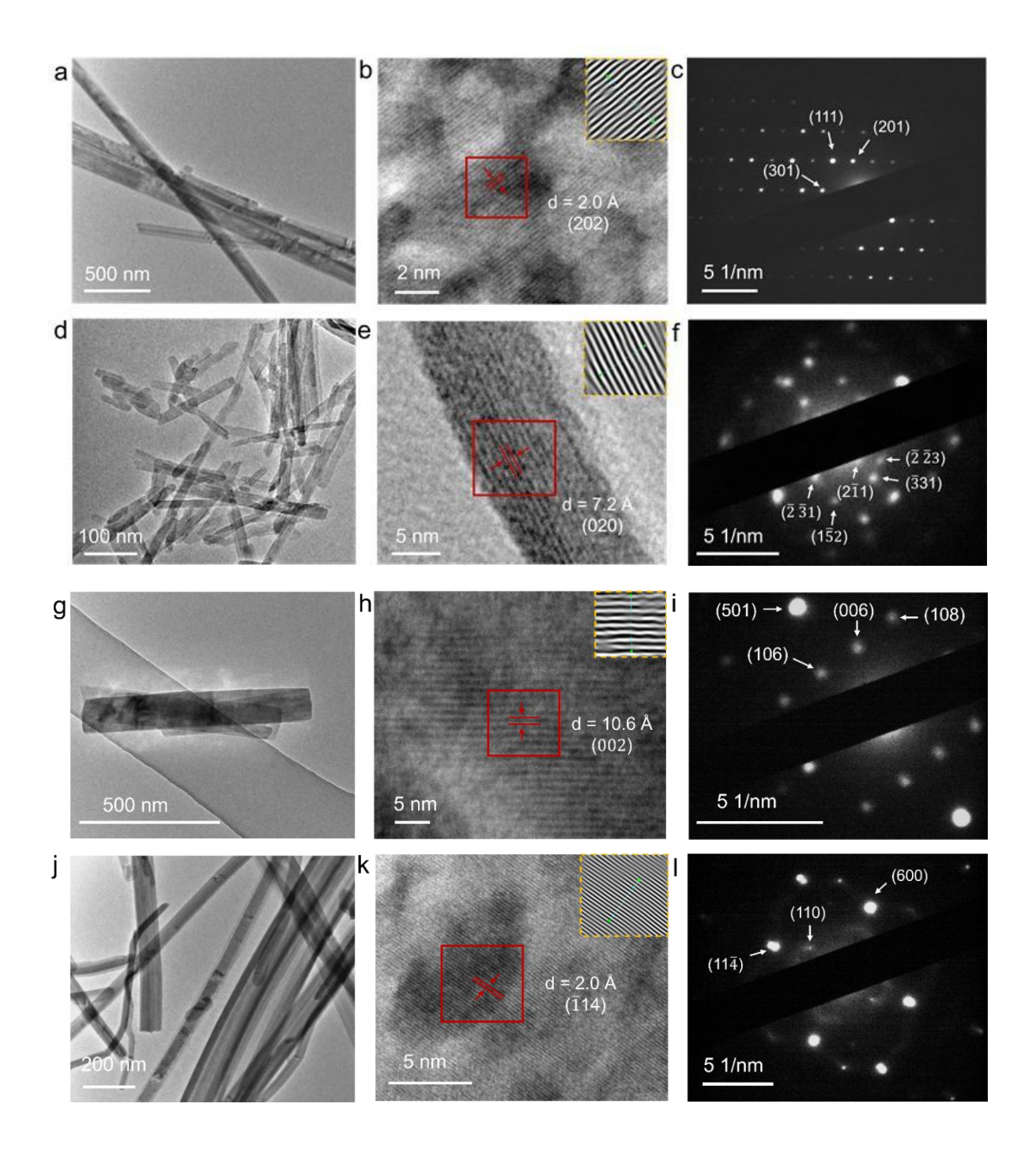


Figure 4.2: TEM and HRTEM images of (a, b) V_2O_5 , (d, e) NH_4 - V_2O_5 , (g, h) Na- V_2O_5 , (j, k) K- V_2O_5 , along with SAED patterns for (c) V_2O_5 , (f) NH_4 - V_2O_5 , (i) Na- V_2O_5 , and (l) K- V_2O_5 . Inset: iFFT patterns from selected areas in HRTEM images. Reproduced with permission. 347 Copyright 2024, Tsinghua University Press.

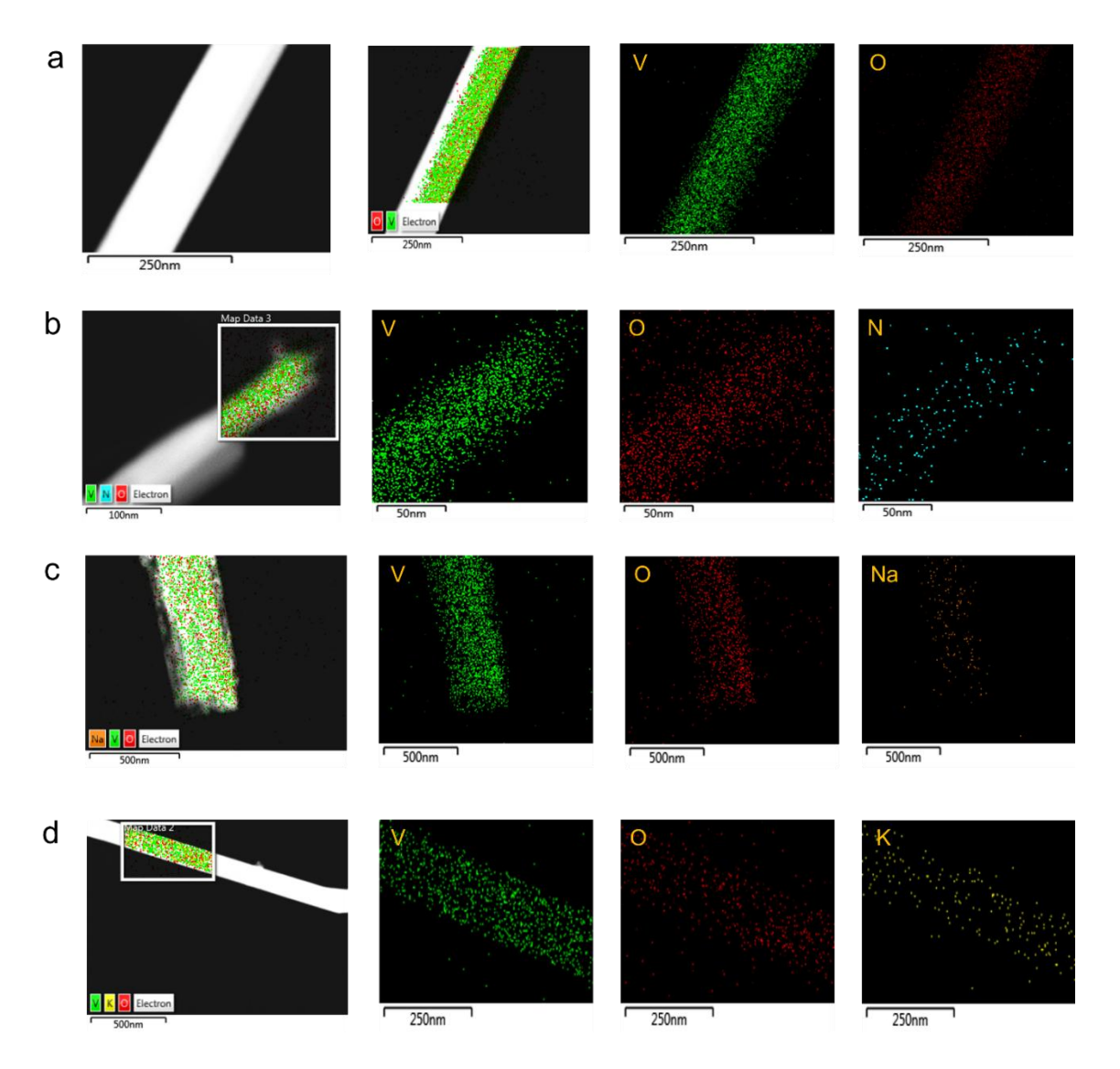


Figure 4.3: EDS elemental maps for (a) V_2O_5 , (b) NH_4 - V_2O_5 , (c) Na- V_2O_5 and (d) K- V_2O_5 . Reproduced with permission. 347 Copyright 2024, Tsinghua University Press.

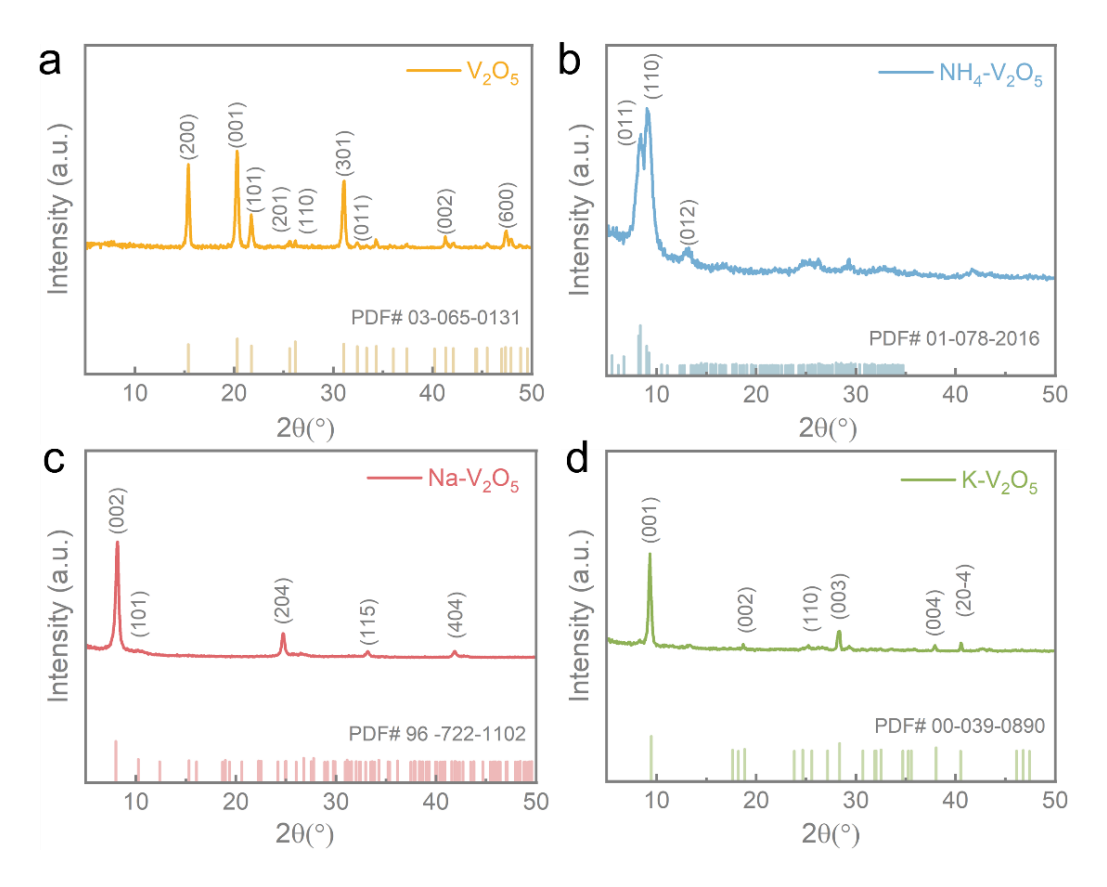


Figure 4.4: XRD patterns for (a) V_2O_5 , (b) $NH_4-V_2O_5$, (c) $Na-V_2O_5$ and (d) $K-V_2O_5$. Reproduced with permission. ³⁴⁷ Copyright 2024, Tsinghua University Press.

The UV–Vis absorption spectra (Figure 4.5) were used to study the optical properties of the samples, revealing notable variations in absorption behaviour. The optical bandgap values were determined to be 2.5 eV for V₂O₅, 2.35 eV for NH₄-V₂O₅, 2.42 eV for Na-V₂O₅, and 2.02 eV for K-V₂O₅. The observed shifts in UV absorption peaks are likely due to lattice expansion and the formation of oxygen vacancies induced by cation pre-doping. Adjustments in the spacing between layers can modify electronic band structures, influencing light absorption or emission, particularly in the UV region. Altering this interlayer distance through techniques like chemical doping, applied pressure, or strain can shift electronic transition energy levels, leading to changes in UV absorption or emission peaks.

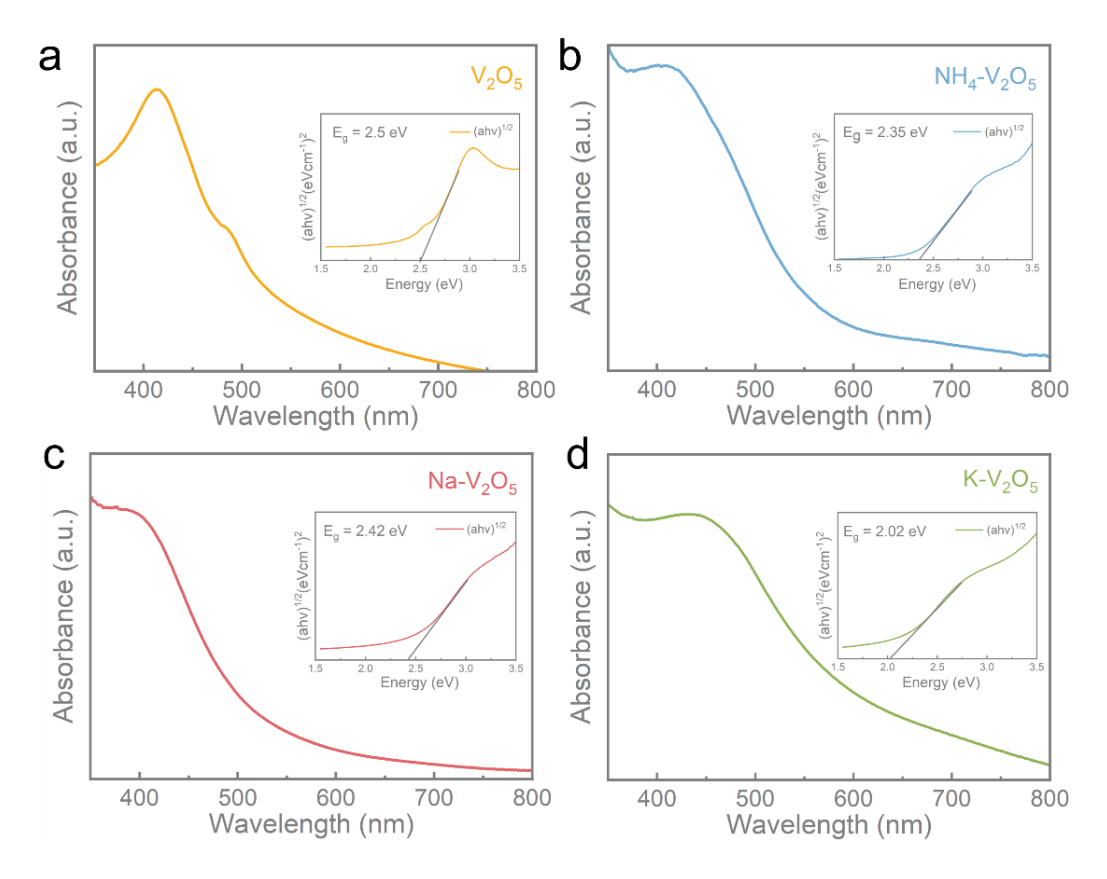


Figure 4.5: UV-Vis absorption spectra for (a) V_2O_5 , (b) NH_4 - V_2O_5 , (c) Na- V_2O_5 , and (d) K- V_2O_5 . Inset: Tauc plots of the respective samples. Reproduced with permission. ³⁴⁷ Copyright 2024, Tsinghua University Press.

The Raman spectra displayed in Figure 4.6 showed distinct shifts. In the V₂O₅ sample, the peak around 994 cm⁻¹ corresponds to the vanadyl bond (V=O) stretching vibration, while the peak near 700 cm⁻¹ is associated with V-O-V bond stretching. Other peaks at approximately 526, 407, 304, 285, and 198 cm⁻¹ represent various bending and stretching vibrations of V-O bonds. Specifically, the peak at around 526 cm⁻¹ relates to the V₃O phonon band, and the peak at 407 cm⁻¹ corresponds to the angle-bending vibration of the V-O₍₃₎-V bond. The peak at 304 cm⁻¹ indicates the bending of the V-O_C bond, while the peak at 285 cm⁻¹ is linked to the O_C-V-O_B bond bending. Additionally, the peak at 198 cm⁻¹ corresponds to O_C-V-O_B bond bending in the A_g mode, and the peak at 144 cm⁻¹ is associated with the vibration mode of V-O-V chains. ¹²⁶ For NH₄-V₂O₅, peaks observed at approximately 142, 194, 283, 407, and 471 cm⁻¹ correspond to bending vibrations of O-V=O and V-O-V bonds. The peak around 691 cm⁻¹ is linked to the V-O bond stretching, ³⁴⁵ and the peak near 993 cm⁻¹ indicates V=O stretching. In Na-V₂O₅, a blue shifted peak at about 137 cm⁻¹ represents the V-O-V chain vibration, while the peak near

691 cm⁻¹ signifies the antisymmetric stretching of $V_{(1)}$ – $O_{(2)}$ – $V_{(1)}$, and the peak at approximately 1017 cm⁻¹ corresponds to $V_{(2)}$ – $O_{(6)}$ stretching. ³⁴⁶ For K- V_2O_5 , the prominent peak at 1004 cm⁻¹ represents V=O stretching, while peaks at approximately 500 and 686 cm⁻¹ are related to V-O bond stretching, and the peak at 419 cm⁻¹ corresponds to V=O bending. ³⁴²

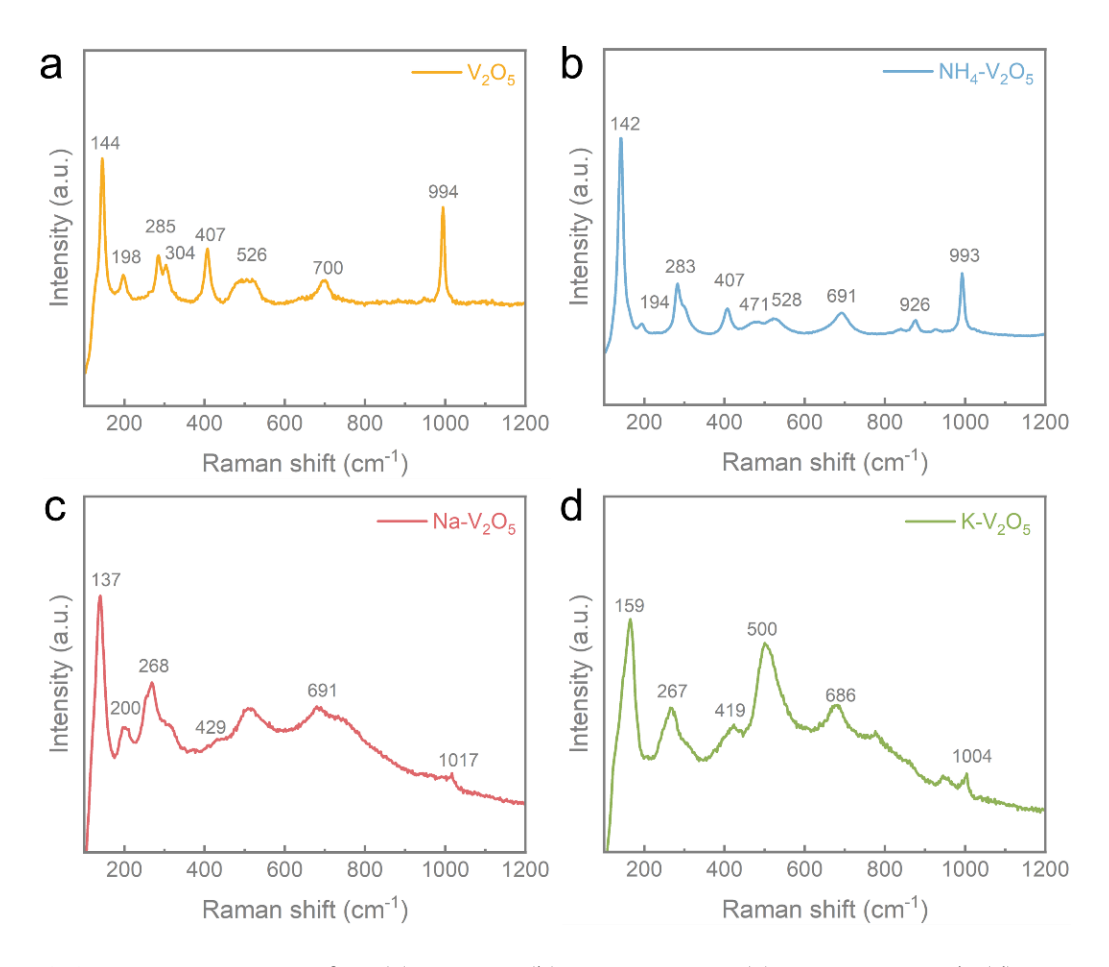


Figure 4.6: Raman spectra for (a) V_2O_5 , (b) NH_4 - V_2O_5 , (c) Na- V_2O_5 and (d) K- V_2O_5 . Reproduced with permission. ³⁴⁷ Copyright 2024, Tsinghua University Press.

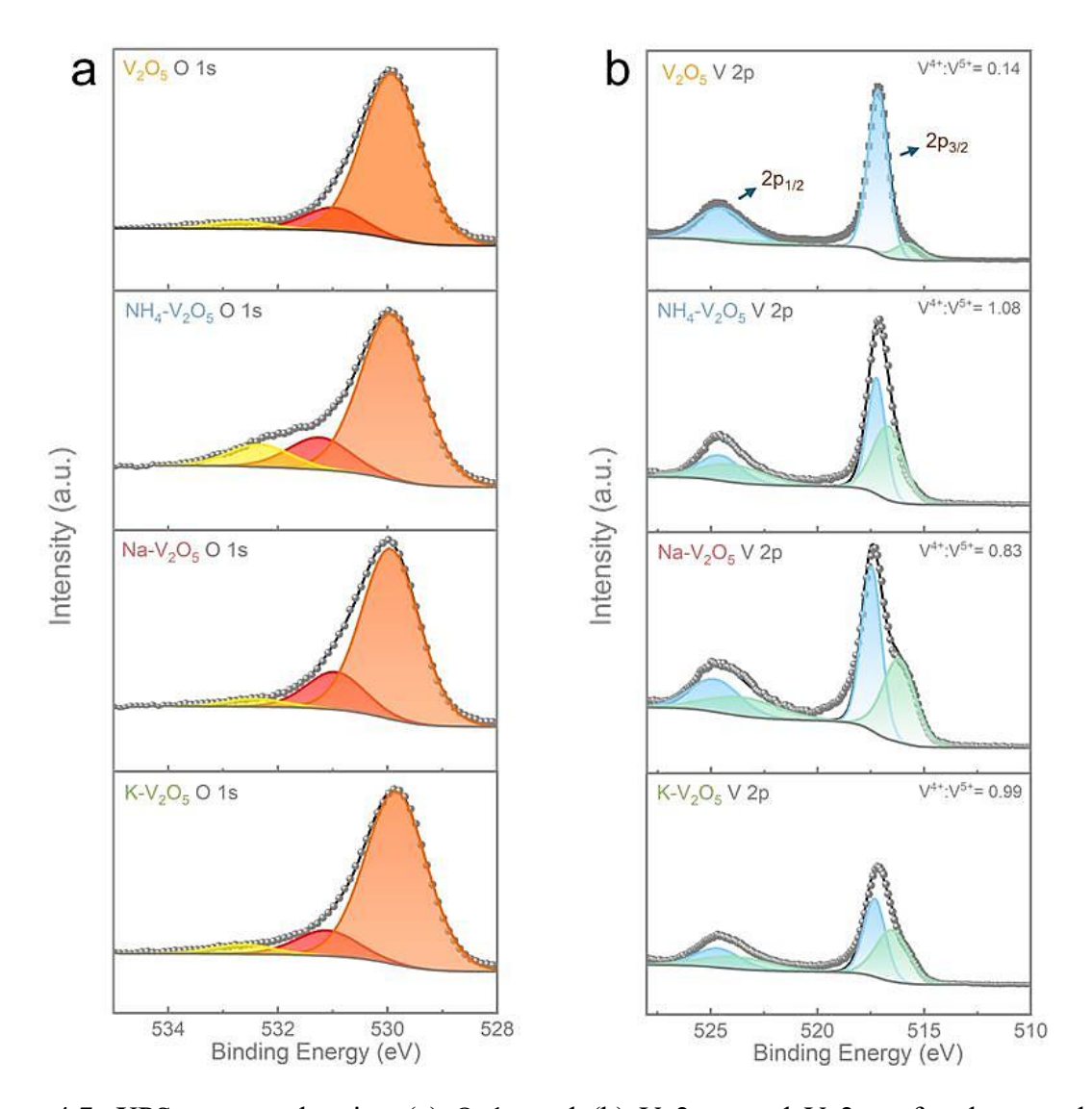


Figure 4.7: XPS spectra showing (a) O 1s and (b) V $2p_{1/2}$ and V $2p_{3/2}$ for the samples. Reproduced with permission. ³⁴⁷ Copyright 2024, Tsinghua University Press.

XPS analysis was conducted to gain insights into the composition and oxidation states of vanadium in the samples. The O 1s spectrum in Figure 4.7 (a) displayed a broad, asymmetric peak that was deconvoluted into three individual peaks, representing various oxygen species. These were identified at approximately 529.95 eV (orange peak), 531.00 eV (red peak), and 532.40 eV (yellow peak), corresponding to lattice oxygen (O^{2-}), adsorbed H₂O molecules, and oxygen vacancies, respectively. ³²⁷ The intensity of the peaks linked to adsorbed water and oxygen vacancies was significantly higher in NH₄-V₂O₅ compared to pristine V₂O₅. The levels of adsorbed H₂O were ranked as follows: Na-V₂O₅ (10.25%) > NH₄-V₂O₅ (9.13%) > K-V₂O₅ (7.5%) > V₂O₅ (7.07%). Oxygen vacancy percentages were highest in NH₄-V₂O₅ (6.31%),

followed by K-V₂O₅ (2.76%), V₂O₅ (2.24%), and Na-V₂O₅ (2.14%). The V $2p_{3/2}$ and V $2p_{1/2}$ core-level spectra, shown in Figure 4.7 (b), were deconvoluted into four peaks. Peaks at 517.16 eV and 524.51 eV (light blue) correspond to V⁵⁺, while those at 515.76 eV and 523.10 eV (light green) are associated with V⁴⁺. The V⁴⁺ : V⁵⁺ ratio was higher in the doped samples, following the order: NH₄-V₂O₅ (1.08) > K-V₂O₅ (0.99) > Na-V₂O₅ (0.83) > V₂O₅ (0.14). This increased V⁴⁺ content indicates a greater presence of the tetravalent state in the doped samples, with NH₄-V₂O₅ having the highest V⁴⁺ concentration.

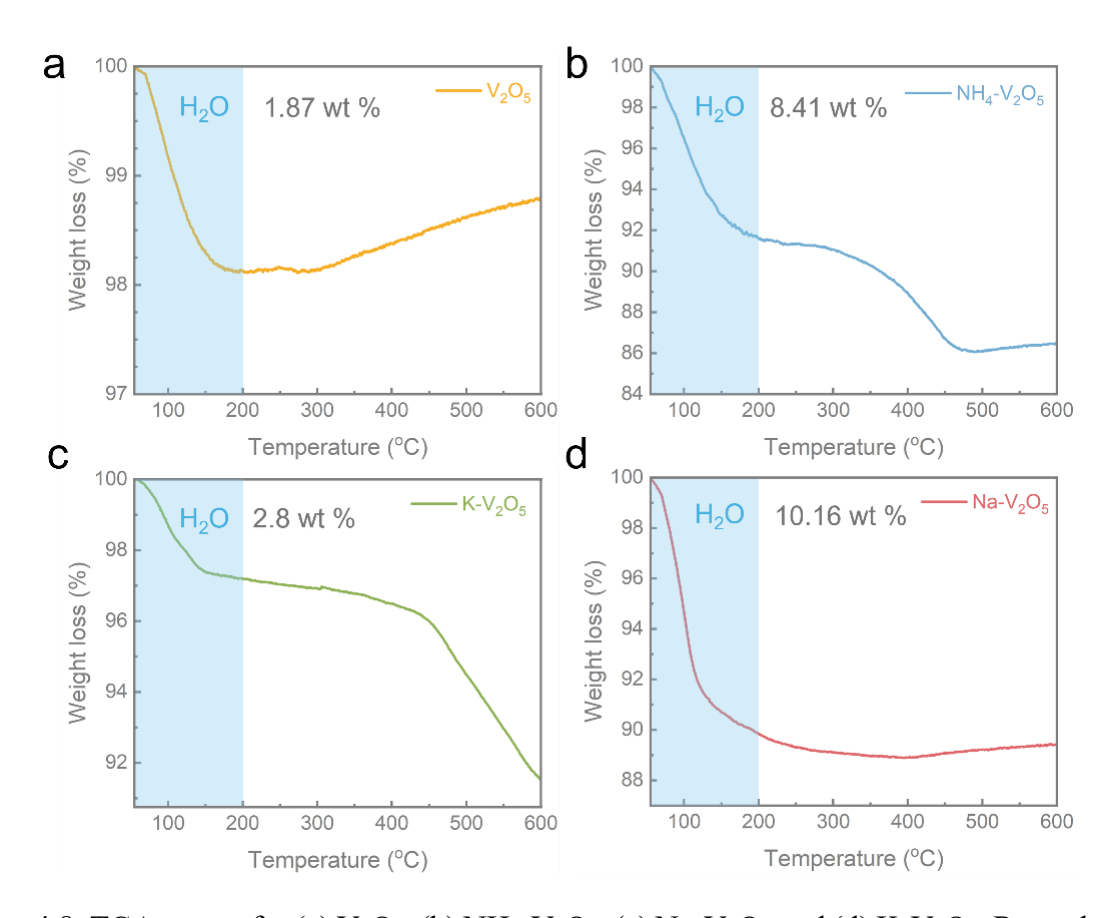


Figure 4.8: TGA curves for (a) V_2O_5 , (b) $NH_4-V_2O_5$, (c) $Na-V_2O_5$ and (d) $K-V_2O_5$. Reproduced with permission. ³⁴⁷ Copyright 2024, Tsinghua University Press.

Figure 4.8 illustrates the TGA curves for each sample. The weight losses observed between 55 and 200 °C: 1.87% for V₂O₅, 8.41% for NH₄-V₂O₅, 10.16% for Na-V₂O₅, and 2.80% for K-V₂O₅ are associated with the release of adsorbed and structural water molecules. These results are consistent with the XPS findings on water content presented in Figure 4.7 (a).

4.3.2 Electrochemical Performance

The electrodes' electrochemical properties were comprehensively assessed in coin-cells against a Zn anode, as described in the experimental section. Initial CV was carried out at scan rates from 0.2 to 1.0 mV s⁻¹ within a potential range of 0.2 to 1.6 V. As shown in Figure 4.9, the CV profiles for the V₂O₅ electrode revealed distinct pairs of redox peaks, with prominent peaks around 1.2 V and 0.9 V, and additional minor peaks near 0.7 V and 0.5 V, corresponding to Zn2+ ion intercalation and de-intercalation. 125, 348 In comparison, the NH₄-V₂O₅ electrode showed more intense oxidation and reduction peaks, along with considerably higher peak currents than pristine V₂O₅, suggesting improved charge storage capability. Detailed CVs for the Na-V₂O₅ and K-V₂O₅ electrodes also indicate that all doped electrodes exhibited enhanced charge storage performance over pristine V₂O₅. Among the doped materials, NH₄-V₂O₅ displayed the highest peak responses. A comparison of CVs at 0.5 and 1.0 mV s⁻¹ demonstrated a notable increase in redox peak currents, further underscoring the superior charge storage activity of the doped electrodes. Overall, the doped electrodes, particularly NH₄-V₂O₅, exhibited substantial improvements in electrochemical performance. Theoretically, the peak current (i) and scan rate (v) in the CV curve follows the rule: $i = av^b$ where a and b are adjustable values. If the calculated b value is 0.5, then the electrochemical reaction is determined by the ionic diffusion, whereas if b = 1, the reaction is mainly due to the capacitive behaviour. ^{393,394} Table 4.1 shows the b-values calculated for both cathodic and anodic peaks. For pristine V₂O₅, the cathodic and anodic peaks exhibited b-values of 0.79 and 0.56, respectively. In contrast, for NH₄-V₂O₅, the cathodic peaks had b-values of 0.66 and 0.85, and the anodic peaks were 0.74 and 0.73. These b-values, being greater than 0.5 for both V₂O₅ and NH₄-V₂O₅, suggest that the electrochemical response is governed by a mix of capacitive and diffusion-controlled mechanisms, with capacitive effects playing a dominant role. To further investigate the charge storage mechanism, the current was divided into capacitive-controlled (k_1v) and diffusion-controlled $(k_2v^{1/2})$ components, as described by the equation: $i(V) = k_1 v + k_2 v^{1/2}$. 311, 349 Using this method, the capacitive contribution for each electrode was determined, as depicted in Figure 4.10. At a scan rate of 0.2 mV s⁻¹, the capacitive contributions for V₂O₅, NH₄-V₂O₅, Na-V₂O₅, and K-V₂O₅ were approximately 55.4%, 58.7%, 65%, and 39.7%, respectively. At an increased scan rate of 1.0 mV s⁻¹, these values rose to 75.5%, 75.7%, 80.5%, and 59.4%, respectively. A higher capacitive contribution at increased rates indicates improved performance, making NH₄-V₂O₅ and Na-V₂O₅ suitable for high-rate battery applications.

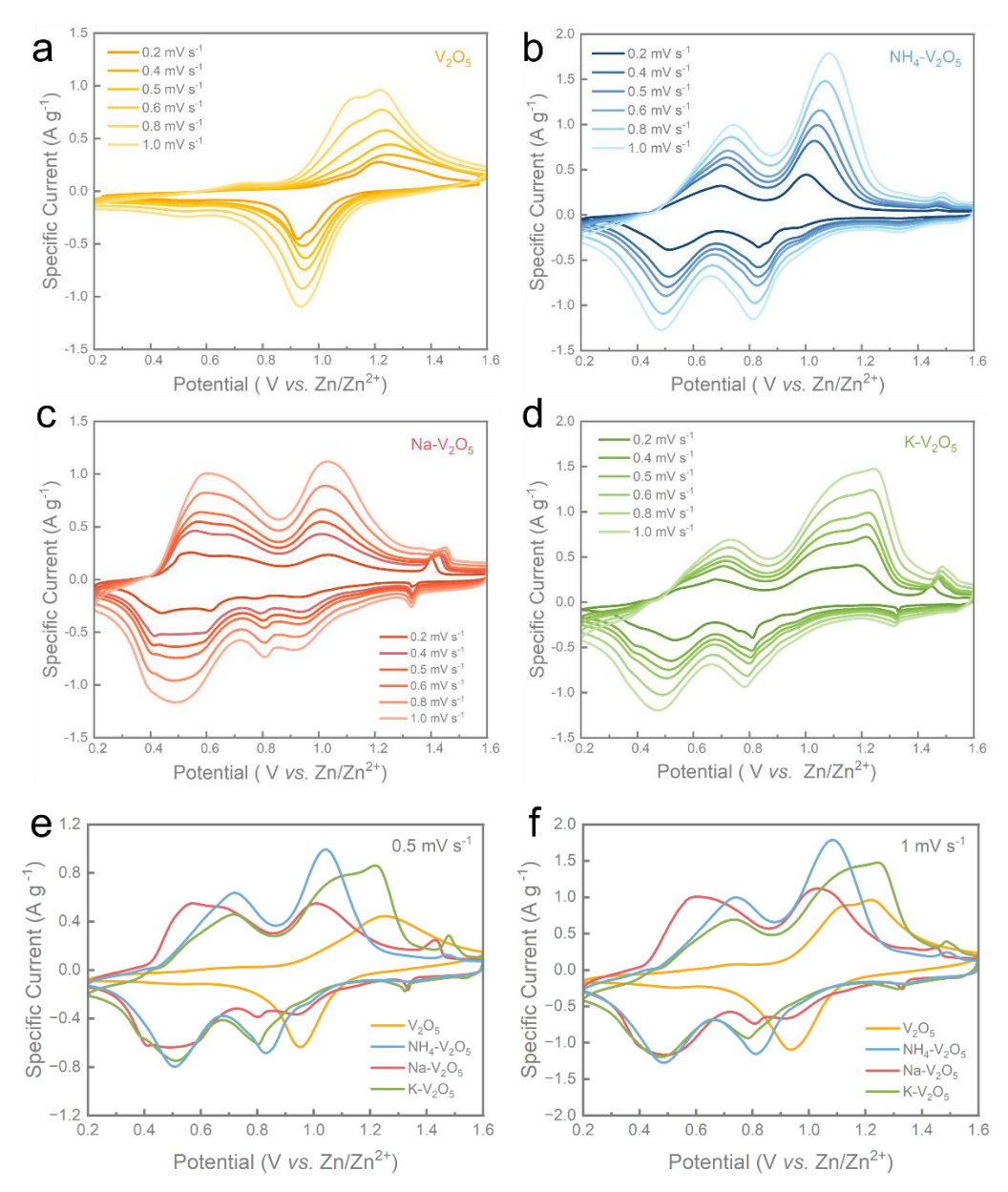


Figure 4.9: CV curves for (a) V_2O_5 , (b) NH_4 - V_2O_5 , (c) Na- V_2O_5 , and (d) K- V_2O_5 electrodes recorded at scan rates from 0.2 to 1.0 mV s⁻¹ within a potential range of 0.2 to 1.6 V. Comparison of CV profiles for all samples at scan rates of (e) 0.5 and (f) 1.0 mV s⁻¹. Reproduced with permission. ³⁴⁷ Copyright 2024, Tsinghua University Press.

To further investigate charge storage, GDC tests were conducted at specific currents ranging from 100 to 5000 mA g^{-1} within a voltage window of 0.2 to 1.6 V. Figure 4.11 shows the GDC curves for the four samples at various specific currents, revealing that NH₄-V₂O₅ achieved higher specific capacities compared to the other electrodes, aligning with the CV results. At a current of 100 mA g^{-1} , the second-cycle specific capacities were measured as 99.6, 302.4,

238.17, and 276 mAh g⁻¹ for V_2O_5 , NH_4 - V_2O_5 , Na- V_2O_5 , and K- V_2O_5 , respectively. Figure 4.11 (e) and (f) highlight the superior capacities of the doped samples over pristine V_2O_5 . At a high current of 5000 mA g⁻¹, NH_4 - V_2O_5 and Na- V_2O_5 displayed nearly identical specific capacities (159 mAh g⁻¹), likely due to a greater capacitive-controlled storage contribution at higher rates. The enhancements in charge storage performance correspond with the V^{4+} : V^{5+} ratio (Figure 4.7 (b)), following the sequence $V_2O_5 < Na$ - $V_2O_5 < K$ - $V_2O_5 < NH_4$ - V_2O_5 . This order aligns with the observed charge storage capabilities, with NH_4 - V_2O_5 showing the highest capacity, mainly due to its elevated V^{4+} content, which improved the efficiency of reversible Zn^{2+} ion storage. $^{350-352}$

Table 4.1: Calculated b-values for the cathodic and anodic peaks of V_2O_5 , $NH_4-V_2O_5$, $Na-V_2O_5$, and $K-V_2O_5$.

Material	b value	b value	b value	b value
	Cathodic Peak 1	Cathodic Peak 2	Anodic Peak 1	Anodic Peak 2
V_2O_5	0.79		0.56	
NH ₄ -V ₂ O ₅	0.66	0.85	0.74	0.73
Na-V ₂ O ₅	0.84	0.96	0.91	0.85
K-V ₂ O ₅	0.61	0.79	0.64	0.53

Alongside the GDC tests, EIS measurements were conducted within a frequency range of 10 mHz to 100 kHz using a 10 mV voltage amplitude. These tests were performed after the second GDC cycle at 0.7 V. The Nyquist plots in Figure 4.12 display the cells' charge transfer resistance, with approximate values of 65.58 Ω for V₂O₅, 17.9 Ω for NH₄-V₂O₅, 19.78 Ω for Na-V₂O₅, and 10.66 Ω for K-V₂O₅. These results confirm that the doped samples possess improved charge transfer kinetics compared to undoped V₂O₅.

Table 4.2 compares the electrochemical performance of NH₄-V₂O₅ with other V₂O₅ studies in ZIBs, demonstrating that NH₄-V₂O₅ offers promising charge storage and enhanced electrochemical characteristics.

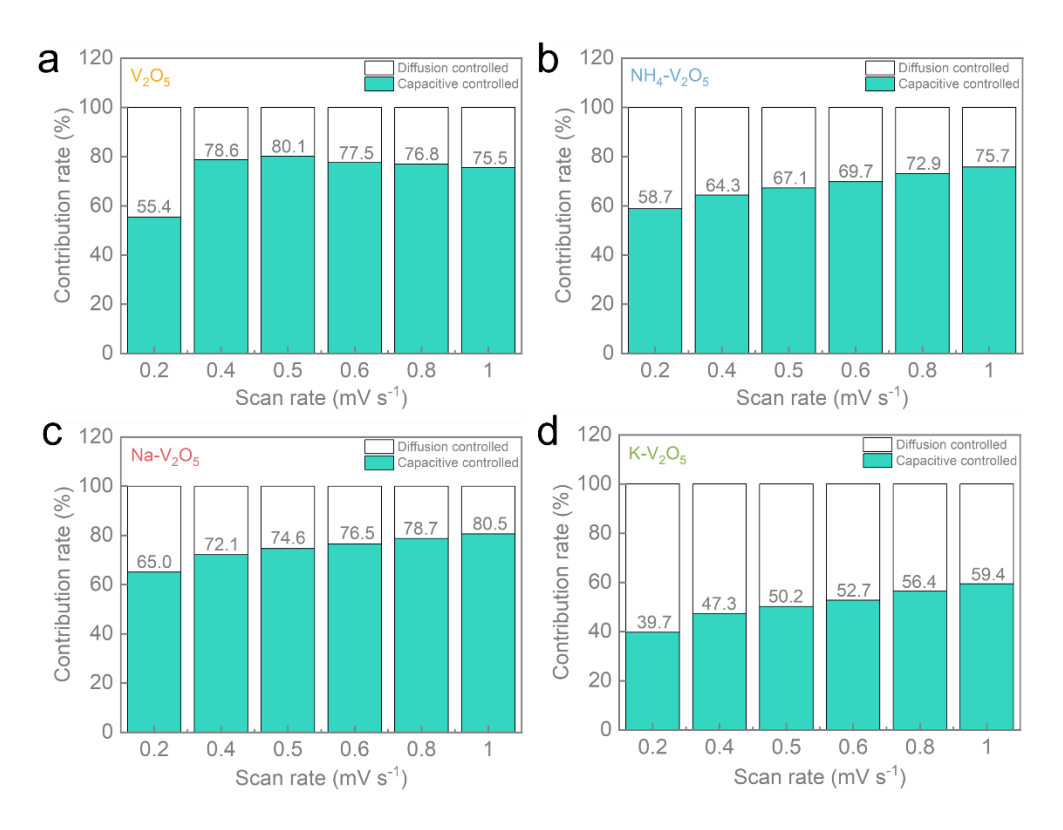


Figure 4.10: Estimated capacity contributions for (a) V_2O_5 , (b) NH_4 - V_2O_5 , (c) Na- V_2O_5 and (d) K- V_2O_5 electrodes. Reproduced with permission. ³⁴⁷ Copyright 2024, Tsinghua University Press.

The long-term cycling stability was assessed at a current density of 1000 mA g⁻¹ over 1000 cycles, as shown in Figure 4.13. The NH₄-V₂O₅ electrode retained around 60.58% of its initial capacity after 1000 cycles, with a Coulombic efficiency close to 100%. Figure 4.14 presents *ex-situ* HRTEM images and d-spacing measurements for NH₄-V₂O₅ before cycling and after 500 and 1000 cycles. The d-spacing of the (110) plane increased slightly from 9.55 Å initially to 9.65 Å after 500 cycles, indicating structural stability during prolonged cycling. After 1000 cycles, the d-spacing was calculated as 13.1 Å, corresponding to the (100) plane of NH₄-V₂O₅, further confirming the material's structural resilience after extended cycling tests.

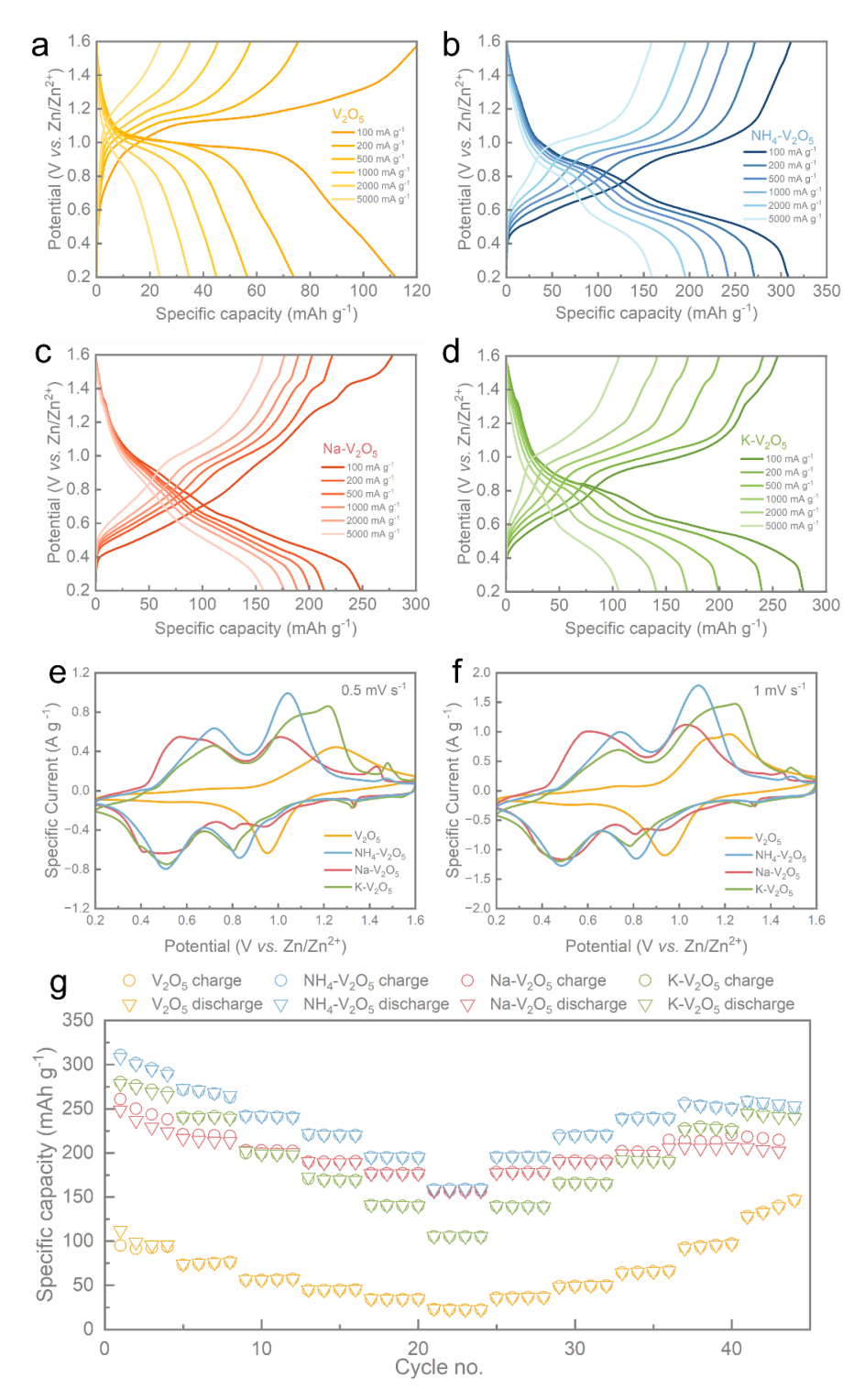


Figure 4.11: GDC curves for (a) V₂O₅, (b) NH₄-V₂O₅, (c) Na-V₂O₅, and (d) K-V₂O₅ at various specific currents from 100 to 5000 mA g⁻¹ within a voltage range of 0.2 to 1.6 V. Comparative GDC curves of the electrodes at specific currents of (e) 500 and (f) 5000 mA g⁻¹, respectively. (g) Rate tests showing the electrodes' performance. Reproduced with permission. ³⁴⁷ Copyright 2024, Tsinghua University Press.

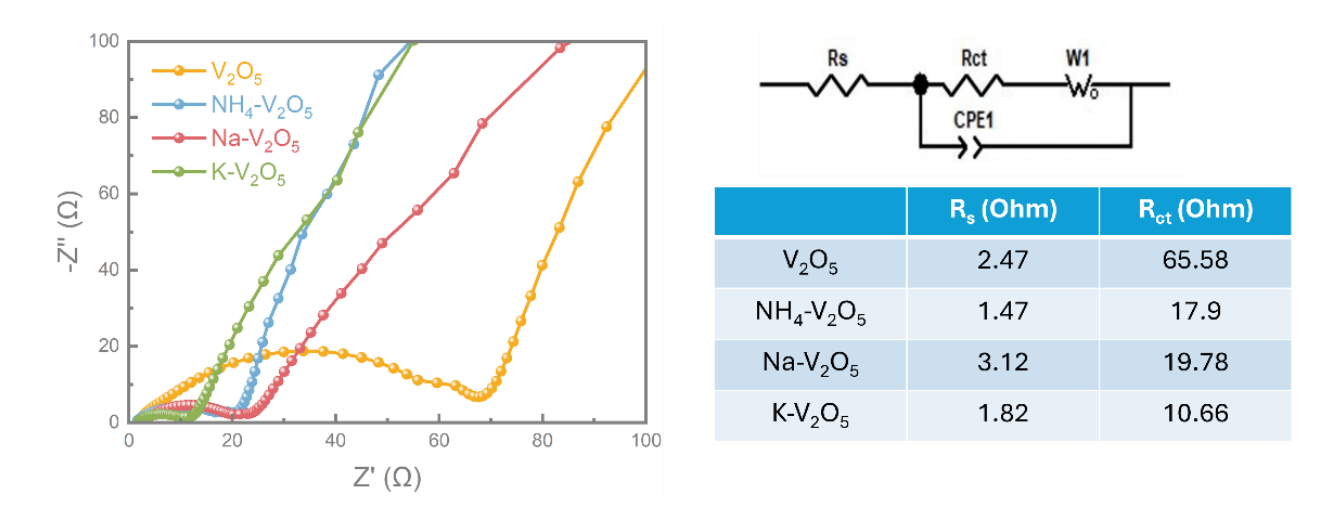


Figure 4.12: Nyquist plots and equivalent circuit model for cells with V_2O_5 , $NH_4-V_2O_5$, $Na-V_2O_5$, and $K-V_2O_5$. Reproduced with permission. ³⁴⁷ Copyright 2024, Tsinghua University Press.

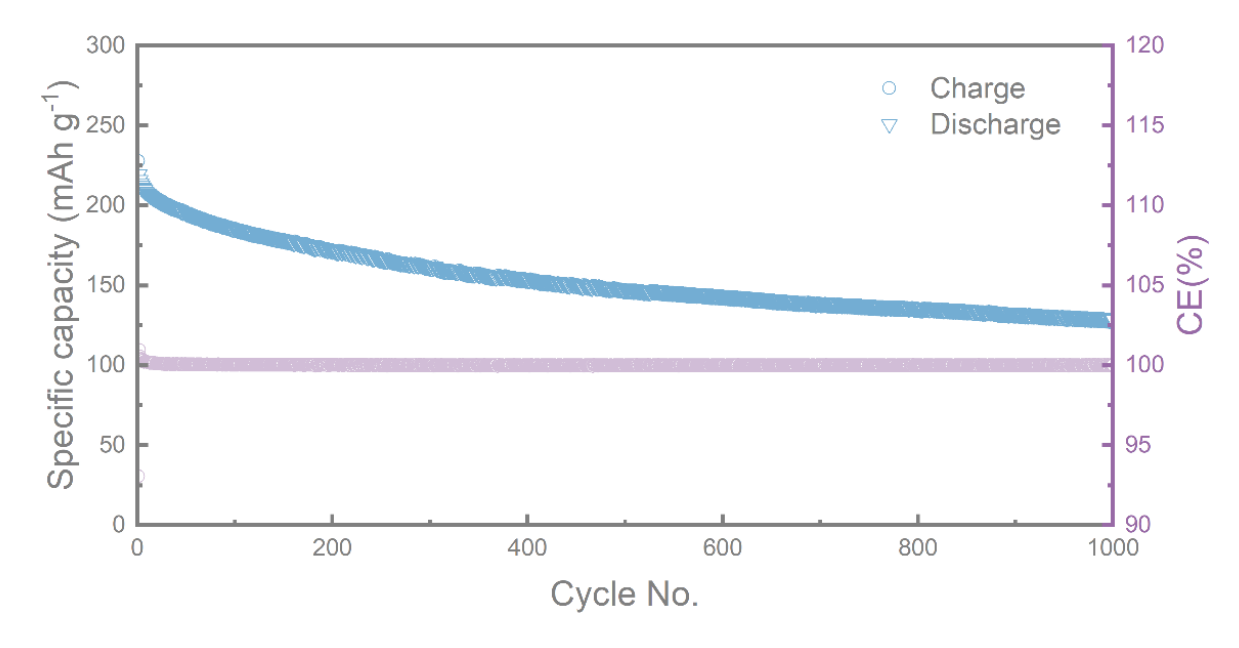


Figure 4.13: Long-term cycling performance of NH₄-V₂O₅, with CE indicating Coulombic efficiency in the plot. Reproduced with permission. ³⁴⁷ Copyright 2024, Tsinghua University Press.

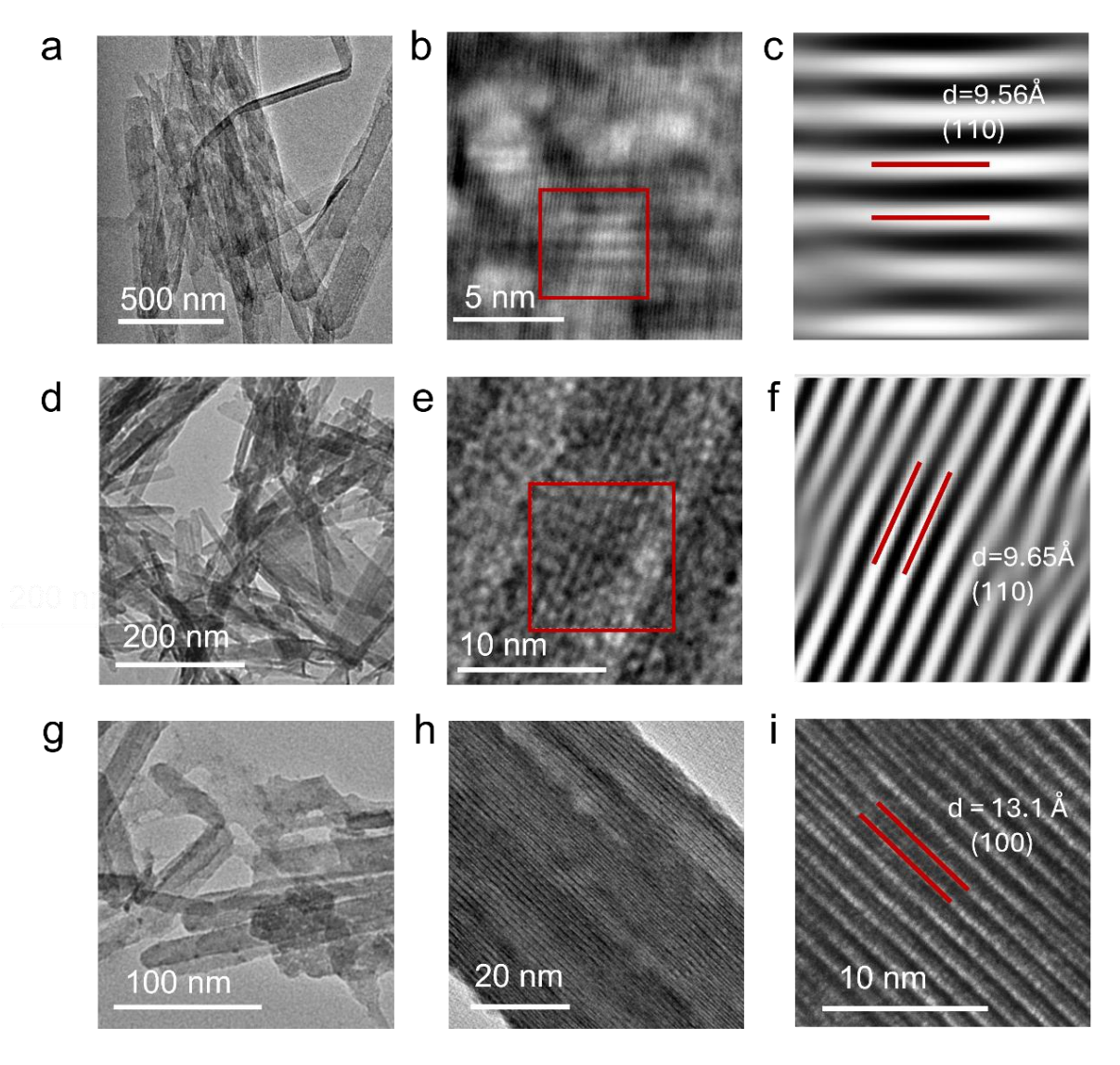


Figure 4.14: TEM and HRTEM images with interlayer d-spacing for (a-c) pristine NH_4 - V_2O_5 , (d-f) NH_4 - V_2O_5 after 500 cycles, and (g-i) NH_4 - V_2O_5 after 1000 cycles. Reproduced with permission. 347 Copyright 2024, Tsinghua University Press.

Table 4.2: Comparison of the electrochemical performance of NH_4 - V_2O_5 in this study with other reported V_2O_5 -based materials in ZIBs from the literature.

Material	Specific Capacity (mAh g ⁻¹)	Specific Current (A g ⁻¹)	Voltage (V)
NH. V.O.	221	1	
NH4-V ₂ O ₅	274	0.2	0.2-1.6
(this work)	314	0.1	
$V_2O_5^{353}$	335	0.05	0.4-1.6
V ₂ O ₅ ¹⁸⁴	460	0.5	0.2-1.6
V ₂ O ₅ 354	224	0.1	0.4-1.4
V ₂ O ₅ 355	319	0.02	0.5-1.5
V ₂ O ₅ ¹⁷⁸	238	0.05	0.2-1.6
Od-V ₂ O ₅ ²⁷⁸	406	0.1	0.1-1.6
Od-V ₂ O ₅ 356	397	0.2	0.4-1.5
V ₂ O ₅ @C ³⁵⁷	362	0.5	0.2-1.5
Na-V ₂ O ₅ 358	277	1	0.2-1.4

4.4 Summary

In summary, this research investigated the impact of pre-doping V_2O_5 with different cations - NH_4^+ , - Na^+ , and - K^+ to enhance charge storage performance in ZIBs. The findings highlighted the significant role of V^{4+} species in boosting the capacity of cathode materials. Notably, introducing NH_4^+ into V_2O_5 (resulting in NH_4 - V_2O_5) brought substantial improvements in electrochemical behaviour. A major advancement was the increase in the interlayer spacing of the (110) plane from 3.4 Å in pristine V_2O_5 to 9.6 Å in NH_4 - V_2O_5 . Additionally, the (100) plane of NH_4 - V_2O_5 with a d-spacing of 13.1 Å was observed via TEM, supporting effective Zn^{2+} ion diffusion. The V^{4+}/V^{5+} redox couple ratio also increased from 0.14 to 1.08, indicating enhanced electrochemical activity. The NH_4 - V_2O_5 electrode achieved a high specific capacity of 310.8

mAh g^{-1} at 100 mA g^{-1} and demonstrated improved cycling stability, showcasing its capacity for high charge storage. This study deepened the understanding of the doping mechanism and the effects of different cations on V_2O_5 , providing valuable insights for optimizing cathode materials in ZIBs. These results contribute to the development of more efficient and sustainable rechargeable battery systems with better charge storage capabilities, advancing the overall sustainability of ZIB technology.

Chapter 5

Development of High-performance Cations Doped V₂O₅ Cathode for Lithium-ion Batteries

This chapter investigates the synthesis of three types of cation-doped V_2O_5 to explore the mechanisms by which cation doping affects the electrochemical performance of LIBs. The results reveal that cation doping induces the formation of oxygen vacancies, which play a crucial role in enhancing ion diffusion and charge transfer. These vacancies also introduce additional storage, adsorption, and active sites for Li^+ ions and intermediate species. Together, these effects significantly improve battery performance, providing valuable insights for designing high-efficiency LIB materials through strategic cation doping.

5.1 Introduction

Orthorhombic V_2O_5 is widely recognized as one of the most promising layered metal oxides for LIB cathodes, owing to its high electrochemical reactivity, considerable energy density, and notably higher capacity relative to traditional cathodes such as $LiCoO_2$ (140 mAh g^{-1}) and $LiFePO_4$ (170 mAh g^{-1}). $^{359\text{-}361}$ Theoretically, V_2O_5 can deliver a capacity of 294 mAh g^{-1} when discharged to 2 V (vs. Li/Li^+), which aligns with the insertion of two lithium ions. Discharging further to 1.5 V (vs. Li/Li^+) allows for the intercalation of three lithium ions, potentially yielding an irreversible capacity of 440 mAh g^{-1} . 362 However, the practical application of V_2O_5 is hindered by its limited cycling stability, as it undergoes structural deterioration during lithium insertion and exhibits low intrinsic conductivity. 363

To address these problems, various strategies have been explored. Research has focused on modifying materials, including nanostructures V₂O₅, ^{87, 364} carbon or compound-coated V₂O₅, ^{153, 365} and defect engineering. ^{93, 280, 366} Such modifications improve electrochemical kinetics, specific capacity and rate performance compared to pristine V₂O₅ due to their specific structures and synergetic effect, which could greatly increase electroactive sites, shorten the diffusion pathways of Li⁺, and enhance conductivity. Additionally, aliovalent-ion doping in V₂O₅ has been proposed as an effective approach. Doping could expand interlayer spacing, improve electronic conductivity, stabilize the layered structure during cycling, create diffusion paths for Li⁺, and reduce charge transfer resistance, thereby enhancing overall electrochemical performance. For instance, Yao et al. developed Y-doped V₂O₅ via a sol-gel process, achieving a specific discharge capacity of 203 mAh g⁻¹ after 100 cycles at a current density of 200 mA g⁻¹ ¹. ³⁶⁷ Yu et al. synthesized Cu doped V₂O₅ flowers by a hydrothermal approach obtaining initial discharge and charge capacities of 266 and 263 mAh g⁻¹ at a current density of 58.8 mA g⁻¹. ³⁶⁸ In addition, Cheah et al. used electrospinning to prepare Al-doped V₂O₅ which exhibited an initial discharge capacity of approximately 350 mAh g⁻¹ and maintained around 85% capacity over 20 cycles at 35 mA g⁻¹. ³⁶⁹

Although various cations have been explored individually for LIBs, the mechanisms behind cation doping remain intricate and are not fully understood, with limited guidelines for selecting the most suitable cations. This study synthesized three different types of cation-doped V₂O₅ (NH₄⁺, Na⁺ and K⁺) to explore how various aspects of cation doping influence electrochemical performance in LIBs. Significantly, cation doping creates oxygen vacancies,

which improve ion diffusion and charge transfer. These vacancies also offer additional storage, adsorption, and active sites for Li⁺ ions and intermediate species, leading to enhanced battery performance.

5.2 Experimental Section

5.2.1 Chemicals

All chemicals used in this study were of analytical grade and were utilized as received, without additional purification. The following materials were obtained from Sigma-Aldrich: vanadium pentoxide, a 30% (w/w) hydrogen peroxide (H₂O₂) solution, ammonium metavanadate (NH₄VO₃), potassium iodide (KI), polyethylene glycol (Mw 4000), sulfuric acid (H₂SO₄, 95–97%), ethanol, poly(vinyl difluoride) (PVDF), lithium bis(trifluoromethanesulfonyl)imide (LiTFSI), propylene carbonate (PC), and ethylene carbonate (EC). N-Methyl-2-pyrrolidone (NMP) was acquired from VWR International. Sodium hydroxide (NaOH) pellets (98%) were sourced from Thermo Scientific. Potassium chloride (KCl) was purchased from EMSURE®. Reduced graphene oxide (rGO) powder and poly(3-hexylthiophene) (P3HT) (Mw = 60,150) were obtained from Ossila.

5.2.2 Synthesis of V₂O₅, NH₄-V₂O₅, Na-V₂O₅ and K-V₂O₅.

Pristine V₂O₅ nanofibers were prepared using a hydrothermal approach. To start, 1.0930 g of V₂O₅ powder was mixed with 90 mL of deionized water and stirred at 300 rpm for 30 minutes at ambient temperature. Then, 15 mL of 30% H₂O₂ was added, and the stirring continued for an additional 30 minutes. This transparent orange solution was transferred into a 150 mL autoclave and heated at 205 °C for 3 days. After cooling to room temperature, the product was rinsed alternately with deionized water and ethanol, followed by drying overnight in a vacuum oven at 120 °C.

For Na-doped V_2O_5 (referred to as NAVO in this chapter), the synthesis method was based on a previously reported procedure. ³⁴⁶ Here, 0.3636 g of the pristine V_2O_5 nanofibers was dissolved in a solution containing 60 mL of deionized water and 0.7 mL of 1 M NaOH. The solution was sonicated for 1 hour at room temperature. Polyethylene glycol (Mw 4000), at 0.2 g, was then introduced, and the solution was stirred for an additional 15 minutes. The mixture

was then placed in a 150 mL autoclave and heated at 180 °C for 2 days. After returning to room temperature, the product was cleaned with DI water and ethanol, followed by drying in a vacuum oven at 120 °C overnight.

NH₄V₂O₅ (referred to as NHVO) was synthesized following an established method. ³⁴⁵ In this process, 1.755 g of NH₄VO₃ was dissolved in 90 mL of DI water and stirred for 30 minutes. Then, 0.9 mL of sulfuric acid was added, and stirring was continued for another 30 minutes. The resulting mixture was transferred to a 150 mL autoclave and heated at 100 °C for 2 days. After cooling, the product was washed alternately with DI water and ethanol, followed by drying in a vacuum oven at 120 °C overnight.

For K-doped V₂O₅ (referred to as KVO), ³⁴² 0.5456 g of pristine V₂O₅ nanofibers, 0.747 g of KI, and 6.709 g of KCl were dissolved in 90 mL of DI water with magnetic stirring for 30 minutes. This solution was then placed in a 150 mL autoclave and heated at 200 °C for 1 day. Upon cooling, the product was washed with DI water and ethanol and then dried in a vacuum oven overnight at 120 °C.

5.2.3 Preparation of cathodes and coin-cells

To prepare the cathodes, 80 mg of the active material (either V₂O₅, NAVO, NHVO, or KVO) was mixed with 10 mg of rGO and 5 mg of P3HT in 2 mL of NMP using sonication. Following this, 5 mg of PVDF was added to the mixture. The resulting electrode slurry was then drop-cast onto carbon fiber current collectors (Sigracet GDL 39 AA carbon graphite paper from SGL Carbon) and dried at 120 °C under vacuum to complete the cathode fabrication.

The CR2032 coin-cells were assembled inside a glovebox. Assembly began by placing a cathode disc on the coin-cell case, followed by a layer of Whatman[®] glass microfiber filter paper serving as the separator. An $80~\mu L$ volume of 3M LiTFSI electrolyte was added, and a lithium metal counter electrode was positioned on top. Finally, the coin-cell was sealed using a hydraulic crimping machine.

5.2.4 Material Characterisations

The synthesized materials underwent characterization using a range of analytical techniques. SEM images were obtained with a JEOL JSM-7600F, operated at 15 kV. TEM, EDS, and SAED

analyses were conducted using a JEOL JEM-2100 at an operating voltage of 200 kV. XRD patterns were collected with a Panalytical Empyrean XRD instrument utilizing Cu Kα radiation, with measurements performed at 40 kV and 40 mA, a step size of 0.05°, and a scanning speed of 0.1° per second, over a 2θ range of 5° to 70°. UV-Vis spectroscopy was performed with a PerkinElmer Lambda 750S instrument. Raman analysis was conducted on a Renishaw inViaTM confocal Raman microscope using a 515 nm laser wavelength. XPS was performed with a ThermoFisher Scientific XPS system. XPS data were acquired with monochromatic Al Kα radiation (1486.6 eV), using pass energies of 50 eV for narrow scans and 200 eV for wide scans. No significant sample charging was detected, and charge correction was referenced to adventitious carbon (C 1s, 284.8 eV). The intensity of the spectra is presented in counts per second, and peak fitting was carried out with CasaXPS software.

5.2.5 Electrochemical Characterisations

CV measurements were conducted using a Biologic VMP-3 galvanostat over a voltage range of 2 to 4 V following a 10-hour resting period for the cells. The tests were carried out at scan rates between 0.2 and 1.0 mV s⁻¹. GDC measurements were also performed within the same potential range, with current densities varying from 100 to 2000 mA g⁻¹. The cycling stability of the electrodes was assessed using a Neware BTS4000 system at a fixed current density of 200 and 1000 mA g⁻¹ over 150 cycles within the defined voltage window. EIS was performed on an Autolab PGSTAT302N across a frequency spectrum from 10 mHz to 100 kHz, with an amplitude of 10 mV.

5.3 Results and Discussion

5.3.1 Cathode Characterizations

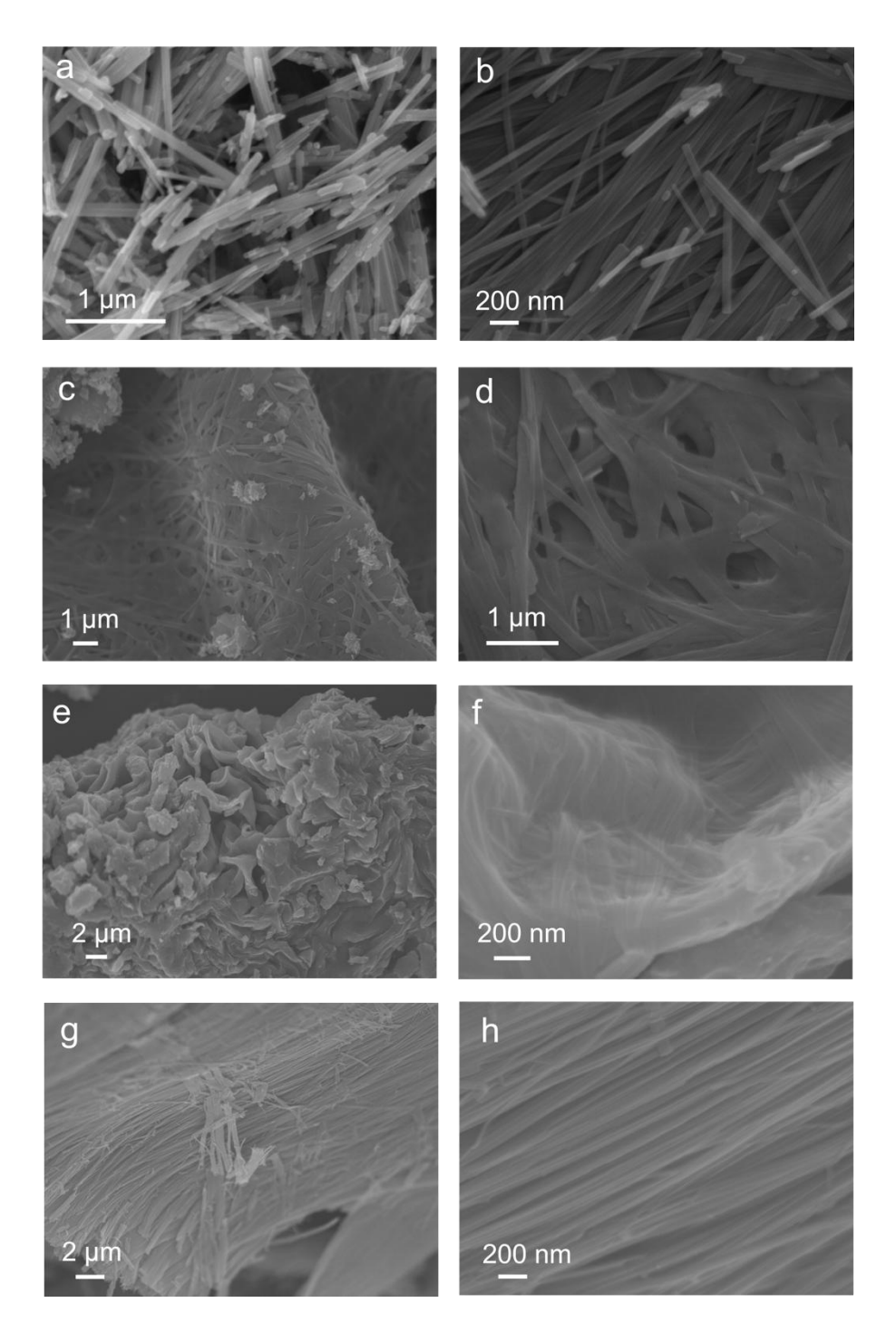


Figure 5.1: SEM images of the (a-b) V₂O₅, (c-d) NAVO, (e-f) NHVO and (g-h) KVO.

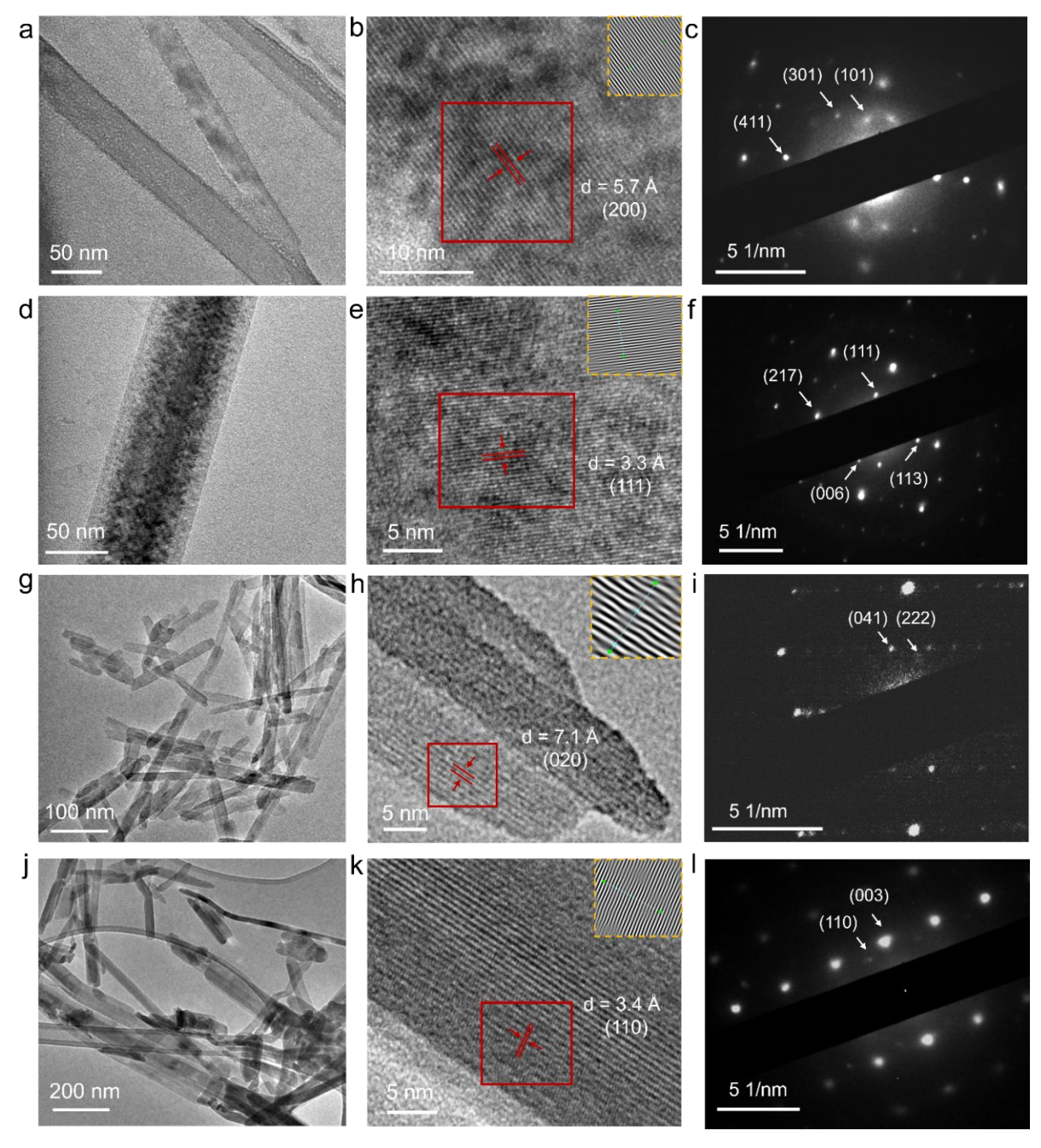


Figure 5.2: TEM and HRTEM images of the (a-b) V_2O_5 , (d-e) NAVO, (g-h) NHVO, (j-k) KVO, and SAED patterns of (c) V_2O_5 , (f) NAVO, (i) NHVO, (l) KVO. Inset: iFFT patterns of selected area in HRTEM images.

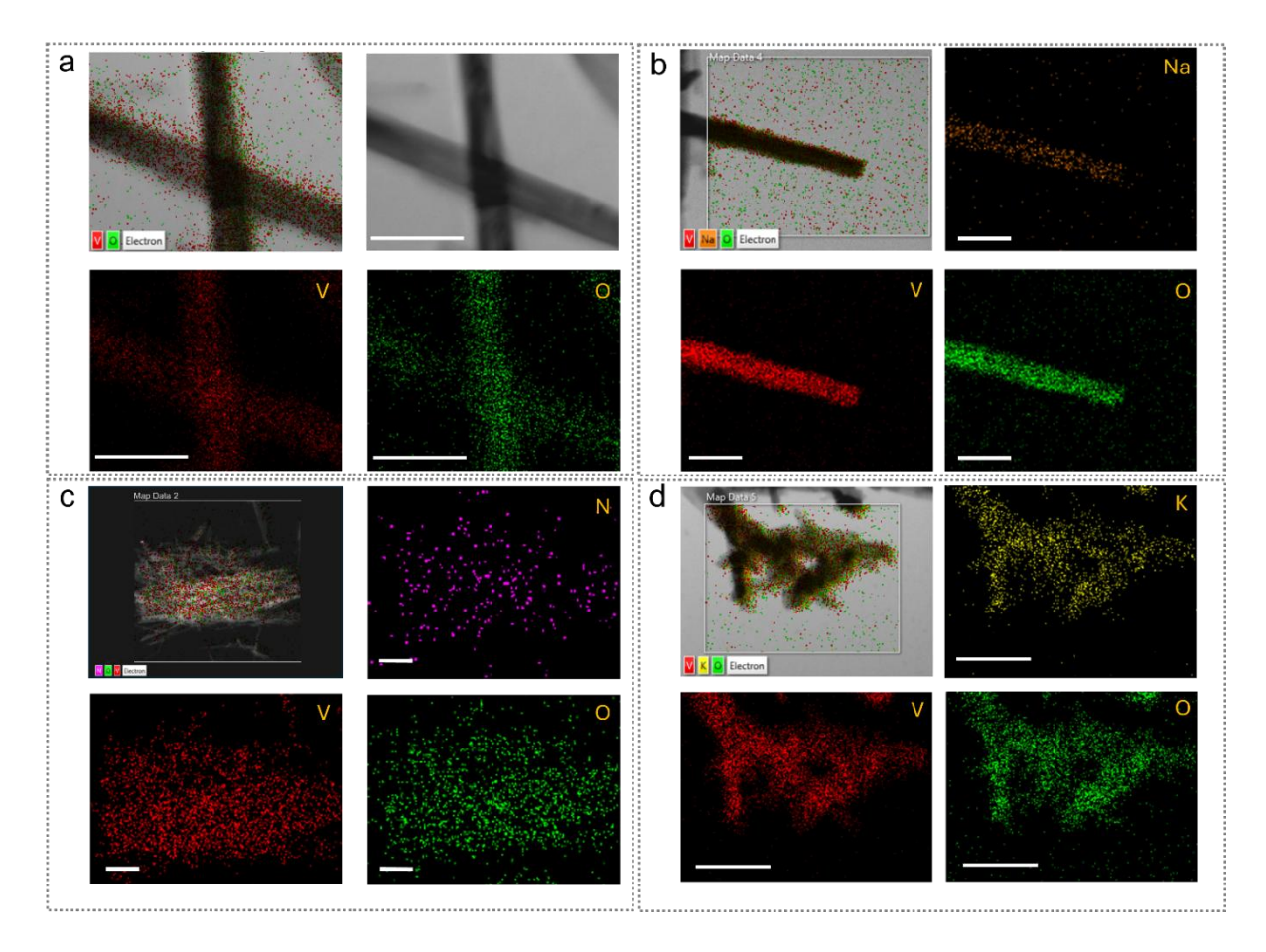


Figure 5.3: EDS elemental mapping of the (a) V_2O_5 , (b) NAVO, (c) NHVO and (d) KVO. All the scale bars represent the 250 nm.

Figure 5.1 shows that all four samples using hydrothermal methods as forementioned in section 5.2 display a nanofiber morphology. The V₂O₅ nanofibers have diameters ranging from 20 to 100 nm and extend several micrometres in length. The NAVO sample exhibits a mesh-like network of nanofibers, while NHVO has a flared shape but retains fibrous structures, as seen in the enlarged SEM image in Figure 5.1 (f). The KVO sample maintains a uniform nanofiber structure, with fibers around 50 nm in diameter. This nanofiber morphology across all samples is further corroborated by TEM images in Figure 5.2. HRTEM images of V₂O₅ reveal a lattice spacing of 5.7 Å, matching the (200) plane of orthorhombic V₂O₅. The corresponding SAED pattern in Figure 5.2 (c) shows the (101), (301), and (411) planes. NAVO nanofibers, approximately 60 nm in diameter, are shown in Figure 5.2 (d), with Figure 5.2 (e) displaying clear lattice fringes with a spacing of 3.3 Å, corresponding to the (111) plane. The SAED pattern indicates planes (111), (113), (006), and (217) with d-spacings of 3.41, 3.06, 3.72, and

2.05 Å, respectively. Figure 5.2 (g-h) provide TEM and HRTEM images of the NH₄-doped sample, showing a lattice spacing of 7.1 Å, aligning with the (020) plane, and the SAED pattern in Figure 5.2 (i) reveals (041) and (222) planes. TEM (Figure 5.2 (j)) and HRTEM (Figure 5.2 (k)) images of the K-doped V₂O₅ show a lattice spacing of 3.4 Å, consistent with the (110) plane, also visible in the SAED pattern in Figure 5.2 (l). Additionally, Figure 5.3 illustrates EDS mapping of these samples, confirming uniform distribution of V, O, Na, N, and K, verifying successful doping.

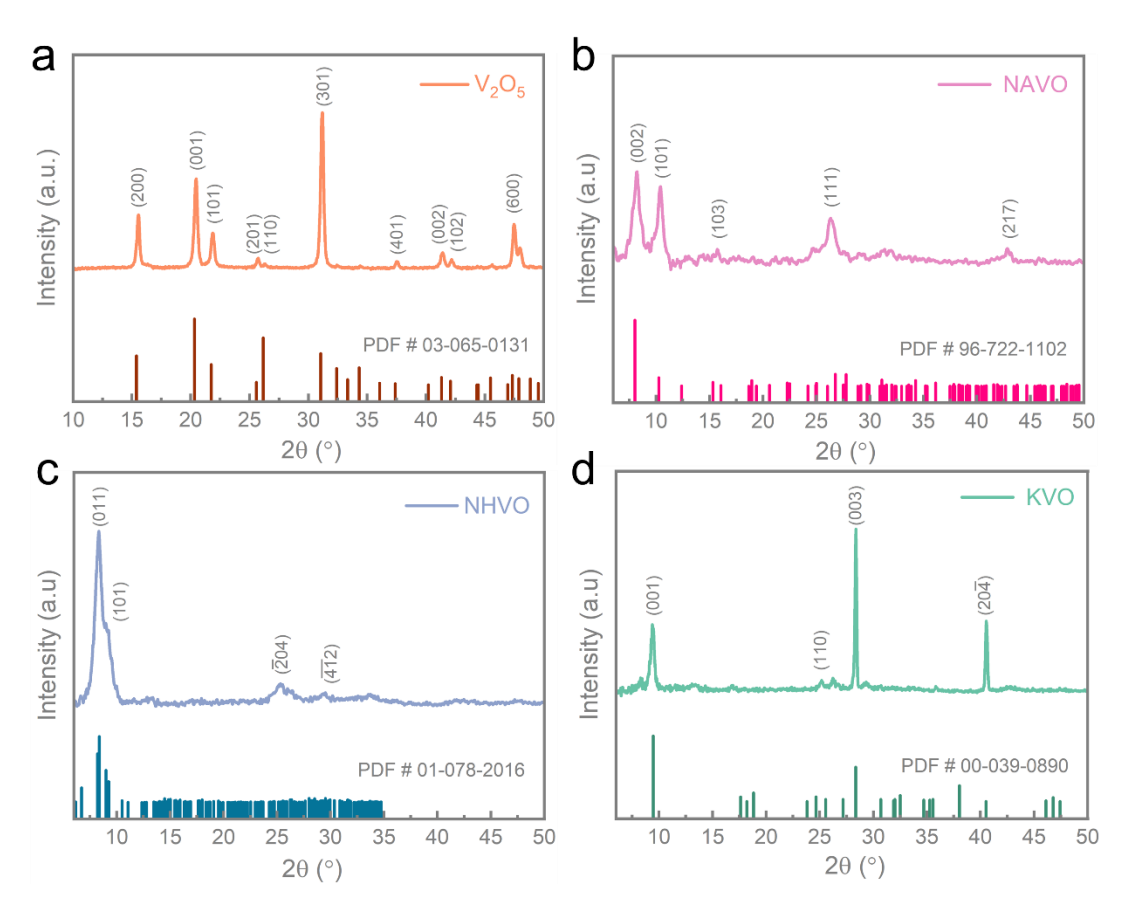


Figure 5.4: XRD patterns of the (a) V₂O₅, (b) NAVO, (c) NHVO and (d) KVO.

Figure 5.4 shows the XRD patterns for the synthesized V_2O_5 , NAVO, NHVO, and KVO samples. The synthesized V_2O_5 exhibits prominent diffraction peaks corresponding to the orthorhombic crystal structure of V_2O_5 with the Pmmn (59) space group (PDF No. 03-065-0131), with reflections at 2θ angles of 15.6° , 20.5° , 21.9° , 31.2° , and 47.5° , associated with the (200), (001), (101), (301), and (600) planes, respectively. For the NAVO sample, the pattern displays peaks characteristic of sodium-doped vanadium oxide (PDF No. 96-722-1102) at 8.2°,

10.4°, 26.3°, and 42.9°, aligning with the (002), (101), (111), and (217) planes. The NHVO sample reveals diffraction peaks attributable to a pure anorthic ammonium vanadium oxide phase (PDF No. 01-078-2016), which has a layered configuration. In the case of KVO, all observed peaks match a monoclinic potassium vanadium oxide phase (PDF No. 00-039-0890), with lattice constants a = 11.657 Å, b = 3.659 Å, and c = 9.460 Å. Additionally, the d-spacing of the (002) plane for NAVO, approximately 11.0 Å, suggests that Na⁺ doping expands the interlayer distance of V_2O_5 , as compared to the original V_2O_5 (d₍₀₀₁₎ = 4.4 Å).

UV–Visible absorption spectroscopy was employed to study the influence of ion doping on the optical characteristics of the samples. Figure 5.5 presents the UV–Vis absorption spectra of the four samples within the wavelength range of 350 to 800 nm. A distinct absorption band appears in the visible region, attributed to electron transfer from oxygen to vanadium (O_{2p} - V_{3d}) in V_2O_5 . ³⁷⁰ With the incorporation of different cations into the lattice, the optical absorption edge shifted towards longer wavelengths, leading to a decrease in the optical band gap. ³⁷¹ The optical band gaps of the undoped and doped samples were determined from Tauc plots using the formula: $(\alpha h v)^{1/2} = B (h v - E_g)$. The calculated band gaps for pristine V_2O_5 , NAVO, NHVO, and KVO were 2.5, 2.43, 2.4, and 1.98 eV, respectively. The reduction in band gap is attributed to lattice expansion due to cation doping and the formation of oxygen vacancies. ³⁷⁰ These structural modifications introduce additional energy levels and facilitate electronic transitions, effectively narrowing the band gap. The calculated band gaps of these samples are relatively consistent with the results presented in the previous section. Minor differences may be attributed to variations in drying temperatures during the sample fabrication process. The overall similarity in results also highlights the reproducibility of the experiment.

Raman spectroscopy provided further insights into the structural details of these samples in Figure 5.6. As for as-synthesized V₂O₅, the detected characteristic Raman bands correspond to stretching vibrations of vanadyl bonds (~995 cm⁻¹), the stretching vibration of V-O bond (B_{2g} mode) and the stretching vibration of V-O-V bond (A_g mode) (around 701 cm⁻¹ and 526 cm⁻¹), the bending vibration of the V-O₍₃₎ bond (484 cm⁻¹), ¹⁰³ the bending vibration of V-O-V bond (A_g mode) (405 cm⁻¹), and bending vibration of V-O (A_g mode) (around 305cm⁻¹), respectively. The peaks at 285 and 198cm⁻¹ derived from the bending vibrations of O-V-O bond (B_{2g} and A_g modes), while the predominant low-wavelength peak, 145 cm⁻¹ was attributed to the skeleton bent vibration (B_{2g} mode). ³⁷² In NAVO fibers, the highest frequency modes located at 142 cm⁻¹ represented the stretching vibrations of particular V-O bonds in the (V1)O6,

(V2)O6, and VO5 polyhedral. 373 The Raman band at 266 cm $^{-1}$ are assigned to the bending δ (V-O-V). 373 The 427 cm $^{-1}$ mode corresponded to the V1-O5-V3 bending vibrations. 374 The stretching vibrations of V3-O7 and the antisymmetric V1-O2-V1 stretching mode locate at 509 and 688 cm $^{-1}$, respectively. 373 The mode at 1003 cm $^{-1}$ originated from the V2-O6. 373 In the sample NHVO, the Raman peaks located at 152 and 512 cm $^{-1}$ matched with O-V-O-V and V3-O, while other three peaks at 264, 407 and 703 cm $^{-1}$ could be ascribed to V2-O of (NH₄)₂V₁₀O₂₅·8 H₂O. 375 Besides, the peaks at 832 cm $^{-1}$ corresponded to an antisymmetric vibration of V-O-V, 376 and the peak at 1027 cm $^{-1}$ can be attributed to V-OH. 375 As for KVO, compared with pristine V₂O₅, the Raman peaks at 995 cm $^{-1}$ disappeared, while the new peaks at 937 and 906 cm $^{-1}$ formed , which can be attributed to the signal of VO $^{3-}$. 377 The peaks at 644, 497, 360 cm $^{-1}$ can be corresponding to the asymmetric, symmetric vibration of V-O-V, the bending δ (VO₂), respectively. 378 Additionally, Geisler *et al.* observed the Raman peaks at 243 and 210 cm $^{-1}$ in K₂O sample. 379

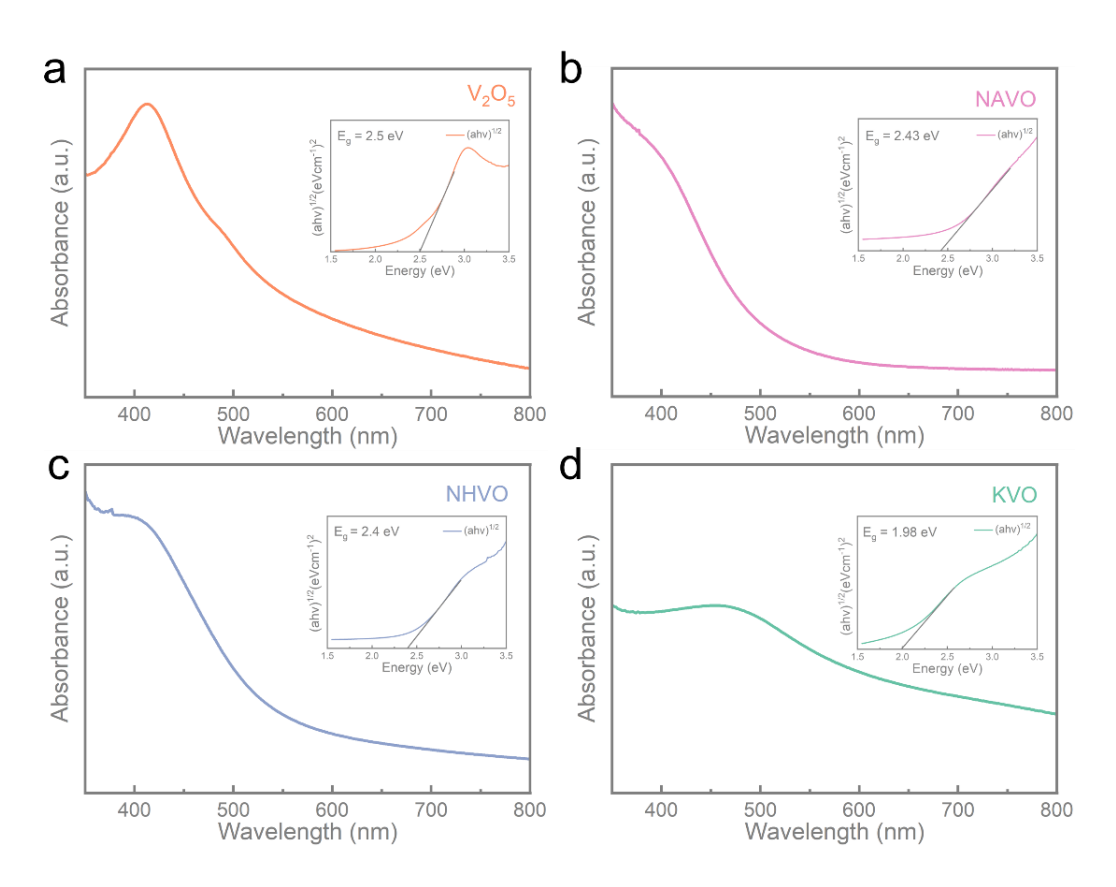


Figure 5.5: UV-Vis absorption spectroscopy of the (a) V_2O_5 , (b) NAVO, (c) NHVO and (d) KVO. Inset: tauc plots of corresponding samples.

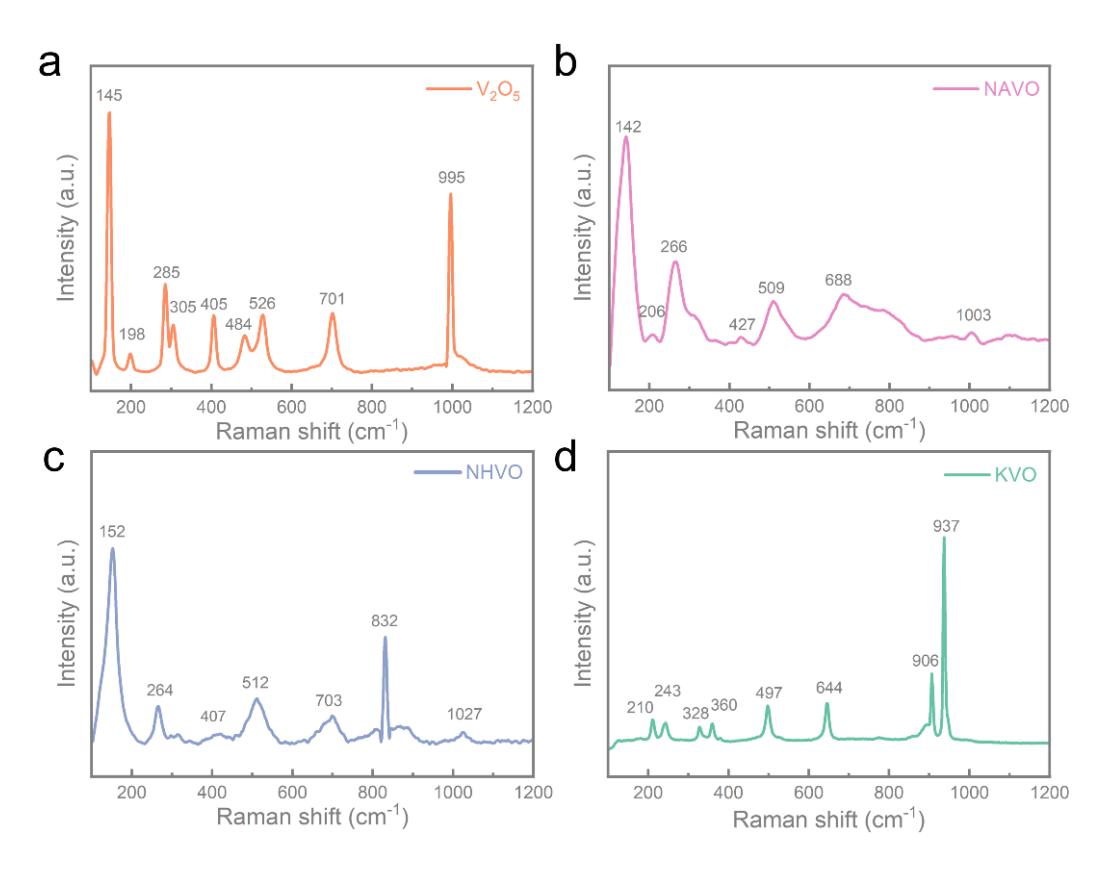


Figure 5.6: Raman spectra of the (a) V₂O₅, (b) NAVO, (c) NHVO and (d) KVO.

The surface chemical composition and elemental valence state of samples V₂O₅, NAVO, NHVO and KVO were analysed using the XPS spectrum shown in Figure 5.7. The XPS V 2p and O 1s spectrum can prove the successful introduction of cation into the V₂O₅ electrode. In detail, the vanadium spectrum (Figure 5.7 (b)) illustrated that characteristic peaks of V₂O₅ at 517.4 and 524.7 eV correspond to V2p_{3/2} and V2p_{1/2} for V⁵⁺ and characteristic peaks at 516.1 and 523.4 eV for V⁴⁺. As for NAVO, the deconvoluted prominent peaks positioned at 517.6 eV $(V2p_{3/2})$ and 525.0 eV $(V2p_{1/2})$ respectively indicating V^{5+} oxidation state, while the peaks at 516.2 (V2p_{3/2}) and 523.5 eV (V2p_{1/2}) indicated V^{4+} oxidation state. In the sample NHVO, the V⁵⁺ oxidation state of V related peaks was identified at 517.6 eV (2p_{3/2}), 524.9 eV (2p_{1/2}), and V^{4+} state-related peak was also identified at 516.8 (2p_{3/2}) and 524.2 eV (2p_{1/2}). For KVO, the peaks corresponding to V $2p_{3/2}$ and V $2p_{1/2}$ for V⁵⁺ appeared at a characteristic binding energy of 517.5 and 524.8 eV, and characteristic peaks at 516.3 and 523.6 eV for V^{4+} . An obvious shift toward high energy from pristine V₂O₅ to cation doped samples embodied the strong electronic interaction between cations and V₂O₅, proving the successful doping of cations. ^{380, 381} The ratio of V⁴⁺ to V⁵⁺ of these four materials was 0.19, 0.87, 0.38 and 0.33, respectively, and NAVO exhibited the highest V⁴⁺ concentration, suggesting that the presence of lower-valence state V⁴⁺

can enhance the conductivity of V_2O_5 , thereby facilitating the intercalation and deintercalation of Li⁺ ions within V_2O_5 . From the XPS results of O 1s (Figure 5.7 (a)), the peak of V_2O_5 at 531.8 eV is ascribed to oxygen vacancy (V_0), while the peaks at 530.3 eV are ascribed to lattice oxygen, respectively. ^{116, 383-385} The two corresponding peaks positioned at 531.7, 530.2 eV for NAVO, 532.1, 530.4 eV for NHVO, and 531.9, 530.2 eV for KVO, respectively. Oxygen vacancies can create additional voids that provide numerous pathways for Li⁺ ions to migrate quickly, aiding in the reversible phase transitions of V_2O_5 during the processes of Li⁺ insertion and extraction. Based on the calculation, the O vacancies concentrations for the four electrodes were 10.7%, 14.5%, 13.0% and 11.5%, respectively, with NAVO showing the highest concentration of oxygen vacancies. Overall, it is believed that the higher V^{4+} ratio could indicate Na⁺ occupies some vanadium sites, forming a certain oxygen vacancy in the NAVO material, which is helpful to increase electrons and mass transfer rate, so as to improve electrochemical performances.

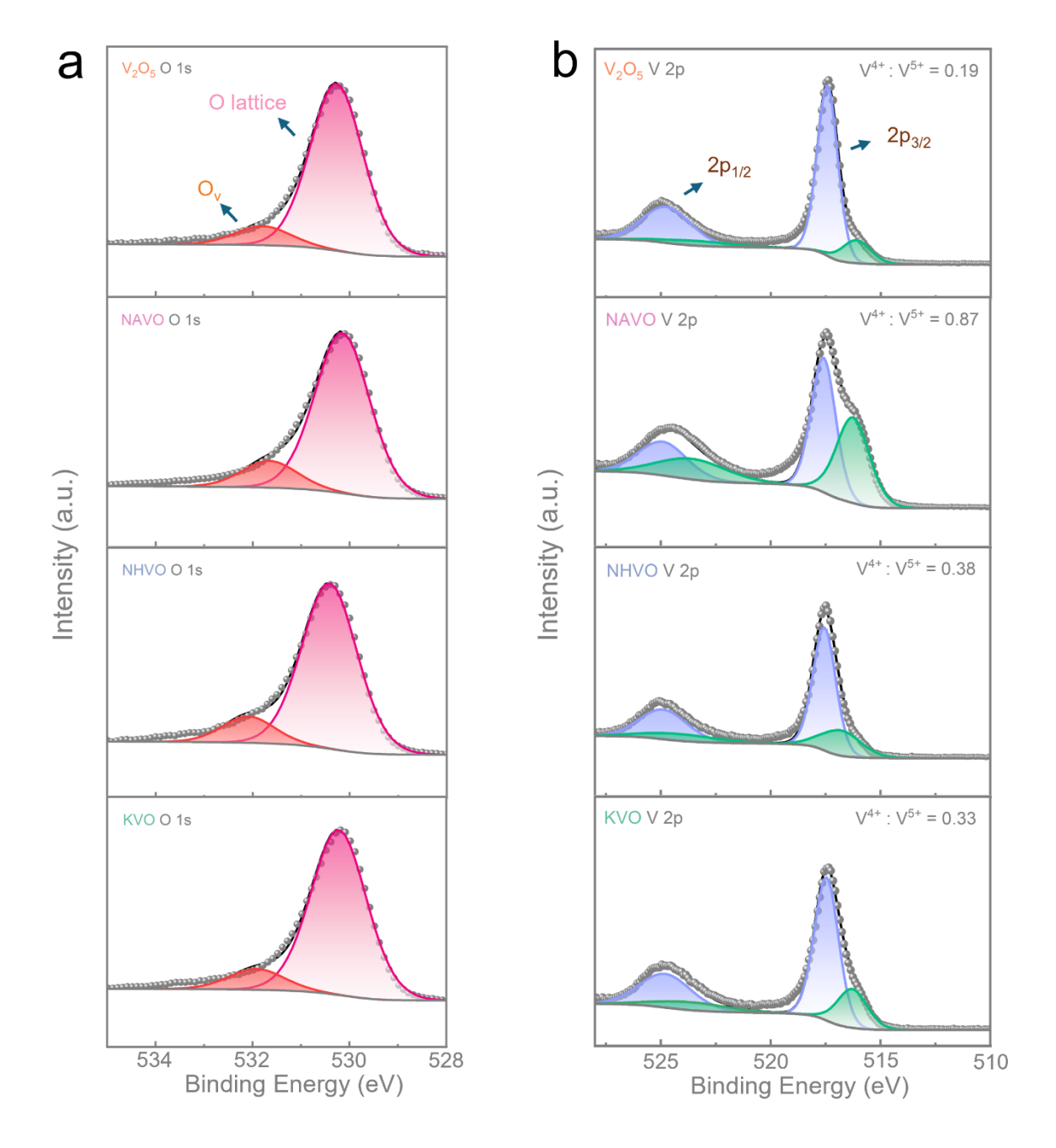


Figure 5.7: XPS spectra of four samples: (a) O 1s and (b) V $2p_{1/2}$ and V $2p_{3/2}$.

5.3.2 Electrochemical Performances

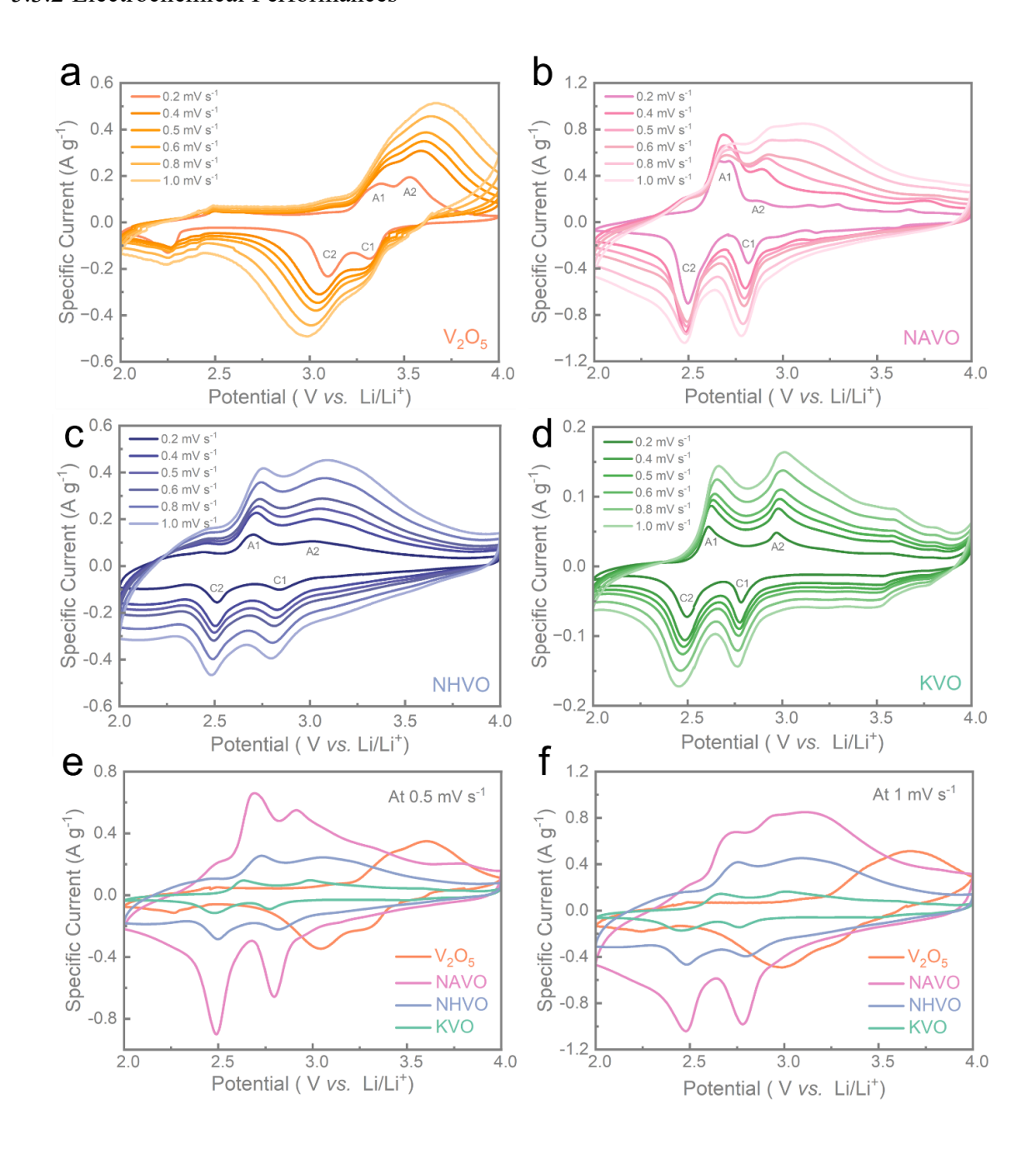


Figure 5.8: CV curves of the (a) V₂O₅, (b) NAVO, (c) NHVO and (d) KVO electrodes recorded at various scan rates ranging from 0.2 to 1.0 mV s⁻¹, within a potential window of 2 to 4 V. A comparison of the CV profiles at scan rates of (e) 0.5 mV s⁻¹ and (f) 1.0 mV s⁻¹ for all samples.

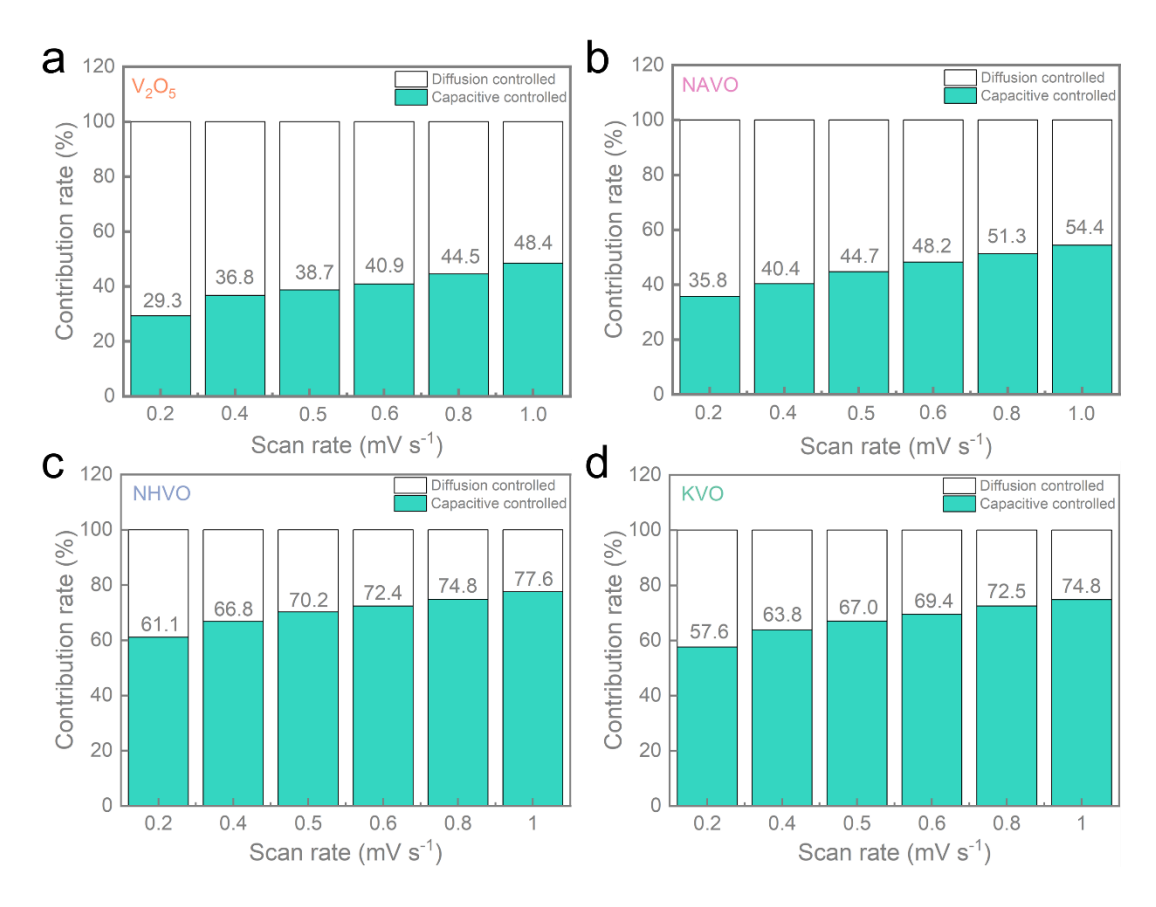


Figure 5.9: The estimated capacity contributions for the (a) V_2O_5 , (b) NAVO, (c) NHVO and (d) KVO electrodes.

Table 5.1: Calculated b-values for anodic and cathodic peaks of V_2O_5 , NAVO, NHVO and KVO.

Material	b value	b value	b value	b value
	Anodic Peak 1	Anodic Peak 2	Cathodic Peak 1	Cathodic Peak 2
V_2O_5	0.513	0.604	0.508	0.508
NAVO		0.887	0.643	
NHVO	0.693	0.900	0.847	0.673
KVO	0.569	0.752	0.639	0.540

Figure 5.8 (a) demonstrated the CV profiles of pristine V_2O_5 nanofibers electrode. Three dominant cathodic peaks at potential of 3.33, 3.10 and 2.26 V are observed, which was attributed to the phase transitions from α -V₂O₅ to ϵ -Li_{0.5}V₂O₅, δ -LiV₂O₅ and γ -Li₂V₂O₅,

respectively. The reduction peaks located around 3.33 and 3.10 V correspond to the intercalation of the first Li^+ in two steps, $V_2O_5 + 0.5Li^+ + 0.5e^- \rightarrow Li_{0.5}V_2O_5$ and $Li_{0.5}V_2O_5 +$ $0.5\text{Li}^+ + 0.5\text{e}^- \rightarrow \text{Li}_{1.0}\text{V}_2\text{O}_5$. The second Li is inserted through one single step around 2.26 V: $Li_{1.0}V_2O_5 + 1.0Li^+ + 1.0e^- \rightarrow Li_{2.0}V_2O_5$. In the subsequent anodic process, three obvious oxidation peaks at potentials of 2.50, 3.37 and 3.54 V can be ascribed to the extraction of the two Li ions and the opposite phase transformations to the cathodic reactions. As shown in Figure 5.8 (b), some main anodic peaks at 2.88 and 2.69 V and cathodic peaks at 2.50 and 2.82 V accompanying several weak peaks (such as 3.29, 3.15 V for oxidation and 3.18 V for reduction) were observed in the sample NAVO, which indicated the complex multistep lithium ions insertion/extraction process. Apart from these peaks, a pair of redox peaks appeared in the high potential region (3.67 V/3.62 V), which can be attributed to the phase transition of the γ/γ system. ^{386, 387} NHVO and KVO had similar redox pairs. As denoted in Figure 5.8 (c-d), (2.70) V/ 2.51 V), (3.02 V/2.84 V) for NHVO and (2.61 V/2.50 V), (2.97 V/2.78 V) for KVO were observed, corresponding to the insertion and desertion process of lithium ions at different sites. As shown in Figure 5.8 (e-f), the NAVO electrodes exhibited the highest redox peak currents at both 0.5 mV s⁻¹ and 1.0 mV s⁻¹, outperforming other cathode materials. This indicated that NAVO had the potential for improved charge storage and electrochemical performance compared to other candidates.

Additionally, Table 5.1 presents the calculated b values for each redox peak of the cathode materials, with values ranging from 0.5 to 1.0. This range suggests that the charge storage mechanism incorporates both diffusion-controlled and capacitive-controlled contributions. Figure 5.9 further illustrates this observation, showing an increase in capacitive contribution percentages as the scan rate rises. Specifically, for V₂O₅, the contribution grew from 29.3% to 48.4%; for NAVO, from 35.8% to 54.4%; for NHVO, from 61.1% to 77.6%; and for KVO, from 57.6% to 74.8%. V₂O₅ and NAVO exhibited a higher degree of diffusion-controlled behaviour, which favours applications like electric vehicles and stationary energy storage due to the potential for enhanced energy density. On the other hand, NHVO and KVO showed a greater capacitive-controlled dominance, making them better suited for high-power applications, such as fast-charging devices and power tools.

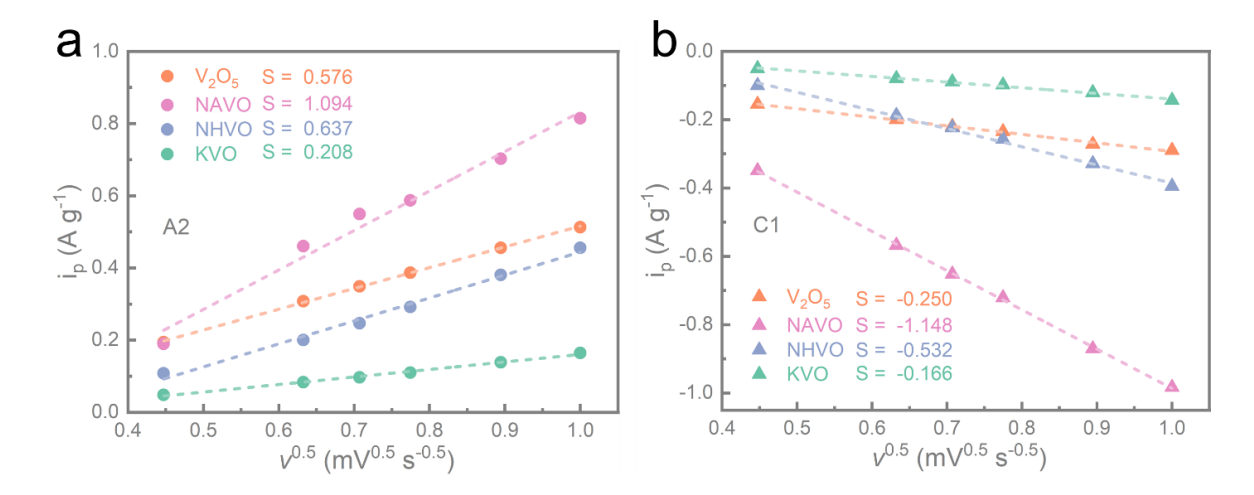


Figure 5.10: Diffusion constant analysis of the V₂O₅, NAVO, NHVO and KVO electrodes for (a) A2 and (b) C1 peaks.

Table 5.2: Slopes for anodic (A1 and A2) and cathodic (C1 and C2) and peaks of V₂O₅, NAVO, NHVO and KVO from the corresponding CV curves.

	Slope			
Materials	A1	A2	C1	C2
V ₂ O ₅	0.381	0.576	-0.250	-0.475
NAVO	0.422	1.094	-1.148	-0.623
NHVO	0.507	0.637	-0.532	-0.554
KVO	0.155	0.208	-0.166	-0.179

Table 5.2 and Figure 5.10 compared the calculated slope values of peak current for the four cathodes. The slope of i_p versus $v^{1/2}$ can suggest the diffusion coefficient of Li⁺ ions within the electrode material, according to the equation $i_p = 0.4463F(F/RT)^{1/2}ACD^{1/2}v^{1/2} = KD^{1/2}v^{1/2}$. Where T represents the cell testing temperature, F is the Faraday constant, C denotes the initial Li⁺ molar concentration in the electrolyte, R is the gas constant, and A signifies the electrode area. ³³² NAVO showed the largest slope, indicating the fastest Li⁺ diffusion rate, which contributed to its superior performance.

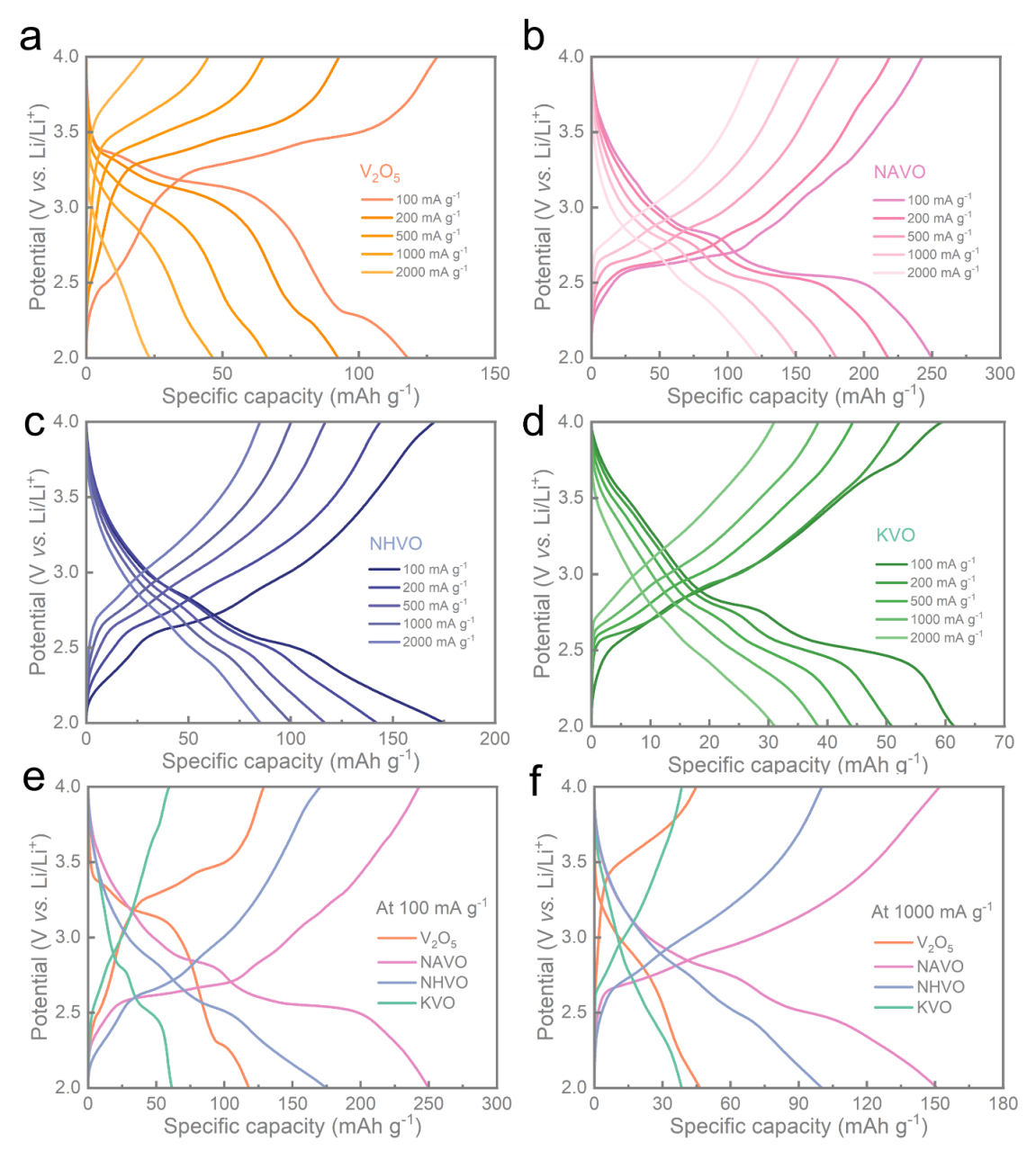


Figure 5.11: GDC curves of the (a) V_2O_5 , (b) NAVO, (c) NHVO and (d) KVO at different specific currents, ranging from 100 to 2000 mA g^{-1} , across the voltage range of 2 to 4 V. Comparative GDC curves of the electrodes at specific currents of (e) 100 and (f) 1000 mA g^{-1} , respectively.

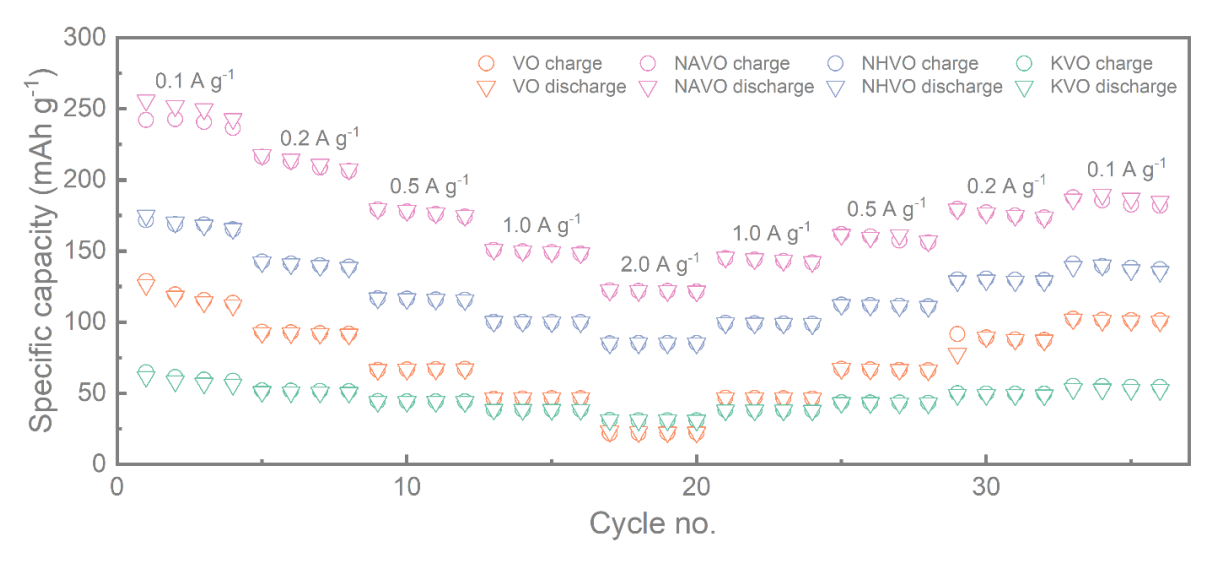


Figure 5.12: Rate tests exhibiting the performance of the electrodes at various current densities.

Figure 5.11 (a-d) displays the GDC profiles for pristine V₂O₅ and its Na⁺-, NH₄⁺-, and K⁺doped versions over a range of current densities from 100 to 2000 mA g⁻¹. The NAVO electrode achieved discharge capacities of 249.1, 216.8, 179.5, 150.2, and 122.0 mAh g⁻¹ at 100, 200, 500, 1000, and 2000 mA g⁻¹, respectively. In contrast, the V₂O₅ nanofiber electrode showed lower discharge capacities, delivering 117, 92.2, 66.0, 46.0, and 22.8 mAh g-1 at the same current densities. For the NHVO electrode, discharge capacity increased from 85.1 to 173.6 mAh g⁻¹ as the current density decreased from 2000 to 100 mA g⁻¹. The KVO electrode exhibited the lowest discharge capacities among the samples, with a peak capacity of only 61.2 mAh g⁻¹ at 100 mA g⁻¹. The plateaus in each sample's GDC curves corresponded well with the cathodic and anodic peaks observed in the CV curves (Figure 5.8). Additionally, Figure 5.11 (e) and (f) provide a comparison of the GDC curves for the four samples at 100 and 1000 mA g⁻¹, respectively, indicating a consistent discharge capacity trend: NAVO > NHVO > V₂O₅ > KVO. Figure 5.12 shows the rate performance of these electrodes, with Na⁺ and NH₄⁺ dopants enhancing capacity at various current densities compared to pristine V₂O₅, suggesting that cation doping can improve the cathode's charge storage. In contrast, the K-doped sample exhibited minimal enhancement, indicating that it did not offer the same performance improvements.

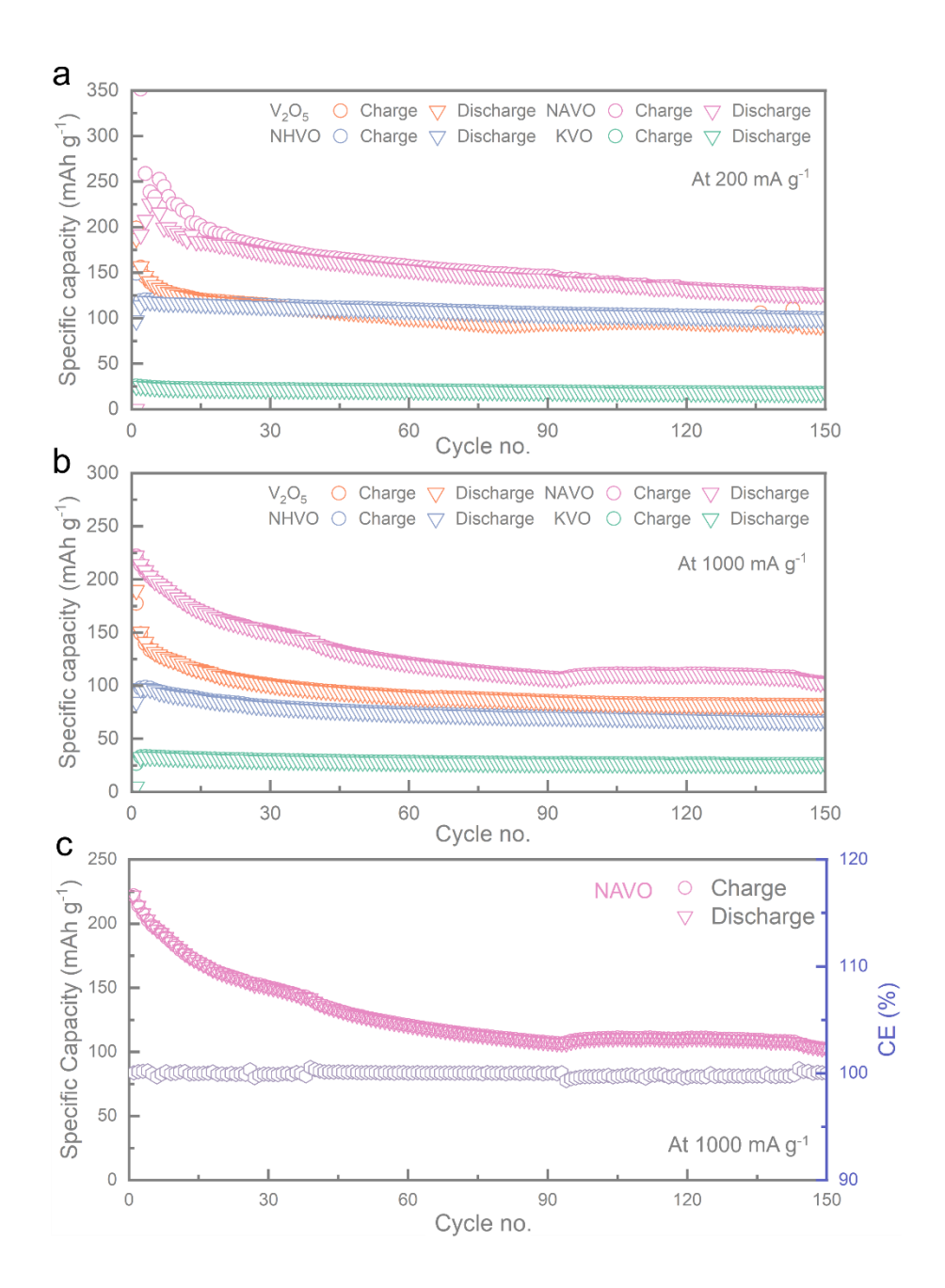


Figure 5.13: Long-term cycling test of V₂O₅, NAVO, NHVO and KVO electrodes at (a) 200, (b) 1000 mA g⁻¹. (c) Long-term cycling test of NAVO, where CE represents Coulombic efficiency in the plot.

Cycling stability remains a critical limitation for V_2O_5 as a cathode material in practical lithium-ion batteries. ³⁶¹ Figure 5.13 illustrates the cycling behaviour of four cathode materials tested at current densities of 200 mA g⁻¹ and 1000 mA g⁻¹ over 150 cycles. Among these, the NAVO electrode demonstrated the highest specific capacity and best cycle stability, while the

KVO electrode exhibited the lowest capacity. At 200 mA g⁻¹, both NAVO and NHVO outperformed pristine V₂O₅; however, at 1000 mA g⁻¹, only NAVO maintained its superior performance, as the other materials showed diminished effectiveness at higher rates. Specifically, NAVO began with an initial specific capacity of 222.1 mAh g⁻¹ at 1000 mA g⁻¹, retaining 150.5 mAh g⁻¹ after 30 cycles, indicating over 67% capacity retention. This capacity drop may be attributed to the formation of a solid electrolyte interphase and irreversible Li⁺ intercalation under deep discharge. From cycle 50 to 150, NAVO's capacity loss rate was only 0.20% per cycle, with a Coulombic efficiency close to 100%, indicating strong cycle stability. NAVO showed both higher capacity and enhanced cycling stability compared to V₂O₅ nanofibers, likely due to the Na⁺ doping effect. This doping expanded the interlayer spacing in V₂O₅, providing more space for charge carriers. Additionally, Na⁺ ions acted as structural pillars, stabilizing the crystal structure during cycling and participating in intercalation and deintercalation, which improved both capacity and conductivity. EIS results (Figure 5.14) confirmed the enhanced conductivity, as the cation-doped electrodes exhibited lower charge transfer resistance (Rct). NHVO had the lowest Rct, while NAVO had the smallest series resistance (R_s).

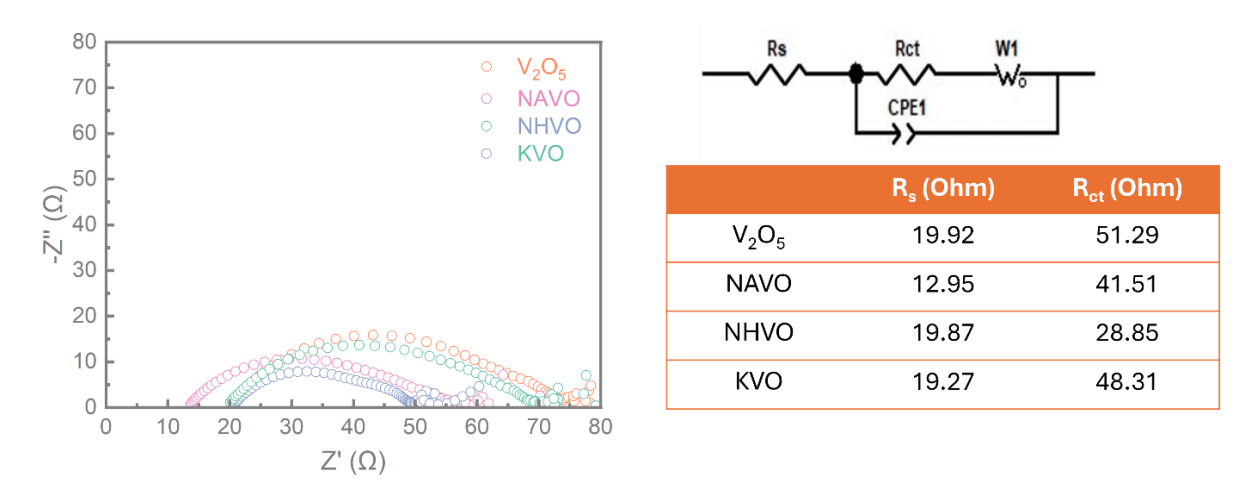


Figure 5.14: Nyquist plots and equivalent circuit model for cells containing V₂O₅, NAVO, NHVO and KVO.

5.4 Summary

In summary, four types of V₂O₅-based nanofiber cathode materials were successfully synthesized using hydrothermal methods, with each incorporating different cation dopants. The introduction of cations led to an increase in the interlayer spacing, a higher concentration of oxygen vacancies, and an elevated V⁴⁺/V⁵⁺ ratio. These modifications collectively contributed to enhanced Li⁺ ion diffusion, improved capacity, stable cycling performance, and reduced charge transfer resistance. Among the synthesized materials, NAVO demonstrated outstanding electrochemical performance, achieving discharge capacities of 249.1 and 122.0 mAh g⁻¹ at current densities of 100 and 2000 mA g⁻¹, respectively. It also showed exceptional cycling stability, with an initial specific capacity of 222.1 mAh g⁻¹ at 1000 mA g⁻¹, retaining 150.5 mAh g-1 after 30 cycles (representing over 67% capacity retention). Furthermore, NAVO exhibited rapid Li⁺ ion diffusion and minimal capacity loss, maintaining a Coulombic efficiency close to 100%. The structural improvements brought by Na⁺ doping played a significant role in enhancing the stability and conductivity of the V₂O₅ lattice, allowing NAVO to sustain high capacity even at elevated current densities. These findings underscore the potential of cation doping as an effective strategy for advancing the design of high-performance cathode materials. By modifying the crystal structure and electronic properties of V₂O₅ through strategic doping, this study offers a pathway toward the development of lithium-ion batteries with improved energy density, power performance, and cycle life. The insights gained from this work contribute to the growing body of knowledge on enhancing cathode materials and hold promise for future applications in high-energy and high-power lithium-ion batteries, particularly in fields requiring both durability and rapid charging capabilities, such as electric vehicles and portable electronics.

Chapter 6

Conclusions and Outlook

6.1 Conclusions

As global energy demand continues to rise, there is an urgent need for sustainable and ecofriendly energy storage solutions like lithium-ion and zinc-ion batteries. However, current lithium-ion batteries face challenges such as high production costs, limited energy and power densities, and safety issues. Similarly, zinc-ion batteries struggle with limitations like low capacity, poor long-term stability, and low ionic and electronic conductivity. This PhD thesis explores advanced approaches including hydrogenation, doping, and defect engineering to improve the electrochemical and optical performance of V₂O₅-based cathode materials. By thoroughly analysing the physicochemical properties and investigating charge storage mechanisms, the thesis emphasizes the importance of V₂O₅ modifications in enhancing battery performance. The insights gained provide guidance for the future development of highperformance, rechargeable metal-ion batteries. This research encompasses three projects: improving the optical and electrochemical properties of hydrogenated V₂O₅ for photoaccelerated lithium-ion batteries, creating pre-doped V₂O₅-based materials for highperformance zinc-ion batteries, and developing cation-doped V₂O₅ electrodes with oxygen vacancies for lithium-ion batteries. The specific aims and outcomes are summarized below.

Chapter 3 discusses a hydrogenation strategy to enhance photocathode performance in photo-assisted lithium-ion batteries. Hydrogenation introduces oxygen vacancies and hydroxyl groups into the V₂O₅ structure, boosting conductivity, photo-response, and ion diffusion. The hydrogenated V₂O₅ (H:V₂O₅) showed better electrochemical performance compared to pristine V₂O₅, with a 43% and 41% increase in specific capacity under dark and illuminated conditions, respectively, at 2000 mA g⁻¹. Enhanced photocurrent generation was linked to defect mid-gap states, associated with oxygen-related defects and hydroxyl groups, which increased optical absorption and photoactivity. DFT simulations highlighted the role of hydroxyl species in charge storage.

In Chapter 4, a doping strategy is introduced to improve the performance of V₂O₅-based cathodes in zinc-ion batteries. Pre-doping with cations such as NH₄⁺, Na⁺, and K⁺ enhanced

charge storage, with NH₄⁺ improving interlayer spacing and boosting the V⁴⁺/V⁵⁺ redox couple. This NH₄⁺-doped V₂O₅ (NH₄-V₂O₅) achieved a high specific capacity of 310.8 mAh g⁻¹ at 100 mA g⁻¹ and significantly reduced charge transfer resistance (~17.9 Ω), compared to 112.5 mAh g⁻¹ and ~65.58 Ω in pristine V₂O₅. This study provides critical insights into pre-doped cation effects for designing high-capacity cathode materials in zinc-ion batteries.

Chapter 5 investigates defect engineering to understand how cation doping improves V₂O₅-based electrodes in lithium-ion batteries. Cation-doped V₂O₅ materials, synthesized via hydrothermal and vacuum drying processes, showed that doping induced oxygen vacancies, enhancing ion diffusion and charge transfer. Na-doped V₂O₅ exhibited high discharge capacities (249.1 mAh g⁻¹ at 100 mA g⁻¹), excellent cycling stability, and rapid Li⁺ diffusion. With a retention rate of over 67% after 30 cycles and consistent Coulombic efficiency near 100%, the findings underscore the role of cation doping in optimizing V₂O₅ as a high-efficiency lithium-ion battery cathode material.

6.2 Outlook

For V₂O₅-based cathode materials, the electrochemical performance can be significantly enhanced via hydrogenation, doping and defect engineering in lithium-ion batteries and zincion batteries. But there are still remaining issues. For example, there is still a large space to increase the conductivity and ionic diffusion, enhance battery capacity, boost structural stability, lower capacity fading after long-term cycling. ^{148, 153, 388} As for photo-accelerated batteries, its photovoltaic conversion efficiency is still low. ¹⁹ Thus, based on the findings presented in this thesis, there are still critical areas requiring further development and refinement to optimize overall performance:

- 1) For synthetic process, the optimization for experimental conditions, such as temperature, time, pH value, for each material can be refined to explore the relationship of structure and performance, thus finding an optimal cathode with superior performance.
- 2) For characterization, some advanced techniques can be additionally employed. For example, X-ray absorption spectroscopy could characterize structural properties and

electronic states of the electrodes and further evaluate the concentration of V⁴⁺ in the cation-doped samples. Electron paramagnetic resonance (EPR) can be used to assess the presence of oxygen vacancies. Galvanostatic intermittent titration technique (GITT) could provide insights into the kinetics of ion transport and the thermodynamics of the electrode materials during the charge and discharge processes. Beyond using TEM to observe structural deformations after long-term cycling, techniques such as SEM, XPS, and XRD might be utilized to analyse morphological and structural changes, aiding in understanding material degradation mechanisms.

- 3) In the lab, the electrochemical performance was evaluated by coin-cells, but coin-cells have some limitations such as low loading mass, flooded electrolyte and high N/P (capacity ratio of negative electrode to positive electrode) ratios, which may not accurately represent practical electrode conditions. ³⁸⁹ To obtain more relevant performance metrics, battery assembly formats such as pouch cells or cylindrical batteries should be considered for future testing.
- 4) For photo-accelerated lithium-ion batteries, the combination of solar and lithium-ion battery technologies in a single device is still challenging because of recombination and decomposition reactions. Current device designs limit the exposure of active material to light, necessitating the development of new setups for more precise performance assessment under illumination.
- 5) Additionally, while hydrogenated V₂O₅ showed enhanced performance, cation-doped materials were evaluated under illuminated conditions, their performance did not improve and, in some cases, even deteriorated, indicating a need to explore the underlying mechanisms that contribute to increased photocurrent. Moreover, photo-degradation and/or side reactions with electrolytes need to be considered to increase the cycling life of the photo-batteries.

Furthermore, to enhance the practical performance of lithium-ion batteries and zinc-ion batteries, future research should focus on several critical aspects:

In terms of lithium-ion batteries, the key factors driving its development for efficient energy applications include energy density, cost, lifespan, and safety. Achieving high-energy anodes and cathodes for these applications is challenged by issues such as (1) aging and degradation, (2) the need for enhanced safety, (3) material costs, and (4) recyclability. Temperature plays a

critical role in all chemical and side reactions within the cell and operating outside the optimal temperature range of 15 – 35 °C can significantly impair performance. ³⁹⁰ In extreme cases, it can trigger self-heating and thermal runaway, potentially leading to catastrophic failure. Besides, recycling the ever-increasing quantities of spent batteries has become a major challenge that urgently needs to be resolved. The recycling Li, Co, Ni from lithium-ion batteries is of importance because it reduces the mining of limited resources and prevents harmful emissions into the soil, contributing to a greener economy and energy systems.

In terms of zinc-ion batteries, advancing toward higher energy density is impeded by several critical challenges related to finding optimal cathode materials that meet following requirements: 1) high discharge capacity; 2) elevated nominal voltage; 3) cathode structures that can effectively accommodate Zn²⁺ ions while facilitating their typically sluggish diffusion kinetics; 4) robust crystal structures for long extended cycling; 5) economic and environmental viability. ^{391, 392} Unfortunately, existing cathode materials do not fully align with these criteria, currently, many promising cathode materials, such as V₂O₅ and MnO₂, have been extensively studied, their performance with zinc anodes is not always satisfactory due to dissolution and side reactions in aqueous electrolytes. Also, vanadium-based cathodes face structural degradation and active materials dissolution. These obstacles highlight the need for continued research and innovation to achieve the desired improvements in energy density and cycling life. Addressing these material-related challenges will be crucial to unlock the full potential of zincion batteries for future energy storage applications. Moreover, aqueous electrolytes face operational challenges at subzero temperatures, as water inevitably freezes, preventing the battery from functioning properly. To address these issues, adding effective HER inhibitors, utilizing optimal electrolyte concentration to decrease the freezing point, and applying the flowing electrolyte could be effective solutions. In addition, improving the stability and durability of the zinc electrode is essential.

Finally, moving from small-scale prototypes to large-scale, commercially viable energy storage systems poses a significant challenge for zinc-ion batteries. Achieving practical implementation for grid-scale energy storage requires extensive future research. Key areas of focus include scaling up manufacturing processes while maintaining performance, enhancing the stability and safety of zinc-ion batteries systems, and developing cost-effective, efficient production methods. Additionally, optimizing electrolyte formulations and designing durable,

high-capacity cathode materials that perform consistently under real-world conditions will be crucial for the widespread adoption of zinc-ion batteries in large-scale energy storage applications.

Reference

(1) United Nations. Overview of world population.

https://www.un.org/en/global-issues/population.

(2) ExxonMobil. Energy demand: Three drivers.

https://corporate.exxonmobil.com/what-we-do/energy-supply/global-outlook/energy-demand#Transportation (2024).

- (3) Statista Research Department. Report on the energy global market of the recent years. https://www.statista.com/markets/408/topic/436/energy/ (2024).
- (4) IEA. Climate Change.

https://www.iea.org/topics/climate-change (2023).

(5) NASA Global Climate Change. Carbon Dioxide.

https://climate.nasa.gov/vital-signs/carbon-dioxide/ (2024).

(6) UN. The Paris Agreement.

https://www.un.org/en/climatechange/paris-

agreement#:~:text=substantially%20reduce%20global%20greenhouse%20gas,and%20impact s%20of%20climate%20change.

- (7) United Nations Climate Change. COP 28 UN Climate Change Conference. https://unfccc.int/cop28 (2023).
- (8) CNESA. CNESA Global Energy Storage Market Analysis—2020.Q2 (Summary). https://en.cnesa.org/latest-news/2020/9/26/cnesa-global-energy-storage-market-analysis2020q2-summary#:~:text=Q2%20(Summary),-

CNESA%20Admin&text=As%20of%20the%20end%20of,compared%20to%20Q2%20of%202019. (2022).

(9) Statista Research Department. Forecast battery energy storage market value worldwide from 2023 to 2028.

 $https://www.statista.com/statistics/1307133/forecast-battery-energy-storage-market-value/\#: \sim: text= The \%20 global \%20 battery \%20 energy \%20 storage, battery \%20 storage \%20 mark et \%20 in \%202026. (2023).$

(10) Statista. Distribution of electrochemical energy storage projects worldwide in 2022, by technology.

https://www.statista.com/statistics/1360525/electrochemical-energy-storage-projects-share-by-technology-worldwide/#statisticContainer (2023).

- (11) Hu, P.; Hu, P.; Vu, T. D.; Li, M.; Wang, S.; Ke, Y.; Zeng, X.; Mai, L.; Long, Y. Vanadium oxide: phase diagrams, structures, synthesis, and applications. *Chemical Reviews* **2023**, *123* (8), 4353-4415.
- (12) Langeslay, R. R.; Kaphan, D. M.; Marshall, C. L.; Stair, P. C.; Sattelberger, A. P.; Delferro, M. Catalytic applications of vanadium: a mechanistic perspective. *Chemical reviews* **2018**, *119* (4), 2128-2191.
- (13) Lamsal, C.; Ravindra, N. M. Vanadium oxides: synthesis, properties, and applications. *Semiconductors: synthesis, properties and applications* **2019**, 127-218.
- (14) Wriedt, H. The OV (oxygen-vanadium) system. *Bulletin of Alloy Phase Diagrams* **1989**, *10* (3), 271-277.
- (15) Zavalij, P. Y.; Whittingham, M. S. Structural chemistry of vanadium oxides with open frameworks. *Acta Crystallographica Section B: Structural Science* **1999**, *55* (5), 627-663.
- (16) Le, T. K.; Kang, M.; Kim, S. W. A review on the optical characterization of V₂O₅ micronanostructures. *Ceramics International* **2019**, *45* (13), 15781-15798.
- (17) Schneider, K. Optical properties and electronic structure of V₂O₅, V₂O₃ and VO₂. *Journal of Materials Science: Materials in Electronics* **2020**, *31* (13), 10478-10488.
- (18) Zhai, T.; Liu, H.; Li, H.; Fang, X.; Liao, M.; Li, L.; Zhou, H.; Koide, Y.; Bando, Y.; Golberg, D. Centimeter-Long V₂O₅ Nanowires: From Synthesis to Field-Emission, Electrochemical, Electrical Transport, and Photoconductive Properties. *Advanced Materials* **2010**, *23* (22), 2547-2552.
- (19) Lu, Y.; Andersen, H.; Wu, R.; Ganose, A. M.; Wen, B.; Pujari, A.; Wang, T.; Borowiec, J.; Parkin, I. P.; De Volder, M. Hydrogenated V₂O₅ with Improved Optical and Electrochemical Activities for Photo-Accelerated Lithium-Ion Batteries. *Small* **2024**, *20* (14), 2308869.
- (20) Dhoundiyal, H.; Das, P.; Bhatnagar, M. C. Electrical and magnetic properties of V₂O₅ microstructure formed by self-assembled nanorods. *Physica B: Condensed Matter* **2021**, *603*, 412622.
- (21) Yang, Z.; Ko, C.; Ramanathan, S. Oxide electronics utilizing ultrafast metal-insulator transitions. *Annual Review of Materials Research* **2011**, *41* (1), 337-367.
- (22) Brahlek, M.; Zhang, L.; Lapano, J.; Zhang, H.-T.; Engel-Herbert, R.; Shukla, N.; Datta, S.; Paik, H.; Schlom, D. G. Opportunities in vanadium-based strongly correlated electron systems. *MRS Communications* **2017**, *7* (1), 27-52.

- (23) Liu, M.; Su, B.; Tang, Y.; Jiang, X.; Yu, A. Recent advances in nanostructured vanadium oxides and composites for energy conversion. *Advanced Energy Materials* **2017**, *7* (23), 1700885.
- (24) Wu, C.; Feng, F.; Xie, Y. Design of vanadium oxide structures with controllable electrical properties for energy applications. *Chemical Society Reviews* **2013**, *42* (12), 5157-5183.
- (25) Chang, T.-C.; Cao, X.; Bao, S.-H.; Ji, S.-D.; Luo, H.-J.; Jin, P. Review on thermochromic vanadium dioxide based smart coatings: from lab to commercial application. *Advances in Manufacturing* **2018**, *6*, 1-19.
- (26) Kainulainen, T.; Niemelä, M.; Krause, A. Ethene hydroformylation on Co/SiO₂ catalysts. *Catalysis letters* **1998**, *53*, 97-101.
- (27) Weckhuysen, B. M.; Keller, D. E. Chemistry, spectroscopy and the role of supported vanadium oxides in heterogeneous catalysis. *Catalysis Today* **2003**, *78* (1-4), 25-46.
- (28) Robinson, W. R. High-temperature crystal chemistry of V₂O₃ and 1% chromium-doped V₂O₃. *Acta Crystallographica Section B: Structural Crystallography and Crystal Chemistry* **1975**, *31* (4), 1153-1160.
- (29) Xu, X.; Xiong, F.; Meng, J.; Wang, X.; Niu, C.; An, Q.; Mai, L. Vanadium-based nanomaterials: a promising family for emerging metal-ion batteries. *Advanced Functional Materials* **2020**, *30* (10), 1904398.
- (30) Zhu, K.; Wei, S.; Shou, H.; Shen, F.; Chen, S.; Zhang, P.; Wang, C.; Cao, Y.; Guo, X.; Luo, M. Defect engineering on V₂O₃ cathode for long-cycling aqueous zinc metal batteries. *Nature Communications* **2021**, *12* (1), 6878.
- (31) Feinleib, J.; Paul, W. Semiconductor-to-metal transition in V₂O₃. *Physical Review* **1967**, 155 (3), 841.
- (32) Sahoo, S.; Jana, A.; Bagri, A.; Majumder, S.; Rajput, P.; Jha, S. N.; De Groot, F. M.; Choudhary, R. J.; Phase, D. M. Realizing low-temperature charge-transfer-type insulating ground state in strained V₂O₃ thin film. *ACS Applied Electronic Materials* **2022**, *4* (6), 3036-3048.
- (33) Grygiel, C.; Pautrat, A.; Rodiere, P. Galvanomagnetic properties and noise in a barely metallic film of V₂O₃. *Physical Review B—Condensed Matter and Materials Physics* **2009**, 79 (23), 235111.
- (34) Trastoy, J.; Camjayi, A.; Del Valle, J.; Kalcheim, Y.; Crocombette, J.-P.; Gilbert, D. A.; Borchers, J.; Villegas, J.; Ravelosona, D.; Rozenberg, M. Magnetic field frustration of the metal-insulator transition in V₂O₃. *Physical Review B* **2020**, *101* (24), 245109.

- (35) Hu, L.; Xie, C.; Zhu, S.; Zhu, M.; Wei, R.; Tang, X.; Lu, W.; Song, W.; Dai, J.; Zhang, R. Unveiling the mechanisms of metal-insulator transitions in V₂O₃: The role of trigonal distortion. *Physical Review B* **2021**, *103* (8), 085119.
- (36) Liu, J.; Chen, W. Mechanical Bending Strain-Actuated Modulation of Metal–Insulator Transition Temperature in Flexible Epitaxial V₂O₃ Films. *ACS Applied Electronic Materials* **2024**, *6* (5), 3666-3675.
- (37) Thees, M.; Lee, M.-H.; Bouwmeester, R. L.; Rezende-Gonçalves, P. H.; David, E.; Zimmers, A.; Fortuna, F.; Frantzeskakis, E.; Vargas, N. M.; Kalcheim, Y. Imaging the itinerant-to-localized transmutation of electrons across the metal-to-insulator transition in V₂O₃. *Science advances* **2021**, *7* (45), eabj1164.
- (38) Lin, W.; Zhang, H.; Kalcheim, Y.; Zhou, X.; Yang, F.; Shi, Y.; Feng, Y.; Wang, Y.; Huang, J.; Schuller, I. K. Direct visualization of percolating metal-insulator transition in V₂O₃ using scanning microwave impedance microscopy. *Science China Physics, Mechanics & Astronomy* **2022**, *65* (9), 297411.
- (39) Qi, B.; Gunnlaugsson, H.; Ólafsson, S.; Gislason, H.; Thorsteinsson, E.; Arnalds, U.; Mantovan, R.; Unzueta, I.; Zyabkin, D.; Ram, K. B. Metal-insulator transition in crystalline V₂O₃ thin films probed at atomic-scale using emission Mössbauer spectroscopy. *Thin Solid Films* **2020**, *714*, 138389.
- (40) Tranchant, A.; Messina, R.; Perichon, J. Mechanism of electrochemical reduction of vanadium oxides. *Journal of Electroanalytical Chemistry and Interfacial Electrochemistry* **1980**, *113* (2), 225-232.
- (41) Li, H.; Balaya, P.; Maier, J. Li-storage via heterogeneous reaction in selected binary metal fluorides and oxides. *Journal of the Electrochemical Society* **2004**, *151* (11), A1878.
- (42) Jin, T.; Li, H.; Li, Y.; Jiao, L.; Chen, J. Intercalation pseudocapacitance in flexible and self-standing V₂O₃ porous nanofibers for high-rate and ultra-stable K ion storage. *Nano Energy* **2018**, *50*, 462-467.
- (43) Sun, Y.; Jiang, S.; Bi, W.; Wu, C.; Xie, Y. Highly ordered lamellar V₂O₃-based hybrid nanorods towards superior aqueous lithium-ion battery performance. *Journal of Power Sources* **2011**, *196* (20), 8644-8650.
- (44) Luo, H.; Wang, B.; Wang, F.; Yang, J.; Wu, F.; Ning, Y.; Zhou, Y.; Wang, D.; Liu, H.; Dou, S. Anodic oxidation strategy toward structure-optimized V₂O₃ cathode via electrolyte regulation for Zn-ion storage. *Acs Nano* **2020**, *14* (6), 7328-7337.

- (45) Deng, Q.; Wang, L.; Li, J.; Cheng, Q.; Liu, X.; Chen, C.; Zhang, Q.; Zhong, W.; Wang, H.; Wu, L. Constructing oxygen-deficient V₂O₃@ C nanospheres for high performance potassium ion batteries. *Chinese Chemical Letters* **2023**, *34* (3), 107372.
- (46) Li, L.; Liao, S.; Dong, G.; Jiang, K.; Liu, Y.; Zhang, C.; Yan, J.; Ye, K.; Yao, J.; Wang, G. V₂O₃ nanoparticles anchored on an interconnected carbon nanosheet network toward high-performance sodium-ion batteries. *ACS Applied Energy Materials* **2022**, *5* (10), 12707-12715. (47) Li, L.; Wang, C.; Zhang, C.; Cao, X.; Bai, J.; Li, R. Yolk-shell V₂O₃/nitrogen-doped carbon spheres as an ultra-long life anode for half/full sodium-ion batteries. *Journal of Energy Storage* **2023**, *66*, 107504.
- (48) Jang, G.; Joe, Y. S.; Lee, S. J.; Cho, H. G.; Baek, S. H.; Xiong, P.; Shin, K. H.; Yeon, J. S.; Kang, M. S.; Oh, S. H. Crystal reconstruction of V₂O₃/carbon heterointerfaces via anodic hydration for ultrafast and reversible Mg-ion battery cathodes. *InfoMat* **2024**, *6* (3), e12517.
- (49) Ge, Y.; He, T.; Wang, Z.; Han, D.; Li, J.; Wu, J.; Wu, J. Chemical looping oxidation of CH4 with 99.5% CO selectivity over V₂O₃-based redox materials using CO₂ for regeneration. *AIChE Journal* **2020**, *66* (1), e16772.
- (50) Zhang, Y.; Zhang, J.; Nie, J.; Zhong, Y.; Liu, X.; Huang, C. Facile synthesis of V₂O₃/C composite and the effect of V₂O₃ and V₂O₃/C on decomposition of ammonium perchlorate. *Micro & Nano Letters* **2012**, *7* (8), 782-785.
- (51) Hu, M.; Huang, J.; Zhang, S.; Liu, Z.; Li, Q.; Yang, M.; Li, H.; Goto, T.; Tu, R. In situ synthesis of V₂O₃@ Ni as an efficient hybrid catalyst for the hydrogen evolution reaction in alkaline and neutral media. *International Journal of Hydrogen Energy* **2021**, *46* (13), 9101-9109.
- (52) Zhou, J.; Xiao, H.; Weng, W.; Gu, D.; Xiao, W. Interfacial confinement of Ni- V₂O₃ in molten salts for enhanced electrocatalytic hydrogen evolution. *Journal of Energy Chemistry* **2020**, *50*, 280-285.
- (53) Xu, H.; Liu, L.; Gao, J.; Du, P.; Fang, G.; Qiu, H.-J. Hierarchical nanoporous V₂O₃ Nanosheets anchored with alloy nanoparticles for efficient electrocatalysis. *ACS applied materials & interfaces* **2019**, *11* (42), 38746-38753.
- (54) Zhang, H.; Qian, G.; Chen, X.; Jiang, W.; Yu, T.; Wang, Y.; Luo, L.; Yin, S. V₂O₃-decorated spinel CoFe₂O₄ with carbon-encapsulated mesoporous nanosheets for efficient water splitting. *ACS Sustainable Chemistry & Engineering* **2021**, *9* (2), 980-986.

- (55) Pan, X.; Ren, G.; Hoque, M. N. F.; Bayne, S.; Zhu, K.; Fan, Z. Fast supercapacitors based on graphene-bridged V₂O₃/VO_x core–shell nanostructure electrodes with a power density of 1 MW kg⁻¹. *Advanced Materials Interfaces* **2014**, *I* (9), 1400398.
- (56) Hassan, N.; Riaz, J.; Qureshi, M. T.; Razaq, A.; Rahim, M.; Toufiq, A. M.; Shakoor, A. Vanadium oxide (V₂O₃) for energy storage applications through hydrothermal route. *Journal of Materials Science: Materials in Electronics* **2018**, *29*, 16021-16026.
- (57) Yan, Y.; Li, B.; Guo, W.; Pang, H.; Xue, H. Vanadium based materials as electrode materials for high performance supercapacitors. *Journal of Power Sources* **2016**, *329*, 148-169.
- (58) Andersson, G. Studies on vanadium oxides. Acta chem. scand 1954, 8 (9), 1599-1606.
- (59) Gray, M.; Kershaw, R.; Croft, W.; Dwight, K.; Wold, A. Crystal chemistry of V₃O₅ and related structures. *Journal of Solid State Chemistry* **1986**, *62* (1), 57-63.
- (60) Chen, D.; Tan, H.; Rui, X.; Zhang, Q.; Feng, Y.; Geng, H.; Li, C.; Huang, S.; Yu, Y. Oxyvanite V₃O₅: A new intercalation-type anode for lithium-ion battery. *InfoMat* **2019**, *1* (2), 251-259.
- (61) Wan, Q.; Zhang, Y.; Qi, Q.; Feng, H.; Feng, Y.; Bai, F.; Zhang, C.; Hu, J. Hydrothermal synthesis of FeCoNi/ V₃O₅ heterojunctions as highly efficient electrocatalysts for the oxygen evolution reaction. *Materials Letters* **2024**, *365*, 136485.
- (62) Abdullah, H.; Jhuang, S.-J.; Shuwanto, H.; Kuo, D.-H. Nickel-doped V₃O₅ pseudocapacitive cathode with a superb charge storage. *Journal of Energy Storage* **2022**, *55*, 105435.
- (63) Lee, S.; Ivanov, I. N.; Keum, J. K.; Lee, H. N. Epitaxial stabilization and phase instability of VO₂ polymorphs. *Scientific reports* **2016**, *6* (1), 19621.
- (64) Li, M.; Magdassi, S.; Gao, Y.; Long, Y. Hydrothermal synthesis of VO₂ polymorphs: advantages, challenges and prospects for the application of energy efficient smart windows. *Small* **2017**, *13* (36), 1701147.
- (65) Wang, S.; Jiang, T.; Meng, Y.; Yang, R.; Tan, G.; Long, Y. Scalable thermochromic smart windows with passive radiative cooling regulation. *Science* **2021**, *374* (6574), 1501-1504.
- (66) Tang, K.; Dong, K.; Li, J.; Gordon, M. P.; Reichertz, F. G.; Kim, H.; Rho, Y.; Wang, Q.; Lin, C.-Y.; Grigoropoulos, C. P. Temperature-adaptive radiative coating for all-season household thermal regulation. *Science* **2021**, *374* (6574), 1504-1509.
- (67) Cen, Y.; Li, S.; Zhou, Y.; Cai, X.; Wang, X.; Xiang, Q.; Hu, B.; Yu, D.; Liu, Y.; Chen, C. Ultrathin VO₂ (B) nanosheets as cathode material for high-performance hybrid magnesium-lithium ion batteries. *Journal of The Electrochemical Society* **2019**, *166* (8), A1660.

- (68) Jang, W. Y.; Reddy, C. V.; Wang, R.; Choi, J.; Son, J.; Kakarla, R. R.; Aminabhavi, T. M.; Shim, J. Synthesis of 1D/2D VO₂ (B) nanowire/g-C₃N₄ hybrid architectures as cathode materials for high-performance Li-ion batteries. *Chemical Engineering Journal* **2023**, *476*, 146786.
- (69) Kang, M. S.; Park, S. K.; Nakhanivej, P.; Shin, K. H.; Yeon, J. S.; Park, H. S. Mesoporous VO₂ (B) nanorods deposited onto graphene architectures for enhanced rate capability and cycle life of Li ion battery cathodes. *Journal of Alloys and Compounds* **2021**, *855*, 157361.
- (70) Gu, L.; Wang, J.; Ding, J.; Li, B.; Yang, S. W-doped VO₂ (B) nanosheets-built 3D networks for fast lithium storage at high temperatures. *Electrochimica Acta* **2019**, *295*, 393-400.
- (71) Zhang, W.; Xiao, Y.; Zuo, C.; Tang, W.; Liu, G.; Wang, S.; Cai, W.; Dong, S.; Luo, P. Adjusting the valence state of vanadium in VO₂ (B) by extracting oxygen anions for high-performance aqueous zinc-ion batteries. *ChemSusChem* **2021**, *14* (3), 971-978.
- (72) Guan, K.; Duan, K.; Yang, G.; Tao, L.; Zhang, H.; Wan, H.; Yang, R.; Zhang, J.; Wang, H.; Wang, H. Ultra-long cycle H-doped VO₂ (B) cathode for high capacity aqueous Zn-ion battery. *Materials Today Advances* **2022**, *14*, 100230.
- (73) Zhang, Q.; Liu, B.; Li, L.; Ji, Y.; Wang, C.; Zhang, L.; Su, Z. Maximized Schottky Effect: The Ultrafine V₂O₃/Ni Heterojunctions Repeatedly Arranging on Monolayer Nanosheets for Efficient and Stable Water-to-Hydrogen Conversion. *Small* **2021**, *17* (13), 2005769.
- (74) Lv, Q.; Yang, L.; Wang, W.; Lu, S.; Wang, T.; Cao, L.; Dong, B. One-step construction of core/shell nanoarrays with a holey shell and exposed interfaces for overall water splitting. *Journal of Materials Chemistry A* **2019**, *7* (3), 1196-1205.
- (75) Wang, Y.; Zhang, Z.; Zhu, Y.; Li, Z.; Vajtai, R.; Ci, L.; Ajayan, P. M. Nanostructured VO₂ photocatalysts for hydrogen production. *ACS nano* **2008**, *2* (7), 1492-1496.
- (76) Chen, G.; Zhang, X.; Guan, L.; Zhang, H.; Xie, X.; Chen, S.; Tao, J. Phase transition-promoted hydrogen evolution performance of MoS₂/ VO₂ hybrids. *The Journal of Physical Chemistry C* **2018**, *122* (5), 2618-2623.
- (77) Abd-Alghafour, N.; Ahmed, N. M.; Hassan, Z.; Almessiere, M. A. Hydrothermal synthesis and structural properties of V₂O₅ nanoflowers at low temperatures. In *Journal of Physics: Conference Series*, 2018; IOP Publishing: Vol. 1083, p 012036.
- (78) Amiri, V.; Roshan, H.; Mirzaei, A.; Sheikhi, M. H. A review of nanostructured resistive-based vanadium oxide gas sensors. *Chemosensors* **2020**, *8* (4), 105.

- (79) Zou, C.; Fan, L.; Chen, R.; Yan, X.; Yan, W.; Pan, G.; Wu, Z.; Gao, W. Thermally driven V₂O₅ nanocrystal formation and the temperature-dependent electronic structure study. *CrystEngComm* **2012**, *14* (2), 626-631.
- (80) Yao, J.; Li, Y.; Massé, R. C.; Uchaker, E.; Cao, G. Revitalized interest in vanadium pentoxide as cathode material for lithium-ion batteries and beyond. *Energy Storage Materials* **2018**, *11*, 205-259.
- (81) Eyert, V.; Höck, K.-H. Electronic structure of V₂O₅: role of octahedral deformations. *Physical Review B* **1998**, *57* (20), 12727.
- (82) Roginskii, E. M.; Smirnov, M. B.; Smirnov, K. S.; Baddour-Hadjean, R.; Pereira-Ramos, J.-P.; Smirnov, A. N.; Davydov, V. Y. A computational and spectroscopic study of the electronic structure of V₂O₅-based cathode materials. *The Journal of Physical Chemistry C* **2021**, *125* (10), 5848-5858.
- (83) Wu, Q.-H.; Thissen, A.; Jaegermann, W.; Schüz, M.; Schmidt, P. Resonant photoemission spectroscopy study of electronic structure of V₂O₅. *Chemical physics letters* **2006**, *430* (4-6), 309-313.
- (84) Smirnov, M. B.; Roginskii, E. M.; Smirnov, K. S.; Baddour-Hadjean, R.; Pereira-Ramos, J.-P. Unraveling the structure–Raman spectra relationships in V₂O₅ polymorphs via a comprehensive experimental and DFT study. *Inorganic chemistry* **2018**, *57* (15), 9190-9204.
- (85) Laubach, S.; Schmidt, P. C.; Thißen, A.; Fernandez-Madrigal, F. J.; Wu, Q.-H.; Jaegermann, W.; Klemm, M.; Horn, S. Theoretical and experimental determination of the electronic structure of V₂O₅, reduced V₂O_{5-x} and sodium intercalated NaV₂O₅. *Physical Chemistry Chemical Physics* **2007**, *9* (20), 2564-2576.
- (86) Khyzhun, O. Y.; Strunskus, T.; Grünert, W.; Wöll, C. Valence band electronic structure of V_2O_5 as determined by resonant soft X-ray emission spectroscopy. *Journal of electron spectroscopy and related phenomena* **2005**, *149* (1-3), 45-50.
- (87) Yue, Y.; Liang, H. Micro-and nano-structured vanadium pentoxide (V₂O₅) for electrodes of lithium-ion batteries. *Advanced Energy Materials* **2017**, *7* (17), 1602545.
- (88) Whittingham, M. S. The role of ternary phases in cathode reactions. *Journal of The Electrochemical Society* **1976**, *123* (3), 315.
- (89) Delmas, C.; Brethes, S.; Menetrier, M. ω -Li_xV₂O₅—a new electrode material for rechargeable lithium batteries. *Journal of power sources* **1991**, *34* (2), 113-118.

- (90) Leger, C.; Bach, S.; Soudan, P.; Pereira-Ramos, J.-P. Structural and electrochemical properties of ω -Li_xV₂O₅ (0.4 \leq x \leq 3) as rechargeable cathodic material for lithium batteries. *Journal of The Electrochemical Society* **2004**, *152* (1), A236.
- (91) Delmas, C.; Cognac-Auradou, H.; Cocciantelli, J.; Ménétrier, M.; Doumerc, J. The Li_xV₂O₅ system: An overview of the structure modifications induced by the lithium intercalation. *Solid State Ionics* **1994**, *69* (3-4), 257-264.
- (92) Liu, Y.; Clark, M.; Zhang, Q.; Yu, D.; Liu, D.; Liu, J.; Cao, G. V₂O₅ nano-electrodes with high power and energy densities for thin film li-ion batteries. *Advanced Energy Materials* **2011**, *1* (2), 194-202.
- (93) Scanlon, D. O.; Walsh, A.; Morgan, B. J.; Watson, G. W. An ab initio study of reduction of V₂O₅ through the formation of oxygen vacancies and Li intercalation. *The Journal of Physical Chemistry C* **2008**, *112* (26), 9903-9911.
- (94) Liu, Q.; Liu, Y.; Sun, C.-J.; Li, Z.-f.; Ren, Y.; Lu, W.; Stach, E. A.; Xie, J. The structural evolution of V₂O₅ nanocystals during electrochemical cycling studied using in operando synchrotron techniques. *Electrochimica Acta* **2014**, *136*, 318-322.
- (95) Reddy, M. V.; Subba Rao, G.; Chowdari, B. Metal oxides and oxysalts as anode materials for Li ion batteries. *Chemical reviews* **2013**, *113* (7), 5364-5457.
- (96) Xue, L.; Li, Y.; Lin, W.; Chen, F.; Chen, G.; Chen, D. Electrochemical properties and facile preparation of hollow porous V₂O₅ microspheres for lithium-ion batteries. *Journal of Colloid and Interface Science* **2023**, *638*, 231-241.
- (97) Dong, X.; Dong, F.; Zhang, Y.; Fu, C.; Cui, C.; Wang, L.; Zeng, S. Preparation of V₂O₅ porous microstructures with enhanced performances of lithium ion batteries. *Materials Chemistry and Physics* **2022**, *277*, 125489.
- (98) Su, Z.; Zhao, M.; Zheng, Q.; Jiao, L.; Shi, M.; Li, M.; Xu, T.; Zhao, X. Ultrafast rate capability of V₂O₅ yolk-shell microspheres with hierarchical nanostructure as an aqueous lithium-ion battery anode. *Electrochimica Acta* **2022**, *410*, 139792.
- (99) Zhou, T.; Gao, G. V₂O₅-based cathodes for aqueous zinc ion batteries: mechanisms, preparations, modifications, and electrochemistry. *Nano Energy* **2024**, 109691.
- (100) Liu, Y.; Liu, Y.; Yamauchi, Y.; Alothman, Z. A.; Kaneti, Y. V.; Wu, X. Enhanced zinc ion storage capability of V₂O₅ electrode materials with hollow interior cavities. *Batteries & Supercaps* **2021**, *4* (12), 1867-1873.

- (101) Wang, X.; Li, Y.; Wang, S.; Zhou, F.; Das, P.; Sun, C.; Zheng, S.; Wu, Z. S. 2D amorphous V₂O₅/graphene heterostructures for high-safety aqueous Zn-ion batteries with unprecedented capacity and ultrahigh rate capability. *Advanced energy materials* **2020**, *10* (22), 2000081.
- (102) Su, D.; Wang, G. Single-crystalline bilayered V₂O₅ nanobelts for high-capacity sodiumion batteries. *ACS nano* **2013**, *7* (12), 11218-11226.
- (103) Fu, Q.; Sarapulova, A.; Zhu, L.; Melinte, G.; Missyul, A.; Welter, E.; Luo, X.; Knapp, M.; Ehrenberg, H.; Dsoke, S. In operando study of orthorhombic V₂O₅ as positive electrode materials for K-ion batteries. *Journal of Energy Chemistry* **2021**, *62*, 627-636.
- (104) Attias, R.; Salama, M.; Hirsch, B.; Pant, R.; Gofer, Y.; Aurbach, D. Anion effects on cathode electrochemical activity in rechargeable magnesium batteries: a case study of V₂O₅. *ACS Energy Letters* **2018**, *4* (1), 209-214.
- (105) Wang, D.; Liu, H.; Elliott, J. D.; Liu, L.-M.; Lau, W.-M. Robust vanadium pentoxide electrodes for sodium and calcium ion batteries: thermodynamic and diffusion mechanical insights. *Journal of Materials Chemistry A* **2016**, *4* (32), 12516-12525.
- (106) Diem, A. M.; Fenk, B.; Bill, J.; Burghard, Z. Binder-free V₂O₅ cathode for high energy density rechargeable aluminum-ion batteries. *Nanomaterials* **2020**, *10* (2), 247.
- (107) Velmurugan, R.; Premkumar, J.; Pitchai, R.; Ulaganathan, M.; Subramanian, B. Robust, flexible, and binder free highly crystalline V₂O₅ thin film electrodes and their superior supercapacitor performances. *ACS sustainable chemistry & engineering* **2019**, 7 (15), 13115-13126.
- (108) Sahu, V.; Goel, S.; Tomar, A. K.; Singh, G.; Sharma, R. K. Graphene nanoribbons@ vanadium oxide nanostrips for supercapacitive energy storage. *Electrochimica Acta* **2017**, *230*, 255-264.
- (109) Sun, W.; Gao, G.; Zhang, K.; Liu, Y.; Wu, G. Self-assembled 3D N-CNFs/ V₂O₅ aerogels with core/shell nanostructures through vacancies control and seeds growth as an outstanding supercapacitor electrode material. *Carbon* **2018**, *132*, 667-677.
- (110) De Jesus, L. R.; Horrocks, G. A.; Liang, Y.; Parija, A.; Jaye, C.; Wangoh, L.; Wang, J.; Fischer, D. A.; Piper, L. F.; Prendergast, D. Mapping polaronic states and lithiation gradients in individual V₂O₅ nanowires. *Nature communications* **2016**, *7* (1), 12022.
- (111) Shen, F.-C.; Wang, Y.; Tang, Y.-J.; Li, S.-L.; Wang, Y.-R.; Dong, L.-Z.; Li, Y.-F.; Xu, Y.; Lan, Y.-Q. CoV₂O₆–V₂O₅ coupled with porous N-doped reduced graphene oxide composite as a highly efficient electrocatalyst for oxygen evolution. *ACS Energy Letters* **2017**, *2* (6), 1327-1333.

- (112) Mounasamy, V.; Srividhya, G.; Ponpandian, N. Well-defined 2D transition vanadium pentoxide (V_2O_5) flat nanorods with large-scale synthesis feasibility as an electrocatalyst for the oxygen evolution reaction (OER). *Energy Advances* **2023**, *2* (6), 784-788.
- (113) Zheng, X.; Qin, M.; Ma, S.; Chen, Y.; Ning, H.; Yang, R.; Mao, S.; Wang, Y. Strong oxide-support interaction over IrO₂/V₂O₅ for efficient pH-universal water splitting. *Advanced Science* **2022**, *9* (11), 2104636.
- (114) Jafari, F.; Rahsepar, F. R. V₂O₅–Fe₃O₄/rGO ternary nanocomposite with dual applications as a dye degradation photocatalyst and OER electrocatalyst. *ACS omega* **2023**, *8* (38), 35427-35439.
- (115) Li, Y. H.; Liu, P. F.; Pan, L. F.; Wang, H. F.; Yang, Z. Z.; Zheng, L. R.; Hu, P.; Zhao, H. J.; Gu, L.; Yang, H. G. Local atomic structure modulations activate metal oxide as electrocatalyst for hydrogen evolution in acidic water. *Nature communications* **2015**, *6* (1), 8064.
- (116) Zhang, J.; Zhang, H.; Liu, M.; Xu, Q.; Jiang, H.; Li, C. Cobalt-stabilized oxygen vacancy of V₂O₅ nanosheet arrays with delocalized valence electron for alkaline water splitting. *Chemical Engineering Science* **2020**, *227*, 115915.
- (117) Meena, A.; Ha, M.; Chandrasekaran, S. S.; Sultan, S.; Thangavel, P.; Harzandi, A. M.; Singh, B.; Tiwari, J. N.; Kim, K. S. Pt-like hydrogen evolution on a V₂O₅/Ni(OH)₂ Electrocatalyst. *Journal of Materials Chemistry A* **2019**, 7 (26), 15794-15800.
- (118) Zhong, X.; Zhang, L.; Tang, J.; Chai, J.; Xu, J.; Cao, L.; Yang, M.; Yang, M.; Kong, W.; Wang, S. Efficient coupling of a hierarchical V₂O₅@ Ni₃S₂ hybrid nanoarray for pseudocapacitors and hydrogen production. *Journal of Materials Chemistry A* **2017**, *5* (34), 17954-17962.
- (119) Kumar, R. R.; Karunagaran, B.; Kumar, V. S.; Jeyachandran, Y.; Mangalaraj, D.; Narayandass, S. K. Structural properties of V₂O₅ thin films prepared by vacuum evaporation. *Materials Science in semiconductor processing* **2003**, *6* (5-6), 543-546.
- (120) Fauzi, M.; Esmaeilzadeh, F.; Mowla, D.; Sahraeian, N. The effect of various capping agents on V₂O₅ morphology and photocatalytic degradation of dye. *Journal of Materials Science: Materials in Electronics* **2021**, *32*, 10473-10490.
- (121) Malhotra, N.; Kaur, N.; Ghosh, A.; Mehta, M.; Kodan, N. Enhanced Photoelectrochemical Response of the ZnO/V₂O₅ Heterojunction Via Improved Visible-Light Absorption and Charge Carrier Separation. *ACS Applied Energy Materials* **2023**, *6* (13), 6926-6933.

- (122) Oliveira, A. T.; Rodriguez, M.; Andrade, T. S.; de Souza, H. E.; Ardisson, J. D.; Oliveira, H. S.; Oliveira, L. C.; Lorençon, E.; Silva, A. C.; Nascimento, L. L. High water oxidation performance of W-doped BiVO₄ photoanodes coupled to V₂O₅ rods as a photoabsorber and hole carrier. *Solar RRL* **2018**, *2* (8), 1800089.
- (123) Hou, T.-F.; Johar, M. A.; Boppella, R.; Hassan, M. A.; Patil, S. J.; Ryu, S.-W.; Lee, D.-W. Vertically aligned one-dimensional ZnO/V₂O₅ core–shell hetero-nanostructure for photoelectrochemical water splitting. *Journal of Energy Chemistry* **2020**, *49*, 262-274.
- (124) Momeni, M. M.; Renani, A. S.; Lee, B.-K. Light-chargeable two-electrode photo-supercapacitors based on MnS nanoflowers deposited on V₂O₅-BiVO₄ photoelectrodes. *Journal of Alloys and Compounds* **2023**, *962*, 171204.
- (125) Boruah, B. D.; Mathieson, A.; Wen, B.; Feldmann, S.; Dose, W. M.; De Volder, M. Photorechargeable zinc-ion batteries. *Energy & Environmental Science* **2020**, *13* (8), 2414-2421.
- (126) Boruah, B. D.; Wen, B.; De Volder, M. Light rechargeable lithium-ion batteries using V₂O₅ cathodes. *Nano Letters* **2021**, *21* (8), 3527-3532.
- (127) Wilhelm, M.; Adam, R.; Bhardwaj, A.; Neumann, I.; Cho, S. H.; Yamada, Y.; Sekino, T.; Tao, J.; Hong, Z.; Fischer, T. Carbon-coated electrospun V₂O₅ nanofibers as photoresponsive cathode for lithium-ion batteries. *Advanced Engineering Materials* **2023**, *25* (1), 2200765.
- (128) Han, Y.; Liu, B.; Xiao, Z.; Zhang, W.; Wang, X.; Pan, G.; Xia, Y.; Xia, X.; Tu, J. Interface issues of lithium metal anode for high-energy batteries: challenges, strategies, and perspectives. *InfoMat* **2021**, *3* (2), 155-174.
- (129) Zhang, X.; Hu, J. P.; Fu, N.; Zhou, W. B.; Liu, B.; Deng, Q.; Wu, X. W. Comprehensive review on zinc-ion battery anode: challenges and strategies. *InfoMat* **2022**, *4* (7), e12306.
- (130) Olivetti, E. A.; Ceder, G.; Gaustad, G. G.; Fu, X. Lithium-ion battery supply chain considerations: analysis of potential bottlenecks in critical metals. *Joule* **2017**, *1* (2), 229-243.
- (131) Whittingham, M. S. Electrical energy storage and intercalation chemistry. *Science* **1976**, *192* (4244), 1126-1127.
- (132) Godshall, N. A.; Raistrick, I.; Huggins, R. Thermodynamic investigations of ternary lithium-transition metal-oxygen cathode materials. *Materials Research Bulletin* **1980**, *15* (5), 561-570.
- (133) Mizushima, K.; Jones, P.; Wiseman, P.; Goodenough, J. B. LixCoO₂ (0< x<-1): A new cathode material for batteries of high energy density. *Materials Research Bulletin* **1980**, *15* (6), 783-789.

- (134) Amatucci, G.; Tarascon, J.; Klein, L. CoO₂, the end member of the Li_xCoO₂ solid solution. *Journal of The Electrochemical Society* **1996**, *143* (3), 1114.
- (135) Ohzuku, T.; Makimura, Y. Layered lithium insertion material of LiCo1/3Ni1/3Mn1/3O2 for lithium-ion batteries. *Chemistry letters* **2001**, *30* (7), 642-643.
- (136) Lu, Z.; MacNeil, D.; Dahn, J. Layered Li [Ni_xCo_{1-2x}Mn_x] O₂ Cathode materials for lithium-ion batteries. *Electrochemical and Solid-State Letters* **2001**, *4* (12), A200.
- (137) Li, Z.; Chernova, N. A.; Roppolo, M.; Upreti, S.; Petersburg, C.; Alamgir, F. M.; Whittingham, M. S. Comparative study of the capacity and rate capability of LiNi_yMn_yCo_{1-2y}O₂ (y= 0.5, 0.45, 0.4, 0.33). *Journal of the Electrochemical Society* **2011**, *158* (5), A516.
- (138) Xia, Y.; Zheng, J.; Wang, C.; Gu, M. Designing principle for Ni-rich cathode materials with high energy density for practical applications. *Nano Energy* **2018**, *49*, 434-452.
- (139) Min, K.; Seo, S.-W.; Song, Y. Y.; Lee, H. S.; Cho, E. A first-principles study of the preventive effects of Al and Mg doping on the degradation in LiNi_{0.8}Co_{0.1}Mn_{0.1}O₂ cathode materials. *Physical chemistry chemical physics* **2017**, *19* (3), 1762-1769.
- (140) Chen, M.; Zhao, E.; Chen, D.; Wu, M.; Han, S.; Huang, Q.; Yang, L.; Xiao, X.; Hu, Z. Decreasing Li/Ni disorder and improving the electrochemical performances of Ni-rich LiNi₀. 8Co_{0.1}Mn_{0.1}O₂ by Ca doping. *Inorganic Chemistry* **2017**, *56* (14), 8355-8362.
- (141) Liang, L.; Hu, G.; Jiang, F.; Cao, Y. Electrochemical behaviours of SiO₂-coated LiNi_{0.8}Co_{0.1}Mn_{0.1}O₂ cathode materials by a novel modification method. *Journal of Alloys and Compounds* **2016**, *657*, 570-581.
- (142) Schipper, F.; Bouzaglo, H.; Dixit, M.; Erickson, E. M.; Weigel, T.; Talianker, M.; Grinblat, J.; Burstein, L.; Schmidt, M.; Lampert, J. From surface ZrO₂ coating to bulk Zr doping by high temperature annealing of nickel-rich lithiated oxides and their enhanced electrochemical performance in lithium ion batteries. *Advanced Energy Materials* **2018**, *8* (4), 1701682.
- (143) Vernardou, D.; Drosos, C.; Kafizas, A.; Pemble, M. E.; Koudoumas, E. Towards high performance chemical vapour deposition V₂O₅ cathodes for batteries employing aqueous media. *Molecules* **2020**, *25* (23), 5558.
- (144) West, K.; Zachau-Christiansen, B.; Jacobsen, T.; Skaarup, S. Vanadium oxide xerogels as electrodes for lithium batteries. *Electrochimica acta* **1993**, *38* (9), 1215-1220.
- (145) Kumagai, N.; Kitamoto, H.; Baba, M.; Durand-Vidal, S.; Devilliers, D.; Groult, H. Intercalation of lithium in rf-sputtered vanadium oxide film as an electrode material for lithiumion batteries. *Journal of applied electrochemistry* **1998**, *28*, 41-48.

- (146) Zhou, F.; Zhao, X.; Xu, H.; Yuan, C. Hydrothermal synthesis of metastable VO₂ nanorods as cathode materials for lithium ion batteries. *Chemistry letters* **2006**, *35* (11), 1280-1281.
- (147) Lin, D.; Liu, Y.; Cui, Y. Reviving the lithium metal anode for high-energy batteries. *Nature nanotechnology* **2017**, *12* (3), 194-206.
- (148) Huang, X.; Rui, X.; Hng, H. H.; Yan, Q. Vanadium pentoxide-based cathode materials for lithium-ion batteries: morphology control, carbon hybridization, and cation doping. *Particle & Particle Systems Characterization* **2015**, *32* (3), 276-294.
- (149) Chen, Y.-C.; Xie, K.; Pan, Y.; Zheng, C.-M.; Wang, H.-L. High power nano-LiMn₂O₄ cathode materials with high-rate pulse discharge capability for lithium-ion batteries. *Chinese Physics B* **2011**, *20* (2), 028201.
- (150) Lai, F.; Zhang, X.; Wang, H.; Hu, S.; Wu, X.; Wu, Q.; Huang, Y.; He, Z.; Li, Q. Three-dimension hierarchical Al2O3 nanosheets wrapped LiMn₂O₄ with enhanced cycling stability as cathode material for lithium ion batteries. *ACS applied materials & interfaces* **2016**, *8* (33), 21656-21665.
- (151) Kalluri, S.; Yoon, M.; Jo, M.; Park, S.; Myeong, S.; Kim, J.; Dou, S.; Guo, Z.; Cho, J. Adv. Energy Mater. 2017, 7, 1601507; d) S. Jouanneau, KW Eberman, LJ Krause, JR Dahn. *J. Electrochem. Soc* **2003**, *150*, A1637.
- (152) Tron, A.; Jo, Y. N.; Oh, S. H.; Park, Y. D.; Mun, J. Surface modification of the LiFePO₄ cathode for the aqueous rechargeable lithium ion battery. *ACS Applied Materials & Interfaces* **2017**, *9* (14), 12391-12399.
- (153) Yuan, B.; Yuan, X.; Zhang, B.; An, Z.; Luo, S.; Chen, L. Lithium ion batteries cathode material: V₂O₅. *Chinese Physics B* **2022**, *31* (3), 038203.
- (154) Zhu, Y.; Yang, M.; Huang, Q.; Wang, D.; Yu, R.; Wang, J.; Zheng, Z.; Wang, D. V₂O₅ textile cathodes with high capacity and stability for flexible lithium-ion batteries. *Advanced materials* **2020**, *32* (7), 1906205.
- (155) Parker, J. F.; Chervin, C. N.; Pala, I. R.; Machler, M.; Burz, M. F.; Long, J. W.; Rolison, D. R. Rechargeable nickel–3D zinc batteries: An energy-dense, safer alternative to lithium-ion. *Science* **2017**, *356* (6336), 415-418.
- (156) Wang, S.; Yang, Y.; Dong, Y.; Zhang, Z.; Tang, Z. Recent progress in Ti-based nanocomposite anodes for lithium ion batteries. *Journal of Advanced Ceramics* **2019**, *8*, 1-18.
- (157) Trading Economics. Global price of commodities. https://tradingeconomics.com/commodities (2024).

- (158) Ariel Cohen. Lithium: Price Collapse Secures Green Transition, Causes Headaches. The Forbes https://www.forbes.com/sites/arielcohen/2023/12/27/lithium-price-collapse-secures-green-transition-causes-headaches/?sh=3879d8474a61 (2023).
- (159) Lv, T.; Peng, Y.; Zhang, G.; Jiang, S.; Yang, Z.; Yang, S.; Pang, H. How about vanadium-based compounds as cathode materials for aqueous zinc ion batteries? *Advanced Science* **2023**, *10* (12), 2206907.
- (160) Zhu, J.; Tie, Z.; Bi, S.; Niu, Z. Towards More Sustainable Aqueous Zinc-Ion Batteries. *Angewandte Chemie* **2024**, e202403712.
- (161) Yi, T.-F.; Qiu, L.; Qu, J.-P.; Liu, H.; Zhang, J.-H.; Zhu, Y.-R. Towards high-performance cathodes: Design and energy storage mechanism of vanadium oxides-based materials for aqueous Zn-ion batteries. *Coordination Chemistry Reviews* **2021**, *446*, 214124.
- (162) Winter, M.; Brodd, R. J. What are batteries, fuel cells, and supercapacitors? *Chemical reviews* **2004**, *104* (10), 4245-4270.
- (163) Maiche, L. French Patent 127,069, 1878.
- (164) Zhu, Y.; Guan, P.; Zhu, R.; Zhang, S.; Feng, Z.; Li, M.; Wan, T.; Hu, L.; Liu, Y.; Li, Q. Recent advances in flexible alkaline Zinc-based batteries: Materials, structures, and perspectives. *Journal of Energy Chemistry* **2023**.
- (165) Yamamoto, T.; Shoji, T. Rechargeable Zn| ZnSO₄| MnO₂-type cells. *Inorganica chimica acta* **1986**, *117* (2), L27-L28.
- (166) Parker, J. F.; Ko, J. S.; Rolison, D. R.; Long, J. W. Translating materials-level performance into device-relevant metrics for zinc-based batteries. *Joule* **2018**, *2* (12), 2519-2527.
- (167) Xu, C.; Du, H.; Li, B.; Kang, F.; Zeng, Y. Reversible insertion properties of zinc ion into manganese dioxide and its application for energy storage. *Electrochemical and Solid-State Letters* **2009**, *12* (4), A61.
- (168) Xu, C.; Li, B.; Du, H.; Kang, F. Energetic zinc ion chemistry: the rechargeable zinc ion battery. *Angewandte Chemie International Edition* **2012**, *51* (4), 933-935.
- (169) Pan, H.; Shao, Y.; Yan, P.; Cheng, Y.; Han, K. S.; Nie, Z.; Wang, C.; Yang, J.; Li, X.; Bhattacharya, P. Reversible aqueous zinc/manganese oxide energy storage from conversion reactions. *Nature Energy* **2016**, *1* (5), 1-7.
- (170) Deng, W.; Li, Z.; Ye, Y.; Zhou, Z.; Li, Y.; Zhang, M.; Yuan, X.; Hu, J.; Zhao, W.; Huang, Z. Zn²⁺ induced phase transformation of K₂MnFe (CN)₆ boosts highly stable zinc-ion storage. *Advanced Energy Materials* **2021**, *11* (31), 2003639.

- (171) Du, M.; Geng, P.; Pei, C.; Jiang, X.; Shan, Y.; Hu, W.; Ni, L.; Pang, H. High-Entropy Prussian Blue Analogues and Their Oxide Family as Sulfur Hosts for Lithium-Sulfur Batteries. *Angewandte Chemie International Edition* **2022**, *61* (41), e202209350.
- (172) Zhao, Y.; Zhu, Y.; Zhang, X. Challenges and perspectives for manganese-based oxides for advanced aqueous zinc-ion batteries. *InfoMat* **2020**, *2* (2), 237-260.
- (173) Li, Y.; Zhang, D.; Huang, S.; Yang, H. Y. Guest-species-incorporation in manganese/vanadium-based oxides: Towards high performance aqueous zinc-ion batteries. *Nano Energy* **2021**, *85*, 105969.
- (174) Hurlbutt, K.; Wheeler, S.; Capone, I.; Pasta, M. Prussian blue analogs as battery materials. *Joule* **2018**, *2* (10), 1950-1960.
- (175) Xu, C.; Yang, Z.; Zhang, X.; Xia, M.; Yan, H.; Li, J.; Yu, H.; Zhang, L.; Shu, J. Correction to: Prussian Blue Analogues in Aqueous Batteries and Desalination Batteries. *Nano-Micro Letters* **2021**, *13*, 187-187.
- (176) Yan, J.; Wang, J.; Liu, H.; Bakenov, Z.; Gosselink, D.; Chen, P. Rechargeable hybrid aqueous batteries. *Journal of Power Sources* **2012**, *216*, 222-226.
- (177) Häupler, B.; Rössel, C.; Schwenke, A. M.; Winsberg, J.; Schmidt, D.; Wild, A.; Schubert, U. S. Aqueous zinc-organic polymer battery with a high rate performance and long lifetime. *NPG Asia Materials* **2016**, *8* (7), e283-e283.
- (178) Hu, P.; Yan, M.; Zhu, T.; Wang, X.; Wei, X.; Li, J.; Zhou, L.; Li, Z.; Chen, L.; Mai, L. Zn/V₂O₅ aqueous hybrid-ion battery with high voltage platform and long cycle life. *ACS* applied materials & interfaces **2017**, *9* (49), 42717-42722.
- (179) Han, D.; Cui, C.; Zhang, K.; Wang, Z.; Gao, J.; Guo, Y.; Zhang, Z.; Wu, S.; Yin, L.; Weng, Z. A non-flammable hydrous organic electrolyte for sustainable zinc batteries. *Nature Sustainability* **2022**, *5* (3), 205-213.
- (180) Zhang, M.; Liang, R.; Or, T.; Deng, Y.-P.; Yu, A.; Chen, Z. Recent progress on high-performance cathode materials for zinc-ion batteries. *Small Structures* **2021**, *2* (2), 2000064.
- (181) Wan, F.; Niu, Z. Design strategies for vanadium-based aqueous zinc-ion batteries. *Angewandte Chemie* **2019**, *131* (46), 16508-16517.
- (182) Cheng, F.; Chen, J.; Gou, X.; Shen, P. High-power alkaline Zn-MnO₂ batteries using γ-MnO₂ nanowires/nanotubes and electrolytic zinc powder. *Advanced Materials (Weinheim)* **2005**, *17*.

- (183) Jie, Z.; Xia, H.; Zhong, S.-L.; Feng, Q.; Li, S.; Liang, S.; Zhong, H.; Liu, Z.; Gao, Y.; Zhao, H. The gut microbiome in atherosclerotic cardiovascular disease. *Nature communications* **2017**, *8* (1), 845.
- (184) Zhang, N.; Dong, Y.; Jia, M.; Bian, X.; Wang, Y.; Qiu, M.; Xu, J.; Liu, Y.; Jiao, L.; Cheng, F. Rechargeable aqueous Zn–V₂O₅ battery with high energy density and long cycle life. *ACS Energy Letters* **2018**, *3* (6), 1366-1372.
- (185) Ding, J.; Du, Z.; Gu, L.; Li, B.; Wang, L.; Wang, S.; Gong, Y.; Yang, S. Ultrafast Zn²⁺ intercalation and deintercalation in vanadium dioxide. *Advanced Materials* **2018**, *30* (26), 1800762.
- (186) Zhu, Z.; Zheng, Z.; Zhang, F.; Wu, Y.; Trzaskowski, M.; Maier, R.; Robinson, M. R.; McGrath, J. J.; Visscher, P. M.; Wray, N. R. Causal associations between risk factors and common diseases inferred from GWAS summary data. *Nature communications* **2018**, *9* (1), 1-12.
- (187) Ming, F.; Liang, H.; Lei, Y.; Kandambeth, S.; Eddaoudi, M.; Alshareef, H. N. Layered Mg x V₂O₅· n H₂O as cathode material for high-performance aqueous zinc ion batteries. *ACS Energy Letters* **2018**, *3* (10), 2602-2609.
- (188) Wang, R. Y.; Wessells, C. D.; Huggins, R. A.; Cui, Y. Highly reversible open framework nanoscale electrodes for divalent ion batteries. *Nano letters* **2013**, *13* (11), 5748-5752.
- (189) Li, S.; Dong, Y.; Xu, L.; Xu, X.; He, L.; Mai, L. Effect of carbon matrix dimensions on the electrochemical properties of Na₃V₂(PO₄)₃ nanograins for high-performance symmetric sodium-ion batteries. *Advanced Materials* **2014**, *26* (21), 3545-3553.
- (190) Cheng, Y.; Luo, L.; Zhong, L.; Chen, J.; Li, B.; Wang, W.; Mao, S. X.; Wang, C.; Sprenkle, V. L.; Li, G. Highly reversible zinc-ion intercalation into chevrel phase Mo₆S₈ nanocubes and applications for advanced zinc-ion batteries. *ACS applied materials & interfaces* **2016**, 8 (22), 13673-13677.
- (191) Kundu, D.; Oberholzer, P.; Glaros, C.; Bouzid, A.; Tervoort, E.; Pasquarello, A.; Niederberger, M. Organic cathode for aqueous Zn-ion batteries: taming a unique phase evolution toward stable electrochemical cycling. *Chemistry of materials* **2018**, *30* (11), 3874-3881.
- (192) Marcus, Y. Ion properties; CRC Press, 1997.
- (193) Chayambuka, K.; Mulder, G.; Danilov, D. L.; Notten, P. H. From li-ion batteries toward Na-ion chemistries: challenges and opportunities. *Advanced energy materials* **2020**, *10* (38), 2001310.

- (194) Yabuuchi, N.; Kubota, K.; Dahbi, M.; Komaba, S. Research development on sodium-ion batteries. *Chemical reviews* **2014**, *114* (23), 11636-11682.
- (195) Vaalma, C.; Buchholz, D.; Weil, M.; Passerini, S. A cost and resource analysis of sodiumion batteries. *Nature reviews materials* **2018**, *3* (4), 1-11.
- (196) Braconnier, J.-J.; Delmas, C.; Fouassier, C.; Hagenmuller, P. Comportement electrochimique des phases Na_xCoO₂. *Materials Research Bulletin* **1980**, *15* (12), 1797-1804.
- (197) Komaba, S.; Hasegawa, T.; Dahbi, M.; Kubota, K. Potassium intercalation into graphite to realize high-voltage/high-power potassium-ion batteries and potassium-ion capacitors. *Electrochemistry Communications* **2015**, *60*, 172-175.
- (198) Kubota, K.; Dahbi, M.; Hosaka, T.; Kumakura, S.; Komaba, S. Towards K-ion and Naion batteries as "beyond Li-ion". *The chemical record* **2018**, *18* (4), 459-479.
- (199) Marcus, Y. Thermodynamic functions of transfer of single ions from water to nonaqueous and mixed solvents: Part 3-Standard potentials of selected electrodes. *Pure and applied chemistry* **1985**, *57* (8), 1129-1132.
- (200) Jian, Z.; Luo, W.; Ji, X. Carbon electrodes for K-ion batteries. *Journal of the American chemical society* **2015**, *137* (36), 11566-11569.
- (201) Luo, W.; Wan, J.; Ozdemir, B.; Bao, W.; Chen, Y.; Dai, J.; Lin, H.; Xu, Y.; Gu, F.; Barone, V. Potassium ion batteries with graphitic materials. *Nano letters* **2015**, *15* (11), 7671-7677.
- (202) Eftekhari, A.; Jian, Z.; Ji, X. Potassium secondary batteries. *ACS applied materials & interfaces* **2017**, *9* (5), 4404-4419.
- (203) Pramudita, J. C.; Sehrawat, D.; Goonetilleke, D.; Sharma, N. An initial review of the status of electrode materials for potassium-ion batteries. *Advanced energy materials* **2017**, *7* (24), 1602911.
- (204) Wu, X.; Leonard, D. P.; Ji, X. Emerging non-aqueous potassium-ion batteries: challenges and opportunities. *Chemistry of Materials* **2017**, *29* (12), 5031-5042.
- (205) Hwang, J. Y.; Myung, S. T.; Sun, Y. K. Recent progress in rechargeable potassium batteries. *Advanced Functional Materials* **2018**, *28* (43), 1802938.
- (206) Kim, H.; Kim, J. C.; Bianchini, M.; Seo, D. H.; Rodriguez-Garcia, J.; Ceder, G. Recent progress and perspective in electrode materials for K-ion batteries. *Advanced Energy Materials* **2018**, *8* (9), 1702384.
- (207) Hosaka, T.; Kubota, K.; Hameed, A. S.; Komaba, S. Research development on K-ion batteries. *Chemical reviews* **2020**, *120* (14), 6358-6466.

- (208) Eftekhari, A. Potassium secondary cell based on Prussian blue cathode. *Journal of Power Sources* **2004**, *126* (1-2), 221-228.
- (209) Elia, G. A.; Kravchyk, K. V.; Kovalenko, M. V.; Chacón, J.; Holland, A.; Wills, R. G. An overview and prospective on Al and Al-ion battery technologies. *Journal of Power Sources* **2021**, *481*, 228870.
- (210) Ambroz, F.; Macdonald, T. J.; Nann, T. Trends in aluminium-based intercalation batteries. *Advanced Energy Materials* **2017**, *7* (15), 1602093.
- (211) Muñoz-Torrero, D.; Palma, J.; Marcilla, R.; Ventosa, E. A critical perspective on rechargeable Al-ion battery technology. *Dalton transactions* **2019**, *48* (27), 9906-9911.
- (212) Kitada, A.; Nakamura, K.; Fukami, K.; Murase, K. AlCl₃-dissolved diglyme as electrolyte for room-temperature aluminum electrodeposition. *Electrochemistry* **2014**, *82* (11), 946-948.
- (213) Li, C.; Hou, C.-C.; Chen, L.; Kaskel, S.; Xu, Q. Rechargeable Al-ion batteries. *EnergyChem* **2021**, *3* (2), 100049.
- (214) Muldoon, J.; Bucur, C. B.; Gregory, T. Quest for nonaqueous multivalent secondary batteries: magnesium and beyond. *Chemical reviews* **2014**, *114* (23), 11683-11720.
- (215) Aurbach, D.; Cohen, Y.; Moshkovich, M. The study of reversible magnesium deposition by in situ scanning tunneling microscopy. *Electrochemical and Solid-State Letters* **2001**, *4* (8), A113.
- (216) Aurbach, D.; Gofer, Y.; Schechter, A.; Chusid, O.; Gizbar, H.; Cohen, Y.; Moshkovich, M.; Turgeman, R. A comparison between the electrochemical behavior of reversible magnesium and lithium electrodes. *Journal of power sources* **2001**, *97*, 269-273.
- (217) Gaddum, L.; French, H. The electrolysis of grignard solutions 1. *Journal of the American Chemical Society* **1927**, *49* (5), 1295-1299.
- (218) Niu, J.; Zhang, Z.; Aurbach, D. Alloy anode materials for rechargeable Mg ion batteries. *Advanced Energy Materials* **2020**, *10* (23), 2000697.
- (219) Liu, F.; Wang, T.; Liu, X.; Fan, L. Z. Challenges and recent progress on key materials for rechargeable magnesium batteries. *Advanced Energy Materials* **2021**, *11* (2), 2000787.
- (220) Monti, D.; Ponrouch, A.; Araujo, R. B.; Barde, F.; Johansson, P.; Palacín, M. R. Multivalent batteries—prospects for high energy density: Ca batteries. *Frontiers in Chemistry* **2019**, *7*, 79.
- (221) Arroyo-de Dompablo, M. E.; Ponrouch, A.; Johansson, P.; Palacín, M. R. Achievements, challenges, and prospects of calcium batteries. *Chemical Reviews* **2019**, *120* (14), 6331-6357.

- (222) Ponrouch, A.; Bitenc, J.; Dominko, R.; Lindahl, N.; Johansson, P.; Palacín, M. R. Multivalent rechargeable batteries. *Energy Storage Materials* **2019**, *20*, 253-262.
- (223) Ji, B.; He, H.; Yao, W.; Tang, Y. Recent advances and perspectives on calcium-ion storage: key materials and devices. *Advanced Materials* **2021**, *33* (2), 2005501.
- (224) Ponrouch, A.; Palacín, M. R. On the road toward calcium-based batteries. *Current Opinion in Electrochemistry* **2018**, *9*, 1-7.
- (225) Stievano, L.; de Meatza, I.; Bitenc, J.; Cavallo, C.; Brutti, S.; Navarra, M. A. Emerging calcium batteries. *Journal of Power Sources* **2021**, *482*, 228875.
- (226) Gao, X.; Wu, H.; Su, C.; Lu, C.; Dai, Y.; Zhao, S.; Hu, X.; Zhao, F.; Zhang, W.; Parkin, I. P. Recent advances in carbon-based nanomaterials for multivalent-ion hybrid capacitors: a review. *Energy & Environmental Science* **2023**, *16* (4), 1364-1383.
- (227) Kim, J.; Kim, M.; Lee, J.; An, J.; Yang, S.; Ahn, H. C.; Yoo, D.-J.; Choi, J. W. Insights from Li and Zn systems for advancing Mg and Ca metal batteries. *Chemical Society Reviews* **2024**.
- (228) Liang, Y.; Dong, H.; Aurbach, D.; Yao, Y. Current status and future directions of multivalent metal-ion batteries. *Nature Energy* **2020**, *5* (9), 646-656.
- (229) Xing, L.-L.; Zhao, G.-G.; Huang, K.-J.; Wu, X. A yolk–shell V₂O₅ structure assembled from ultrathin nanosheets and coralline-shaped carbon as advanced electrodes for a high-performance asymmetric supercapacitor. *Dalton transactions* **2018**, *47* (7), 2256-2265.
- (230) Liu, X.; Liu, C.; Wang, Z.; Chen, H.; Liu, Z.; Yang, J.; Lau, W.-M.; Zhou, D. Facile hydrothermal synthesis of V₂O₅ nanofibers as cathode material for aqueous zinc-ion batteries. *Journal of Alloys and Compounds* **2022**, *896*, 163071.
- (231) Javed, M. S.; Lei, H.; Wang, Z.; Liu, B.-t.; Cai, X.; Mai, W. 2D V₂O₅ nanosheets as a binder-free high-energy cathode for ultrafast aqueous and flexible Zn-ion batteries. *Nano Energy* **2020**, *70*, 104573.
- (232) Mohan, V.; Hu, B.; Qiu, W.; Chen, W. Synthesis, structural, and electrochemical performance of V₂O₅ nanotubes as cathode material for lithium battery. *Journal of applied electrochemistry* **2009**, *39*, 2001-2006.
- (233) Niu, C.; Li, J.; Jin, H.; Shi, H.; Zhu, Y.; Wang, W.; Cao, M. Self-template processed hierarchical V₂O₅ nanobelts as cathode for high performance lithium ion battery. *Electrochimica Acta* **2015**, *182*, 621-628.

- (234) Balamuralitharan, B.; Cho, I.-H.; Bak, J.-S.; Kim, H.-J. V₂O₅ nanorod electrode material for enhanced electrochemical properties by a facile hydrothermal method for supercapacitor applications. *New Journal of Chemistry* **2018**, *42* (14), 11862-11868.
- (235) Wang, Y.; Nie, Z.; Pan, A.; Zhang, Y.; Kong, X.; Zhu, T.; Liang, S.; Cao, G. Self-templating synthesis of double-wall shelled vanadium oxide hollow microspheres for high-performance lithium ion batteries. *Journal of Materials Chemistry A* **2018**, *6* (16), 6792-6799.
- (236) Kim, K.; Lee, M.-J. Template-assisted solvothermal assembly of size-controlled hierarchical V_2O_5 hollow microspheres with tunable nanoscale building blocks and their enhanced lithium storage properties. *Electrochimica Acta* **2017**, *258*, 942-950.
- (237) Uchaker, E.; Zhou, N.; Li, Y.; Cao, G. Polyol-mediated solvothermal synthesis and electrochemical performance of nanostructured V₂O₅ hollow microspheres. *The Journal of Physical Chemistry C* **2013**, *117* (4), 1621-1626.
- (238) Chen, D.; Yi, R.; Chen, S.; Xu, T.; Gordin, M. L.; Lv, D.; Wang, D. Solvothermal synthesis of V₂O₅/graphene nanocomposites for high performance lithium ion batteries. *Materials Science and Engineering: B* **2014**, *185*, 7-12.
- (239) Partheeban, T.; Kesavan, T.; Vivekanantha, M.; Sasidharan, M. One-pot solvothermal synthesis of V₂O₅/MWCNT composite cathode for Li ion batteries. *Applied Surface Science* **2019**, *493*, 1106-1114.
- (240) Li, Q.; Chen, D.; Tan, H.; Zhang, X.; Rui, X.; Yu, Y. 3D porous V₂O₅ architectures for high-rate lithium storage. *Journal of Energy Chemistry* **2020**, *40*, 15-21.
- (241) Karami, H.; Mohammadi, A. Poly vinyl alcohol-based sol-gel synthesis of V₂O₅ nanoflakes as positive electrodes of Li-ion batteries. *International Journal of Electrochemical Science* **2015**, *10* (9), 7392-7408.
- (242) Prześniak-Welenc, M.; Szreder, N.; Winiarski, A.; Łapiński, M.; Kościelska, B.; Barczyński, R. J.; Gazda, M.; Sadowski, W. Electrical conductivity and relaxation processes in V₂O₅ nanorods prepared by sol–gel method. *physica status solidi (b)* **2015**, *252* (9), 2111-2116. (243) Gorobtsov, P. Y.; Simonenko, T. L.; Simonenko, N. P.; Simonenko, E. P.; Kuznetsov, N. T. Preparation of V₂O₅ Thin Film by Sol–Gel Technique and Pen Plotter Printing. *Colloids and Interfaces* **2023**, *7* (1), 20.
- (244) Shao, L.; Wu, K.; Lin, X.; Shui, M.; Ma, R.; Wang, D.; Long, N.; Ren, Y.; Shu, J. Solgel preparation of V₂O₅ sheets and their lithium storage behaviors studied by electrochemical and in-situ X-ray diffraction techniques. *Ceramics International* **2014**, *40* (4), 6115-6125.

- (245) Chen, X.; Pomerantseva, E.; Banerjee, P.; Gregorczyk, K.; Ghodssi, R.; Rubloff, G. Ozone-based atomic layer deposition of crystalline V₂O₅ films for high performance electrochemical energy storage. *Chemistry of Materials* **2012**, *24* (7), 1255-1261.
- (246) Sreedhara, M.; Ghatak, J.; Bharath, B.; Rao, C. Atomic layer deposition of ultrathin crystalline epitaxial films of V₂O₅. *ACS applied materials & interfaces* **2017**, *9* (3), 3178-3185.
- (247) Donsanti, F.; Kostourou, K.; Decker, F.; Ibris, N.; Salvi, A. M.; Liberatore, M.; Thissen, A.; Jaegerman, W.; Lincot, D. Alkali ion intercalation in V₂O₅: preparation and laboratory characterization of thin films produced by ALD. Surface and Interface Analysis: An International Journal devoted to the development and application of techniques for the analysis of surfaces, interfaces and thin films 2006, 38 (4), 815-818.
- (248) Badot, J.-C.; Mantoux, A.; Baffier, N.; Dubrunfaut, O.; Lincot, D. Electrical properties of V₂O₅ thin films obtained by atomic layer deposition (ALD). *Journal of Materials Chemistry* **2004**, *14* (23), 3411-3415.
- (249) Chen, X.; Pomerantseva, E.; Gregorczyk, K.; Ghodssi, R.; Rubloff, G. Cathodic ALD V₂O₅ thin films for high-rate electrochemical energy storage. *RSC advances* **2013**, *3* (13), 4294-4302.
- (250) Ko, W. C.; Kim, K. M.; Kwon, Y. J.; Choi, H.; Park, J. K.; Jeong, Y. K. ALD-assisted synthesis of V₂O₅ nanoislands on SnO₂ nanowires for improving NO₂ sensing performance. *Applied Surface Science* **2020**, *509*, 144821.
- (251) Gao, W.; Michalička, J.; Pumera, M. Hierarchical atomic layer deposited V₂O₅ on 3D printed nanocarbon electrodes for high-performance aqueous zinc-ion batteries. *Small* **2022**, *18* (1), 2105572.
- (252) Chen, X.; Wang, L.; Li, H.; Cheng, F.; Chen, J. Porous V₂O₅ nanofibers as cathode materials for rechargeable aqueous zinc-ion batteries. *Journal of Energy Chemistry* **2019**, *38*, 20-25.
- (253) Takahashi, K.; Limmer, S. J.; Wang, Y.; Cao, G. Synthesis and electrochemical properties of single-crystal V₂O₅ nanorod arrays by template-based electrodeposition. *The Journal of Physical Chemistry B* **2004**, *108* (28), 9795-9800.
- (254) Lee, J.-K.; Kim, G.-P.; Song, I. K.; Baeck, S.-H. Electrodeposition of mesoporous V₂O₅ with enhanced lithium-ion intercalation property. *Electrochemistry communications* **2009**, *11* (8), 1571-1574.

- (255) Pan, A.; Zhang, J.-G.; Nie, Z.; Cao, G.; Arey, B. W.; Li, G.; Liang, S.-q.; Liu, J. Facile synthesized nanorod structured vanadium pentoxide for high-rate lithium batteries. *Journal of Materials Chemistry* **2010**, *20* (41), 9193-9199.
- (256) Chan, C. K.; Peng, H.; Twesten, R. D.; Jarausch, K.; Zhang, X. F.; Cui, Y. Fast, completely reversible Li insertion in vanadium pentoxide nanoribbons. *Nano letters* **2007**, *7* (2), 490-495.
- (257) Li, Y.; Yao, J.; Uchaker, E.; Zhang, M.; Tian, J.; Liu, X.; Cao, G. Sn-doped V₂O₅ film with enhanced lithium-ion storage performance. *The Journal of Physical Chemistry C* **2013**, 117 (45), 23507-23514.
- (258) Li, X.; Su, Y.; Lang, X.; Li, L.; Yao, C.; Cai, K. High-performance surface optimized Mg-doped V₂O₅ (Mg@ V₂O₅) cathode material via a surfactant-assisted hydrothermal technology for lithium-ion and lithium-sulfur batteries. *Ionics* **2022**, *28* (4), 1511-1521.
- (259) Wu, F.; Wang, Y.; Ruan, P.; Niu, X.; Zheng, D.; Xu, X.; Gao, X.; Cai, Y.; Liu, W.; Shi, W. Fe-doping enabled a stable vanadium oxide cathode with rapid Zn diffusion channel for aqueous zinc-ion batteries. *Materials Today Energy* **2021**, *21*, 100842.
- (260) Ma, L.; Li, N.; Long, C.; Dong, B.; Fang, D.; Liu, Z.; Zhao, Y.; Li, X.; Fan, J.; Chen, S. Achieving both high voltage and high capacity in aqueous zinc-ion battery for record high energy density. *Advanced Functional Materials* **2019**, *29* (46), 1906142.
- (261) Ren, X.; Liu, H.; Wang, N.; Hu, L.; Sun, M.; Bo, L.; Li, Z.; Jia, C. Dual Pre-Insertion Strategy to Achieve High-Performance Vanadium Oxide toward Advanced Cylindrical Zinc Ion Batteries. *ACS Sustainable Chemistry & Engineering* **2023**, *11* (48), 16965-16974.
- (262) Zhu, D.; Liu, H.; Lv, L.; Yao, Y.; Yang, W. Hollow microspheres of V₂O₅ and Cu-doped V₂O₅ as cathode materials for lithium-ion batteries. *Scripta Materialia* **2008**, *59* (6), 642-645.
- (263) Zhang, Y.; Zou, Z.; Liu, J.; Zhang, S.; Zhang, H. Effect of Ga doping on structure and properties of V₂O₅ lithium-ion batteries. *Materials Technology* **2020**, *35* (13-14), 887-895.
- (264) Li, Z.; Zhang, C.; Liu, C.; Fu, H.; Nan, X.; Wang, K.; Li, X.; Ma, W.; Lu, X.; Cao, G. Enhanced electrochemical properties of Sn-doped V₂O₅ as a cathode material for lithium ion batteries. *Electrochimica Acta* **2016**, *222*, 1831-1838.
- (265) Chen, P.; Zheng, G.; Guo, G.; Wang, Z.; Tang, J.; Li, S.; Wen, Z.; Ji, S.; Sun, J. Ce-doped V₂O₅ microspheres with improved electrochemical performance for high-power rechargeable lithium ion batteries. *Journal of Alloys and Compounds* **2019**, 784, 574-583.
- (266) Xu, W.; Zhou, T.; Ji, J.; Li, Y.; Le, S. Enhanced Lithium Storage Performance of Al-Doped V₂O₅ Nanowire Cathode Materials. *General Chemistry* **2024**, *10* (1-2), 230005.

- (267) Kou, L.; Cao, L.; Song, J.; Huang, J.; Wang, Y.; Kajiyoshi, K. Cobalt-doped vanadium pentoxide microflowers as superior cathode for lithium-ion battery. *Jom* **2021**, *73*, 808-814.
- (268) Zeng, H.; Liu, D.; Zhang, Y.; See, K. A.; Jun, Y.-S.; Wu, G.; Gerbec, J. A.; Ji, X.; Stucky,
- G. D. Nanostructured Mn-doped V₂O₅ cathode material fabricated from layered vanadium jarosite. *Chemistry of Materials* **2015**, *27* (21), 7331-7336.
- (269) Coustier, F.; Passerini, S.; Smyrl, W. Dip-coated silver-doped V₂O₅ xerogels as host materials for lithium intercalation. *Solid State Ionics* **1997**, *100* (3-4), 247-258.
- (270) Chen, J.; Zhang, W.; Zhang, X.; Li, Z.; Ma, J.; Zhao, L.; Jian, W.; Chen, S.; Yin, J.; Lin, X. Sodium Pre-Intercalated Carbon/ V₂O₅ Constructed by Sustainable Sodium Lignosulfonate for Stable Cathodes in Zinc-Ion Batteries: A Comprehensive Study. *ChemSusChem* **2022**, *15* (14), e202200732.
- (271) Feng, H.; Wang, Y.; Qiu, W.; Liu, Z.; Tao, Y.; Lu, X. Sodium ion pre-intercalation regulates the electron density and structural stability of vanadium oxide nanowires for Ca—ion batteries. *Inorganic Chemistry Frontiers* **2024**.
- (272) Li, S.; Jia, X.; Liu, J.; Liu, Z.; Cao, G. Engineering hydrated vanadium oxide by K⁺ and Ni²⁺ incorporation for aqueous zinc ion batteries. *Materials Chemistry and Physics* **2022**, *287*, 126358.
- (273) Ding, Z.; Huang, J.; Xie, Y.; Wang, X.; Jiang, R.; Wen, J.; Li, X.; Zhang, W.; Ren, Y.; Liu, Z. Crystallization and electrochemical properties of K_xV₂O₅ nano-ribbons obtained via a solvothermal process as a promising cathode for PIBs. *Physical Chemistry Chemical Physics* **2024**, *26* (30), 20562-20575.
- (274) Li, Y.; Xu, W.; Sun, T.; Yao, J. Preparation and sodium storage performance of 2D bilayered V₂O₅· nH₂O nanomaterial with Zn²⁺ intercalation. *Journal of Electroanalytical Chemistry* **2023**, *937*, 117416.
- (275) Muthuraj, D.; Sarkar, A.; Panda, M. R.; Adil, M.; Sagdeo, A.; Mitra, S. Zirconium-doped vanadium oxide and ammonium linked layered cathode to construct a full-cell magnesium-ion battery: a realization and structural, electrochemical study. *Batteries & Supercaps* **2021**, *4* (11), 1757-1770.
- (276) Shan, L.; Yang, Y.; Zhang, W.; Chen, H.; Fang, G.; Zhou, J.; Liang, S. Observation of combination displacement/intercalation reaction in aqueous zinc-ion battery. *Energy Storage Materials* **2019**, *18*, 10-14.

- (277) Yoo, G.; Ryu, G. H.; Koo, B.-R.; An, G.-H. Interfacial defect engineering via combusted graphene in V₂O₅ nanochips to develop high-rate and stable zinc-ion batteries. *Ceramics International* **2021**, 47 (22), 31817-31825.
- (278) Qi, Z.; Xiong, T.; Chen, T.; Shi, W.; Zhang, M.; Ang, Z. W. J.; Fan, H.; Xiao, H.; Lee, W. S. V.; Xue, J. Harnessing oxygen vacancy in V₂O₅ as high performing aqueous zinc-ion battery cathode. *Journal of Alloys and Compounds* **2021**, *870*, 159403.
- (279) Zhao, D.; Zhu, Q.; Li, X.; Dun, M.; Wang, Y.; Huang, X. Oxygen vacancies of commercial V₂O₅ induced by mechanical force to enhance the diffusion of zinc ions in aqueous zinc battery. *Batteries & Supercaps* **2022**, *5* (4), e202100341.
- (280) Hu, M.; Liu, Z.; Zhang, H.; Huang, Z.-H.; Kang, F.; Lv, R. Defect engineering of vanadium pentoxide for efficient lithium-ion storage. *Electrochimica Acta* **2020**, *333*, 135513.
- (281) Ye, J. J.; Li, P. H.; Zhang, H. R.; Song, Z. Y.; Fan, T.; Zhang, W.; Tian, J.; Huang, T.; Qian, Y.; Hou, Z. Manipulating oxygen vacancies to spur ion kinetics in V₂O₅ structures for superior aqueous zinc-ion batteries. *Advanced Functional Materials* **2023**, *33* (46), 2305659.
- (282) Wang, Z.; Liang, P.; Zhang, R.; Liu, Z.; Li, W.; Pan, Z.; Yang, H.; Shen, X.; Wang, J. Oxygen-defective V₂O₅ nanosheets boosting 3D diffusion and reversible storage of zinc ion for aqueous zinc-ion batteries. *Applied Surface Science* **2021**, *562*, 150196.
- (283) Yan, M.; He, P.; Chen, Y.; Wang, S.; Wei, Q.; Zhao, K.; Xu, X.; An, Q.; Shuang, Y.; Shao, Y. Water-lubricated intercalation in V₂O₅· nH₂O for high-capacity and high-rate aqueous rechargeable zinc batteries. *Advanced materials* **2018**, *30* (1), 1703725.
- (284) Wang, J.; Curtis, C. J.; Schulz, D. L.; Zhang, J.-G. Influences of treatment temperature and water content on capacity and rechargeability of V₂O₅ xerogel films. *Journal of The Electrochemical Society* **2003**, *151* (1), A1.
- (285) Wang, Y.; Shang, H.; Chou, T.; Cao, G. Effects of Thermal Annealing on the Li+Intercalation Properties of V₂O₅· nH₂O Xerogel Films. *The Journal of Physical Chemistry B* **2005**, *109* (22), 11361-11366.
- (286) Clites, M.; W Byles, B.; Pomerantseva, E. Bilayered vanadium oxide as the host material for reversible beyond lithium ion intercalation. *Advanced Materials Letters* **2017**, *8* (6), 679-688.
- (287) Sun, Q.; Cheng, H.; Yuan, Y.; Liu, Y.; Nie, W.; Zhao, K.; Wang, K.; Yao, W.; Lu, X.; Lu, J. Uncovering the fundamental role of interlayer water in charge storage for bilayered V₂O₅· nH₂O xerogel cathode materials. *Advanced Energy Materials* **2023**, *13* (3), 2202515.

- (288) Sun, Q.; Cheng, H.; Sun, C.; Liu, Y.; Nie, W.; Zhao, K.; Lu, X.; Zhou, J. Architecting a hydrated Ca_{0. 24} V₂O₅ cathode with a facile desolvation interface for superior-performance aqueous zinc ion batteries. *ACS Applied Materials & Interfaces* **2021**, *13* (50), 60035-60045.
- (289) Liu, X.; Ma, L.; Du, Y.; Lu, Q.; Yang, A.; Wang, X. Vanadium pentoxide nanofibers/carbon nanotubes hybrid film for high-performance aqueous zinc-ion batteries. *Nanomaterials* **2021**, *11* (4), 1054.
- (290) Juggernauth, K. A.; Kim, M.; Kim, K.; Li, J.; McLane, A. A.; Lee, J.; Hart, A. J.; Ok, J. G. Carbon nanotube-mediated three-dimensional vanadium oxide nanoarchitectures with tunable morphology and translatable functionality. *Ceramics International* **2021**, *47* (22), 32342-32348.
- (291) Zhang, X.; Tang, Y.; He, P.; Zhang, Z.; Chen, T. Edge-rich vertical graphene nanosheets templating V₂O₅ for highly durable zinc ion battery. *Carbon* **2021**, *172*, 207-213.
- (292) Li, Y.; Yao, J.; Uchaker, E.; Yang, J.; Huang, Y.; Zhang, M.; Cao, G. Leaf-like V₂O₅ nanosheets fabricated by a facile green approach as high energy cathode material for lithiumion batteries. *Advanced Energy Materials* **2013**, *3* (9), 1171-1175.
- (293) Ng, S.-H.; Patey, T. J.; Büchel, R.; Krumeich, F.; Wang, J.-Z.; Liu, H.-K.; Pratsinis, S. E.; Novák, P. Flame spray-pyrolyzed vanadium oxide nanoparticles for lithium battery cathodes. *Physical Chemistry Chemical Physics* **2009**, *11* (19), 3748-3755.
- (294) Mai, L.; Xu, L.; Han, C.; Xu, X.; Luo, Y.; Zhao, S.; Zhao, Y. Electrospun ultralong hierarchical vanadium oxide nanowires with high performance for lithium ion batteries. *Nano letters* **2010**, *10* (11), 4750-4755.
- (295) Tang, Y.; Rui, X.; Zhang, Y.; Lim, T. M.; Dong, Z.; Hng, H. H.; Chen, X.; Yan, Q.; Chen, Z. Vanadium pentoxide cathode materials for high-performance lithium-ion batteries enabled by a hierarchical nanoflower structure via an electrochemical process. *Journal of Materials Chemistry A* **2013**, *I* (1), 82-88.
- (296) Seyfouri, M. M.; Binions, R. Sol-gel approaches to thermochromic vanadium dioxide coating for smart glazing application. *Solar Energy Materials and Solar Cells* **2017**, *159*, 52-65.
- (297) Zhang, Y.; Liu, X.; Xie, G.; Yu, L.; Yi, S.; Hu, M.; Huang, C. Hydrothermal synthesis, characterization, formation mechanism and electrochemical property of V₃O₇· H₂O single-crystal nanobelts. *Materials Science and Engineering: B* **2010**, *175* (2), 164-171.

- (298) Volkov, A.; Sharlaev, A.; Berezina, O. Y.; Tolstopjatova, E.; Fu, L.; Kondratiev, V. Electrospun V₂O₅ nanofibers as high-capacity cathode materials for zinc-ion batteries. *Materials Letters* **2022**, *308*, 131212.
- (299) Roex, E.; Boschini, F.; Delaval, V.; Schrijnemakers, A.; Cloots, R.; Mahmoud, A. Spraydried V₂O₅ as cathode material for high-performance aqueous zinc-ion batteries. *Journal of Electroanalytical Chemistry* **2023**, *929*, 117133.
- (300) Rehnlund, D.; Valvo, M.; Edström, K.; Nyholm, L. Electrodeposition of vanadium oxide/manganese oxide hybrid thin films on nanostructured aluminum substrates. *Journal of The Electrochemical Society* **2014**, *161* (10), D515.
- (301) Shandilya, M.; Rai, R.; Singh, J. Hydrothermal technology for smart materials. *Advances in Applied Ceramics* **2016**, *115* (6), 354-376.
- (302) Byrappa, K.; Keerthiraj, N.; Byrappa, S. M. Hydrothermal growth of crystals—design and processing. In *Handbook of Crystal Growth*, Elsevier, 2015; pp 535-575.
- (303) Yang, G.; Park, S.-J. Conventional and microwave hydrothermal synthesis and application of functional materials: A review. *Materials* **2019**, *12* (7), 1177.
- (304) Yadav, S.; Sharma, A. Importance and challenges of hydrothermal technique for synthesis of transition metal oxides and composites as supercapacitor electrode materials. *Journal of Energy Storage* **2021**, *44*, 103295.
- (305) Yang, X.; Xu, G.; Ren, Z.; Wei, X.; Chao, C.; Gong, S.; Shen, G.; Han, G. The hydrothermal synthesis and formation mechanism of single-crystalline perovskite BiFeO₃ microplates with dominant (012) facets. *CrystEngComm* **2014**, *16* (20), 4176-4182.
- (306) Byrappa, K.; Yoshimura, M. *Handbook of hydrothermal technology*; William Andrew, 2012.
- (307) Suchanek, W. L.; Lencka, M.; McCandlish, L.; Pfeffer, R. L.; Oledzka, M.; Mikulka-Bolen, K.; Rossetti, G. A.; Riman, R. E. Hydrothermal Deposition of <001> Oriented Epitaxial Pb (Zr, Ti) O₃ Films under Varying Hydrodynamic Conditions. *Crystal growth & design* **2005**, *5* (5), 1715-1727.
- (308) Gurung, A.; Qiao, Q. Solar charging batteries: advances, challenges, and opportunities. *Joule* **2018**, *2* (7), 1217-1230.
- (309) Liu, Y.-H.; Qu, J.; Chang, W.; Yang, C.-Y.; Liu, H.-J.; Zhai, X.-Z.; Kang, Y.; Guo, Y.-G.; Yu, Z.-Z. A photo-assisted reversible lithium-sulfur battery. *Energy Storage Materials* **2022**, *50*, 334-343.

- (310) Salunke, A. D.; Chamola, S.; Mathieson, A.; Boruah, B. D.; de Volder, M.; Ahmad, S. Photo-rechargeable Li-Ion batteries: device configurations, mechanisms, and materials. *ACS Applied Energy Materials* **2022**, *5* (7), 7891-7912.
- (311) Deka Boruah, B.; Mathieson, A.; Park, S. K.; Zhang, X.; Wen, B.; Tan, L.; Boies, A.; De Volder, M. Vanadium dioxide cathodes for high-rate photo-rechargeable zinc-ion batteries. *Advanced Energy Materials* **2021**, *11* (13), 2100115.
- (312) Paolella, A.; Vijh, A.; Guerfi, A.; Zaghib, K.; Faure, C. Li-ion photo-batteries: challenges and opportunities. *Journal of The Electrochemical Society* **2020**, *167* (12), 120545.
- (313) Ahmad, S.; George, C.; Beesley, D. J.; Baumberg, J. J.; De Volder, M. Photo-rechargeable organo-halide perovskite batteries. *Nano letters* **2018**, *18* (3), 1856-1862.
- (314) Tewari, N.; Shivarudraiah, S. B.; Halpert, J. E. Photorechargeable lead-free perovskite lithium-ion batteries using hexagonal Cs₃Bi₂I₉ nanosheets. *Nano Letters* **2021**, *21* (13), 5578-5585.
- (315) Kumar, A.; Thakur, P.; Sharma, R.; Puthirath, A. B.; Ajayan, P. M.; Narayanan, T. N. Photo Rechargeable Li-Ion Batteries Using Nanorod Heterostructure Electrodes. *Small* **2021**, *17* (51), 2105029.
- (316) Wang, J.; Wang, Y.; Zhu, C.; Liu, B. Photoinduced rechargeable lithium-ion battery. *ACS Applied Materials & Interfaces* **2022**, *14* (3), 4071-4078.
- (317) Kresse, G.; Hafner, J. Ab initio molecular dynamics for liquid metals. *Physical review B* **1993**, *47* (1), 558.
- (318) Kresse, G.; Hafner, J. Ab initio molecular-dynamics simulation of the liquid-metal–amorphous-semiconductor transition in germanium. *Physical Review B* **1994**, *49* (20), 14251.
- (319) Kresse, G.; Furthmüller, J. Efficiency of ab-initio total energy calculations for metals and semiconductors using a plane-wave basis set. *Computational materials science* **1996**, 6 (1), 15-50.
- (320) Kresse, G.; Furthmüller, J. Efficient iterative schemes for ab initio total-energy calculations using a plane-wave basis set. *Physical review B* **1996**, *54* (16), 11169.
- (321) Perdew, J. P.; Burke, K.; Ernzerhof, M. Generalized gradient approximation made simple. *Physical review letters* **1996**, 77 (18), 3865.
- (322) Henkelman, G.; Jónsson, H. Improved tangent estimate in the nudged elastic band method for finding minimum energy paths and saddle points. *The Journal of chemical physics* **2000**, *113* (22), 9978-9985.

- (323) Mosquera-Lois, I.; Kavanagh, S. R.; Walsh, A.; Scanlon, D. O. ShakeNBreak: Navigating the defect configurational landscape. *Journal of Open Source Software* **2022**, *7* (80), 4817.
- (324) Peng, X.; Zhang, X.; Wang, L.; Hu, L.; Cheng, S. H. S.; Huang, C.; Gao, B.; Ma, F.; Huo, K.; Chu, P. K. Hydrogenated V₂O₅ nanosheets for superior lithium storage properties. *Advanced Functional Materials* **2016**, *26* (5), 784-791.
- (325) Boruah, B. D.; Wen, B.; Nagane, S.; Zhang, X.; Stranks, S. D.; Boies, A.; De Volder, M. Photo-rechargeable zinc-ion capacitors using V₂O₅-activated carbon electrodes. *ACS Energy Letters* **2020**, *5* (10), 3132-3139.
- (326) Liao, M.; Wang, J.; Ye, L.; Sun, H.; Wen, Y.; Wang, C.; Sun, X.; Wang, B.; Peng, H. A deep-cycle aqueous zinc-ion battery containing an oxygen-deficient vanadium oxide cathode. *Angewandte Chemie* **2020**, *132* (6), 2293-2298.
- (327) Wu, D.; Zhuang, Y.; Wang, F.; Yang, Y.; Zeng, J.; Zhao, J. High-rate performance magnesium batteries achieved by direct growth of honeycomb-like V₂O₅ electrodes with rich oxygen vacancies. *Nano Research* **2021**, 1-8.
- (328) Liu, L.; Yuan, T.; Li, Z.; Chen, K.; Huang, W. Hydrogenated V₂O₅ with fast Zn-ion migration kinetics as high-performance cathode material for aqueous zinc-ion batteries. *Electrochimica Acta* **2023**, *439*, 141717.
- (329) Le, T. K.; Pham, P. V.; Dong, C.-L.; Bahlawane, N.; Vernardou, D.; Mjejri, I.; Rougier, A.; Kim, S. W. Recent advances in vanadium pentoxide (V₂O₅) towards related applications in chromogenics and beyond: fundamentals, progress, and perspectives. *Journal of Materials Chemistry C* **2022**, *10* (11), 4019-4071.
- (330) Ling, C.; Guo, T.; Shan, M.; Zhao, L.; Sui, H.; Ma, S.; Xue, Q. Oxygen vacancies enhanced photoresponsive performance of ZnO nanoparticles thin film/Si heterojunctions for ultraviolet/infrared photodetector. *Journal of Alloys and Compounds* **2019**, 797, 1224-1231.
- (331) Palanisamy, K.; Um, J. H.; Jeong, M.; Yoon, W.-S. Porous V₂O₅/RGO/CNT hierarchical architecture as a cathode material: Emphasis on the contribution of surface lithium storage. *Scientific reports* **2016**, *6* (1), 31275.
- (332) Denis, Y.; Fietzek, C.; Weydanz, W.; Donoue, K.; Inoue, T.; Kurokawa, H.; Fujitani, S. Study of LiFePO₄ by cyclic voltammetry. *Journal of the electrochemical society* **2007**, *154* (4), A253.
- (333) Ma, W.; Zhou, B.; Wang, J.; Zhang, X.; Jiang, Z. Effect of oxygen vacancy on Li-ion diffusion in a V₂O₅ cathode: a first-principles study. *Journal of Physics D: Applied Physics* **2013**, *46* (10), 105306.

- (334) Mahmood, N.; Tang, T.; Hou, Y. Nanostructured anode materials for lithium ion batteries: progress, challenge and perspective. *Advanced Energy Materials* **2016**, *6* (17), 1600374.
- (335) Passerini, S.; Scrosati, B. Lithium and lithium-ion batteries: challenges and prospects. *The Electrochemical Society Interface* **2016**, *25* (3), 85.
- (336) Huang, Q.; Ni, S.; Jiao, M.; Zhong, X.; Zhou, G.; Cheng, H. M. Aligned Carbon-Based Electrodes for Fast-Charging Batteries: A Review. *Small* **2021**, *17* (48), 2007676.
- (337) Diouf, B.; Pode, R. Potential of lithium-ion batteries in renewable energy. *Renewable Energy* **2015**, *76*, 375-380.
- (338) Chen, Q.; Jin, J.; Kou, Z.; Liao, C.; Liu, Z.; Zhou, L.; Wang, J.; Mai, L. Zn2+ pre-intercalation stabilizes the tunnel structure of MnO₂ nanowires and enables zinc-ion hybrid supercapacitor of battery-level energy density. *Small* **2020**, *16* (14), 2000091.
- (339) Zhang, L.; Chen, L.; Zhou, X.; Liu, Z. Towards High-Voltage Aqueous Metal-Ion Batteries Beyond 1.5 V: The Zinc/Zinc Hexacyanoferrate System. *Advanced Energy Materials* **2015**, *5* (2).
- (340) Chen, H.; Cheng, S.; Chen, D.; Jiang, Y.; Ang, E. H.; Liu, W.; Feng, Y.; Rui, X.; Yu, Y. Vanadate-based electrodes for rechargeable batteries. *Materials Chemistry Frontiers* **2021**, *5* (4), 1585-1609.
- (341) Han, C.; Li, H.; Shi, R.; Zhang, T.; Tong, J.; Li, J.; Li, B. Organic quinones towards advanced electrochemical energy storage: recent advances and challenges. *Journal of Materials Chemistry A* **2019**, *7* (41), 23378-23415.
- (342) Deng, L.; Niu, X.; Ma, G.; Yang, Z.; Zeng, L.; Zhu, Y.; Guo, L. Layered potassium vanadate K_{0.5}V₂O₅ as a cathode material for nonaqueous potassium ion batteries. *Advanced Functional Materials* **2018**, *28* (49), 1800670.
- (343) Xu, X.; Duan, M.; Yue, Y.; Li, Q.; Zhang, X.; Wu, L.; Wu, P.; Song, B.; Mai, L. Bilayered Mg_{0. 25} V₂O₅· H₂O as a stable cathode for rechargeable Ca-ion batteries. *ACS Energy Letters* **2019**, *4* (6), 1328-1335.
- (344) Zheng, J.; Liu, C.; Tian, M.; Jia, X.; Jahrman, E. P.; Seidler, G. T.; Zhang, S.; Liu, Y.; Zhang, Y.; Meng, C. Fast and reversible zinc ion intercalation in Al-ion modified hydrated vanadate. *Nano Energy* **2020**, *70*, 104519.
- (345) Xu, L.; Zhang, Y.; Zheng, J.; Jiang, H.; Hu, T.; Meng, C. Ammonium ion intercalated hydrated vanadium pentoxide for advanced aqueous rechargeable Zn-ion batteries. *Materials Today Energy* **2020**, *18*, 100509.

- (346) He, P.; Zhang, G.; Liao, X.; Yan, M.; Xu, X.; An, Q.; Liu, J.; Mai, L. Sodium ion stabilized vanadium oxide nanowire cathode for high-performance zinc-ion batteries. *Advanced Energy Materials* **2018**, *8* (10), 1702463.
- (347) Lu, Y.; Wang, T.; Naresh, N.; Borowiec, J.; Parkin, I. P.; Boruah, B. D. Pre-doped cations in V₂O₅ for high-performance Zn-ion batteries. *Nano Research Energy* **2024**.
- (348) Li, Y.; Huang, Z.; Kalambate, P. K.; Zhong, Y.; Huang, Z.; Xie, M.; Shen, Y.; Huang, Y. V₂O₅ nanopaper as a cathode material with high capacity and long cycle life for rechargeable aqueous zinc-ion battery. *Nano Energy* **2019**, *60*, 752-759.
- (349) Boruah, B. D.; Wen, B.; De Volder, M. Molybdenum disulfide—zinc oxide photocathodes for photo-rechargeable zinc-ion batteries. *ACS nano* **2021**, *15* (10), 16616-16624.
- (350) Liu, F.; Chen, Z.; Fang, G.; Wang, Z.; Cai, Y.; Tang, B.; Zhou, J.; Liang, S. V₂O₅ nanospheres with mixed vanadium valences as high electrochemically active aqueous zinc-ion battery cathode. *Nano-Micro Letters* **2019**, *11*, 1-11.
- (351) Chen, H.; Huang, J.; Tian, S.; Liu, L.; Qin, T.; Song, L.; Liu, Y.; Zhang, Y.; Wu, X.; Lei, S. Interlayer modification of pseudocapacitive vanadium oxide and Zn (H₂O)_n²⁺ migration regulation for ultrahigh rate and durable aqueous zinc-ion batteries. *Advanced Science* **2021**, *8* (14), 2004924.
- (352) Tian, M.; Liu, C.; Zheng, J.; Jia, X.; Jahrman, E. P.; Seidler, G. T.; Long, D.; Atif, M.; Alsalhi, M.; Cao, G. Structural engineering of hydrated vanadium oxide cathode by K+incorporation for high-capacity and long-cycling aqueous zinc ion batteries. *Energy Storage Materials* **2020**, *29*, 9-16.
- (353) Chen, D.; Rui, X.; Zhang, Q.; Geng, H.; Gan, L.; Zhang, W.; Li, C.; Huang, S.; Yu, Y. Persistent zinc-ion storage in mass-produced V₂O₅ architectures. *Nano Energy* **2019**, *60*, 171-178.
- (354) Zhou, J.; Shan, L.; Wu, Z.; Guo, X.; Fang, G.; Liang, S. Investigation of V₂O₅ as a low-cost rechargeable aqueous zinc ion battery cathode. *Chemical communications* **2018**, *54* (35), 4457-4460.
- (355) She, B.; Shan, L.; Chen, H.; Zhou, J.; Guo, X.; Fang, G.; Cao, X.; Liang, S. Investigation of sodium vanadate as a high-performance aqueous zinc-ion battery cathode. *J. Energy Chem.* **2019**, *37*, 172-175.
- (356) Cao, J.; Zhang, D.; Yue, Y.; Pakornchote, T.; Bovornratanaraks, T.; Sawangphruk, M.; Zhang, X.; Qin, J. Revealing the impacts of oxygen defects on Zn²⁺ storage performance in V₂O₅. *Materials Today Energy* **2021**, *21*, 100824.

- (357) Liu, C.; Li, R.; Liu, W.; Shen, G.; Chen, D. Chitosan-assisted fabrication of a network C@ V₂O₅ cathode for high-performance Zn-ion batteries. *ACS Applied Materials & Interfaces* **2021**, *13* (31), 37194-37200.
- (358) Liu, M.; Li, Z.; Zhang, Y. Na+ Intercalated V₂O₅ Derived from V-MOF as High-Performance Cathode for Aqueous Zinc-Ion Batteries. *Journal of The Electrochemical Society* **2023**, *170* (11), 110524.
- (359) Yang, Y.; Albu, S. P.; Kim, D.; Schmuki, P. Enabling the anodic growth of highly ordered V₂O₅ nanoporous/nanotubular structures. *Angewandte Chemie-International Edition* **2011**, *50* (39), 9071.
- (360) Cao, A. M.; Hu, J. S.; Liang, H. P.; Wan, L. J. Self-assembled vanadium pentoxide (V₂O₅) hollow microspheres from nanorods and their application in lithium-Ion batteries. *Angewandte Chemie International Edition* **2005**, *44* (28), 4391-4395.
- (361) Yang, Y.; Li, L.; Fei, H.; Peng, Z.; Ruan, G.; Tour, J. M. Graphene nanoribbon/ V₂O₅ cathodes in lithium-ion batteries. *ACS applied materials & interfaces* **2014**, *6* (12), 9590-9594.
- (362) Sato, Y.; Nomura, T.; Tanaka, H.; Kobayakawa, K. Charge-Discharge Characteristics of Electrolytically Prepared V₂O₅ as a Cathode Active Material of Lithium Secondary Battery. *Journal of The Electrochemical Society* **1991**, *138* (9), L37.
- (363) Wang, Y.; Zhang, H. J.; Siah, K. W.; Wong, C. C.; Lin, J.; Borgna, A. One pot synthesis of self-assembled V₂O₅ nanobelt membrane via capsule-like hydrated precursor as improved cathode for Li-ion battery. *Journal of Materials Chemistry* **2011**, *21* (28), 10336-10341.
- (364) Fu, Q.; Zhao, H.; Sarapulova, A.; Dsoke, S. V₂O₅ as a versatile electrode material for postlithium energy storage systems. *Applied Research* **2023**, *2* (3), e202200070.
- (365) Thakur, A.; Kaur, H.; Sharma, P. K.; Kumar, A. Vanadium-Based Nanostructure Materials for Advanced Lithium-Ion Batteries: A Review. *Nanostructured Materials for Energy Storage* **2024**, *2*, 563-600.
- (366) Sun, Y.; Xie, Z.; Li, Y. Enhanced lithium storage performance of V₂O₅ with oxygen vacancy. *RSC advances* **2018**, 8 (69), 39371-39376.
- (367) Yao, J.; Yin, Z.; Zou, Z.; Li, Y. Y-doped V₂O₅ with enhanced lithium storage performance. *Rsc Advances* **2017**, *7* (51), 32327-32335.
- (368) Yu, H.; Rui, X.; Tan, H.; Chen, J.; Huang, X.; Xu, C.; Liu, W.; Denis, Y.; Hng, H. H.; Hoster, H. E. Cu doped V₂O₅ flowers as cathode material for high-performance lithium ion batteries. *Nanoscale* **2013**, *5* (11), 4937-4943.

- (369) Cheah, Y. L.; Aravindan, V.; Madhavi, S. Improved elevated temperature performance of Al-intercalated V₂O₅ electrospun nanofibers for lithium-ion batteries. *ACS Applied Materials & Interfaces* **2012**, *4* (6), 3270-3277.
- (370) Vinothini, A.; Conceptulaization, A. M.; Arulkumar, E.; Vedhi, C.; Thanikaikarasan, S. Green route synthesis of transition metal doped V₂O₅ nanoparticles, with emerging biomedical applications. *Results in Chemistry* **2024**, *7*, 101373.
- (371) Neelima, M.; Vandana, S.; Kathirvel, A.; Sivakumar, M.; Maheswari, A. U. Titanium doped V₂O₅ nanostructures by chemical synthesis for photocatalytic performance enhancement. *Optik* **2022**, *252*, 168516.
- (372) Hevia, S. A.; Orive, J.; Guzman, F.; Cisternas, E.; Dietrich, F.; Villarroel, R.; Lisoni, J. High performance of V₂O₅ thin film electrodes for lithium-ion intercalation. *Applied Surface Science* **2022**, *576*, 151710.
- (373) Yan, M.; Zhao, L.; Zhao, K.; Wei, Q.; An, Q.; Zhang, G.; Wei, X.; Ren, W.; Mai, L. The capturing of ionized oxygen in sodium vanadium oxide nanorods cathodes under operando conditions. *Advanced Functional Materials* **2016**, *26* (36), 6555-6562.
- (374) Baddour-Hadjean, R.; Bach, S.; Emery, N.; Pereira-Ramos, J. The peculiar structural behaviour of β-Na_{0.33}V₂O₅ upon electrochemical lithium insertion. *Journal of Materials Chemistry* **2011**, *21* (30), 11296-11305.
- (375) Zhang, J.; Liu, R.; Huang, C.; Dong, C.; Xu, L.; Yuan, L.; Lu, S.; Wang, L.; Zhang, L.; Chen, L. Oxygen defect engineering and amphipathic molecules intercalation co-boosting fast kinetics and stable structure of S-doped (NH₄)₂V₁₀O₂₅· 8H₂O free-standing cathode for aqueous Zn-ion storage. *Nano Energy* **2024**, *122*, 109301.
- (376) Paredes-Pérez, L. F.; Mendoza, A.; García-García, A.; Serrano-De la Rosa, L. E.; Méndez-Rojas, M. A.; Melendez, F. J.; Castro, M. E.; González-Vergara, E. Guanidinium and spermidinium decavanadates: as small biomimetic models to understand non-covalent interactions between decavanadate and arginine and lysine side chains in proteins. *Frontiers in Chemical Biology* **2024**, *3*, 1451167.
- (377) Bulushev, D. A.; Rainone, F.; Kiwi-Minsker, L.; Renken, A. Influence of potassium doping on the formation of vanadia species in V/Ti oxide catalysts. *Langmuir* **2001**, *17* (17), 5276-5282.
- (378) Onodera, S.; Ikegami, Y. Infrared and Raman spectra of ammonium, potassium, rubidium, and cesium metavanadates. *Inorganic Chemistry* **1980**, *19* (3), 615-618.

- (379) Geisler, S.; Vauthey, I.; Farusseng, D.; Zanthoff, H.; Muhler, M. Advances in catalyst development for oxidative ethylbenzene dehydrogenation. *Catalysis today* **2003**, *81* (3), 413-424.
- (380) Fan, K.; Chen, H.; Ji, Y.; Huang, H.; Claesson, P. M.; Daniel, Q.; Philippe, B.; Rensmo, H.; Li, F.; Luo, Y. Nickel–vanadium monolayer double hydroxide for efficient electrochemical water oxidation. *Nature communications* **2016**, *7* (1), 11981.
- (381) Tran, N. Q.; Bui, V. Q.; Le, H. M.; Kawazoe, Y.; Lee, H. Anion–cation double substitution in transition metal dichalcogenide to accelerate water dissociation kinetic for electrocatalysis. *Advanced Energy Materials* **2018**, *8* (15), 1702139.
- (382) Liu, D.; Liu, Y.; Pan, A.; Nagle, K. P.; Seidler, G. T.; Jeong, Y.-H.; Cao, G. Enhanced lithium-ion intercalation properties of V₂O₅ xerogel electrodes with surface defects. *The Journal of Physical Chemistry C* **2011**, *115* (11), 4959-4965.
- (383) Cui, Y.; Xue, Y.; Zhang, R.; Zhang, J.; Li, X. a.; Zhu, X. Vanadium–cobalt oxyhydroxide shows ultralow overpotential for the oxygen evolution reaction. *Journal of Materials Chemistry A* **2019**, 7 (38), 21911-21917.
- (384) Zhang, H.; Chen, B.; Jiang, H.; Duan, X.; Zhu, Y.; Li, C. Boosting water oxidation electrocatalysts with surface engineered amorphous cobalt hydroxide nanoflakes. *Nanoscale* **2018**, *10* (27), 12991-12996.
- (385) Xu, L.; Jiang, Q.; Xiao, Z.; Li, X.; Huo, J.; Wang, S.; Dai, L. Plasma-engraved Co₃O₄ nanosheets with oxygen vacancies and high surface area for the oxygen evolution reaction. *Angewandte Chemie* **2016**, *128* (17), 5363-5367.
- (386) Baddour-Hadjean, R.; Marzouk, A.; Pereira-Ramos, J. Structural modifications of Li_x V_2O_5 in a composite cathode ($0 \le x < 2$) investigated by Raman microspectrometry. *Journal of Raman Spectroscopy* **2012**, *43* (1), 153-160.
- (387) Song, H.; Liu, C.; Zhang, C.; Cao, G. Self-doped V⁴⁺–V₂O₅ nanoflake for 2 Li-ion intercalation with enhanced rate and cycling performance. *Nano Energy* **2016**, *22*, 1-10.
- (388) Zhang, W.; Zuo, C.; Tang, C.; Tang, W.; Lan, B.; Fu, X.; Dong, S.; Luo, P. The current developments and perspectives of V₂O₅ as cathode for rechargeable aqueous zinc-ion batteries. *Energy Technology* **2021**, *9* (2), 2000789.
- (389) Liu, S.; Zhang, R.; Wang, C.; Mao, J.; Chao, D.; Zhang, C.; Zhang, S.; Guo, Z. Zinc ion Batteries: Bridging the Gap from Academia to Industry for Grid-Scale Energy Storage. *Angewandte Chemie International Edition* **2024**, *63* (17), e202400045.

- (390) Wulandari, T.; Fawcett, D.; Majumder, S. B.; Poinern, G. E. Lithium-based batteries, history, current status, challenges, and future perspectives. *Battery Energy* **2023**, *2* (6), 20230030.
- (391) Blanc, L. E.; Kundu, D.; Nazar, L. F. Scientific challenges for the implementation of Znion batteries. *Joule* **2020**, *4* (4), 771-799.
- (392) Li, G.; Sun, L.; Zhang, S.; Zhang, C.; Jin, H.; Davey, K.; Liang, G.; Liu, S.; Mao, J.; Guo, Z. Developing cathode materials for aqueous zinc ion batteries: challenges and practical prospects. *Advanced Functional Materials* **2024**, *34* (5), 2301291.
- (393) Zhu, Y.-r.; Zeng, S.-h.; Deng, W.-j.; Si, J.-t.; Pan, B.-c.; Chen, C.-h. Heterovalent dualion interlayer-confined vanadium oxide nanobelts as a stable cathode for zinc storage. *Journal of Energy Storage* **2024**, *97*, 112836.
- (394) Brezesinski, T.; Wang, J.; Tolbert, S. H.; Dunn, B. Ordered mesoporous α -MoO₃ with iso-oriented nanocrystalline walls for thin-film pseudocapacitors. *Nature materials* **2010**, *9* (2), 146-151.

Publication List

Publications related to this thesis:

- Lu, Y.; Andersen, H.; Wu, R.; Ganose, A. M.; Wen, B.; Pujari, A.; Wang, T.; Borowiec, J.; Parkin, I. P.; De Volder, M. Hydrogenated V2O5 with Improved Optical and Electrochemical Activities for Photo-Accelerated Lithium-Ion Batteries. *Small* 2024, 20 (14), 2308869.
- Lu, Y.; Wang, T.; Naresh, N.; Borowiec, J.; Parkin, I. P.; Boruah, B. D. Pre-doped cations in V 2 O 5 for high-performance Zn-ion batteries. *Nano Research Energy* 2024, DOI: 10.26599/NRE.2024.9120125

Other publications during PhD study:

- Fan, Y.; Pinnock, I.; Hu, X.; Wang, T.; Lu, Y.; Li, R.; Wang, M.; Parkin, I. P.; De Volder, M.; Boruah, B. D. Planar Zn-Ion Microcapacitors with High-Capacity Activated Carbon Anode and VO2 (B) Cathode. *Nano Letters* 2024, 24 (35), 10874-10882.
- 2. Kiatikajornjumroen, S.; Liu, X.; Lu, Y.; Deka Boruah, B. 3D Framework Carbon for High-Performance Zinc-Ion Capacitors. *Micromachines* **2023**, *14* (7), 1476.
- 3. Liu, X.; Andersen, H.; Lu, Y.; Wen, B.; Parkin, I. P.; De Volder, M.; Boruah, B. D. Porous Carbon Coated on Cadmium Sulfide-Decorated Zinc Oxide Nanorod Photocathodes for Photo-accelerated Zinc Ion Capacitors. *ACS Applied Materials & Interfaces* 2023, *15* (5), 6963-6969.

Manuscript in preparation:

1. Lu Y. et al. Development of High-performance Cations Doped V₂O₅ Cathode for Lithiumion Batteries